

②

Bulletin 53
(Part 2 of 4 Parts)

A134453

THE SHOCK AND VIBRATION BULLETIN

Part 2
Fluid-Structure Dynamics
and Dynamic Analysis

MAY 1983

A Publication of
THE SHOCK AND VIBRATION
INFORMATION CENTER
Naval Research Laboratory, Washington, D.C.



DTIC
ELECTE
NOV 7 1983
S B D

Office of
The Under Secretary of Defense
for Research and Engineering

Approved for public release; distribution unlimited.

DTIC FILE COPY

83 11 / 03 146

SYMPOSIUM MANAGEMENT

THE SHOCK AND VIBRATION INFORMATION CENTER

Henry C. Pusey, Director

Rudolph H. Volin

J. Gordan Showalter

Jessica Hileman

Elizabeth A. McLaughlin

Mary K. Gobbett

Bulletin Production

Publications Branch, Technical Information Division,
Naval Research Laboratory

Bulletin 53
(Part 2 of 4 Parts)

THE SHOCK AND VIBRATION BULLETIN

MAY 1983

**A Publication of
THE SHOCK AND VIBRATION
INFORMATION CENTER
Naval Research Laboratory, Washington, D.C.**

The 53rd Symposium on Shock and Vibration was held at the Radisson Ferncroft Hotel, Danvers, MA on October 26-28, 1982. The U.S. Army Materials and Mechanics Research Center, Watertown, MA, was the host.

**Office of
The Under Secretary of Defense
for Research and Engineering**

CONTENTS

PAPERS APPEARING IN PART 2

Fluid Structure Dynamics

EXPERIMENTAL VALIDATION OF THE COMPONENT SYNTHESIS METHOD FOR PREDICTING VIBRATION OF LIQUID-FILLED PIPING	1
F. J. Hatfield and D. C. Wiggert, Michigan State University, East Lansing, MI, and L. C. Davidson, David Taylor Naval Ship Research and Development Center, Annapolis, MD	
ACOUSTIC RESPONSES OF COUPLED FLUID-STRUCTURE SYSTEM BY ACOUSTIC-STRUCTURAL ANALOGY	11
Y. S. Shin, Naval Postgraduate School, Monterey, CA and M. K. Chargin, NASA Ames Research Center, Moffett Field, CA	
FLUID-STRUCTURE INTERACTION BY THE METHOD OF CHARACTERISTICS	23
F. D. Hains, Naval Surface Weapons Center, White Oak, Silver Spring, MD	
A SOLUTION TO THE AXISYMMETRIC BULK CAVITATION PROBLEM	33
F. A. Costanzo and J. D. Gordon, David Taylor Naval Ship Research and Development Center, Underwater Explosions Research Division, Portsmouth, VA	
A SOLUTION TO THE ONE-DIMENSIONAL BULK CAVITATION PROBLEM	53
B. M. Stow and J. D. Gordon, David Taylor Naval Ship Research and Development Center, Underwater Explosions Research Division, Portsmouth, VA	

Dynamic Analysis

DYNAMIC SIMULATION OF STRUCTURAL SYSTEMS WITH ISOLATED NONLINEAR COMPONENTS	63
L. Minnetyan, Clarkson College of Technology, Potsdam, NY, J. A. Lyons, Niagara Mohawk Power Corporation, Syracuse, NY, and T. G. Gerardi, AFWAL/FIX, Wright-Patterson AFB, OH	
EXPERIMENTAL AND ANALYTICAL INVESTIGATION OF ACTIVE LOADS CONTROL FOR AIRCRAFT LANDING GEAR	79
D. L. Morris, Air Force Wright Aeronautical Laboratories, Wright-Patterson AFB, OH, and J. R. McGehee, NASA Langley Research Center, Hampton, VA	
ON THE MODAL IDENTIFICATION OF MULTIPLE DEGREE OF FREEDOM SYSTEMS FROM EXPERIMENTAL DATA	91
D. I. G. Jones, Materials Laboratory, AFWAL/MLLN, Wright-Patterson AFB, OH, and A. Muszynska, Bently Nevada Corporation, Minden, NV	
AN APPLICATION OF THE KINETIC ENERGY CALCULATION AS AN AID IN MODE IDENTIFICATION	111
G. J. Brown and G. R. Parker, Hughes Helicopters, Inc., Culver City, CA	
DYNAMICS OF A SIMPLE SYSTEM SUBJECTED TO RANDOM IMPACT	125
T. T. Soong, State University of New York, Amherst Campus, Buffalo, NY	
APPROXIMATE NUMERICAL PREDICTIONS OF IMPACT-INDUCED STRUCTURAL RESPONSES	131
R. W. Wu, Lockheed Missiles and Space Co., Inc., Sunnyvale, CA	
ON THE FACE-SHEAR VIBRATIONS OF CONTOURED CRYSTAL PLATES	139
S. De, National Research Institute, W. Bengal, India	
DYNAMIC BEHAVIOR OF COMPOSITE LAYERED BEAMS BY THE FINITE ELEMENT METHOD	151
P. Trompette, R. Gaertner, I.N.S.A., Laboratoire de Mecanique des Structures, Villeurbanne, France	

PAPERS APPEARING IN PART 1

WELCOME

Dr. Edward Wright, Director, U.S. Army Materials and Mechanics Research Center, Watertown, MA

Keynote Address

KEYNOTE ADDRESS — AVRADCOM RESEARCH IN HELICOPTER VIBRATIONS

Major General Story C. Stevens, Commanding General, U.S. Army Aviation Research and Development Command, St. Louis, MO

Invited Papers

TECHNICAL INFORMATION SUPPORT FOR SURVIVABILITY

Henry C. Pusey, Rudolph H. Volin and J. Gordan Showalter, Shock and Vibration Information Center, Naval Research Laboratory, Washington, DC

AIRCRAFT SURVIVABILITY

Dale B. Atkinson, Chairman, Joint Technical Coordinating Group on Aircraft Survivability, Naval Air Systems Command, Washington, DC

UNITED STATES FLEET SURVIVABILITY OF U.S. NAVAL COMBATANT SHIPS

Captain F. S. Hering, USN, Director, Survivability and Readiness Subgroup, Naval Sea Systems Command, Washington, DC

ELIAS KLEIN MEMORIAL LECTURE —

VIBRATION CHALLENGES IN MICROELECTRONICS MANUFACTURING

Dr. Eric Ungar, Bolt Beranek and Newman, Inc., Cambridge, MA and
Collin G. Gordon, Bolt Beranek and Newman, Inc., Canoga Park, CA

MAURICE BIOT 50TH ANNIVERSARY LECTURE —

THE EVOLUTION OF SPECTRAL TECHNIQUES IN NAVY SHOCK DESIGN

Gene M. Remmers, David Taylor Naval Ship Research and Development Center, Bethesda, MD

MATERIALS IMPLICATIONS OF ADVANCED THERMAL AND KINETIC ENERGY THREATS

Robert Fitzpatrick and John Mescall, U.S. Army Materials and Mechanics Research Center, Watertown, MA

SUMMARY OF MIL-STD-810D PANEL SESSION

Pyrotechnic Shock and Shock Testing and Analysis

PYROTECHNIC SHOCK TEST AND TEST SIMULATION

M. E. Hughes, Martin Marietta Corporation, Orlando, FL

STRAIN HISTORIES ASSOCIATED WITH STAGE SEPARATION SYSTEMS USING LINEAR SHAPED CHARGE

D. R. Powers, McDonnell Douglas Astronautics Company, Huntington Beach, CA

SHOCK SPECTRAL ANALYSIS BY PERSONAL COMPUTER, USING THE IFT ALGORITHM

C. T. Morrow, Consultant, Encinitas, CA

AN EXPLOSIVE DRIVEN SHOCK TUBE FOR VERIFYING SURVIVAL OF RADIOISOTOPE

HEAT SOURCES DURING SPACE SHUTTLE LAUNCH ACCIDENT

F. H. Mathews, Sandia National Laboratories, Albuquerque, NM

CALCULATION OF THE SHOCK WAVE FROM A PENTOLITE TAPERED CHARGE

J. T. Gordon and D. K. Davison, Physics International Company, San Leandro, CA

EFFECT OF MEASUREMENT SYSTEM PHASE RESPONSE ON SHOCK SPECTRUM COMPUTATION

P. L. Walter, Sandia National Laboratories, Albuquerque, NM

EFFICIENT ALGORITHMS FOR CALCULATING SHOCK SPECTRA ON GENERAL PURPOSE COMPUTERS

F. W. Cox, Computer Sciences Corporation, Houston, TX

EVALUATION AND CONTROL OF CONSERVATISM IN DROP TABLE SHOCK TESTS

T. J. Baca, Sandia National Laboratories, Albuquerque, NM

ICE IMPACT TESTING OF SPACE SHUTTLE THERMAL PROTECTION SYSTEM MATERIALS

P. H. DeWolfe, Rockwell International, Downey, CA

PROCEDURES FOR SHOCK TESTING ON NAVY CLASS H. I. SHOCK MACHINES

E. W. Clements, Naval Research Laboratory, Washington, DC

EQUIVALENT NUCLEAR YIELD AND PRESSURE BY THE RESPONSE SPECTRUM FIT METHOD

J. R. Bruce and H. E. Lindberg, SRI International, Menlo Park, CA

PAPERS APPEARING IN PART 3

Vehicle Dynamics

RESEARCHING THE MAN-MACHINE SYSTEM AS A FUNCTION OF SOIL-ENVIRONMENT SYSTEM

A. Massinas, University of Patras, Patras, Greece, and P. Drakatos, Visiting Professor, M.I.T., Cambridge, MA

A STOCHASTIC MODEL FOR THE MAN-MACHINE-SOIL-ENVIRONMENT SYSTEM (MMSES) AND THE INFLUENCE OF VIBRATIONS

A. Massinas, University of Patras, Patras, Greece, and P. Drakatos, Visiting Professor, M.I.T., Cambridge, MA

AN OPTIMUM SEAT-SUSPENSION FOR OFF-ROAD VEHICLES

S. Rakheja and S. Sankar, Concordia University, Montreal, Canada

FREQUENCY AND TIME DOMAIN ANALYSES OF OFF-ROAD MOTORCYCLE SUSPENSION

M. van Vliet, S. Sankar and C. N. Bapat, Concordia University, Montreal, Canada

BRAKING-TURNING-MANEUVERING STABILITY OF HEAVY TRANSPORTERS

P. Woods, Martin Marietta Corporation, Denver, CO

ACOUSTIC ENVIRONMENTS FOR JPL SHUTTLE PAYLOADS BASED ON EARLY FLIGHT DATA

M. R. O'Connell and D. L. Kern, Jet Propulsion Laboratory, California Institute of Technology, Pasadena, CA

COMPUTER AIDED SYNTHESIS OF A SATELLITE ANTENNA STRUCTURE WITH PROBABILISTIC CONSTRAINTS

V. K. Jha, SPAR Aerospace Limited, Ste. Anne de Bellevue, Quebec, Canada, and

T. S. Sankar and R. B. Bhat, Concordia University, Montreal, Quebec, Canada

DYNAMIC BEHAVIOUR OF A SATELLITE ANTENNA STRUCTURE IN RANDOM VIBRATION ENVIRONMENT

V. K. Jha, SPAR Aerospace Limited, Ste. Anne de Bellevue, Quebec, Canada, and

T. S. Sankar and R. B. Bhat, Concordia University, Montreal, Quebec, Canada

INVESTIGATION OF THE ACOUSTIC CHARACTERISTICS OF AIRCRAFT/ENGINES OPERATING IN A DRY-COOLED JET ENGINE MAINTENANCE TEST FACILITY

V. R. Müller, G. A. Pizak, J. M. Chinn, Air Force Wright Aeronautical Laboratories, Wright-Patterson AFB, OH, and

R. J. Reilly, Independent Consultant, St. Paul, MN

Vibration: Test and Criteria

CRITERIA FOR ACCELERATED RANDOM VIBRATION TESTS WITH NON-LINEAR DAMPING

R. G. Lambert, General Electric Company, Utica, NY

VIBRATION TEST ENVIRONMENTS FOR ELECTRONICS MOUNTED IN A REMOTELY PILOTED VEHICLE

V. R. Beatty, Harris Corporation, Melbourne, FL

VIBRATION TEST SOFTWARE FOR ELECTRONICS MOUNTED IN A REMOTELY PILOTED VEHICLE

S. M. Landro, Harris Corporation, Melbourne, FL

AUTOMATED VIBRATION SCHEDULE DEVELOPMENT FOR WHEELED AND TRACKED VEHICLES AT ABERDEEN PROVING GROUND

W. H. Connon, III, Materiel Testing Directorate, Aberdeen Proving Ground, MD

TESTING FOR SEVERE AERODYNAMICALLY INDUCED VIBRATION ENVIRONMENTS

H. N. Roos and G. R. Waymon, McDonnell Douglas Corporation, St. Louis, MO

EVALUATION OF MODAL TESTING TECHNIQUES FOR SPACECRAFT STRUCTURES

K. Shiraki and H. Mitsuma, National Space Development Agency of Japan, Tokyo, Japan

A FREE-FREE MODAL SURVEY SUSPENSION SYSTEM FOR LARGE TEST ARTICLES

R. Webb, Martin Marietta Corporation, Denver, CO

PAPERS APPEARING IN PART 4

Damping

EXPERIMENTAL INVESTIGATION OF CONTROLLING VIBRATIONS USING MULTI-UNIT IMPACT DAMPERS
C. N. Bapat and S. Sankar, Concordia University, Montreal, Quebec, Canada, and
N. Popplewell, University of Manitoba, Winnipeg, Manitoba, Canada

AS EXPERIMENTAL HYBRID MODEL FOR A BILINEAR HYSTERETIC SYSTEM
K. R. McLachlan, Department of Civil Engineering, N. Popplewell and W. J. McAllister, Department of
Mechanical Engineering, University of Manitoba, Winnipeg, Manitoba, Canada, and
C. S. Chang, Institute of Mechanics, Peking, People's Republic of China

MEASUREMENT AND ANALYSIS OF PLATFORM DAMPING IN ADVANCED TURBINE BLADE RESONANCE
T. J. Lagnese and D. I. G. Jones, Air Force Wright Aeronautical Laboratories, AFWAL/MLLN,
Wright-Patterson AFB, OH

A VIBRATION DAMPING TREATMENT FOR HIGH TEMPERATURE GAS TURBINE APPLICATIONS
A. D. Nashif, Anatrol Corporation, Cincinnati, OH, W. D. Brentnall, Solar Turbines, Inc., San Diego, CA,
and D. I. G. Jones, Air Force Wright Aeronautical Laboratories, AFWAL/MLLN, Wright-Patterson AFB, OH

EXPERIMENTAL MEASUREMENT OF MATERIAL DAMPING USING DIGITAL TEST EQUIPMENT
P. W. Whaley and P. S. Chen, University of Nebraska, Lincoln, NB

ELECTRONIC DAMPING OF A LARGE OPTICAL BENCH
R. L. Forward, Hughes Research Laboratories, Malibu, CA, C. J. Swigert, Hughes Aircraft Company,
Culver City, CA, and M. Obal, Air Force Weapons Laboratory, Kirtland AFB, NM

MEASUREMENT OF STRUCTURAL DAMPING USING THE RANDOM DECREMENT TECHNIQUE
J. C. S. Yang, N. G. Dagalakia, University of Maryland, College Park, MD, and
G. C. Everstine, Y. F. Wang, David Taylor Naval Ship Research and Development Center, Bethesda, MD

DAMPED PNEUMATIC SPRING AS SHOCK ISOLATOR: GENERALIZED ANALYSIS AND DESIGN PROCEDURE
M. S. Hundal, University of Vermont, Burlington, VT

Machinery Dynamics

ANALYTICAL AND EXPERIMENTAL INVESTIGATION OF ROTATING BLADE RESPONSE
DUE TO NOZZLE PASSING FREQUENCY EXCITATION
J. S. Rao, Indian Institute of Technology, New Delhi, H. M. Jadvani, Regional Engineering College, Surat, and
P. V. Reddy, Escorts Scientific Research Centre, Faridabad

PREDICTION OF CRITICAL SPEEDS, UNBALANCE AND NONSYNCHRONOUS FORCED
RESPONSE OF ROTORS
P. Berthier, G. Ferraris, and M. Lalanne, I.N.S.A., Laboratoire de Mechanique des Structures, Villeurbanne, France

UNBALANCE RESPONSE OF A SINGLE MASS ROTOR MOUNTED ON DISSIMILAR HYDRODYNAMIC BEARINGS
R. Subbiah, R. B. Bhat and T. S. Sankar, Concordia University, Montreal, Quebec, Canada

NONLINEAR COUPLING RESPONSES TO VARIABLE FREQUENCY EXCITATIONS
F. H. Wolff and A. J. Molnar, Engineering-Analytical Dynamics Corporation, Trafford, PA

SIMPLE APPROXIMATE MODELS FOR A CLASS OF STRUCTURES
A. J. Molnar and F. H. Wolff, Engineering-Analytical Dynamics Corporation, Trafford, PA

SOURCE SIGNATURE RECOVERY IN REVERBERANT STRUCTURES
R. H. Lyon, Massachusetts Institute of Technology, Cambridge, MA

COMPARISON OF STATISTICAL ENERGY ANALYSIS AND FINITE ELEMENT ANALYSIS
VIBRATION PREDICTION WITH EXPERIMENTAL RESULTS
L. K. H. Lu, W. J. Hawkins, and D. F. Downard, Westinghouse Electric Corporation, Sunnyvale, CA, and
R. G. Dejong, Cambridge Collaborative, Cambridge, MA

**TITLES AND AUTHORS OF PAPERS PRESENTED IN THE
SHORT DISCUSSION TOPICS SESSION**

NOTE: These papers were only presented at the Symposium. They are not published
in the Bulletin and are only listed here as a convenience.

**THE DEVELOPMENT OF A VISCOELASTIC AEROSPACE STRUCTURES TECHNOLOGY DAMPING
DESIGN GUIDE**

J. Soovers, Lockheed-California Co., Burbank, CA, M. Drake, University of Dayton Research Institute, Dayton, OH,
L. Rogers and V. Miller, Air Force Wright Aeronautical Laboratories, Wright Patterson AFB, OH

APPROXIMATE RELAXATION MODULUS FROM THE FRACTIONAL REPRESENTATION OF COMPLEX MODULUS

L. Rogers, Air Force Wright Aeronautical Laboratories, Wright Patterson AFB, OH

DEVELOPMENT OF HIGH FREQUENCY ISOLATION SYSTEM

F. J. Andrews, Barry Controls, Watertown, MA

**A RECENT APPLICATION EMPLOYING ELASTOMERIC TECHNOLOGY TO ISOLATE A HIGH RESOLUTION
AERIAL RECONNAISSANCE CAMERA**

D. F. Reynolds, Barry Controls, Watertown, MA

MERCURY ISOLATION SYSTEM/DESIGN, DEVELOPMENT MANUFACTURE AND TEST

M. Peretti, Barry Controls, Watertown, MA

LOOSENING OF BOLTED JOINTS DURING VIBRATION TESTING

J. J. Kerley, Jr., Goddard Space Flight Center, Greenbelt, MD

BOLTS AND FASTENER TIGHTENING TO BROCHURE IDEALNESS THROUGH VIBRATION SIGNATURES

A. S. R. Murty, Indian Institute of Technology, Kharagpur, India

**DEVELOPMENT OF A MATERIAL TESTING MACHINE CAPABLE OF HIGH CYCLE LOADINGS SUPERIMPOSED
ONTO LOW CYCLE LOADINGS**

R. C. Goodman, University of Dayton Research Institute, Dayton, OH

PREDICTION OF STRUCTURAL RELIABILITY FROM VIBRATION MEASUREMENTS

P. Mlakar, U.S. Army Engineer Waterways Experiment Station, Vicksburg, MS

PROGRESS REPORT ON U.S. STATE OF THE ART ASSESSMENT OF MOBILITY MEASUREMENTS PROGRAM

D. J. Ewins, Imperial College of Science and Technology, London, England

UNDERWATER SHOCK ANALYSIS OF A MISSILE LAUNCH TUBE

K. C. Kiddy, Naval Surface Weapons Center, Silver Spring, MD

THE VIBRATION OF SLIGHTLY CURVED RECTANGULAR PLATES UNDER COMPRESSION

S. M. Dickinson and S. Ilanko, University of Western Ontario, London, Ontario, Canada and
S. C. Tillman, University of Manchester, Manchester, England

SHOCK ANALYSIS OF DICED DISK TRANSDUCER USING ANSYS

A. Haecker and H. Mitson, Gould, Inc., Cleveland, OH



**SOAP BY
THE SHOCK AND VIBRATION INFORMATION CENTER
NAVAL RESEARCH LABORATORY
MAIL CODE 5804
WASHINGTON D.C. 20375
US REQUESTOR - \$147.00 PER SET - \$35.00 PER PART
FOREIGN REQUESTOR - \$175.00 PER SET - \$43.75 PER PART**

Accession For	
NTIS GRA&I	<input checked="" type="checkbox"/>
DTIC TAB	<input type="checkbox"/>
Unannounced	<input type="checkbox"/>
Justification	
By	
Distribution/	
Availability Codes	
Dist	Avail and/or Special
A-1	21

SESSION CHAIRMEN AND COCHAIRMEN

<u>Date</u>	<u>Session Title</u>	<u>Chairmen</u>	<u>Cochairmen</u>
Tuesday, 26 Oct. A.M.	Opening Session	Mr. Richard Shea, U.S. Army Materials and Mechanics Research Center, Watertown, MA	Mr. Henry C. Pusey, Shock and Vibration Information Center, Naval Research Laboratory, Washington, DC
Tuesday, 26 Oct. P.M.	Elias Klein Memorial Lecture Plenary A	Mr. Henry C. Pusey, Shock and Vibration Information Center, Naval Research Laboratory, Washington, DC	
Tuesday, 26 Oct. P.M.	Machinery Dynamics	Dr. Ronald L. Eshleman, The Vibration Institute, Clarendon Hills, IL	Mr. Samuel Feldman, NKF Engineering Associates, Inc., Vienna, VA
Tuesday, 26 Oct. P.M.	Pyrotechnic Shock-Measurement/Simulation	Mr. C. Douglas Hinckley, TRW Systems, Ogden, UT	Mr. Peter Bouelin, Naval Weapons Center, China Lake, CA
Tuesday, 26 Oct. P.M.	MIL-STD-810D Panel Session	Mr. Preston Scott Hall, Air Force Wright Aeronautical Laboratories, Wright Patterson Air Force Base, OH	Mr. Rudolph H. Volin, Shock and Vibration Information Center, Naval Research Laboratory, Washington, DC
Wednesday, 27 Oct. A.M.	Maurice Biot 50th Anniversary Lecture Plenary B	Mr. George J. O'Hara, Naval Research Laboratory, Washington, DC	
Wednesday, 27 Oct. A.M.	Vibration: Test and Criteria	Mr. John Wafford, Aeronautical Systems Division, Wright Patterson Air Force Base, OH	Mr. Howard D. Camp, Jr., U.S. Army Electronic Research and Development Command, Ft. Monmouth, NJ
Wednesday, 27 Oct. A.M.	Shock Testing and Analysis	Mr. Edwin Rzepka, Naval Surface Weapons Center, Silver Spring, MD	Mr. Ami Frydman, Harry Diamond Laboratories, Adelphi, MD
Wednesday, 27 Oct. P.M.	Damping	Dr. Frederick C. Nelson, Tufts University, Medford, MA	Dr. Lynn Rogers, Air Force Wright Aeronautical Laboratories, Wright Patterson Air Force Base, OH
Wednesday, 27 Oct. P.M.	Fluid-Structure Dynamics	Dr. Anthony J. Kalinowski, Naval Underwater Systems Center, New London, CT	Dr. Martin W. Wambagans, Argonne National Laboratory, Argonne, IL
Thursday, 28 Oct. A.M.	Plenary C	Mr. Richard Shea, U.S. Army Materials and Mechanics Research Center, Watertown, MA	
Thursday, 28 Oct. A.M.	Dynamic Analysis I	Lt. Col. John J. Allen, Air Force Office of Scientific Research, Washington, DC	Dr. Robert L. Sierakowski, University of Florida, Gainesville, FL
Thursday, 28 Oct. A.M.	Vehicle Dynamics	Dr. Richard A. Lee, U.S. Army Tank-Automotive Command, Warren, MI	Dr. Grant R. Gerhart, U.S. Army Tank-Automotive Command, Warren, MI
Thursday, 28 Oct. P.M.	Dynamic Analysis II	Dr. James J. Richardson, U.S. Army Missile Command, Redstone Arsenal, AL	Mr. Brantley R. Hanks, NASA Langley Research Center, Hampton, VA
Thursday, 28 Oct. P.M.	Short Discussion Topics	Mr. R. E. Seely, Naval Weapons Handling Center, Earle, Colts Neck, NJ	Mr. E. Kenneth Stewart, U.S. Army Armament, Research and Development Command, Dover, NJ

FLUID STRUCTURE DYNAMICS

EXPERIMENTAL VALIDATION OF THE COMPONENT SYNTHESIS METHOD FOR PREDICTING VIBRATION OF LIQUID-FILLED PIPING

F. J. Hatfield and D. C. Wiggert
Michigan State University
East Lansing, Michigan

and

L. C. Davidson
David W. Taylor Naval Ship Research
and Development Center
Annapolis, Maryland

Vibration of piping can be caused by pulsation of contained liquid. Accurate prediction of such vibration requires consideration of the effect of pipe motion on fluid oscillation, as well as of acoustic pressure on pipe walls. Component synthesis is an analytic technique that approximates those interactions by synthesis of plane-wave acoustics of the liquid and normal modes analysis of the pipe structure.

Results of analysis by component synthesis are compared to solutions of partial differential equations of motion and to experimental observations for two example pipe configurations. Differences in the results of the two analyses are small compared to deviations of both predictions from observed responses. Simplifying assumptions common to the two analyses are examined.

INTRODUCTION

Pumps and other sources of periodic pressure or flow initiate acoustic waves in the liquid on which they act. These waves exert axial force on piping at bends and other locations where piping changes direction or diameter. Vibration results if the piping is not rigidly supported. As a result of the interaction, acoustic energy is transmitted from the liquid to solid components of the system, and acoustic waves in the liquid are modified. Analysis of the phenomenon should be part of piping design if noise is to be controlled or if fatigue failure due to pipe vibration is a possibility. The latter problem has been observed in flexibly supported piping serving reciprocating pumps.

BACKGROUND

The following review cites only works directly related to the topic of this paper, ignoring the areas of

non-periodic excitation, instability caused by steady flow, cavitation and turbulence effects, fluid-structure configurations other than liquid-filled pipes, multi-dimensional acoustics, vibration involving lobar distortions of pipe cross section, and non-interactive analyses of acoustics and vibration in piping.

Callaway, Tyzzer and Hardy [1] appear to have been first to report observations of pipe vibration as a response to acoustic excitation of contained liquid.

Regetz [2] and D'Souza and Oldenburger [3] studied the dynamic elongation of straight pipes containing pulsating liquid. Wood [4] devised an analysis for a single degree of freedom oscillator driven by pulsation of liquid in a pipe.

Blade, Lewis and Goodykoontz [5] and Davidson and Smith [6] developed analytical methods applicable to pipe bends, and validated their analyses with experiments conducted on liquid-filled

piping incorporating a single bend. The analysis reported by the latter investigators involves formulating the partial differential equations of motion of a pipe bend and contained liquid, and solving the equations by series approximation. Davidson and Samsury [7] extended the analysis to the third dimension and compared analytical predictions to experimental measurements for non-planar piping incorporating three bends. Wilkinson [8] presented an analysis method for piping with miter bends and tees in which waves in liquid and solid components are coupled at discrete points.

Gibert, Axisa and Villard [9] developed a finite element method for analysis of piping that includes both fluid and solid elements. Hatfield and Wiggert [10] devised the component synthesis approach which is an extension of the modal synthesis technique for dynamic analysis of structures.

ANALYSIS

The component synthesis method consists of two steps. The first is normal modes analysis of the pipe structure augmented by the mass of contained liquid. Supporting structure such as hangers and racks can be included. Normal modes analysis is an option in most computer programs for finite element analysis.

The second step synthesizes structural and fluid behavior to predict responses of the coupled system. Derivation of the synthesis step has been presented in an earlier work [10] and will be reviewed only briefly.

If the structure is linearly elastic, excitation is harmonic and damping is proportional to stiffness and/or mass, then the principle of modal superposition may be used to generate compliance expressions from modal parameters obtained in step one. The matrix expression is

$$D_S = G_S F \quad (1)$$

Coupling points are defined at velocity discontinuities. Typically, one coupling point is located at each bend, blind end, tee and reducer, and two are located at each orifice. For each point, the force exerted by the liquid on the solid component is a function of the particular fitting geometry and pressure at that point. In matrix form, force transmission is expressed as

$$F = F' + R P \quad (2)$$

Liquid volume is conserved at coupling points, giving a relation which includes

terms to account for volumetric input to the system, displacement of the liquid, and displacement of the fittings:

$$V = S D_F + T D_S \quad (3)$$

For each prismatic fluid component between adjacent coupling points, a compliance expression may be derived from one-dimensional acoustic theory. Combining the expressions for all the fluid components yields

$$D_F = G_F P \quad (4)$$

Eliminating the unknowns F , D_S , and D_F from Equations (1) through (4) produces the system equation:

$$V - T G_S F' = (S G_F + T G_S R) P \quad (5)$$

The coefficients of Equation (5) are frequency dependent and, if damping is included, complex. Since volumetric input is known (e.g. zero at bends) at those points where pressure is unknown, a subset of Equation (5) may be solved for unknown pressures for each frequency of interest. Back substitution into the other subset of Equation (5) and into Equations (1), (2) and (4) gives values for the remaining unknowns. Velocities and accelerations are computed from displacements by differentiation.

As compared to distributed parameter analyses of fluid-structure interaction in piping, component synthesis has the advantage of avoiding formulation and solution of partial differential equations, which is extremely difficult for pipe systems typically encountered in practice. Component synthesis has the further advantages of utilizing the sophistication of commercially available structural finite element computer programs for part of the analysis, and of providing a way to employ modal survey results, i.e. responses obtained by external excitation of an existing pipe system, to predict responses to internal pulsation. Component synthesis is approximate because continuous structures are represented as assemblages of discrete masses, because responses of structures are expressed as summations of a finite number of mode shapes, and because fluid-structure coupling is assumed to occur at discrete points. The relationship between precision of results and the numbers of elements, modes and coupling points has not been quantified.

First Example

Component synthesis was used to estimate various mobilities of the system described by Table 1 and Figure 1.

NASTRAN [11] was used for the first step of the analysis. The finite element model was comprised of 25 beam elements with maximum length of 4 in. (102 mm). The moment of inertia of elements representing parts of the bend was reduced by an "ovalization" factor [12]. Parameters of the first ten modes, with natural frequencies of 21.9, 47.8, 305, 391, 758, 929, 1139, 1539, 1761, and 2056 Hz, were transcribed from the NASTRAN output for use in the second step. In addition to the natural frequencies, these parameters included apparent stiffnesses and normalized translations of points C and E.

The second step was formulated with a single coupling point at C, sinusoidal force of unit amplitude applied to the liquid at A, and no structural or acoustic damping. Output plots are reproduced in Figure 2. Since the excitation force had unit amplitude, velocity and mobility are identical.

To investigate the magnitude of error introduced by approximation, parts of the analysis were repeated, first with fewer modes and then with fewer structural elements. When only the first four structural modes, instead of the first ten, were used in the second step of analysis, significant differences were apparent for liquid velocities when the frequency of excitation exceeded 700 Hz and for pipe velocities when the frequency of excitation exceeded 400 Hz. When the number of elements in the structural model was reduced from 25 to 13, the maximum changes for the first four modes in natural frequencies and apparent stiffnesses were 1.3% and 3.1%, respectively. For those modes, the maximum change in normalized displacements was 0.12. In general, larger changes were observed in the higher modes.

Second Example

Component synthesis was used to estimate various mobilities of the system described by Table 1 and Figure 3. NASTRAN [11] was used for the first step of the analysis. The finite element model included 28 beam elements with maximum length of 4 in. (102 mm) to represent piping and six stiffness elements to represent the support at K. The moment of inertia of elements representing parts of the bends was reduced by an "ovalization" factor [12]. Parameters of the first twelve modes, with natural frequencies of 24.7, 25.4, 46.5, 57.4, 121, 156, 227, 322, 579, 729, 779, and 1092 Hz, were transcribed from NASTRAN output for use in the second step. In addition to the natural frequencies, these parameters included apparent stiffness and normalized x, y, and z translations of point C, y and z

translations of F, x and z translations of I, and x translation and rotation about y of K.

The second step was formulated with a coupling point at each of the three bends, sinusoidal force of unit amplitude applied to the liquid at A, and no structural or acoustic damping. The output plots, which represent both velocity and mobility, are reproduced in Figure 4.

EXPERIMENT

The experimental work corresponding to the two analyses has been reported earlier [6,7]. For the first example, point A of the piping of Figure 1 was secured to the flange of an acoustic mobility/impedance transducer. This device consists of a diaphragm-supported piston driven by an external force generator. A nominal force amplitude of 1 lb (4.4 N) was used. The driving point mobility was determined from an accelerometer and hydrophone incorporated in the excitation device. The liquid velocity response at point E was determined with a hydrophone placed 1/2 in. (13 mm) below the free surface. The pressure at this point is proportional to acceleration at the surface since the 1/2 in. (13 mm) liquid column behaves as a simple inertance in the frequency range of interest. The structural responses at point E were determined from accelerometers. Observed mobilities are plotted in Figure 2.

For the second example, point K of the piping shown in Figure 3 was attached to a plate structure. That end of the pipe was sealed with a rubber membrane to simulate an open end. Excitation of the liquid at point A was produced by a sound generator suspended above the unattached pipe end and acoustically coupled to the liquid through a rigid cone adapter. An air gap of 1/64 in. (.4 mm) was maintained between the cone and the pipe. Microphones in the cone detected excitation pressure. The liquid response at K was determined from a hydrophone mounted a short distance from the end of the pipe. Structural responses at K were determined from accelerometers. Observed mobilities are plotted in Figure 4.

DISCUSSION

Figures 2 and 4 compare experimental observations to results of component synthesis and to results obtained by formulating and solving the partial differential equations of motion of the systems. The latter analysis has been described previously [6,7], although the plotted results reflect solution by a more precise series approximation.

TABLE 1
Description of Examples

	First Example	Second Example
Material	70% Cu, 30% Ni	Steel
Density lb-s ² /in. ⁴ (kg/m ³)	8.4x10 ⁻⁴ (9000)	7.35x10 ⁻⁴ (7850)
Modulus of elasticity lb/in. ² (GPa)	2.28x10 ⁷ (157)	2.95x10 ⁷ (203)
Outside diameter in. (mm)	4.5 (114)	4.5 (114)
Inside diameter in. (mm)	4.03125 (102)	4.03125 (102)
Radius of bends in. (mm)	4 (102)	6 (152)
Lengths in. (m).		
AB	36 (.914)	18.5 (.470)
DE	36 (.914)	12 (.305)
GH	--	12.5 (.318)
JK	--	7.5 (.190)
Support stiffness:		
A	rigid	--
K, x translation lb/in. (N/m)	--	1.25x10 ⁶ (2.19x10 ⁸)
y and z translations lb/in. (N/m)	--	3.0x10 ⁷ (5.25x10 ⁹)
x rotation lb-in./rad (N-m/rad)	--	5.0x10 ⁸ (.65x10 ⁷)
y and z rotations lb-in./rad (N-m/rad)	--	2.5x10 ⁷ (2.82x10 ⁶)
Liquid	oil	oil
Density lb-s ² /in. ⁴ (kg/m ³)	8.16x10 ⁻⁵ (872)	8.16x10 ⁻⁵ (872)
Sound speed in situ in./s (m/s)	54000 (1372)	54000 (1372)
Boundary conditions at pipe ends	open-open	open-open

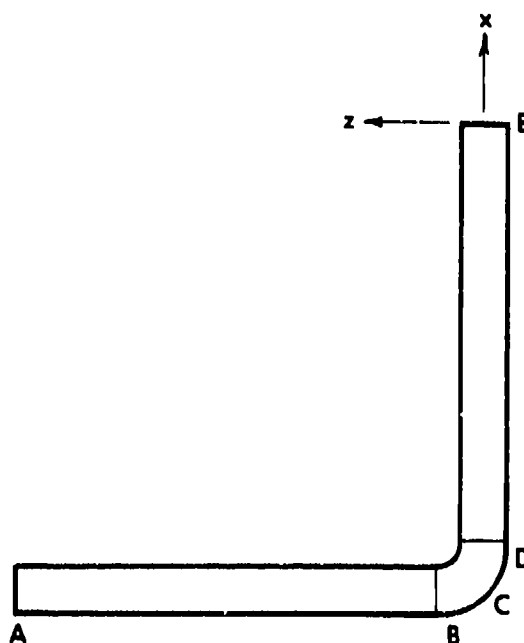


Fig. 1 - Piping for first example.

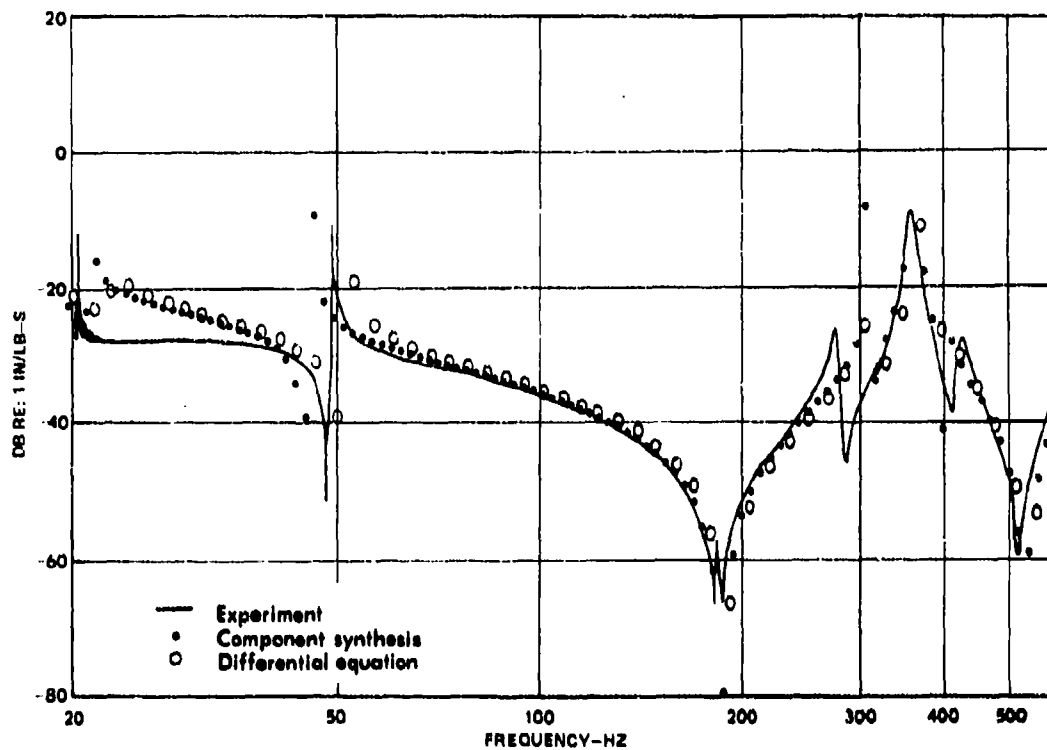


Fig. 2a - Amplitude of mobility of liquid at A.

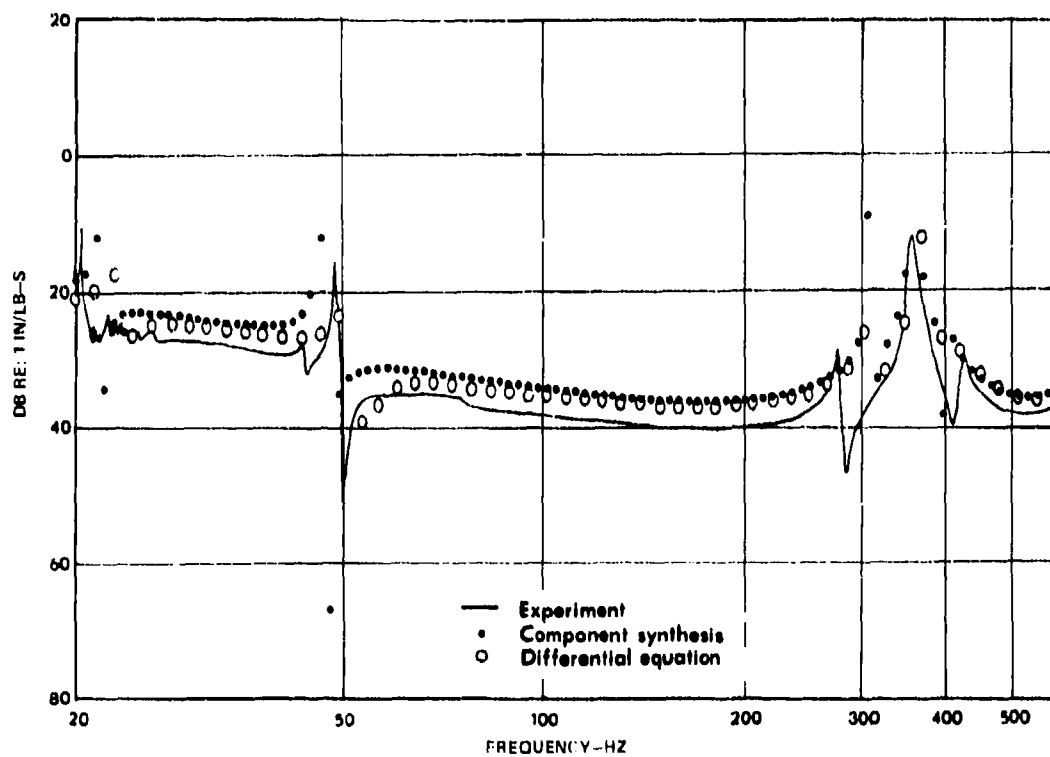


Fig. 2b - Amplitude of mobility of liquid at B.

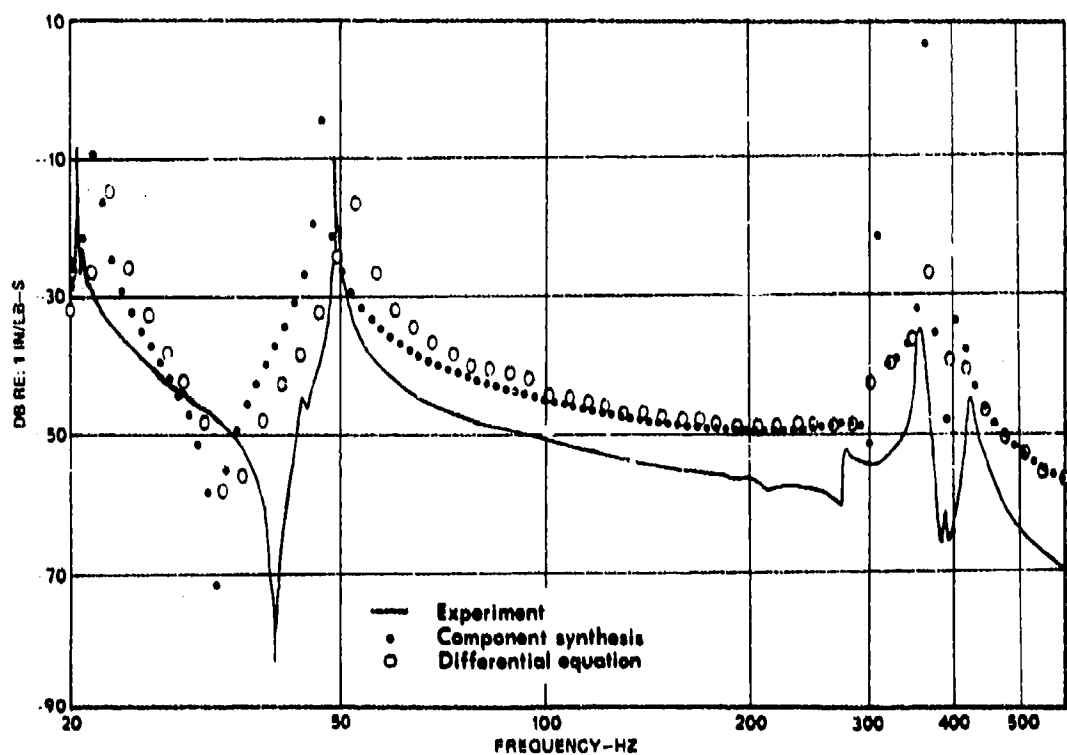


Fig. 2c - Amplitude of mobility of pipe at E in x direction.

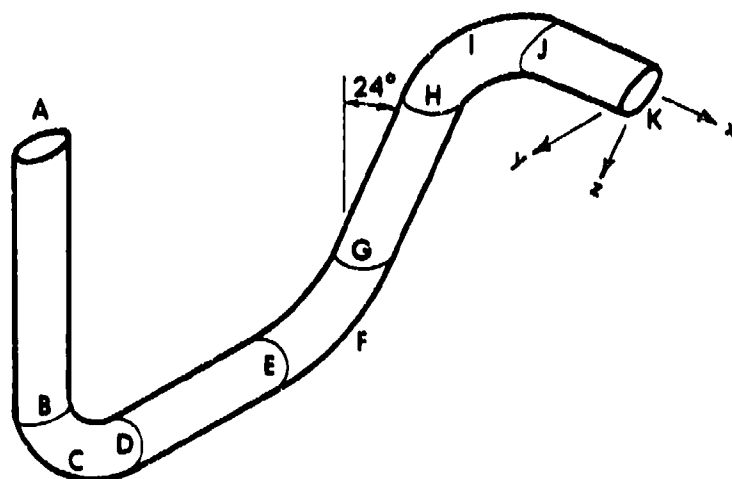


Fig. 3 - Piping for second example.

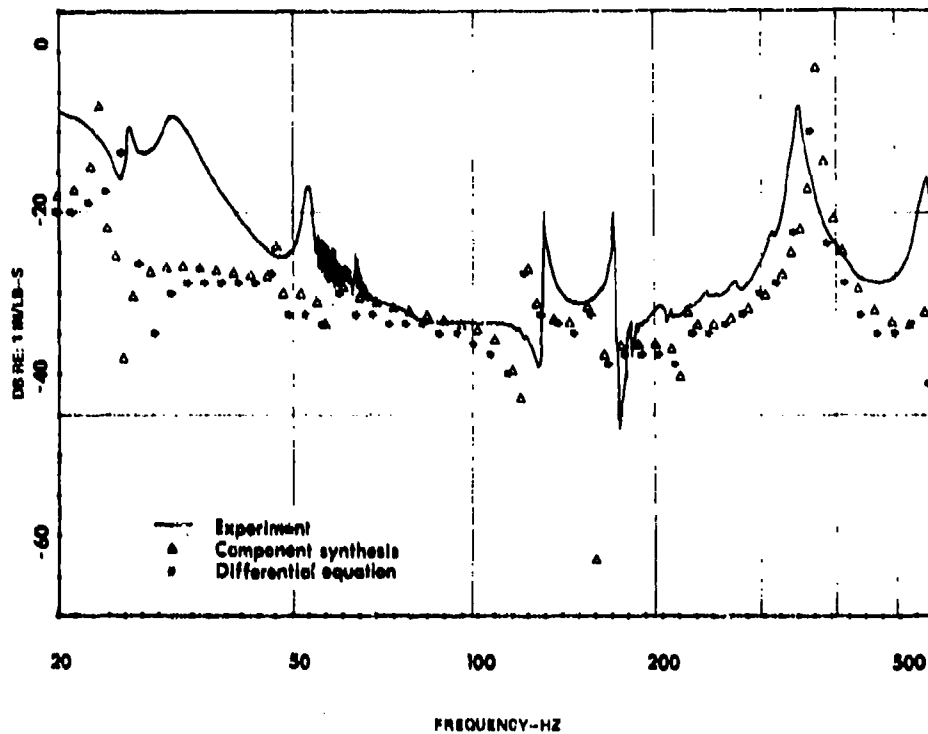


Fig. 4a - Amplitude of mobility of liquid at K.

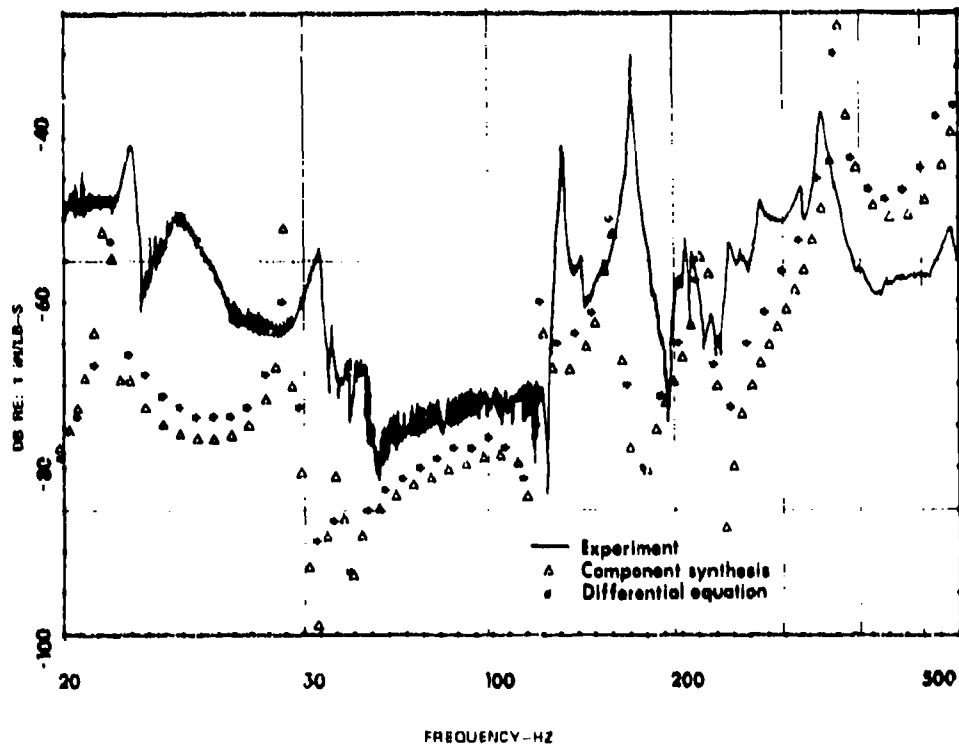


Fig. 4b - Amplitude of mobility of pipe at K in x direction.

Discrepancies in predicted and measured responses in the vicinity of peak amplitudes are caused by inaccurate, but different, estimates of damping used in the two analyses. In non-resonant frequency ranges, differences in the responses predicted by the two analyses are minor compared to the deviations of both predictions from observed responses. That is, component synthesis, despite its three approximations, predicts observed behavior nearly as accurately as the more precise but mathematically demanding approach of forming and solving partial differential equations of motion. Efforts to identify significant sources of inaccuracy will be more productive if directed at assumptions common to both analysis techniques, rather than at the approximations peculiar to component synthesis. Those common assumptions, and the corresponding experimental conditions, are:

The piping is linearly elastic. For the pressures, section properties, and configurations of the example systems, the elastic limits of the pipe materials were not approached.

Dilation of pipe cross section is not coupled to axial strain. This assumption may cause significant error [13], but is necessary in the case of component synthesis because available finite element programs do not provide a two-node element with coupled radial and axial strains.

The fluid is a linearly elastic continuum. The test conditions were such that these constraints were not violated, i.e. dynamic pressure amplitudes were small fractions of the mean system pressure (atmospheric), and vapor pressure was never approached.

Steady flow velocity is small. In addition to being a necessary condition for the familiar formulation of acoustic behavior, this assumption eliminates the effect of internal flow on the natural frequencies of piping [14]. The experiments were conducted with no steady flow.

Centrifugal force on a bend due to circumferential motion of the contained fluid is neglected. Preliminary investigation indicates that this assumption is not a significant source of error for the examples.

Sound propagates as plane waves throughout the liquid. In straight reaches of rigid-walled pipe, an accepted condition for plane wave behavior is a ratio of wave length to pipe diameter exceeding six [15]. For the pipe and

liquid of the experiments, this condition corresponds to a frequency of over 2000 Hz, which is well beyond the maximum frequency of interest. For compliant pipe walls, deviation from plane wave behavior is expected at frequencies near and above the natural frequency of the first lobar mode of the pipe section. Kito's [16] formula for resonant frequencies of liquid-filled pipes, with the ratio of wall thickness to pipe length conservatively taken as zero, predicts 850 and 1000 Hz as the resonant frequencies of the first lobar mode for the two examples. Those limits are comfortably higher than the maximum frequencies of interest.

In propagating through a bend, a wave cannot retain both constant velocity and a planar front. Several investigators have provided evidence of the distortion of plane waves at bends. In a theoretical analysis of long wave propagation in two-dimensional curved ducts, Rostafinski [17] demonstrated that the presence of a bend causes a set of axial and radial waves that modify the plane wave entering the bend, a radial standing wave sustained by the duct curvature, and attenuation of the wave transmitted through the bend. Wave propagation in the curved duct was found to be influenced profoundly by radius of curvature. In an experimental study of wave propagation around a bend, Swaffield [18] observed that attenuation and reflection are dependent on geometry of the bend. Neither investigation considered the effect of motion of the bend on waves in the contained liquid. Since the results of both component synthesis and differential equation analysis deviate more from experimental observations for the example that incorporates the greater number and proportional length of bends, it seems probable that the false assumption of plane wave behavior in bends contributes significantly to these deviations.

CONCLUSIONS

For the two examples, component synthesis approximates results given by the more precise, but more difficult, approach of formulating and solving partial differential equations of motion.

Differences in results of the two analytical methods are minor compared to their shared deviations from experimental observations.

Possible sources of inaccuracy in

both analyses are absence of coupling of pipe cross section dilation to axial strain, and the assumption of plane wave acoustics in bends.

ACKNOWLEDGEMENT

The work of one of the authors (Hatfield) was supported by the U.S. Navy - American Society for Engineering Education Summer Faculty Research Program. Results were presented at the ASME Pressure Vessel and Piping Conference, Orlando, June 27 - July 2, 1982.

NOMENCLATURE

- D_F = vector of complex absolute fluid displacements at coupling points and open pipe ends
- D_S = vector of complex displacements of structural degrees of freedom
- F = vector of complex forces on structural degrees of freedom
- F' = vector of externally applied complex forces on structural degrees of freedom
- G_F = matrix of complex fluid compliances
- G_S = matrix of complex structural compliances
- P = vector of complex pressures at coupling points and closed pipe ends
- R, S, T = connectivity matrices
- V = vector of complex fluid volumetric displacements into pipe system

REFERENCES

1. Callaway, D.B., Tytzer, F.G., and Hardy, H.C., "Resonant Vibrations in a Water-Filled Piping System," Journal of the Acoustical Society of America, vol. 23, no. 5, Sept., 1951, pp. 550-553.
2. Regetz, J.D., Jr., "An Experimental Determination of the Dynamic Response of a Long Hydraulic Line," NASA Technical Note D-576, Dec., 1960.
3. D'Souza, A.F., and Oldenburger, R., "Dynamic Response of Fluid Lines," Journal of Basic Engineering, Transactions of the American Society of Mechanical Engineers, vol. 86, Sept., 1964, pp. 589-598.
4. Wood, D.J., "A Study of the Response of Coupled Liquid Flow-Structural Systems Subjected to Periodic Disturbances," Journal of Basic Engineering, Transactions of the American Society of Mechanical Engineers, vol. 90, Dec., 1968, pp. 532-540.
5. Blade, R.J., Lewis, W., and Goodykoontz, J.H., "Study of Sinusoidally Perturbed Flow in a Line Including a 90 deg Elbow with Flexible Supports," NASA Technical Note D-1216, 1962.
5. Davidson, L.C., and Smith, J.E., "Liquid-Structure Coupling in Curved Pipes," Shock and Vibration Bulletin, no. 40, part 4, Dec., 1969, pp. 197-207.
7. Davidson, L.C., and Samsury, D.R., "Liquid-Structure Coupling in Curved Pipes - II," Shock and Vibration Bulletin, no. 42, part 1, Jan., 1972, pp. 123-135.
8. Wilkinson, D.H., "Acoustic and Mechanical Vibrations in Liquid-Filled Pipework Systems," Proceedings of the BNES Vibration in Nuclear Plant Conference, Paper no. 8:5, May, 1978.
9. Gibert, R.J., Axisa, F., and Villard, B., "Flow Induced Vibrations of Piping Systems (Vibration Sources - Mechanical Response of Pipes)," Proceedings of the BNES Vibration in Nuclear Plant Conference, Paper no. 6:2, May, 1978.
10. Hatfield, F.J., Wiggert, D.C., and Otwell, R.S., "Fluid Structure Interaction in Piping by Component Synthesis," Journal of Fluids Engineering, Transactions of the American Society of Mechanical Engineers, vol. 104, Sept., 1982, pp. 318 - 325.
11. NASTRAN Theoretical Manual, NASA SP-221(05), Dec., 1978.
12. Vigness, I., "Elastic Properties of Curved Tubes," Transactions of the American Society of Mechanical Engineers, vol. 65, 1943, pp. 105 - 117.
13. Skalak, R., "An Extension of the Theory of Water Hammer," Transactions of the American Society of Mechanical Engineers, vol. 78, Jan., 1956, pp. 105-116.
14. Blevins, R.D., Formulas for Natural Frequency and Mode Shape, Van Nostrand Reinhold Co., 1979, pp. 419-420.
15. Baranek, L.L., Acoustics, McGraw-Hill Book Co., 1954, pp. 29.
16. Kito, F., "The Vibration of Penstocks," Water Power, Oct., 1959, pp. 379-385, 392.
17. Rostafinski, W., "On Propagation of Long Waves in Curved Ducts," Journal of the Acoustical Society of America, vol. 52, no. 5, part 2, 1972, pp. 1411-1420.
18. Swaffield, J.A., "The Influence of Bends on Fluid Transients Propagated in Incompressible Pipe Flow," Proceedings of the Institution of Mechanical Engineers, vol. 183, pt. 1, no. 29, 1968-1969, pp. 603-614.

DISCUSSION

Voice: You used modal synthesis; you took the eigenvalues or the eigenvectors of each system, and you put them together. Is that right?

Mr. Hatfield: No. It is a mixed method. We used a modal representation of the structure, but we used acoustic representations of the fluid columns, and then we coupled those. So it is a mixed modal-acoustic approach.

Voice: I kept looking for a continuity equation. Did you have one?

Mr. Hatfield: Yes, I had a continuity equation, and that formed the basis for the system equations of motion. The first equation is a symbolic continuity expression.

ACOUSTIC RESPONSES OF COUPLED FLUID-STRUCTURE

SYSTEM BY ACOUSTIC-STRUCTURAL ANALOGY

Y. S. Shin
Department of Mechanical Engineering
Naval Postgraduate School
Monterey, California

and

M. K. Chargin
NASA Ames Research Center
Moffett Field, California

The use of an analogy between structural mechanics and acoustics makes it possible to solve fluid-structural interaction(FSI) problems using an existing structural analysis computer program. This method was implemented in MSC/NASTRAN program and the FSI analysis was performed using 2-dimensional coupled fluid-beam model to assess and evaluate the adequacy of this approach. The coupled modal analysis of 3-D model is also briefly discussed. This paper presents the normal mode, modal frequency response and transient response analysis of 2-D coupled fluid-beam system. The significant reduction of the acoustic pressure response at the fluid-structure interface is observed as a result of fluid-structure interaction.

INTRODUCTION

The interaction of an acoustic fluid with an elastic structure has been an important subject, particularly in the structural design against underwater shock or the evaluation of the boundary wall pressure field of an acoustic fluid in the loss of coolant accident in the nuclear reactor vessel. An incompressible acoustic model of the fluid is used in many engineering problems to take into account the added mass effect of the fluid. However, the need for the compressible acoustic fluid model is inevitable in many problems, particularly useful in the transient response analysis of the coupled fluid-structure system.

A direct finite element treatment of both the compressible fluid and structure was first given by Zienkiewicz and Newton[1] to solve the coupled fluid-structure interaction problem. The finite element modelling includes both acoustic fluid and structure, leading to a system of unsymmetric equations of motion in matrix form to be solved[1]. Symmetry can be restored by matrix manipulation which produces completely full symmetric matrices of same order as the original matrices, or it can be restored by condensing out

interior degrees of freedom in either the fluid or the structure field, and reducing the system to purely structural or purely fluid equation[2]. MacNeal developed a method utilizing an uncoupled mode formulation of the fluid equations, or of the structural equations, or of both, and it introduces a set of auxiliary variables which restores symmetry to the coupled equations[3].

The use of an analogy between structural mechanics and acoustics makes it possible to solve fluid-structure interaction(FSI) problems using an existing structural analysis computer program. This method was implemented in MSC/NASTRAN[4] and the FSI analysis was performed using 2-dimensional coupled fluid-beam model to assess and evaluate the adequacy. The coupled modal analysis of 3-D model is also briefly discussed. Furthermore, the same technique was successfully used to evaluate the effect of the structural motion on the fluid boundary pressure of Boiling Water Reactor pressure suppression pool in the loss of coolant accident situation and the predicted results were in good agreement with the experimental results [5]. This paper presents the normal mode, modal frequency and transient response analysis of 2-dimensional coupled fluid

beam system. For the modal frequency and transient responses, a static approximation is added to the dynamic response of lower modes to compensate for the truncated higher order modes of the fluid[6]. The results of normal mode analysis are compared with the theoretical ones with an excellent agreement.

FLUID-STRUCTURE INTERACTION ANALYSIS

The calculation of pressure response in a finite acoustic fluid medium contained in a flexible structure is a problem in which two sets of coupled linear partial differential equations must be solved.

The governing acoustic field equation for a nonviscous, compressible, irrotational fluid with pressure, p , can be written as,

$$\nabla^2 p = \frac{1}{C^2} \frac{\partial^2 p}{\partial t^2} \quad (1)$$

where C is the acoustic velocity in the fluid ($=\sqrt{\chi/\rho_f}$), χ is the fluid bulk modulus, ρ_f is the fluid mass density, t is the time, and ∇ is the gradient operator. The corresponding boundary conditions are as follows; at free surfaces,

$$p = 0 \quad (2)$$

at the interface along the wetted surface of fluid and structure,

$$\nabla p \cdot \vec{n} = -\rho_f \frac{\partial^2 u}{\partial t^2} \quad (3)$$

where $\nabla p \cdot \vec{n}$ is the pressure gradient normal to the surface, u is the displacement in the normal direction of boundary. For a rigid boundary, the equation (3) reduces to,

$$\nabla p \cdot \vec{n} = 0 \quad (4)$$

The governing equation of a structure in matrix form can be written as,

$$[M](\ddot{u}) + [\hat{C}](\dot{u}) + [K](u) = (P) \quad (5)$$

where $[M]$, $[\hat{C}]$, $[K]$ are mass, damping and stiffness matrices respectively, and (P) is the equivalent fluid nodal force vector, (u) is the displacement vector and $"."$ denotes the derivative with

respect to time.

ACOUSTIC-STRUCTURAL ANALOGY

The use of an analogy between structural mechanics and acoustics makes it possible to solve FSI problem using a structural analysis program. The analogy is summarized and its details are described in Ref. 7.

1. Acoustic fluid pressure, p , is represented by a component of structural displacement, u_x . Since the acoustic fluid pressure is the only degree of freedom at the grid point, all degrees of freedom except u_x at each grid point should be constrained.

$$u_x = p$$

2. The structural mass density, ρ_s , corresponds to the inverse of the fluid bulk modulus, χ ,

$$\rho_s = \frac{1}{\chi}$$

The stress-strain relation for the fluid is equivalent (numerically) to choosing the shear modulus G and Young's modulus E as shown in (3) and (4) below; [8]

3. The structural shear modulus, G , corresponds to the inverse of the fluid density, ρ_f

$$G = \frac{1}{\rho_f}$$

4. Choose the structural Young's modulus as follows; For a three-dimensional fluid model,

$$E = \alpha G, \quad \alpha \gg 1$$

where α is large enough so that $\alpha+1$ is indistinguishable (numerically) from α ;

$\alpha = 10^{20}$ suffices.

For two-dimensional fluid model,

$$E = \beta G, \quad \beta \ll 1$$

where β is not so small that $1+\beta$ is indistinguishable (numerically) from unity. $\beta = 0.0001$ suffices.

For one-dimensional fluid model,

$$E = G$$

5. The structural stresses, σ_x , τ_{xy} and τ_{xz} correspond to negative accelerations, $-\ddot{w}_x$, $-\ddot{w}_y$ and $-\ddot{w}_z$ in x, y and z directions, respectively.

$$\sigma_x = \frac{1}{\rho_f} \frac{\partial p}{\partial x} = -\ddot{w}_x$$

$$\tau_{xy} = \frac{1}{\rho_f} \frac{\partial p}{\partial y} = -\ddot{w}_y$$

$$\tau_{xz} = \frac{1}{\rho_f} \frac{\partial p}{\partial z} = -\ddot{w}_z$$

where w is fluid displacement. As a result of this analogy, stress data recovery will produce the acceleration components within the fluid, with a change in sign.

6. Fluid boundary conditions are treated as follows:

At free surface, set $u = p = 0$

At rigid wall, take no action.

At the surface where the normal component of fluid acceleration is known, apply the grid point load,

$$F_x(t) = -A \ddot{w}_x(t)$$

where A is the area associated with the grid point.

7. For fluid grid points lying in a plane of symmetry or anti-symmetry, the boundary conditions are, [8]

$$\frac{\partial p}{\partial n} = 0 \quad \text{for symmetry}$$

$$p = 0 \quad \text{for anti-symmetry}$$

In the finite element analysis, the symmetry condition on p is a natural boundary condition and is satisfied if no action is taken.

NASTRAN/FSI ANALYSIS

The coupled fluid-structure interaction model produces, in general, non-symmetric coupling terms in the formulation, and, as a consequence, a

relatively slow unsymmetric eigenvalue extraction method has to be employed. However, MacNeal, et al [2,3] developed a method to restore the symmetry by matrix manipulation which produce full symmetric matrices of the same order as the original matrices. This allows an efficient symmetric eigenvalue extraction method to be used. The interior degrees of freedom (DOF) may be condensed out in either the fluid or the structural field and the system can be reduced to purely structural or purely fluid equations.

The coupled matrix equation for the fluid-structure system can be written as,

$$\begin{bmatrix} M_s + K_s & -A^T \\ s^T A & C_0 s^T + K_f \end{bmatrix} \begin{Bmatrix} u \\ p \end{Bmatrix} = \begin{Bmatrix} F \\ 0 \end{Bmatrix} \quad (6)$$

where [M] is the structural mass matrix, [K_s] is the structural stiffness matrix, s is d/dt, s² = d²/dt² (an operator), [C₀] is the acoustic mass matrix (inversely proportional to the fluid bulk modulus), [K_f] is the acoustic stiffness matrix (inversely proportional to ρ_f), [A] is the wetted surface interface area matrix, {u} is the structural displacement vector, {p} is the acoustic pressure vector, and {F} is the vector of applied nodal forces. {p} includes pressures at points within the fluid and on the surface. Similarly, {u} includes normal components of motion at the interface, and other components of motion within the structure which do not couple with the fluid. [A] is a rectangular matrix of total number of structural DOF by total number of pressure DOF. Each nonzero term is the tributary area of a grid point associated with a specific pressure DOF and a structural DOF at the interface.

Let the modal representation of displacements and pressure be written as

$$\{u\} = [\phi_s] \{r_s\} \quad (7)$$

$$\{p\} = [\phi_f] \{r_f\} \quad (8)$$

where [φ_s], [φ_f] are the matrices of eigenvectors, and {r_s}, {r_f} are the generalized coordinate vector for displacement and pressure, respectively. The resulting modal matrix equation is,

$$\begin{bmatrix} ms^2 + k_s & -\phi_s^T \\ s^2 \hat{\phi} & m_f s^2 + k_f \end{bmatrix} \begin{Bmatrix} \xi_s \\ \xi_f \end{Bmatrix} = \begin{Bmatrix} \phi_s^T F \\ 0 \end{Bmatrix} \quad (9)$$

where

$$[\hat{\phi}] = [\phi_f]^T [A] [\phi_s]$$

$$[m] = [\phi_s]^T [M] [\phi_s]$$

$$[m_f] = [\phi_f]^T [C_0] [\phi_f]$$

$$[k_s] = [\phi_s]^T [K_s] [\phi_s]$$

and $[k_f] = [\phi_f]^T [K_f] [\phi_f]$

$[_]$ indicates a diagonal matrix.

By matrix manipulation and with definition of the following auxiliary parameters,

$$\{\hat{\xi}\} = \left[\frac{1}{k_s}\right] [\hat{\phi}]^T \{\xi_f\}$$

$$= \left[\frac{1}{k_s}\right] [\phi_s]^T [A]^T \{P\}$$

$$\{F_f\} = \left[\frac{k_s}{m}\right] [\phi_s]^T \{P\}$$

$$\{\lambda\} = [k] \{\hat{\xi} - \xi_s\}$$

$$[\bar{k}] = \left[\frac{k_s}{m}\right]$$

$$[\bar{m}] = [k_s]$$

Equation (9) can be written in the following form, where the pressure within the fluid appears explicitly: [3]

$$\begin{bmatrix} C_0 s^2 + K_f & 0 & 0 & A \phi_s \frac{1}{k_s} \\ 0 & \bar{m} s^2 + \bar{k} & -\bar{k} & 0 \\ 0 & -\bar{k} & \bar{k} & -I \\ \frac{1}{k_s} \phi_s^T A^T & 0 & -I & 0 \end{bmatrix} \begin{Bmatrix} p \\ \xi_s \\ \hat{\xi} \\ \lambda \end{Bmatrix} = \begin{Bmatrix} 0 \\ F_f \\ -F_f \\ 0 \end{Bmatrix} \quad (10)$$

Equation (10) is an advantageous form for the boundary wall acoustic pressure calculation.

The following steps are carried out for NASTRAN/FSI analysis:

1. Set up a finite element model for the dry structure and calculate enough vibration modes to adequately represent its structural behavior.

2. Calculate the wetted tributary area for each grid point at the fluid-structure interface. This area is the element of the $[A]$ matrix.

3. Compute the matrices, $[\bar{m}]$, $[\bar{k}]$ and the matrix product $[1/k_s][\phi_s]^T[A]^T$ appearing in equation (10).

4. Set up a finite element model for the fluid. Append to this model the additional scalar degrees of freedom $\{\xi\}$ and $\{\lambda\}$ together with the scalar springs, $[\bar{k}]$ and the scalar masses, $[\bar{m}]$.

5. Analyze the resulting system for its vibration modes, or for its response to dynamic excitation.

6. Compute structural displacements using equation (7), once $\{\xi_s\}$ has been evaluated.

The solution is based on expansion of the pressure and displacement field in modal coordinates. One disadvantage of this method is the loss of contributions of the truncated modes to the static (low frequency) response of the system. This problem was remedied by making an independent calculation of the static response which is added to the response obtained from the direct solution of equation (10). NASTRAN program was employed to implement the FSI analysis capabilities because of its easiness to control the program using Direct Matrix Programming (DMP).

2-DIMENSIONAL FLUID-BEAM SYSTEM

A simply supported beam has one side in contact with a finite acoustic fluid as shown in Figure 1(a). The following physical properties of the beam and fluid are used.

Beam:
 Weight Density(ρ_b) $7.682 \times 10^4 \text{ N/m}^3$
 (0.283 lb/in^3)
 Young's Modulus(E) $2.068 \times 10^{11} \text{ Pa}$
 ($30 \times 10^6 \text{ psi}$)
 Section Moment of Inertia(I) $0.1675 \times 10^{-6} \text{ m}^4$
 (40.24 in^4)
 Length of Beam(L) 3.048 m
 (10.0 ft)

Fluid:
 Weight Density(ρ_f) 9802.25 N/m^3
 (62.4 lb/ft^3)
 Acoustic Speed(C) 1524 m/s
 (5000 ft/sec)
 Height of Fluid 6.096 m
 (20 ft)

A unit width of the fluid is considered.

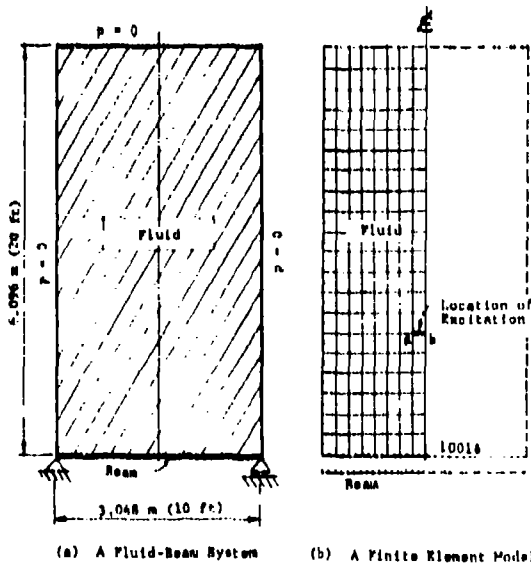


Figure 1. A Beam with a Finite Acoustic Fluid

THEORETICAL SOLUTION

The coupled modal frequencies of the fluid-beam system are to be determined. The equation of motion of the beam is,

$$m \frac{\partial^2 y}{\partial t^2} + EI \frac{\partial^4 y}{\partial x^4} = q(x, t) \quad (11)$$

where m is the mass of beam per unit length, E is Young's modulus of beam, I is the section moment of inertia, and $q(x, t)$ is the distributed load on the beam.

The governing acoustic field equation in Cartesian coordinates can be written as,

$$\frac{\partial^2 p}{\partial x^2} + \frac{\partial^2 p}{\partial y^2} = \frac{1}{C^2} \frac{\partial^2 p}{\partial t^2} \quad (12)$$

The boundary conditions of the beam and fluid are,

Beam:

$$y = 0 \quad \left. \vphantom{\begin{matrix} y = 0 \\ \frac{\partial^2 y}{\partial x^2} = 0 \end{matrix}} \right\} \text{ at } x=0 \text{ and } x=L \quad (13)$$

$$\frac{\partial^2 y}{\partial x^2} = 0$$

$$\text{Fluid: } p = 0 \quad \text{at } x=0, L, \text{ and } y=H \quad (14)$$

Beam-fluid interface:

$$\frac{\partial p}{\partial y} = -\rho_f \frac{\partial^2 y}{\partial t^2} \quad (15)$$

Solving this set of equations (11) through (15), the following frequency equation can be easily obtained.

$$\text{For } \alpha_n^2 = \frac{\omega_n^2}{C^2} - \left(\frac{n\pi}{L}\right)^2 > 0,$$

$$\omega_n^2 \left[m + \frac{\rho_f \tanh(\alpha_n H)}{\alpha_n} \right] = EI \left(\frac{n\pi}{L} \right)^4 \quad n=1, 2, 3, \dots \quad (16)$$

$$\text{For } \alpha_n^2 = \frac{\omega_n^2}{C^2} - \left(\frac{n\pi}{L}\right)^2 < 0;$$

$$\text{let } \hat{\alpha}_n^2 = -\alpha_n^2,$$

$$\omega_n^2 \left[m + \frac{\rho_f \tanh(\hat{\alpha}_n H)}{\hat{\alpha}_n} \right] = EI \left(\frac{n\pi}{L} \right)^4$$

$$n=1,2,3,\dots \quad (17)$$

The equation of mode shapes for the acoustic fluid pressure are expressed by,

$$\text{For } \alpha_n^2 > 0,$$

$$P_n(x,y) = \frac{\rho_f \omega_n^2}{\alpha_n} \left(\sin \frac{n\pi x}{L} \right) (\sin \alpha_n y - \tanh \alpha_n H \cos \alpha_n y) \quad (18)$$

$$\text{For } \alpha_n^2 < 0, \text{ and let } \hat{\alpha}_n^2 = -\alpha_n^2,$$

$$P_n(x,y) = \frac{\rho_f \omega_n^2}{\hat{\alpha}_n} \left(\sin \frac{n\pi x}{L} \right) (\sinh \hat{\alpha}_n y - \tanh \hat{\alpha}_n H \cosh \hat{\alpha}_n y) \quad (19)$$

2D-NASTRAN FINITE ELEMENT MODEL

The 2D finite element model for FSI analysis consists of the beam and the fluid. Using the symmetry about the center of the beam and the fluid, only half portions of the beam and the fluid are modeled using 16 BAR elements and 128 8-node QUAD8 elements respectively. The fluid-beam finite element model is shown in Figure 1(b).

NORMAL MODE ANALYSIS

To understand the basic dynamic characteristics of the system and to make a basis to compare the results with the theoretical ones, the normal mode analyses of the following cases are performed, (1) dry structure (beam only), (2) fluid with rigid boundary at beam location, and (3) coupled fluid beam system.

Dry Structure (Beam Only)

There were five modes under 5000 Hz and the first five natural frequencies

and mode shapes are plotted as shown in Figure 2.

Fluid with Rigid Boundary at Beam Location

There were thirteen acoustic pressure modes under 1000 Hz. The first six modes are depicted in Figure 3, plotting the pressure variation along the x-axis. The first mode is the coupled lateral 1/2 wave-vertical 1/4 wave mode, and the second mode as the coupled lateral 1/2-vertical 3/4 wave mode.

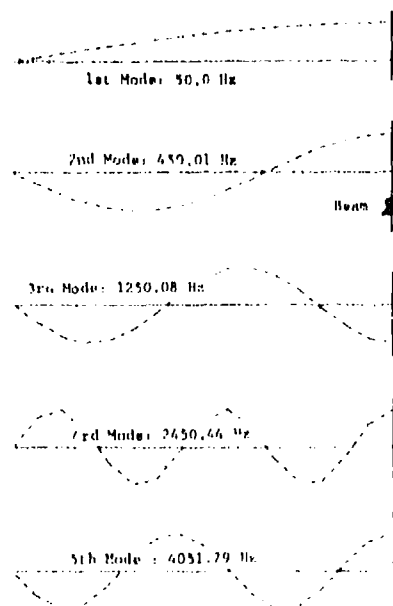


Figure 2. Natural Frequencies and Mode Shapes of Dry Structure (Beam Only)

Coupled Fluid-Beam System

Five dry structure modes and thirteen fluid modes were included to perform the modal analysis of the coupled system. The first seven coupled acoustic pressure modes are depicted in Figure 4. The first mode at 39.18 Hz and fourth mode at 403.20 Hz are clearly the local pressure mode induced by the structure.

The results also indicate that the structural motion shifts the dominant acoustic frequencies. The finite element results are compared with the theoretical results based on the equations (16) through (19), and it has an excellent agreement. The comparison of the natural frequencies are shown in Table 1.

Table 1. Comparison of Coupled Natural Frequencies between Theoretical and Finite Element Results

Mode	Theory	Finite Element
1	39.27	39.18
2	269.97	270.17
3	328.18	328.44
4	403.21	403.20
5	414.01	414.18
6	515.40	515.54
7	625.19	625.43
8	739.76	740.32
9	756.89	757.82
10	779.55	781.61

system. The 5% coupled modal damping was assumed for both cases.

MODAL FREQUENCY RESPONSES

The unit acceleration excitation was applied at the middle of the fluid (location x_5 shown in Figure 1(b)) and the excitation frequencies were swept from 0 to 700 Hz with the log increment of the frequencies. The frequency responses of both the fluid with rigid boundary and the coupled fluid-beam system were calculated. The case of the fluid with rigid boundary identifies the significant fluid modes, and the coupled fluid-beam system shows the FSI effects on the coupled responses of the

Fluid with Rigid Boundary at Beam Location

The acoustic pressure frequency response at the center of beam is shown in Figure 5. The acoustic pressure response was dominant at 257 Hz (first acoustic pressure mode), and the second peak was observed at 400 Hz (third acoustic pressure mode). There was no significant response peak at the second mode since it is being forced at a node.

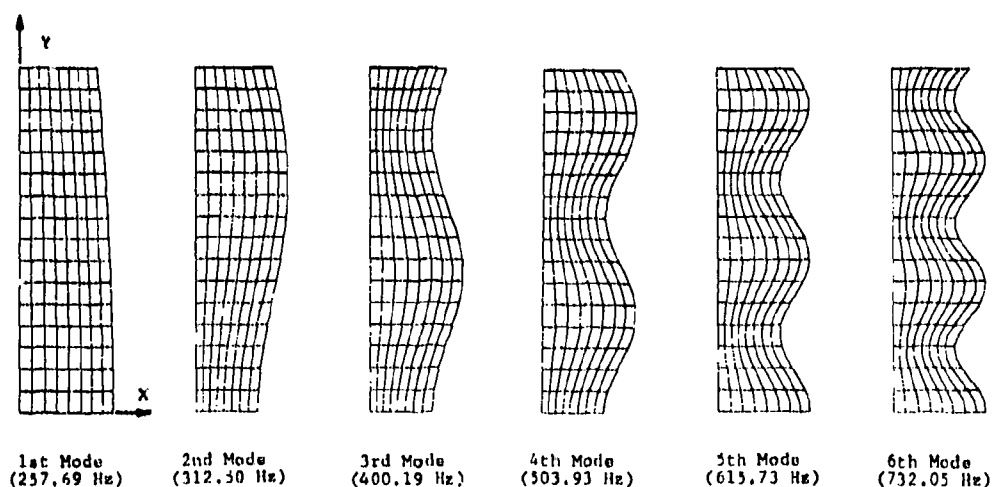


Figure 3. The First Six Natural Frequencies and Acoustic Pressure Modes of the Fluid with Rigid Boundary at the Beam Location

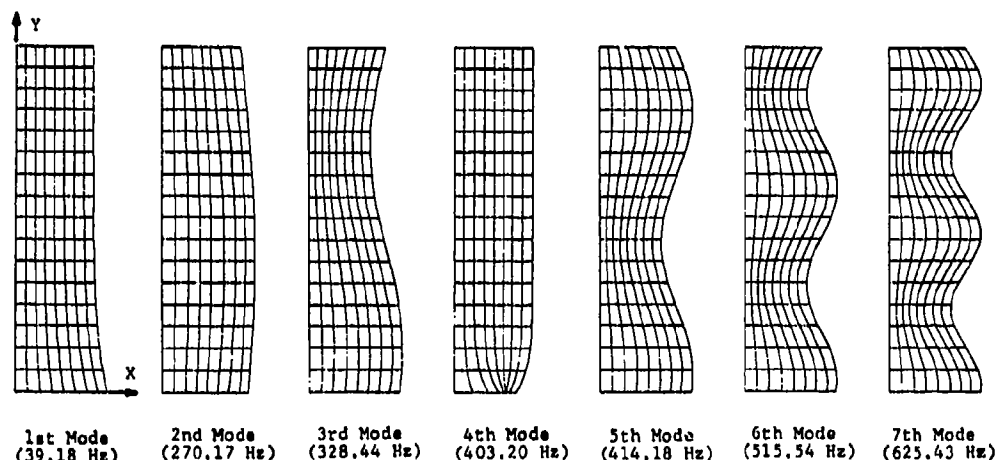
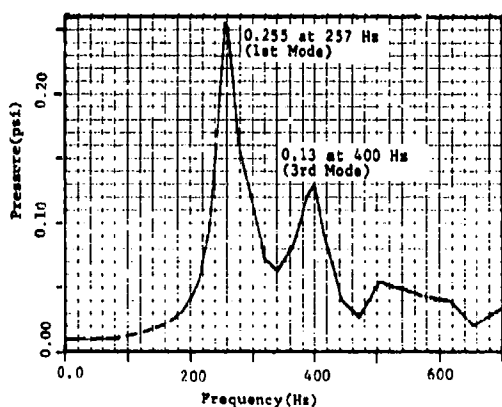
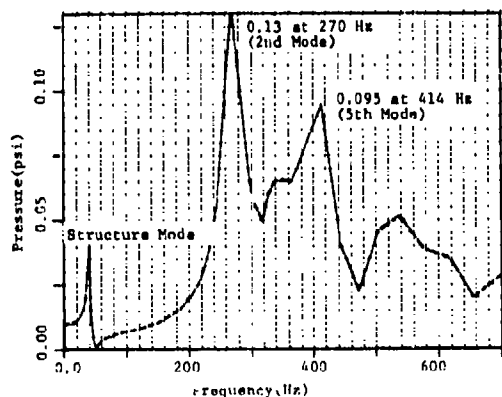


Figure 4. The First Seven Natural Frequencies and Acoustic Pressure Modes of the Coupled Fluid-Beam System

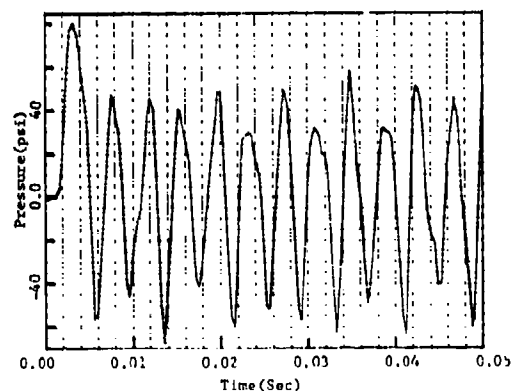


(a) Fluid with Rigid Boundary at Beam Location

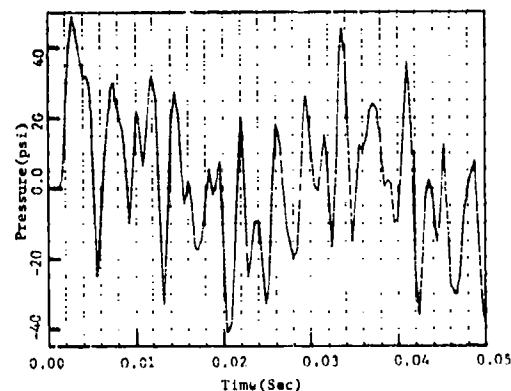


(b) Fluid Coupled with Beam

Figure 5. Acoustic Pressure Frequency Response at the Center of Beam (Grid 10016)



(a) Fluid with Rigid Boundary at the Beam Location



(b) Fluid Coupled with Beam

Figure 6. Acoustic Pressure Transient Response at the Center of Beam (Grid 10016)

Coupled Fluid-Beam System

The acoustic pressure frequency response at the center of beam is shown in Figure 5. The results show that the acoustic pressure response was dominant at 270 Hz (first pressure mode), and the second peak was observed at 414 Hz (fifth pressure mode). The small sharp acoustic pressure response peak at 39 Hz was caused by structural motion.

The dominant acoustic pressure response peak was reduced about 50% at the center of the beam due to the fluid-structure interaction.

MODAL TRANSIENT RESPONSES

Impulse acceleration was applied at the middle of the fluid (location \bar{x} shown in Figure 1(b)). The input excitation was a symmetrical triangular impulse of 127 m/s^2 (5000 in/sec^2) peak at 3 msec, with a duration of 6 msec. The first five beam and fluid modes are included to perform the modal transient response analysis. The damping is assumed to be zero.

Fluid with Rigid Boundary at Beam Location

The modal transient acoustic pressure response at the center of beam is shown in Figure 6. The results show that the peak overpressure occurred during the application of the impulse loading and the peak under-pressure occurred after termination of the impulse.

It also indicates clearly that the dominant frequency was 257 Hz, the first acoustic pressure mode.

Coupled Fluid-Beam System

The modal transient acoustic pressure response at the center of beam is in Figure 6. The results show that the peak over-pressure occurred during the application of the impulse loading and the peak under-pressure occurred after termination of the impulse. It also indicates that the dominant frequency was 270 Hz, the second modal frequency, and there was a higher frequency contribution which was small compared to the pressure peak at 270 Hz. They also show the participation of the first local mode at 39 Hz.

There was a significant decrease of the acoustic fluid pressure due to the boundary flexibility. At the center of beam, the peak over-pressure was reduced by about 40%, and the peak under-pressure showed about 39% decrease due to the FSI effect.

DIRECT TRANSIENT RESPONSES OF COUPLED FLUID-BEAM SYSTEM

To check the accuracy of the modal responses, the direct transient response analysis was also performed using the equation (6), the coupled unsymmetric matrix equation of motion. The same input excitation used for the modal transient response at the center of beam is calculated. The comparison of modal and direct transient responses showed an excellent agreement.

3D-NASTRAN/FINITE ELEMENT ANALYSIS

The rectangular shape pool with the contained fluid is considered and the 3D finite element model is shown in Figure 7. The vertical sides and the bottom floor of the pool are assumed to be rigid. Using the vertical plane of symmetry along the center of the pool, one half portions of the plate and the fluid are modelled using 48 4-node QUAD4 elements and 672 8-node HEXA elements.

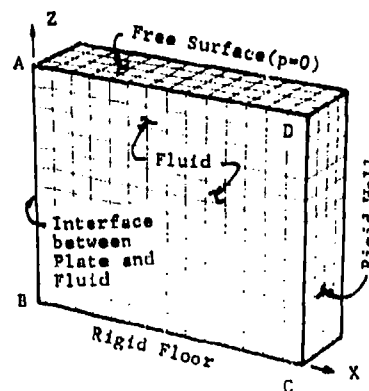


Figure 7. 3D-Finite Element Model

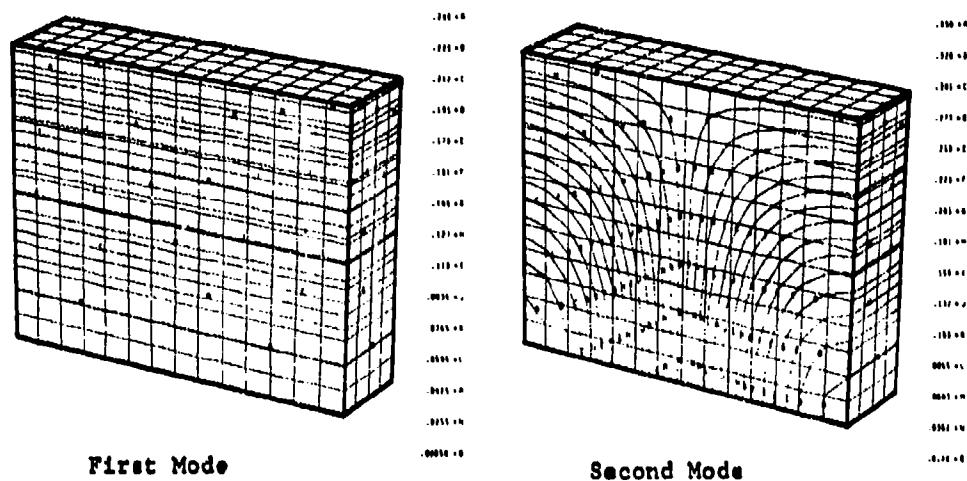


Figure 8. The First Two Acoustic Fluid Pressure Modes of the Fluid with Rigid Boundary at the Vertical Plate Location

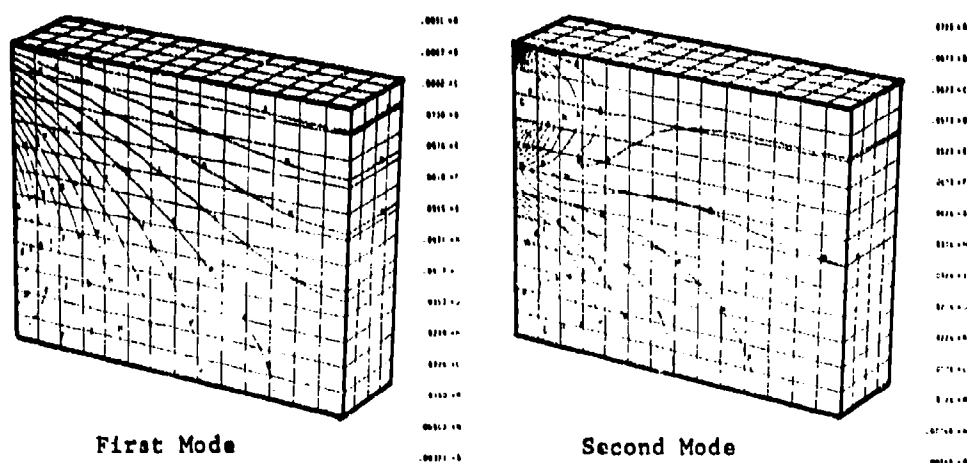


Figure 9. The First Two Acoustic Fluid Pressure Modes of the Coupled Fluid-Structure System

Only normal mode analysis is performed to look into the effect of the boundary flexibility on the acoustic fluid pressure modes. For the fluid with rigid boundary at the plate location (See Figure 8), the first mode is a vertical quarter wave mode, and the second mode is a coupled vertical $1/4$ wave-horizontal $1/2$ wave mode. For the coupled fluid-structure system (see

Figure 9), the strong effects of the boundary flexibility to the acoustic fluid pressure modes are observed. The first mode shows the combination of the vertical and the horizontal wave modes, whose dominant frequency is in the neighborhood of the fundamental frequency of the structure. The second mode shows the local acoustic pressure mode induced by the structure.

The strong participation of the vertical 1/4 wave (first mode) and 3/4 wave (third mode not shown) to the total response is anticipated. With the non-symmetric excitation to the fluid across the significant participation of the horizontal mode is anticipated.

CONCLUSIONS

An analogy between structural mechanics and acoustics was implemented on MSC/NASTRAN program to solve the fluid-structure problem. It shows that the modal approach produces excellent results compared with the theoretical results and the results of the direct step-by-step analysis.

The significant reduction of the acoustic pressure responses at the fluid-structure interface is observed as a result of fluid-structure interaction.

REFERENCES

1. O. C. Zienkiewicz and R. E. Newton, "Coupled Vibrations of a Structure Submerged in a Compressible Fluid", International Symp. on Finite Element Technique, Stuttgart, W. Germany, June 1969
2. R. H. MacNeal, R. L. Citerly and M. K. Chargin, "New Method for Analyzing Fluid-Structure Interaction Using NASTRAN", paper presented at 5th SMIRT Conference, Berlin, W. Germany, August 1979
3. R. H. MacNeal, R. L. Citerly and M. K. Chargin, "A Symmetric Modal Formulation of Fluid-Structure Interaction Including a Static Approximation to Higher Order Fluid Modes", paper presented at the NASTRAN User's Conference, Pasadena, Calif., March 1980
4. Y. S. Shin, "User's Guide to NASTRAN FSI Analysis", NEDE-25338, General Electric Company, Nuclear Division, San Jose, Calif., December 1980
5. Y. S. Shin, "Fluid-Structure Interaction Analysis of Full-Scale JAERI CRT Facilities", NEDE-25351, General Electric Company, Nuclear Division, San Jose, Calif., July 1981
6. R. H. MacNeal, "A Hybrid Method of Component Mode Synthesis", Computer & Structures, Vol. 1, (pp581-601), 1971

7. "Acoustic-Structure Analogy", MSC/NASTRAN Memo, RHM-70, MacNeal-Schwendler Corporation, Los Angeles, Calif., September, 1978

8. G. C. Everstine, "NASTRAN Implementation of the Doubly asymptotic Approximation for Underwater Shock Responses", NASA TMX-3428, (pp207-208), October, 1976

DISCUSSION

Mr. Kalinowski (Naval Underwater Systems Center): You mentioned you introduced Lagrange multipliers to make the matrices symmetric so that the solution procedure would be streamlined. But recently Gordon Everstine, at NARDC, has come up with a procedure for making the matrices symmetric without introducing Lagrange multipliers; therefore, you don't pay any penalty for increasing the number of degrees of freedom in the system. I think he published it in the Journal of Sound Vibration a few months ago.

Mr. Shin: I know about his work. It was done last year.

Mr. Kalinowski: I just thought I'd bring the point up. A second point is people who use this method should be aware of a problem with COSMIC-NASTRAN; whenever you have the number of internal degrees of freedom greater than 2¹⁵, which is roughly 32,000, there is a bug in the program that puts the entries in the cards for assigning mass and stiffness for fluid structure coupling in the wrong places on the inside of the program. Even though you put them in correctly on the data cards, it still puts them in the wrong places inside. We fixed this up in the latest version that will be coming out in the next issue. It only happens on a VAX computer, or any computer that has a 32 bit word. It won't happen on CDC or UNIVAC computers.

Mr. Shin: I used MSC NASTRAN, and I am not sure whether exactly the same bug is in there or not, but I doubt it. Another bad option in NASTRAN is if you have 1,000 or 2,000 degrees of freedom, which are constrained out of 5,000 degrees of freedom, you need storage space for a 6,000 degree of freedom system. Something has to be done about that; otherwise, you can't run it. My largest problem size was a 24,000 degree of freedom system for a suppression pool analysis which had about 16,000 degrees of freedom that should be constrained because the pressure mode had only one degree of freedom per node. We discovered that later. We found the way to get rid of that from the beginning so I didn't have to deal with the G size and use much more core than I actually needed.

FLUID-STRUCTURE INTERACTION BY THE METHOD OF CHARACTERISTICS

Franklin D. Hains
Naval Surface Weapons Center
White Oak, Silver Spring, Maryland

Linearized formulations for the pressure loading on submerged structures are inadequate when applied to impulsive loads from strong underwater shock waves. The limitations are discussed briefly, and a new approach based on the method of characteristics is presented. A non-linear, exact relation is obtained for the pressure loading on a compliant structure produced by a plane shock wave. The characteristics in the physical and state planes are described for the interaction of three-dimensional, curved shock fronts with a structure. An approximate, non-linear relation is obtained for impulsive shock loading on compliant surfaces by curved shocks. This relation can be used to improve the accuracy of computer codes that currently use linearized interaction formulations.

INTRODUCTION

The reflection of an underwater shock from a submerged structure leads to a complex fluid-structure interaction problem. The approach that is generally used to solve this problem is to decouple the fluid mechanics from the structural mechanics (1). The pressure loading is expressed as a function of two variables: The pressure field on a rigid structure, and the velocity of the surface of the structure. For relatively weak shocks moving just above the speed of sound, this linearized approximation may be adequate as long as the structural velocity does not increase to such an extent that the theory predicts unrealistic negative values of pressure that pull back on the moving surface. Some computer codes that handle fluid-structure interaction problems appear to have no restrictions on the magnitude of tension the water can sustain. The output from these codes often do not include plots of the computed pressure loading on the moving surface of the structure. Without knowing the actual pressure loading that produces the deformation of the structure, it is difficult to place much confidence in the numerical results generated by such codes.

In general, the fluid-structure interaction problem is non-linear, and the pressure loading at any instant in time is a function of the previous history of the motion of the structure. In this paper, the method of characteristics is used to obtain a non-linear approximation for the pressure loading which is independent of the previous

history of the motion. This approximation can be used to improve the accuracy of fluid-structure interaction computer codes.

A MODIFIED EQUATION OF STATE FOR WATER

The reflection of a shock from an underwater structure compresses the water in contact with the wall. As the increased pressure begins to move the wall, the water also moves with it, but the volume of a moving element of water also increases. This volumetric change leads to a reduction in the density of the water which, in turn, leads to a reduction in pressure. Very often, the pressure will fall below atmospheric, and cavitation will occur. In this paper, the water is treated as a continuum even if cavitation occurs.

The Tait equation of state for water is

$$p^* = a [\rho^*]^g - b \quad (1)$$

where $a = 3001$, $b = 3000$, and $g = 7.15$. The pressure in atmospheres is related to the dimensionless pressure p^* by

$$p = p_0 p^* \quad (2)$$

where p_0 is the pressure at a reference state which is chosen here as one atmosphere. Similarly, the water density in grams per cubic centimeter is related to the dimensionless density ρ^* by

$$\rho = \rho_0 \rho^* \quad (3)$$

where ρ_0 is the water density at the reference state. In this paper, all quantities with an asterisk (*) are dimensionless quantities.

As indicated in Figure 1, the pressure can go negative if the density is reduced sufficiently. With the standard Tait equation, the pressure drops to -3000 atmospheres when the density reaches zero. Such high values of tension are not realistic. The Tait equation can be modified by resetting the coefficients a, b, and g to a new set of values A, B, and G when pressure p^* drops below 1.0. The constant B (or b in the case of the Tait equation) is equal to the absolute value of p^* when the density vanishes. As shown in Figure 1, the values of the constants A and G are chosen so that the dashed curves merge into the solid Tait equation curve so that the slopes and values are continuous at point J. In this way, the state of the water is represented by a continuous curve so that the sound speed is also continuous.

The speed of sound for low pressures can be computed from the expression

$$c = \sqrt{\frac{dp}{d\rho}} \quad (4)$$

Since the slope of the state equation plotted in Figure 1 approaches zero as the water density is reduced, the speed of sound also approaches zero with the density. With this modification of the Tait equation, water can be treated as a continuum with continuous changes in pressure, density, and sound speed, even though cavitation may occur.

REFLECTION OF A PLANE SHOCK WAVE

The dynamics of shock wave-structure interaction can best be understood by first treating a simple problem in a number of logical steps. To accomplish this, we have chosen the configuration shown in Figure 2 where a plane shock approaches a wall. The conditions behind the shock are assumed to be uniform, leading to the step function distribution in pressure shown at the bottom of the figure. The pressure is raised from the ambient level p_a to the level p_i behind the incident shock.

The pressure loading after shock reflection is dependent on the physical characteristics of the structure. If the structure is perfectly rigid so that it cannot move, as shown in Figure 3, a reflected pressure denoted by P is produced in the region between the shock and the wall. On the other hand, if the structure is compliant and begins to move under the

initial reflected pressure loading, expansion waves will be emitted by the moving wall as shown in Figure 4. A train of these expansion waves is shown at the top of the figure, and the corresponding pressure distribution is shown at the bottom. The actual pressure exerted on the wall which produces the motion, which is denoted by p_w , is the combined result of the motion shock waves and expansion waves.

The trajectory of the wall is shown in the physical plane presented on the left side of Figure 5. After the reflected shock produces a peak pressure P in region I which starts the wall moving, expansion waves move back into the water along the II family of characteristics. Along the characteristics, the compatibility conditions given in Reference 2 require

$$dp = \pm \rho c du \quad (5)$$

where the plus and minus signs apply to the II and I families of characteristics in the state plane, respectively. In the state plane shown on the right side of Figure 5, the characteristics are straight lines. There is a change in slope of the characteristics when the coefficients in the modified state equation change their values abruptly at the point where the pressure drops below atmospheric.

The density, sound speed, water velocity, and peak pressure are related to their dimensionless values, indicated by an asterisk, through the expressions

$$\begin{aligned} \rho^* &= \frac{\rho}{\rho_0} & c^* &= \frac{c}{c_0} \\ u^* &= \frac{u}{c_0} & p^* &= \frac{p}{p_0} \end{aligned} \quad (6)$$

where p_0 , ρ_0 and c_0 are the reference values of pressure, density and sound velocity, respectively. In terms of these variables, the integration of Equation (5) along the I family characteristic in the state plane leads to

$$\int_{p^*}^{p^*} dp^* = - \rho^* c^* \int_{u^*}^{u^*} du^* \quad (7)$$

If the acoustic impedance $\rho^* c^* = 1$, Equation (7) reduces to the familiar linearized expression

$$p^* = P^* - \rho^* u^* \quad (8)$$

given in Reference 1. In this acoustic approximation, the density and sound speed of

the water will change across a shock, but will remain constant after the shock passes. Also, all expansion and compression waves will move at the same sound speed, and the water velocity adjacent to a moving wall must always be small compared to the sound speed.

With the aid of Equations (1) and (4), the exact expression for the acoustic impedance is

$$\rho^* c^* = [\rho^*]^n \quad (9)$$

where

$$n = \frac{g+1}{2g} \quad (10)$$

Substitution of Equation (9) into Equation (7) leads to the exact, non-linear pressure relation

$$p^* = -b + a [c^*]^1/m \quad (11)$$

where

$$m = \frac{g-1}{2g} \quad (12)$$

and

$$c^* = \left[\frac{p^* + b}{a} \right]^m = gmu^* \quad (13)$$

Equation (11) relates the pressure acting on the wall to the velocity of the wall. Note that in this case the pressure at any instant is independent of the previous history of the wall motion.

Referring to Figure 5, the shock wave raises c^* from 1.0 in region A, to 2.0 in region 1. Because u^* is still zero, the water in contact with the wall has been instantaneously compressed by the shock, but has not been set into motion. As the wall begins to move, the pressure loading decreases in accordance with Equation (11). Expansion waves are emitted by the wall as shown in the physical plane of Figure 5. The water that is in contact with the wall remains in contact with the wall as it moves. Any change in pressure is always accompanied by a change in water density as prescribed by Equation (1).

The numerical values of points 1 through 4, shown in the state plane of Figure 5, are obtained from Equation (13). The points fall on a characteristic of the I family. If the pressure drops below an atmosphere, the slope of the characteristic increases dramatically so that any further small increase in wall

velocity will produce cavitation and unload the structure. This exact solution for a plane shock in water shows that only a limited amount of energy can be transferred to an underwater structure because of the pressure release produced by the motion of the structure.

A comparison of the numerical results using the non-linear and linear fluid-structure interaction relations is shown in Figure 6. The linearized solutions (dashed lines) were obtained from Equation (8), and the non-linear solutions (solid curves) were obtained from Equation (11). The curves were computed for P^* spanning the range from 4 to 40,000 atmospheres. If the two curves that correspond to a particular value of P^* are examined, it is clear that at the same wall velocity the linear theory predicts a higher pressure on the structure than the exact theory. This means that, in the absence of negative pressure loadings, the linearized theory will predict a larger maximum displacement of a structure than actually occurs.

The maximum velocity of the wall is reached when the wall pressure P^* vanishes. Using Equation (8), the maximum velocity attainable in the linearized case is

$$[u_{\max}^*]_{\text{linear}} = P^*/(ag) \quad (14)$$

The corresponding value in the non-linear case is

$$[u_{\max}^*]_{\text{non-linear}} = \frac{1}{gm} \left[\left(\frac{P^* + b}{a} \right)^m - \left(\frac{b}{a} \right)^m \right] \quad (15)$$

where m is given by Equation (12). The ratio of these maximum velocity values is defined as

$$R = \frac{[u_{\max}^*]_{\text{linear}}}{[u_{\max}^*]_{\text{non-linear}}} \quad (16)$$

Using values of a , b , and g corresponding to the last equation, the values of R shown in Figure 7 were computed. The error associated with the linearized theory increases with shock strength as non-linear effects predominate.

REFLECTION OF A CURVED SHOCK

Most shocks of practical interest are three-dimensional in nature, and therefore, have a curved shape. The surface area of a

curved shock tends to increase with time, and its strength tends to decrease with time. As shown in Figure 8, a curved shock is weakened by a train of expansion waves emitted by the shock as it moves through the water. These waves produce the impulsive pressure distribution shown at the bottom of the figure. The reflection, of a curved shock from a rigid wall is illustrated in Figure 9. After reflection, the surface area of the shock front continues to increase, and the shock is weakened further by the emitted expansion waves. These waves move toward the wall and serve to reduce the increase in wall pressure initially imparted by the reflected shock. The resultant pressure loading on the wall is impulsive, and decays rapidly with time.

If the wall is compliant, so that it begins to move under the applied impulsive loading, it will also emit its own train of expansion waves as shown in Figure 10. These waves tend to reduce the wall pressure further so that the loading becomes even more impulsive. This can be seen from the pressure distributions shown in Figures 9 and 10.

An overall view of the shock-structure interaction is shown in Figure 11. The deceleration of the incident and reflected shocks by the emitted expansion waves produces the curved paths shown in the diagram. If the shocks were plane instead of curved, no expansion waves would be emitted by the shocks and the paths would be straight lines. The pressure loading produced by the reflected shock is modified by expansion waves emitted from the reflected shock and by expansion waves emitted from the moving wall. When the wall has reached its maximum velocity and begins to decelerate, it starts to emit compression waves instead of expansion waves. These compression waves will eventually overcome the influence of the expansion waves from the shock so that the pressure loading reaches a minimum and begins to increase, producing a secondary pressure peak.

The physical and state planes for curved shock reflection from a compliant wall are shown in Figure 12. Because waves of both families of characteristics impinge on the wall, the path of conditions in the state plane for regions 1 through 7 follow a zigzag path. The simple integration of Equation (5) used for plane shocks is no longer possible because of the continual change in sign of the right-hand side of the equation as the solution jumps from one family of characteristics to the other. This means the wall pressure at any instant in time is dependent not only on the current wall velocity, but is a function of the previous

history of the motion of the wall. The pressure loading can be computed step-wise in time by the computational technique described in Reference 3.

A NON-LINEAR APPROXIMATION FOR FLUID-STRUCTURE INTERACTION

It is desirable to have a fluid-structure interaction model that has greater accuracy than the linearized theory, but is not as complicated as the exact method of characteristics. This can be accomplished by a modification of the exact solution presented earlier for a plane shock wave. When a rigid wall is struck by a plane shock, the pressure loading has the constant value P^* . If a rigid wall is struck by a curved shock, the pressure loading has an impulsive distribution denoted by p_R^* . In Equation (11), the fluid-structure interaction equation for a plane shock, the pressure loading is a function of the local sound speed of the water in contact with the wall. As indicated by Equation (13), the sound speed for the plane shock case, is a function of P^* , the rigid wall pressure loading. In the curved shock case, it is reasonable to replace P^* in Equation (13) by p_R^* so that Equation (13) becomes

$$c^* = \left[\frac{p_R^* + b}{a} \right]^m - \gamma u^* \quad (17)$$

Now, the sound speed c^* on the wall is influenced by expansion waves from the shock as well as by expansion waves emitted from the moving wall. Substitution of Equation (17) into Equation (13) leads to the non-linear fluid-structure interaction formula

$$p^* = -b + a \left[\left(\frac{p_R^* + b}{a} \right)^{\frac{g-1}{2g}} - \left(\frac{g-1}{2} \right) u^* \right]^{\frac{2g}{g-1}} \quad (18)$$

where a , b , and g are coefficients in the Tait equation of state for water. These coefficients are replaced by A , B , and G where the pressure falls below one atmosphere. If the changes in u^* are small, Equation (18) reduces to the linearized formula given by Equation (8).

The physical and state planes that correspond to this approximation are shown in Figure 13. Across the dashed horizontal

lines shown in the physical plane, there is an instantaneous drop in c^* as indicated by the vertical dashed lines in the state plane. Because this drop occurs without any change in wall velocity u^* , Equation (17) shows that the drop is a result of the decay of p_0^* with time. The change across the II family of characteristics in the physical plane is along the I family of characteristics in the state plane. Thus, the path from region 1 to region 7 in the state plane is comprised of segments along I family characteristics separated by vertical jumps between characteristics. Since the path is only along one family of characteristics, Equation (8) can be integrated as before using only the negative sign of the right-hand side of the equation. The final result of this integration is Equation (18).

A comparison of the paths in the state planes of Figures (10) and (13) suggests that this non-linear approximation should give results in close agreement with the exact solution by the method of characteristics. The use of the non-linear formulation in structural codes can be implemented in two ways. The satisfaction of Equation (18) at any time step can be met through an iteration procedure, or Equation (18) can be satisfied one time step later.

CONCLUSIONS

Underwater fluid-structure interaction for pressure loadings from plane and curved shocks has been studied with the method of characteristics. The Tait equation of state for water was modified to handle the low pressure and negative pressure regime where cavitation can occur. With the modified equation of state, the water can be treated as a continuum over the entire pressure loading regime.

An exact expression was obtained for the pressure loading from a plane shock wave which is modified by wall motion. Comparisons with the corresponding expression from linearized theory shows that for the same wall velocity, linearized theory predicts a higher pressure loading than the exact theory. This means that linearized expressions for fluid-structure interaction tend to overpredict the deformation of submerged structures from underwater shocks.

An approximate, non-linear fluid structure interaction relation was obtained for the case of impulsive pressure loading from a curved shock wave acting on a compliant structure. In the limit of weak shocks, this expression reduces to the linearized expression obtained by acoustic theory.

REFERENCES

1. Bleich, H. H., "Dynamic Interaction between Structures and Fluid," Structural Mechanics, Proceedings of the First Symposium on Naval Mechanics (New York: Pergamon Press, 1960), p. 273.
2. Stanyukovich, K. P., "Unsteady Motion of Continuous Media," (New York: Pergamon Press, 1960), pp. 64-75.
3. Hains, F. D., Yoler, Y. A., and Ehlers, E., "Axially Symmetric Hydromagnetic Channel Flow," Dynamics of Conducting Gases (Evanston: Northwestern University Press, 1960), pp. 86-103.

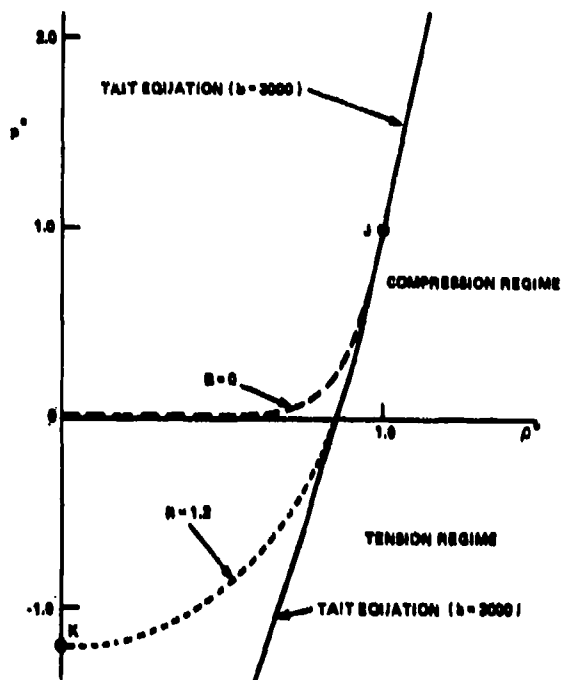


FIGURE 1. THE EQUATION OF STATE FOR WATER

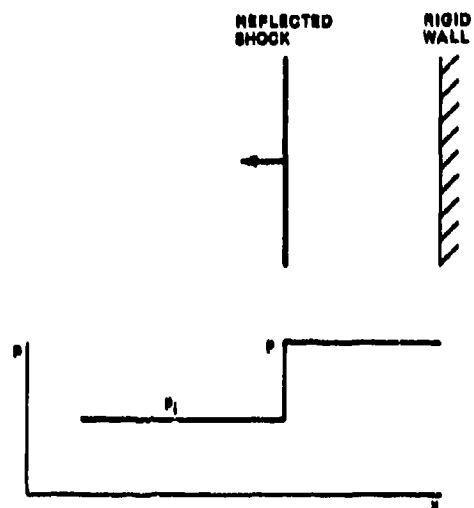


FIGURE 3. REFLECTION OF A PLANE SHOCK FROM A RIGID WALL

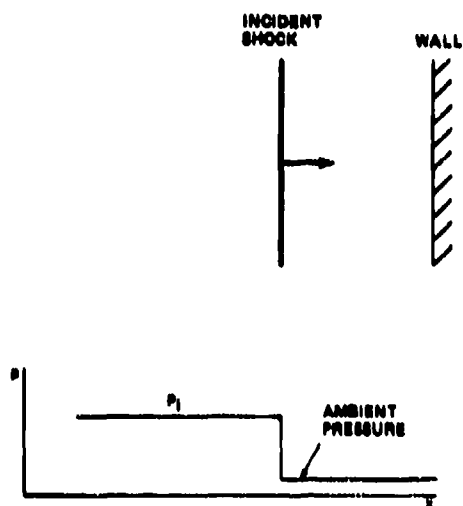


FIGURE 2. A PLANE SHOCK APPROACHING A WALL

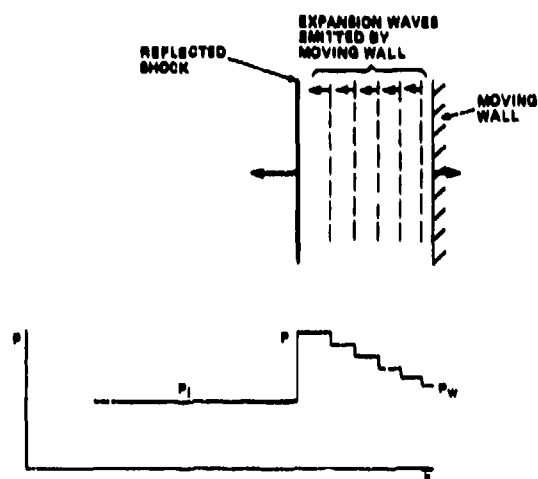


FIGURE 4. REFLECTION OF A PLANE SHOCK FROM A COMPLIANT WALL

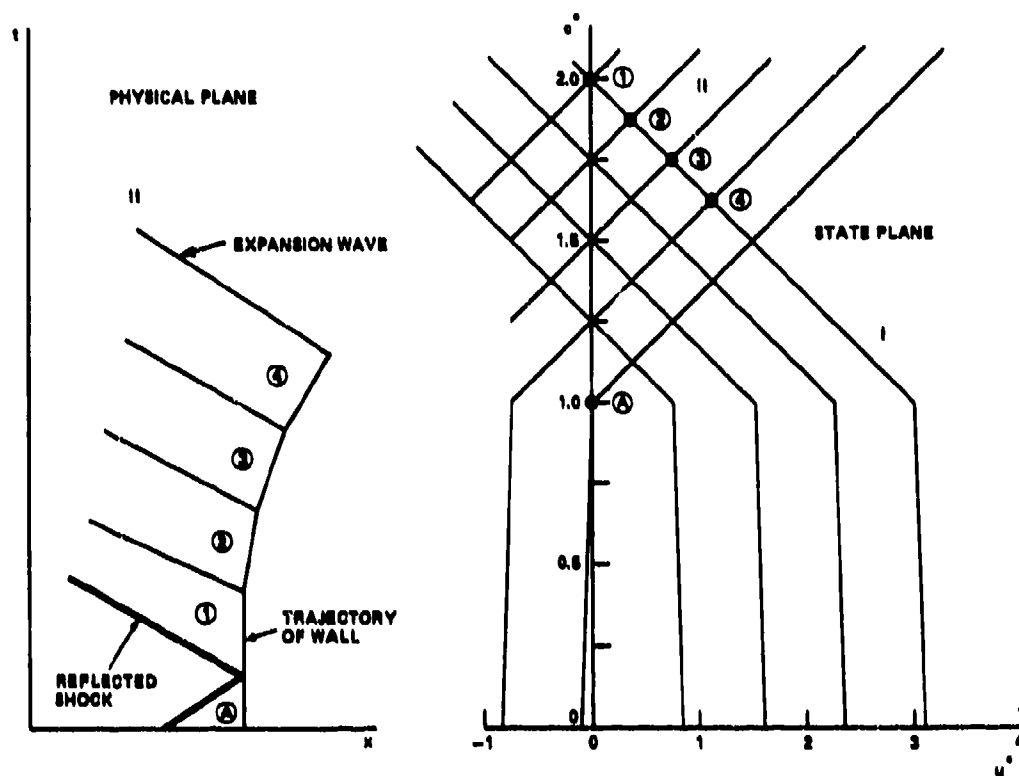


FIGURE 5. PHYSICAL AND STATE PLANES FOR PLANE SHOCK REFLECTION FROM A COMPLIANT WALL

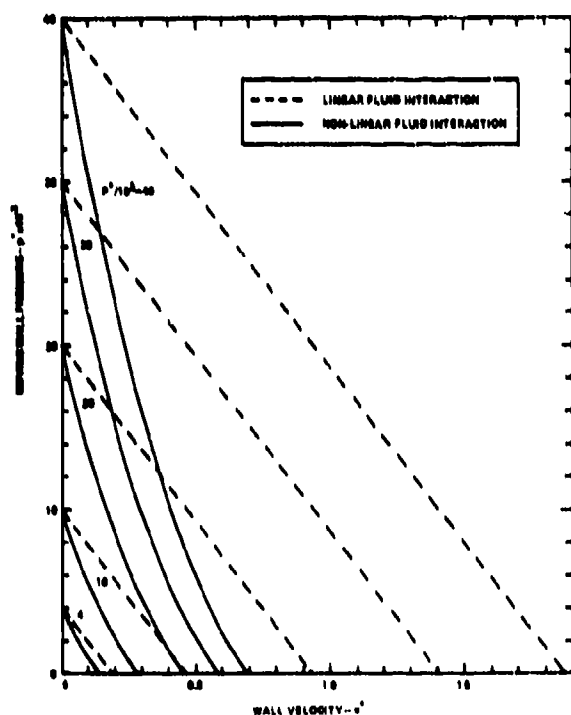


FIGURE 6. COMPARISON OF LINEAR AND NON-LINEAR WALL PRESSURES

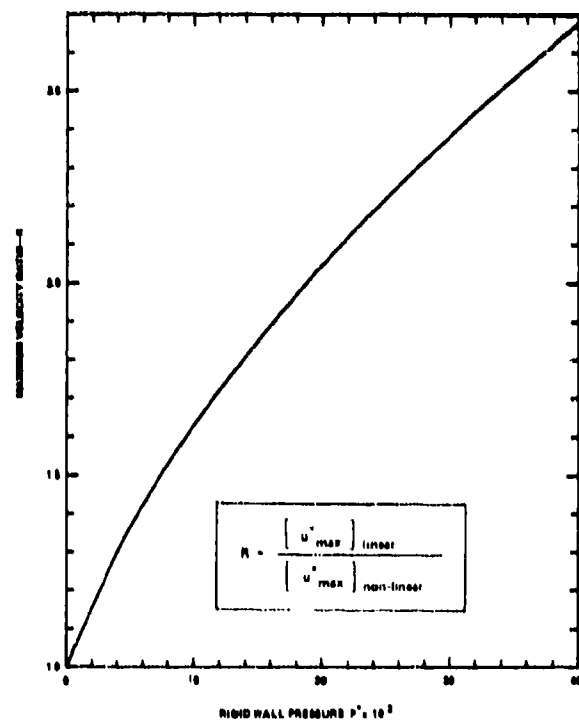


FIGURE 7. DISTRIBUTION OF MAXIMUM VELOCITY RATIO

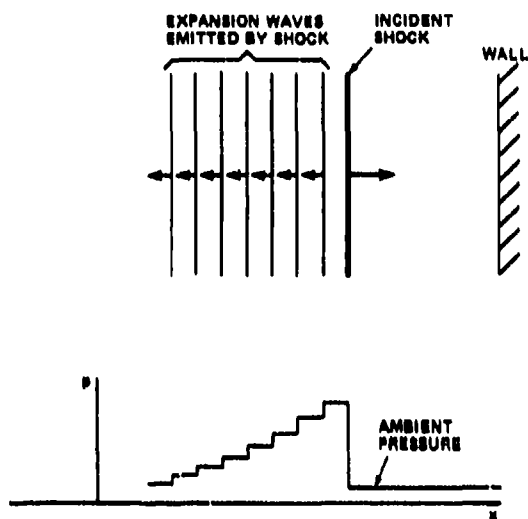


FIGURE 9. A CURVED SHOCK APPROACHING A WALL

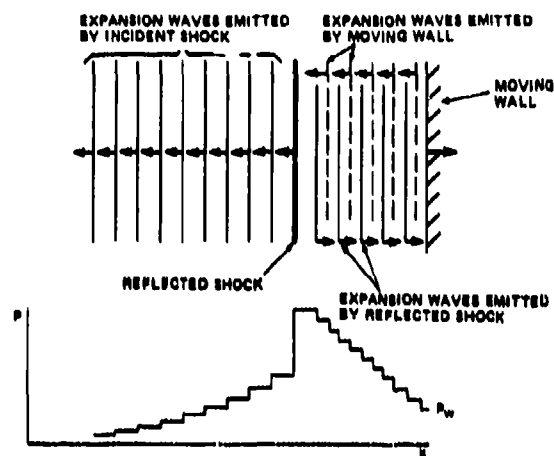


FIGURE 10. REFLECTION OF A CURVED SHOCK FROM A COMPLIANT WALL

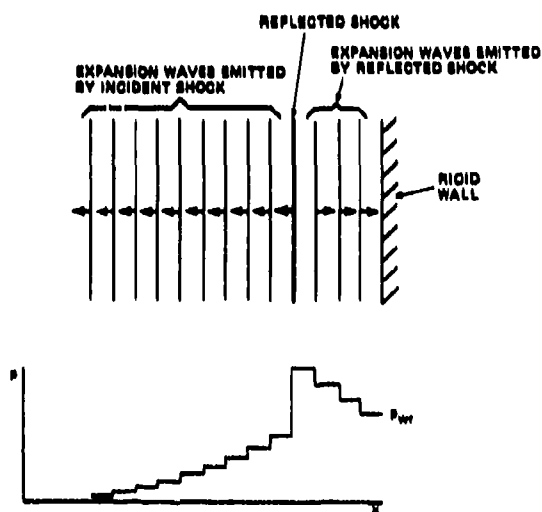


FIGURE 9. REFLECTION OF A CURVED SHOCK FROM A RIGID WALL

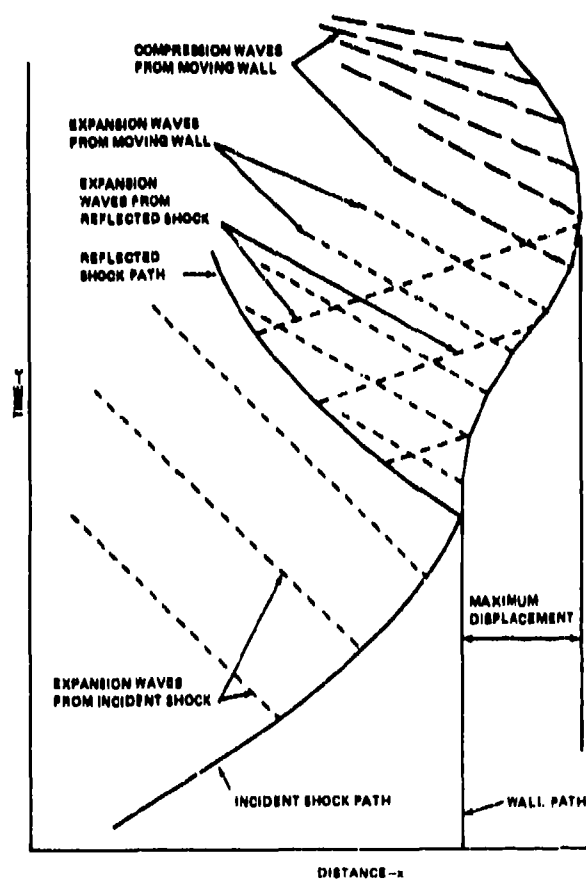


FIGURE 11. INTERACTION OF A CURVED SHOCK WITH A COMPLIANT WALL

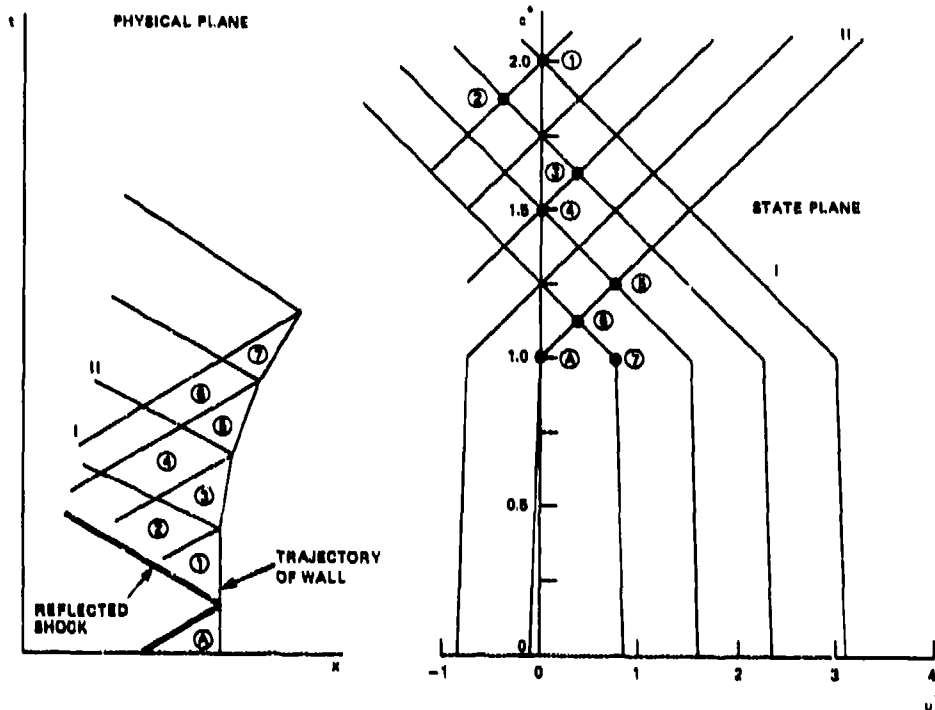


FIGURE 12. PHYSICAL AND STATE PLANES FOR CURVED SHOCK REFLECTION FROM A COMPLIANT WALL

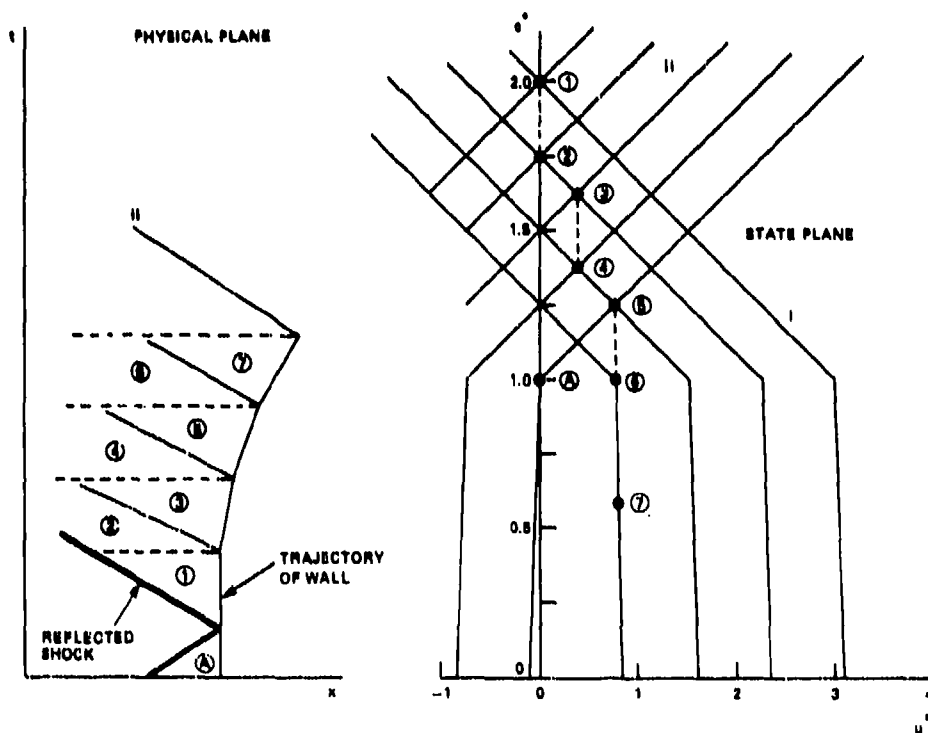


FIGURE 13. PHYSICAL AND STATE PLANES FOR NON-LINEAR APPROXIMATION

DISCUSSION

Mr. Kalinowski (Naval Underwater Systems Center): Is it possible to apply these procedures to two dimensional or three dimensional finite element or finite difference computational schemes?

Mr. Hains: You might have a problem if your formulation is in the form of a linear relation so it can handle matrices and so on; you may have to devise some iteration scheme since the formula is nonlinear.

Mr. Kalinowski: I see. Yes, many of the time schemes, nonlinear schemes, keep changing the matrices as they advance in time, so I would think you would be able to incorporate it then.

Mr. Hains: Yes.

A Solution to the Axisymmetric Bulk Cavitation Problem

Frederick A. Costanzo and John D. Gordon
David Taylor Naval Ship Research and Development Center
Underwater Explosions Research Division
Portsmouth, Virginia

Physical considerations are applied to the analysis of bulk cavitation in order to derive an existing method for determining the upper and lower cavitation boundaries. Then, a closure model is developed which uses the upper and lower cavitation boundaries as input and computes the time and depth of bulk cavitation closure, as well as the magnitude of the pressure pulse generated by the water hammer. Finally, an illustration is given on how to predict pressure and water particle velocity histories associated with the bulk cavitation phenomenon.

INTRODUCTION

Due to the recent shock tests of the nuclear guided missile cruiser, USS ARKANSAS (CGN-41), there has been a rapid growth of interest surrounding the phenomenon of bulk cavitation. Bulk cavitation occurs when compression waves, which are generated by the underwater detonation of an explosive charge, propagate to the surface and are reflected back into the water as rarefaction waves. These rarefaction waves cause a state of tension to occur within a large region of water. Since water cannot ordinarily sustain a significant amount of tension, it cavitates and the surrounding pressure rises to the vapor pressure of water. The region in which this occurs is known as the bulk cavitation region, and it includes all water which cavitates at any time after the detonation of the explosive charge. The upper and lower boundaries, which show the maximum extent of the cavitated region, form what is referred to as the bulk cavitation envelope. It is the extent of the cavitated region and the effects brought about by the contraction or closure of this region which is currently of major concern.

The existing method by Walker and Gordon [1] for calculating the bulk cavitation closure depths and times has been shown to be inconsistent with calculations for the cavitation boundaries. As a result of this, a new bulk cavitation closure theory which will be consistent with these cavitation boundaries must be developed.

OBJECTIVES

The objectives of this investigation are: first, to develop a method for determining the times and depths of closure of the bulk cavitation region which is consistent with the calculations for the cavitation envelope; and second, to use these computed closure times and depths in predicting the pressure and water particle velocity histories at any location within the range of bulk cavitation.

APPROACH

In this study, the method of Arons [2] for determining the bulk cavitation boundaries is derived from physical considerations. Next, a new model for determining the depths and times of cavitation closure is developed using the cavitation boundaries found by the method of Arons as input. Finally, the results obtained from this new model are used in conjunction with plane wave acoustics to predict pressure and water particle velocity histories. Throughout this entire study, the effects of a reflecting bottom are neglected and a free field condition is assumed.

STATEMENT OF THE PROBLEM

An explosive charge of weight, W , detonated in water at a depth, D , is considered. The water in the vicinity of the charge is assumed to be infinitely deep. Attention is focused on a pressure gage located at a point (X, Y) as shown in Fig. 1. Upon detonation, a compressive shock wave is generated and radiates spherically away from the source. Before this

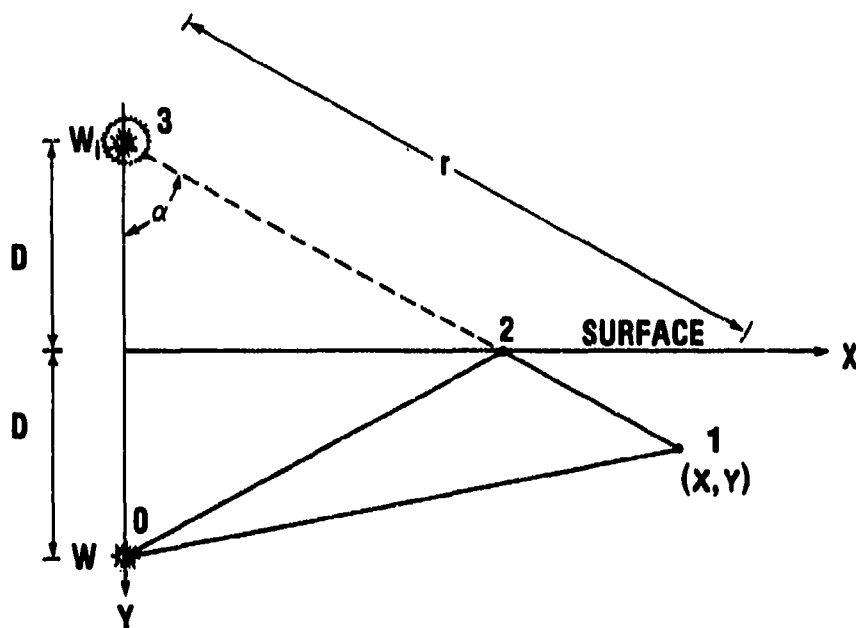


Fig. 1 - Incident and Reflected Wave Paths

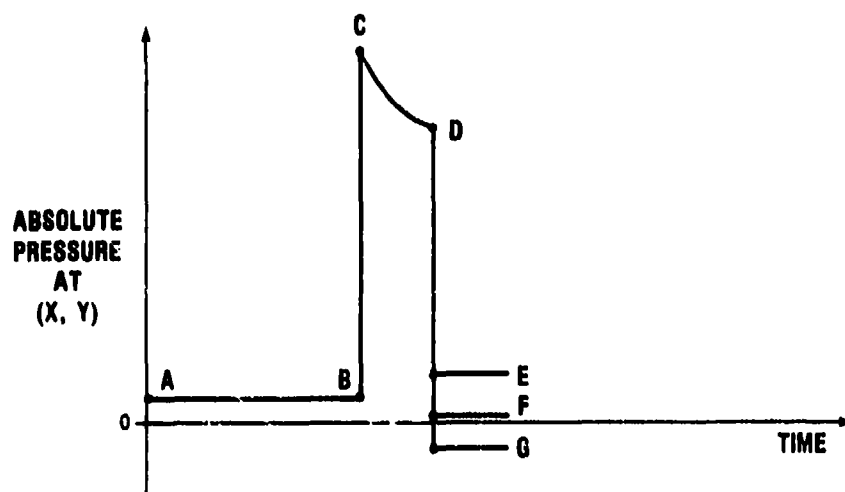


Fig. 2 - Absolute Pressure at a Point

compressive wave reaches the gage location by traveling along line 0-1, the gage, assuming for illustration purposes that it is an absolute pressure gage, measures a pressure denoted by line A-B in Fig. 2. This pressure is simply the sum of the atmospheric and hydrostatic pressures at the gage location. When the shock wave arrives at the point (X, Y), the pressure jumps to point C and then decays exponentially along the curve C-D. In Fig. 1, line 0-2 represents a particular path of the shock wave which travels to the surface. Since the specific acoustic impedance of air is much less than that of water, a rarefaction wave is reflected back into the water along segment 2-1. The arrival of this reflected wave at the gage location is termed surface cutoff and is illustrated in Fig. 2 by a sudden drop in the absolute pressure. This concept of surface cutoff is made clearer by depicting the rarefaction wave as emanating from an image charge, W_1 , and propagating along line 3-2-1 in Fig. 1. This is known as the method of images for computing surface cutoff and is valid since the distance 3-2-1 equals the distance 0-2-1. Fig. 2 illustrates that the rarefaction wave tries to lower the absolute pressure at the gage location to one of three levels; greater than the vapor pressure of water (B), less than the vapor pressure of water but greater than the cavitation pressure (F), or less than the cavitation pressure (G). Here, the cavitation pressure is defined as the pressure at which the water breaks. The next section describes how the method of Arons [2] is used to map out the bounds of the cavitated region that forms when surface cutoff tries to lower the absolute pressure below the cavitation pressure.

DERIVATION OF THE METHOD OF ARONS AND THE TANGENT RULE

Let P be the absolute pressure (overpressure + atmospheric + hydrostatic) at a point (X, Y) in the water at an instant prior to the arrival of the reflected wave from the surface. Then let P be a function of the coordinates α and r as shown in Fig. 1; i.e., $P = P(\alpha, r)$. According to Arons [2], the upper cavitation boundary is defined as the locus of points at which the absolute pressure drops to the cavitation pressure (a negative pressure of a few psi) upon arrival of the rarefaction wave. Water which is in cavitation will remain cavitated as long as the absolute pressure does not rise above the vapor pressure of water (about 0.3 psi). In the method of Arons [2], both the vapor pressure of water and the cavitation pressure are taken to be zero. Thus, the equation defining the upper cavitation boundary is

$$P(\alpha, r) + P_r = 0 \quad (1)$$

If P_r , the reflected wave, is expressed in terms of the charge weight and standoff using the method of images, then $P_r = -A(W^{1/3}/r)^B$.

Substitution of this expression in Eq. (1) gives

$$P(\alpha, r) - A(W^{1/3}/r)^B = 0 \quad (2)$$

Here A and B are constants particular to the type of explosive.

Before the cavitation boundary is discussed, the term breaking pressure must be defined. The breaking pressure is the magnitude of the rarefaction wave (or relief wave, as it is commonly termed) which reduces the absolute pressure at a point to the cavitation pressure. In other words, since the cavitation pressure is taken to be 0 psi absolute, the breaking pressure has a magnitude equal to the absolute pressure at a point prior to the occurrence of cavitation at that point. The equation of the lower cavitation boundary is derived from consideration of the propagation of this breaking pressure into the uncavitated water beneath this boundary. Let $P_r = P(\alpha, R)$ be the breaking pressure for a point lying at the lower cavitation boundary. At this lower boundary, $P(\alpha, R)$ must propagate into uncavitated water with spherical attenuation resulting in $P_r = P(\alpha, R) \times (R/r)^B$. This is represented in Fig. 3. This pressure expression, $P_r = P(\alpha, R) \times (R/r)^B$, must have a faster decay rate than the general expression for absolute pressure, $P = P(\alpha, r)$, or the water located along the dashed line extending below the lower cavitation boundary will continue to cavitate. Thus, at a point on the lower cavitation boundary, the decay rate of both of these pressure expressions is the same. Therefore:

$$\left. \frac{d}{dr} [P(\alpha, R) \times (R/r)^B] \right|_{r=R} = \left. \frac{d}{dr} [P(\alpha, r)] \right|_{r=R}$$

If all terms of this equation are shifted to one side of the equal sign and r^B is factored out, then application of the chain rule to differentiation of a product results in:

$$\left. \frac{d}{dr} [r^B \times P(\alpha, r) - P(\alpha, R) \times R^B] \right|_{r=R} = 0$$

This expression may be simplified further by recognizing that the product, $P(\alpha, R) \times R^B$, pertains to a specific point and thus may be treated as a constant when differentiating. Therefore, this equation becomes:

$$\frac{d}{dr} [r^B \times P(\alpha, r)] = 0 \quad (3)$$

where $r = R$, the point at the lower cavitation boundary for a given α . Eq. (3) is the method of Arons [2] for determining the lower cavitation boundary. It is equivalent to the equation presented for this method in the report by Gaspin and Price [3].

In Fig. 4, the general shape of the bulk cavitation envelope as determined by the method of

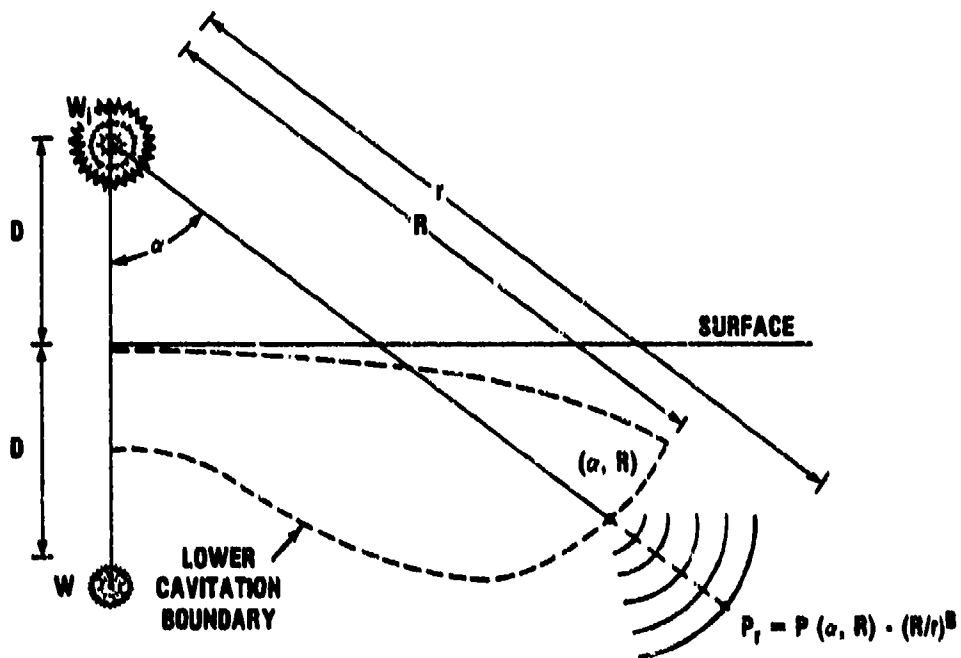


Fig. 3 - Propagation of the Breaking Pressure into Uncavitated Water

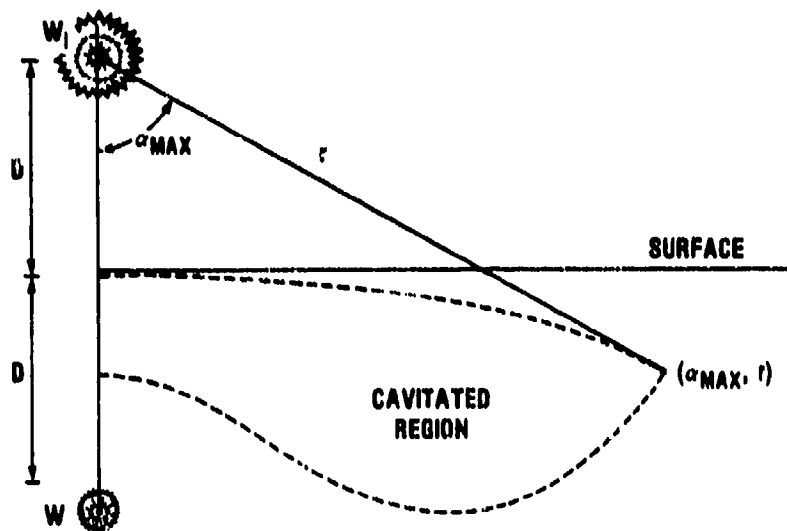


Fig. 4 - Bulk Cavitation Bounds and Rule of Tangency

Arons [2] is given. It is of fundamental interest to the bulk cavitation problem to locate the point at which a line drawn from the image charge is tangent to the upper cavitation boundary. For the derivation of this tangent point, both sides of Eq. (2) are multiplied by r^B and the resulting equation and its total derivative with respect to r are written below as Eqs. (4) and (5), respectively.

$$r^B \times P(\alpha, r) - A(N^{1/3})^B = 0 \quad (4)$$

$$\begin{aligned} \frac{d}{dr} [r^B \times P(\alpha, r) - A(N^{1/3})^B] \\ = \frac{\partial}{\partial r} [r^B \times P(\alpha, r)] \\ + \frac{\partial}{\partial \alpha} [r^B \times P(\alpha, r)] \times \frac{d\alpha}{dr} = 0 \end{aligned} \quad (5)$$

For a given value of da/dr , the simultaneous solution of these two equations gives the corresponding values of α and r . When the ray extending from the image charge is tangent to the upper cavitation boundary, α is a maximum and $da/dr = 0$. When this value for da/dr is substituted into Eq. (5), the following is obtained:

$$\frac{\partial}{\partial r} [r^B \times P(\alpha, r)] = 0 \quad (6)$$

Therefore, the simultaneous solution of Eqs. (4) and (6) gives the values of α and r at the tangent point. Eq. (6) also happens to be equivalent to Eq. (3), the equation whose solution determines the lower cavitation boundary. This indicates that the lower and upper cavitation boundaries intersect at the point at which a line drawn from the image charge is tangent to the upper boundary. This rule of tangency is also illustrated in Fig. (4).

DEVELOPMENT OF THE CLOSURE MODEL

General Description

In Fig. 5, the general representation of a point which lies within the cavitated region is given. Upon the arrival of the relief wave at this point, the vertical component of the instantaneous water particle velocity is the vector sum of the vertical components of the two velocity vectors shown in Fig. 5. This vector sum is termed the vertical water particle kickoff velocity at point (X, Y) and is dependent solely upon the magnitudes and directions of the incident and reflected acoustic water particle velocities. The directions of these velocities are defined by the unit vectors, \hat{i} and \hat{j} , as shown in the figure.

At every horizontal range within the extent of the bulk cavitation envelope, there exists a

column of water which lies between the surface and the upper cavitation boundary. Since this water does not cavitate, it is assumed that all water particles contained in this vertical column are kicked off simultaneously with the kickoff velocity of the water particle located at the upper cavitation boundary. This is illustrated in Fig. 6. This surface layer, which is kicked off at the time of relief wave arrival at the upper cavitation boundary with an initial velocity, \bar{V}_0 , is decelerated by atmospheric pressure and gravity. At a short time later, the water particle lying directly beneath this surface layer is kicked off with an initial velocity, \bar{V}_0 . Since this particle lies within the cavitated region and is kicked off after the surface layer, it becomes separated from the surface layer and therefore has no atmospheric pressure acting upon it. Thus, only gravity decelerates this particle. Eventually, this water particle will collide with the surface layer above it. In the development of the closure model, it is assumed (as was done in the work by Waldo [4]) that this is a perfectly inelastic collision. Thus, this particle and the surface layer above it now form an augmented surface layer which has a velocity derived from a conservation of momentum consideration. As with the original surface layer, this augmented surface layer has atmospheric pressure and gravity acting to decelerate it.

Since the particles lying below the original surface layer are all kicked off at different times with different vertical kickoff velocities, inelastic collisions will occur one at a time between the growing surface layer and the particles directly below it. This process is known as accretion. If the surface layer displacement history at a horizontal range, X , is plotted with $t = 0$ referring to the time of explosive charge detonation, the curve in Fig. 7 is obtained. This curve is not quite a perfect parabola due to the fact that the surface layer mass is changing. Also note that this curve accounts for the initial displacement of the surface layer due to the incident shock wave prior to relief wave arrival at the upper cavitation boundary.

The vertical component of the water particle velocity for the point which lies at the lower cavitation boundary at this same horizontal range, X , also must be determined. Since cavitation does not extend below this point, separation will not occur between the underlying water particles. Hence, the water which lies below this point at the lower cavitation boundary will have a vertical velocity component which is dependent upon the time varying velocities \bar{V}_r and \bar{V}_l and their corresponding afterflow terms. This is depicted for the point (X, Y_l) in Fig. 8. As this lower cavitation boundary moves upward, it catches up with free falling water particles and an accretion similar to that which occurs with the surface layer takes place. However, in this development, it is assumed that particles which have accreted with the moving lower

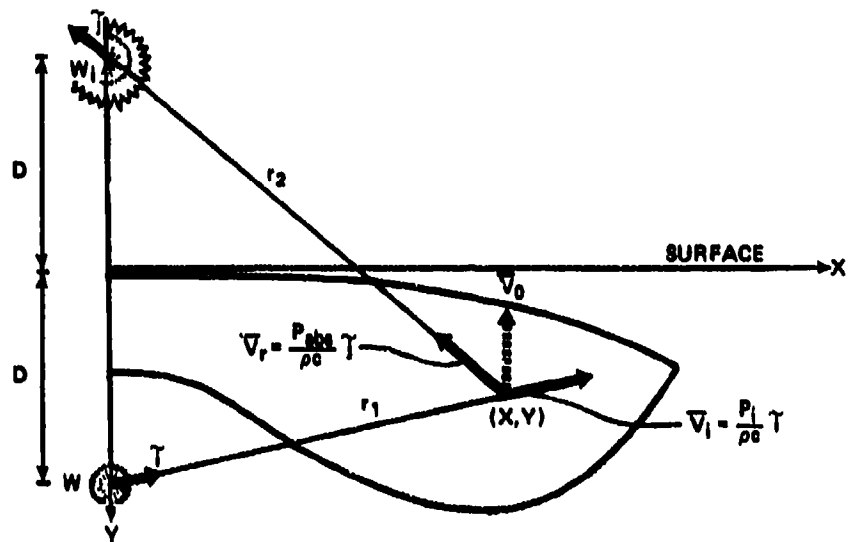


Fig. 5 - General Representation of a Point Lying in the Cavitated Region

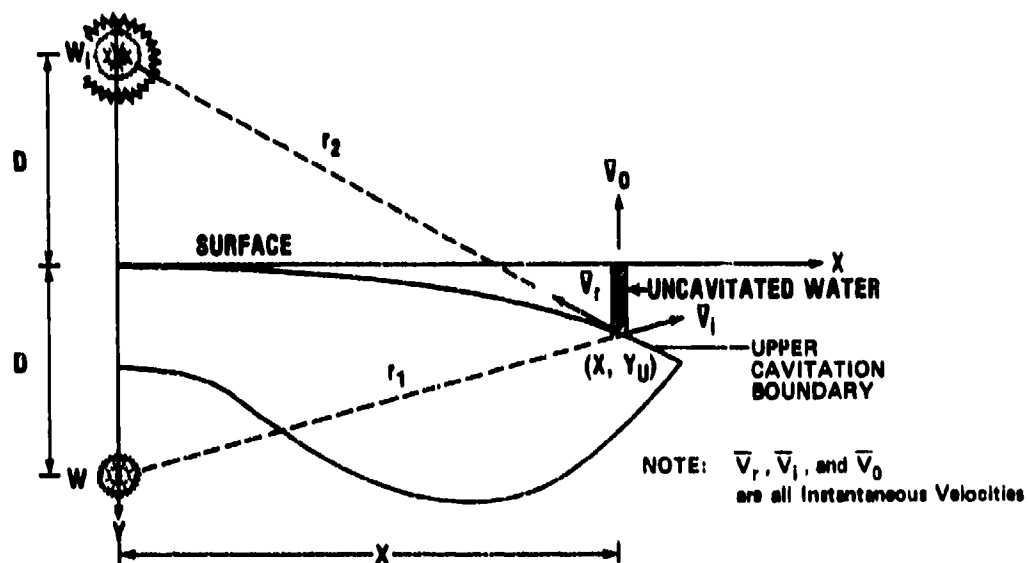


Fig. 6 - Kickoff Velocity of the Surface Layer

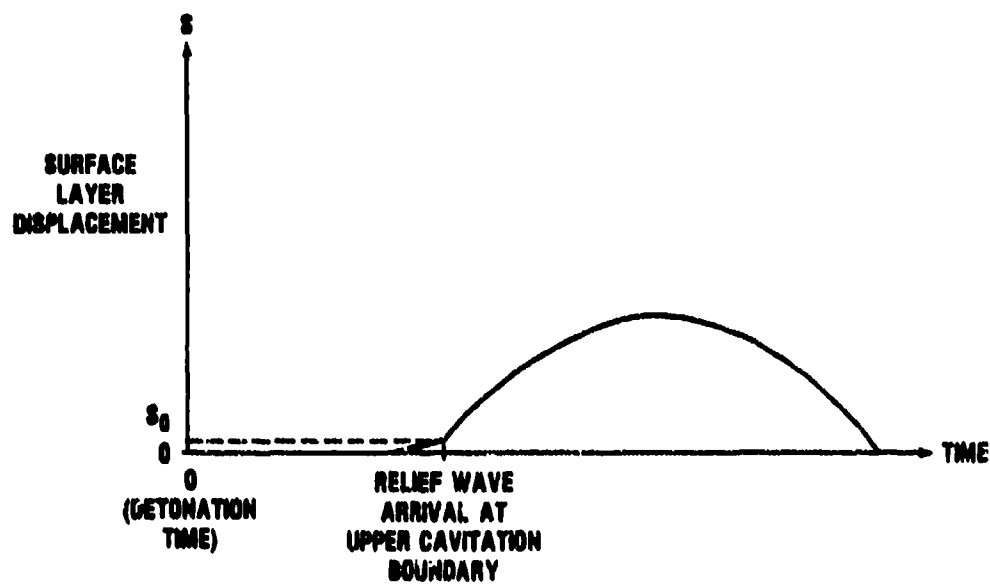


Fig. 7 - Surface Layer Displacement

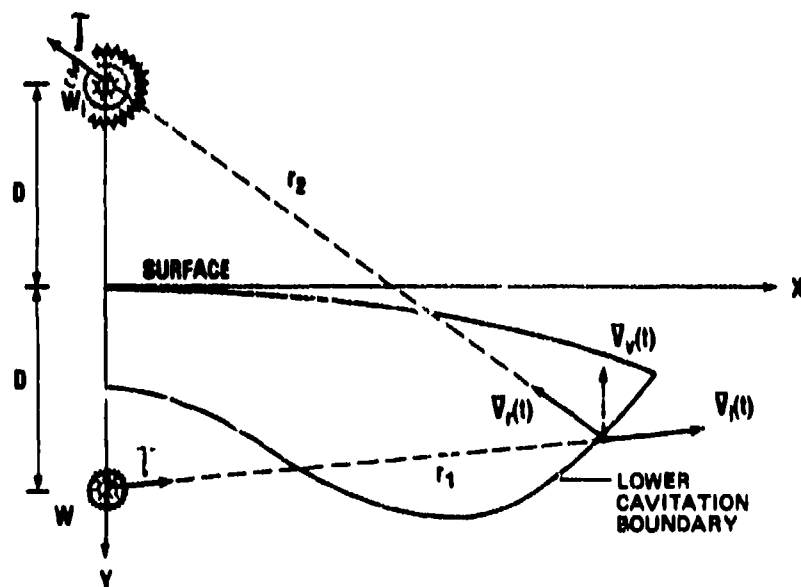


Fig. 8 - Velocity of a Point at the Lower Cavitation Boundary

boundary move with the same velocity as the point which lies at this lower boundary. If the displacement of a water particle at the lower cavitation boundary is plotted with time, the curve in Fig. 9 is obtained. Note that, as in the displacement curve for the surface layer, the displacement prior to relief wave arrival is included.

The time of bulk cavitation closure is defined as the time at which the lower boundary displacement equals the surface layer displacement. It is at this time that the accreting surface layer and the accreting lower boundary collide and generate the water hammer pressure pulse. If the curves of Figs. 7 and 9 are plotted on the same axes, the time, T_c , at which the two curves intersect denotes the time of closure. This is illustrated in Fig. 10.

When the surface layer thickness versus time is plotted for this same horizontal range, the curve in Fig. 11 is obtained. The surface layer thickness, Y_c , corresponding to the time of closure, T_c , from Fig. 11, is the depth of first bulk cavitation closure. Thus, the amount of surface layer growth which has taken place at the instant the lower boundary displacement equals the surface layer displacement determines directly the depth of cavitation closure for this particular horizontal range. Similarly, the amount of accretion which has taken place at the lower boundary also determines the depth of cavitation closure. In this development, however, only the surface layer accretion is calculated.

Surface Layer Motion

The methods discussed in the previous sections for determining the upper and lower cavitation boundaries and the kickoff velocities for points lying in the cavitated region were all developed from a continuum approach. In the development of a model which characterizes surface layer motion and surface layer accretion, it is convenient to depart from the continuum approach and to apply a segmentation technique.

The first step in determining the surface layer motion at a horizontal range, X , is to divide the water at this range into a discrete number of elements ranging from the upper cavitation boundary to the lower cavitation boundary. Each of these elements has an incremental cross sectional area, ΔA , and an incremental depth, ΔY . This segmented column of water, along with the column of water above it which extends to the surface, is shown in Fig. 12 and is considered to be in its quiescent state prior to the arrival of any disturbance. During the time between shock wave arrival and relief wave arrival, the surface layer and each element in this column is displaced an initial amount. When the relief wave arrives at the point at the upper cavitation boundary, the surface layer is kicked off with an initial velocity, V_0 . The equation of motion for this surface

layer is derived by considering dynamic equilibrium in the vertical direction. From this equation of motion we obtain the expression for the motion of the surface layer given in Eq. (7).

$$S = \frac{-g t^2}{2} \left(\frac{P_A}{\rho g Y_{SL}} + 1 \right) + V_0 t + S_0 \quad (7)$$

In this expression, the terms V_0 and S_0 are the velocity and displacement of the surface layer after the most recent collision with an element below it. Prior to the occurrence of the first collision, V_0 and S_0 represent the kickoff velocity and the initial displacement, respectively, of the initial surface layer. P_A and g represent the atmospheric pressure and acceleration due to gravity, respectively, while Y_{SL} represents the current thickness of the accreting surface layer. ρ is the mass density of water. Also, the independent variable, t , represents the time elapsed since the most recent collision.

In a similar fashion, the expression describing the motion of the water element directly below the surface layer is obtained. This expression is given in Eq. (8).

$$Z = \frac{-g(t-t_d)^2}{2} + \dot{Z}_0(t-t_d) + Z_0 \quad (8)$$

Here, \dot{Z}_0 and Z_0 are the kickoff velocity and initial displacement, respectively, of the water element directly below the surface layer. The independent variable, t , is the same as that in Eq. (7), while the t_d term represents the time delay between the new motion of the surface layer after the most recent collision and the kickoff of the water element directly below this accreting surface layer. When Eqs. (7) and (8) are equated, the time elapsed between two successive collisions, denoted t_1 , can be determined. At this point, the surface layer thickness is incremented and the initial conditions for the motion of the accreting surface layer (V_0 and S_0) are updated. Since the closure model considers all collisions to be perfectly inelastic, the resulting velocity of the accreting surface layer immediately after the present collision (V_0) can be determined by a conservation of momentum consideration.

The entire process stated above is repeated for successive collisions and the incremental collision times, t_1 , are summed up to give the total time elapsed since relief wave arrival at the upper cavitation boundary. From this, a surface layer displacement history, such as that shown in Fig. 7, can be plotted. In addition, the surface layer thickness is incremented by one water element thickness after each collision thus giving an accretion versus time curve, such as the one shown in Fig. 11. Surface layer motion and surface layer accretion are computed in this manner for this particular horizontal range until closure occurs. At this time, the surface layer displacement and the lower boundary displacement are equal.

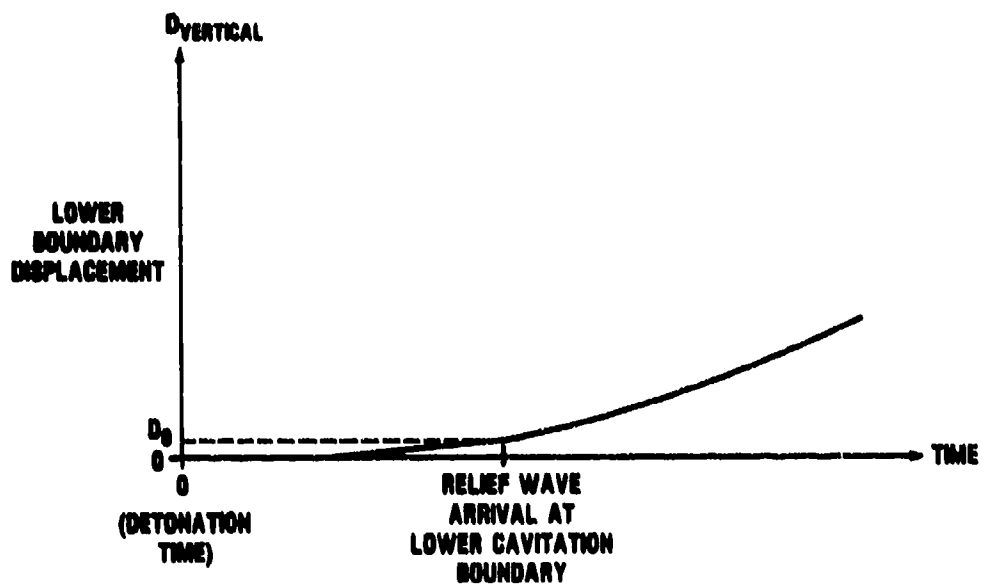


Fig. 9 - Lower Boundary Displacement

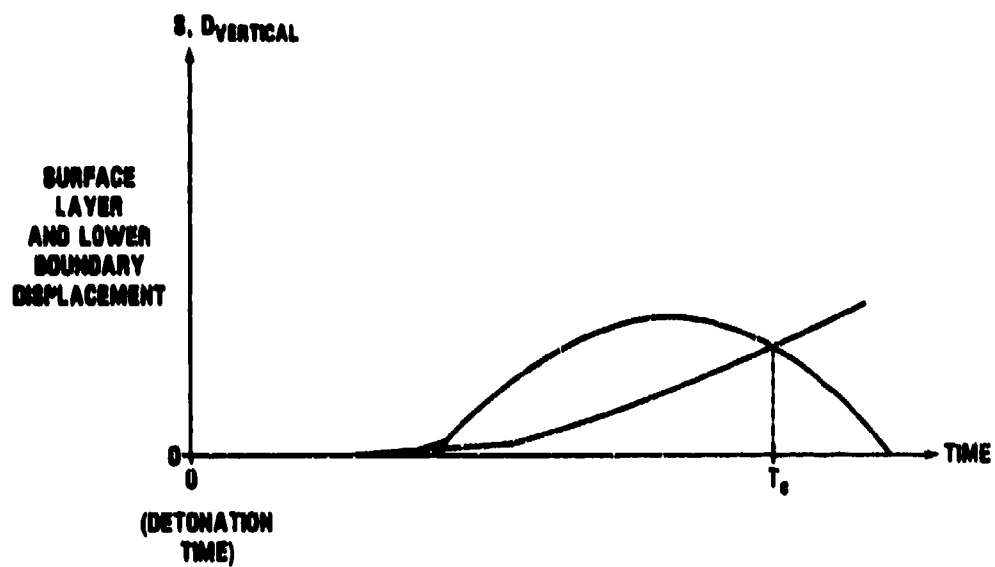


Fig. 10 - Time of Cavitation Closure

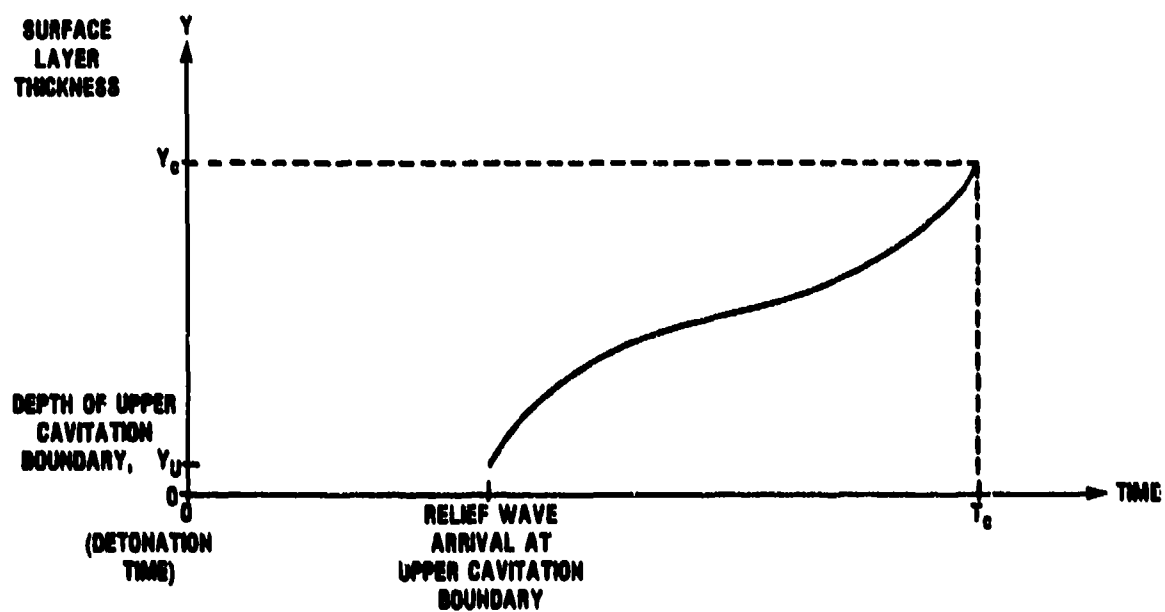


Fig. 11 - Surface Layer Accretion

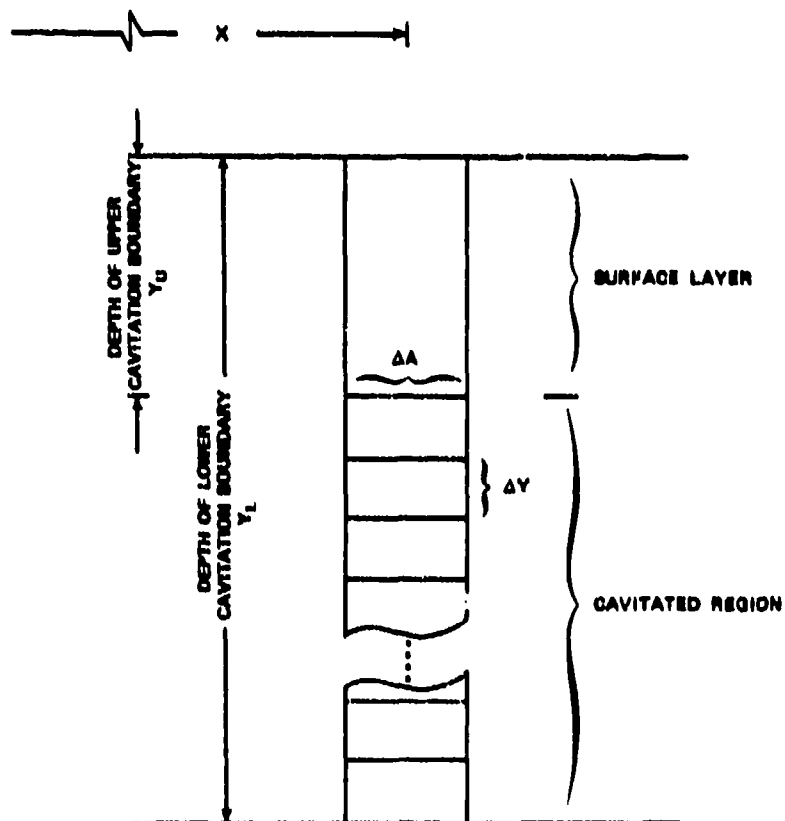


Fig. 12 - Segmented Water Column at Horizontal Range, x

Lower Boundary Motion

Since separation between water particles does not occur below the lower cavitation boundary, for a given horizontal range, X , the displacement of this boundary is determined by the linear superposition of the displacements due to the incident and relief waves for the water particle which lies at this lower boundary. Forces due to gravity are completely offset by the buoyant forces since the water beneath this lower boundary remains homogeneous. However, the displacement of the lower boundary prior to the arrival of the relief wave is included.

The equation of the water particle velocity, including afterflow, as produced by the incident pressure wave is [5]:

$$\bar{V}_i = \left[\frac{P_0 e^{-t/\theta}}{\rho c} + \frac{1}{\rho r_1} \int_0^t P_0 e^{-t/\theta} dt \right] \bar{i} \quad (9)$$

where $P_0 = A(W^{1/3}/r_1)^B$ and $t = 0$ refers to shock wave arrival at the lower cavitation boundary for this particular horizontal range, X . The ray length, r_1 , and the direction, \bar{i} , are defined in Fig. 8. To find the lower boundary displacement due to the incident wave, we integrate Eq. (9) to obtain:

$$\bar{\delta}_i = \frac{P_0 \theta}{\rho c} \left[(e^{-t/\theta} - 1) \left(\frac{c\theta}{r_1} - 1 \right) + \frac{ct}{r_1} \right] \bar{i} \quad (10)$$

This expression does, of course, include the displacement of the lower boundary which occurs prior to relief wave arrival.

The equation for the water particle velocity including afterflow as produced by the relief wave is:

$$\bar{V}_r = \left[\frac{Q}{\rho c} + \frac{1}{\rho r_2} \int_{t_0}^t Q dt \right] \bar{j} \quad (11)$$

where Q is the relief wave pressure whose magnitude equals the absolute pressure at the lower cavitation boundary just prior to relief wave arrival. Thus, $Q = A(W^{1/3}/r_1)^B \times e^{-t_c/\theta} + P_H + P_A$, where P_H is the hydrostatic pressure and t_c is the time between shock wave arrival and relief wave arrival. The ray length, r_2 , and the direction, \bar{j} , are defined in Fig. 8. As in Eqs. (9) and (10), $t = 0$ refers to shock wave arrival at the lower cavitation boundary for this particular horizontal range, X . In this development, the relief wave is treated as a constant pressure drop which propagates into the uncavitated water; i.e., it has no time dependence. To find the displacement of the lower cavitation boundary due to the relief wave, Eq. (11) is integrated to obtain:

$$\bar{\delta}_r = \left[\frac{Q(t-t_c)}{\rho c} + \frac{Q(t-t_c)^2}{2\rho r_2} \right] \bar{j} \quad (\text{for } t > t_c) \quad (12)$$

Finally, the total displacement of the lower cavitation boundary in the vertical direction for the horizontal range, X , is determined by the linear superposition of the vertical components of the displacement vectors in Eqs. (10) and (12).

BULK CAVITATION CLOSURE PULSE

The magnitude of the pressure pulse generated by the collision of the accreting surface layer with the accreting lower cavitation boundary at closure will now be determined. Since in the closure model, the vertical components of the velocities of both the surface layer and the lower cavitation boundary for a particular horizontal range, X , are known at the time of closure, the closure pressure pulse magnitude, P_c , can be calculated by multiplying one half the relative velocity of impact of these two water masses by the characteristic impedance of the medium. That is:

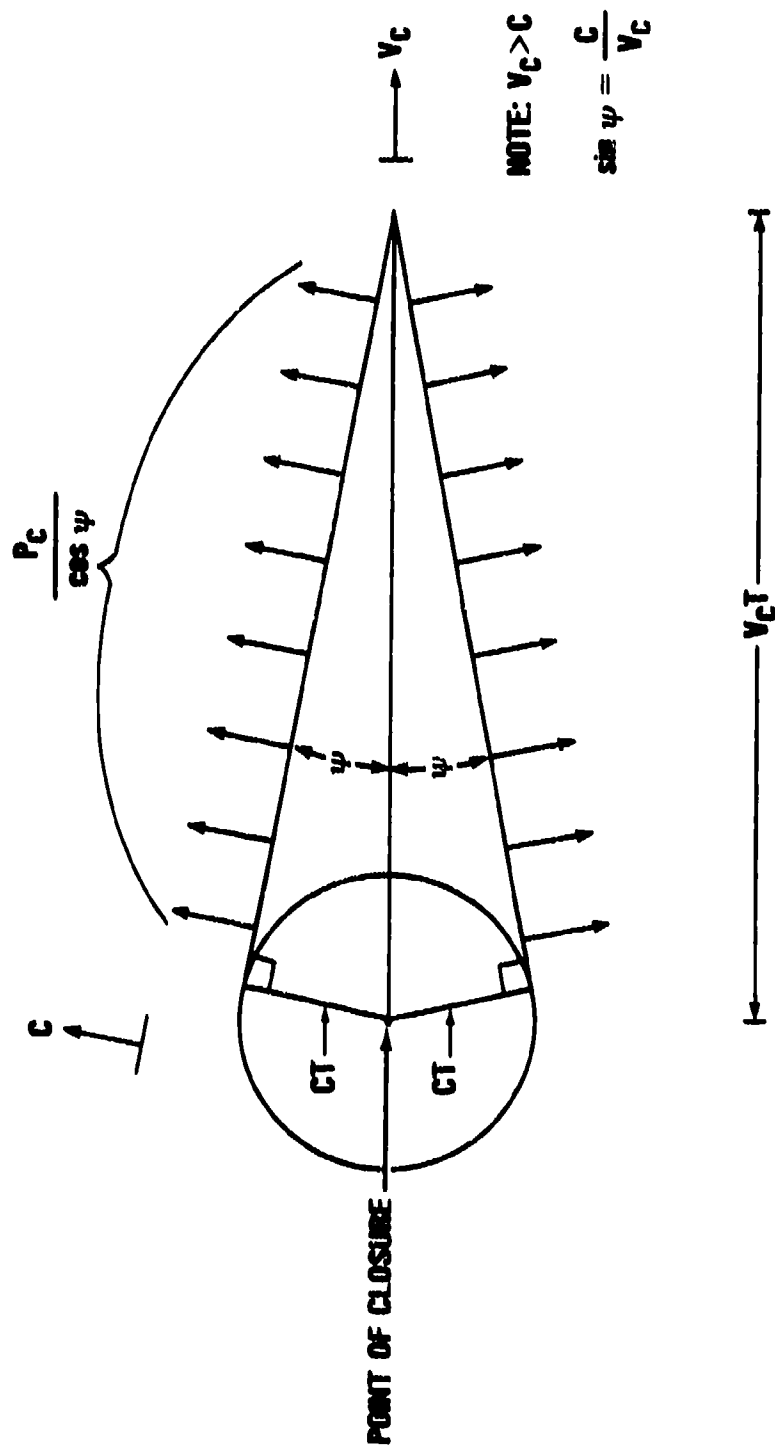
$$P_c = \frac{\rho c}{2} (V_L - V_U) \quad (13)$$

where V is positive upward and V_U and V_L refer to the vertical velocity components at closure of the surface layer and the lower cavitation boundary, respectively. The closure pressure pulse consists of two compressive waves of magnitude, P_c ; one that travels upward and one that travels downward. These closure pressures are most readily superimposed upon the incident shock wave and reflected pressures at the horizontal range at which closure first occurs, since at this range, the direction of propagation of the closure pulse is vertical. At other horizontal ranges, the direction of propagation of the closure pulse varies from the vertical direction by an angle ψ , as shown in Fig. 13. According to the work done by Cushing [6], if c is the sound speed in water and V_c is the speed at which the cavitated region is closing at some horizontal range, X , then:

$$\sin \psi = \frac{c}{V_c} \quad (14)$$

Thus, the magnitude of the pressure pulse which propagates along a path oriented at this angle ψ is determined by dividing the expression of Eq. (13) by $\cos \psi$. That is:

$$P_c = \frac{\rho c (V_L - V_U)}{2 \cos \psi} \quad (15)$$



T ≡ AN INFINITESIMAL TIME INCREMENT AFTER CLOSURE HAS OCCURRED

Fig. 13 - Closure Pulse at a Horizontal Range Different from that of First Closure

The duration time of the closure pulse at the depth of closure is determined by the method of images and is expressed by:

$$t_{\text{duration}} = \frac{2D_c}{c} \cos \psi \quad (16)$$

where D_c is the depth of closure at the horizontal range of interest, X . Thus, regardless of the angle of propagation of the closure pulse, the impulse (pressure \times duration) associated with cavitation closure at a particular horizontal range is the same and may be expressed as shown in Eq. (17).

$$\text{Impulse} = \rho(V_L - V_U) D_c \quad (17)$$

The above method of determining cavitation closure pressures and durations is valid only at horizontal ranges where the speed of closure propagation is greater than the sound speed in water (supersonic). At horizontal ranges where the closure propagation is subsonic, the determination of closure pressures and durations becomes rather complicated and will not be treated here. Fig. 14 shows the general form of the speed of closure propagation plotted against percent of extent of the cavitated region. Such a curve is characteristic of nearly all free field bulk cavitation problems.

CALCULATION OF PRESSURE AND WATER PARTICLE VELOCITY HISTORIES

The use of the foregoing development in calculating pressure and water particle velocity histories will now be illustrated with an example problem. For convenience, calculations of

time histories will be made at the horizontal range corresponding to first closure. Here the velocity of closure propagation is infinite and thus the path of the resulting closure pulse is vertical.

In this example, a 50,000 lb HBX-1 explosive compact charge is detonated at a depth of 300 ft in sea water which is assumed to be infinitely deep. A summary of all numerical values used in this example case is given in Table 1. When the method of Arons [2] and the closure model are applied to this case, the bulk cavitation bounds and closure depths shown in Fig. 15 are obtained. The depths of the upper and lower cavitation boundaries, as well as the depth and time of cavitation closure for various horizontal ranges, are given in Table 2. In Fig. 16 is a cross plot of the surface layer and lower boundary displacement histories for the horizontal range of first closure. A plot of surface layer accretion versus time for this same range is given in Fig. 17.

The remaining time history plots generated for this example case are each the result of a piecewise construction from linear shock wave theory and the nonlinear cavitation theory outlined above. In Fig. 18 is a plot of the vertical component of the surface layer velocity for the horizontal range of first closure (850 ft). The vertical component of the water particle velocity is calculated for an arbitrary depth of 25 ft at this same range and is plotted in Fig. 19. Also, the calculated pressure history for a depth of 25 ft at a horizontal range of 850 ft is given in Fig. 20. Similar plots and tabulated values can be compiled for other horizontal ranges within the extent of the cavitated region by virtue of Ref. 6 and the discussion above.

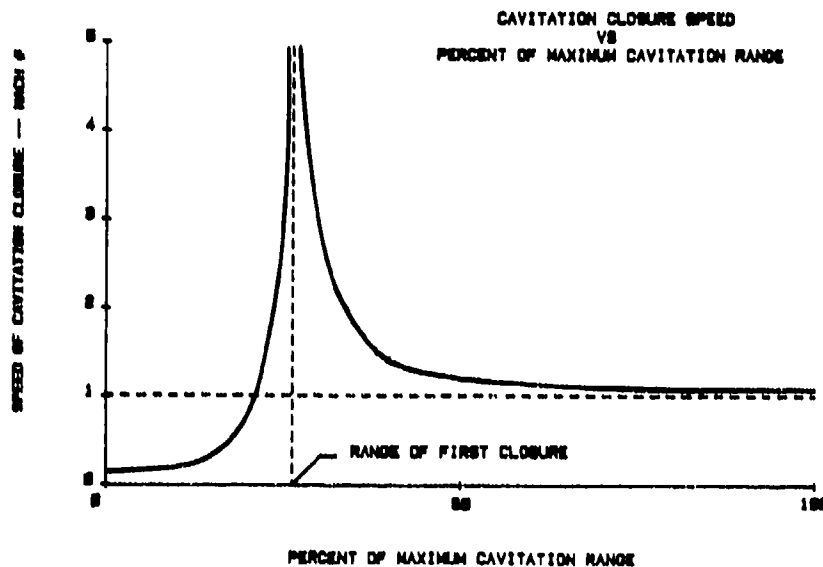


Fig. 14 - Speed of Closure Propagation Plotted Against Percent of Maximum Cavitation Range

TABLE 1
Summary of Numerical Values Used in Example Problem

CHARGE WEIGHT	60000 lb HBX-1
DEPTH OF BURST	300 ft
SHOCK WAVE CONSTANTS: *	
A	23976
B	1.13
K	0.0654
L	-0.18
ACCELERATION DUE TO GRAVITY	32.2 ft/sec ²
SPEED OF SOUND IN WATER	5000 ft/sec
MASS DENSITY OF WATER	1.9876 slugs/ft ³
* PEAK PRESSURE, $P_0 = A(W^{1/3}/r_1)^B$ DECAY CONSTANT, $\theta = KW^{1/3}(W^{1/3}/r_1)^L$	

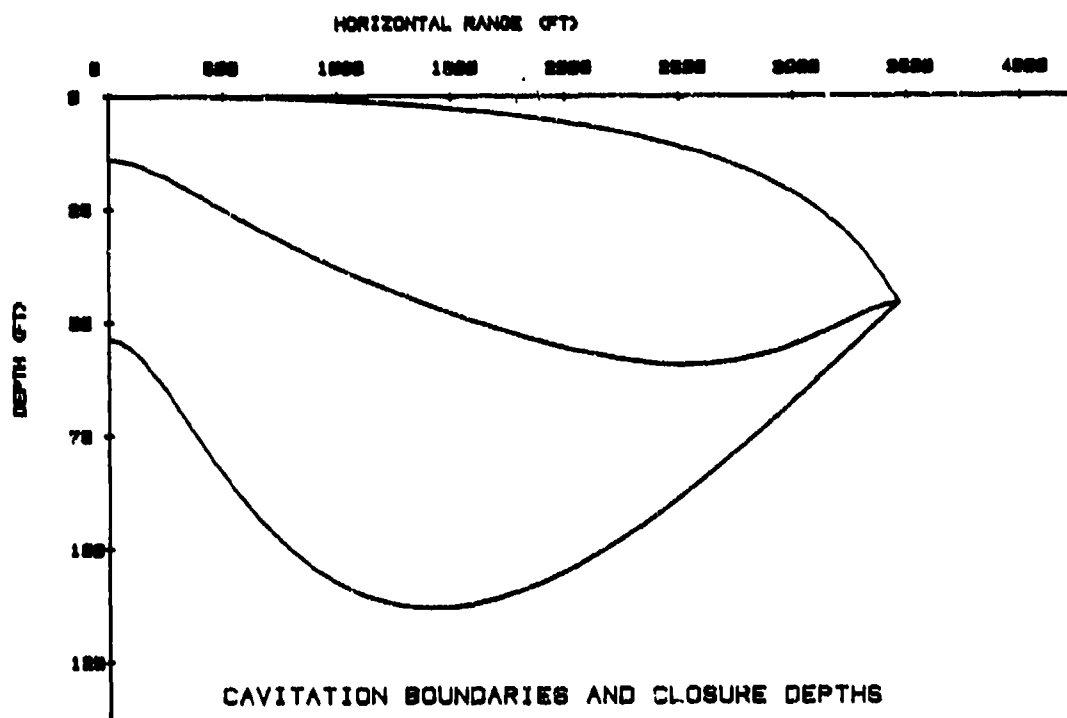


Fig. 15 - Bulk Cavitation Bounds and Closure Depths

TABLE 2
Bulk Cavitation Calculations
(with W = 50000 lb HBX-1
and Depth of Burst = 300 ft)

HORIZONTAL RANGE (ft)	DEPTH OF UPPER BOUNDARY (ft)	DEPTH OF CLOSURE (ft)	DEPTH OF LOWER BOUNDARY (ft)	TIME OF CLOSURE (msec)
0.00	0.06	14.16	53.75	559.99
100.00	0.07	14.92	53.91	542.58
200.00	0.09	16.09	61.45	400.06
300.00	0.14	19.49	68.67	413.92
400.00	0.20	22.30	76.23	361.21
500.00	0.28	25.13	83.43	324.59
600.00	0.39	27.94	89.93	301.78
700.00	0.52	30.62	95.60	286.90
800.00	0.69	33.19	100.41	283.47
* 850.00	0.78	34.39	102.50	282.80
900.00	0.88	35.63	104.37	283.53
1000.00	1.10	37.95	107.53	287.68
1100.00	1.36	40.16	109.93	294.90
1200.00	1.66	42.26	111.61	304.46
1300.00	1.99	44.29	112.63	315.91
1400.00	2.38	46.18	113.04	329.70
1500.00	2.80	48.00	112.88	342.69
1600.00	3.29	49.74	112.20	357.58
1700.00	3.82	51.37	111.04	373.22
1800.00	4.42	52.92	109.44	389.47
1900.00	5.09	54.39	107.44	406.24
2000.00	5.84	55.69	105.07	423.40
2100.00	6.68	56.88	102.36	440.92
2200.00	7.62	57.87	99.35	456.73
2300.00	8.67	58.62	96.06	476.70
2400.00	9.85	59.20	92.53	495.08
2500.00	11.18	59.43	88.78	513.54
2600.00	12.70	59.35	84.84	532.17
2700.00	14.42	58.87	80.72	550.93
2800.00	16.41	58.01	76.45	569.83
2900.00	18.72	56.77	72.05	588.83
3000.00	21.44	55.09	67.55	607.92
3100.00	24.69	53.09	62.95	627.10
3200.00	28.66	50.76	58.28	646.33
3300.00	33.66	48.36	53.56	665.58
3400.00	40.29	46.34	48.79	684.73

* HORIZONTAL RANGE OF FIRST CLOSURE

NOTE: CLOSURE TIMES DATED TO TIME OF EXPLOSIVE CHARGE DETONATION

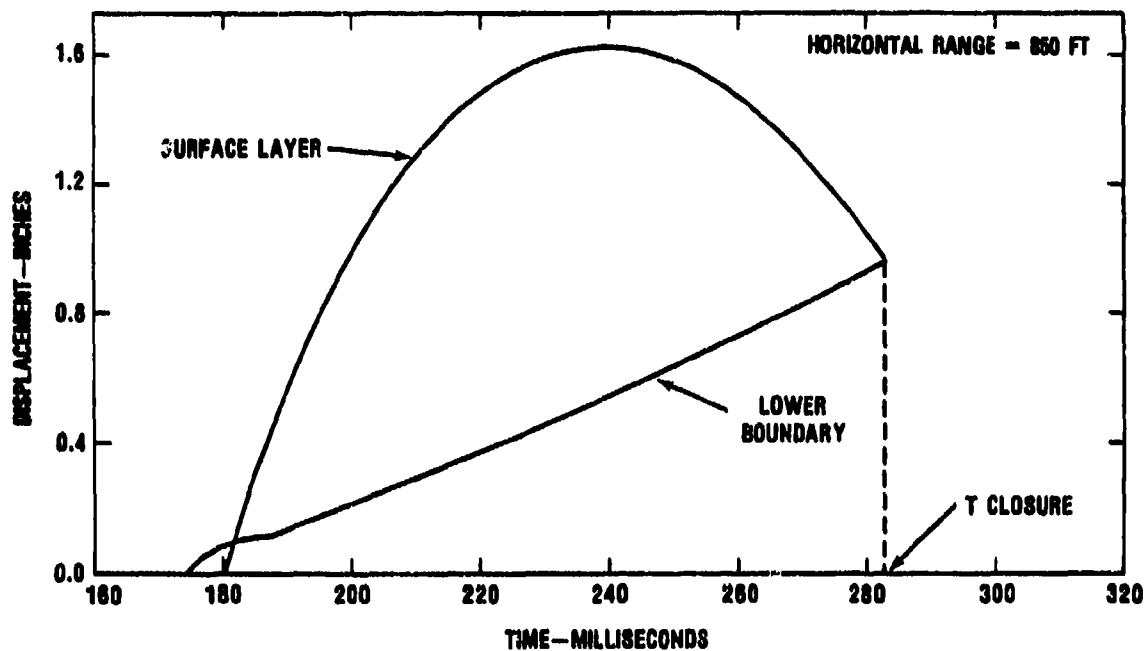


Fig. 16 - Surface Layer and Lower Boundary Displacement Histories (Vertical Component)

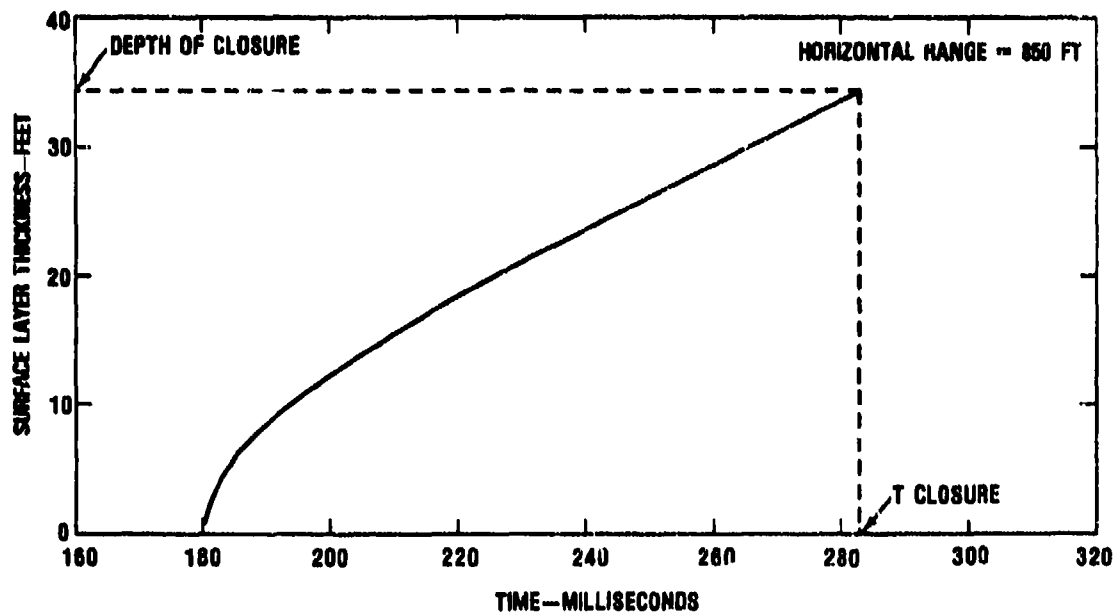


Fig. 17 - Surface Layer Accretion

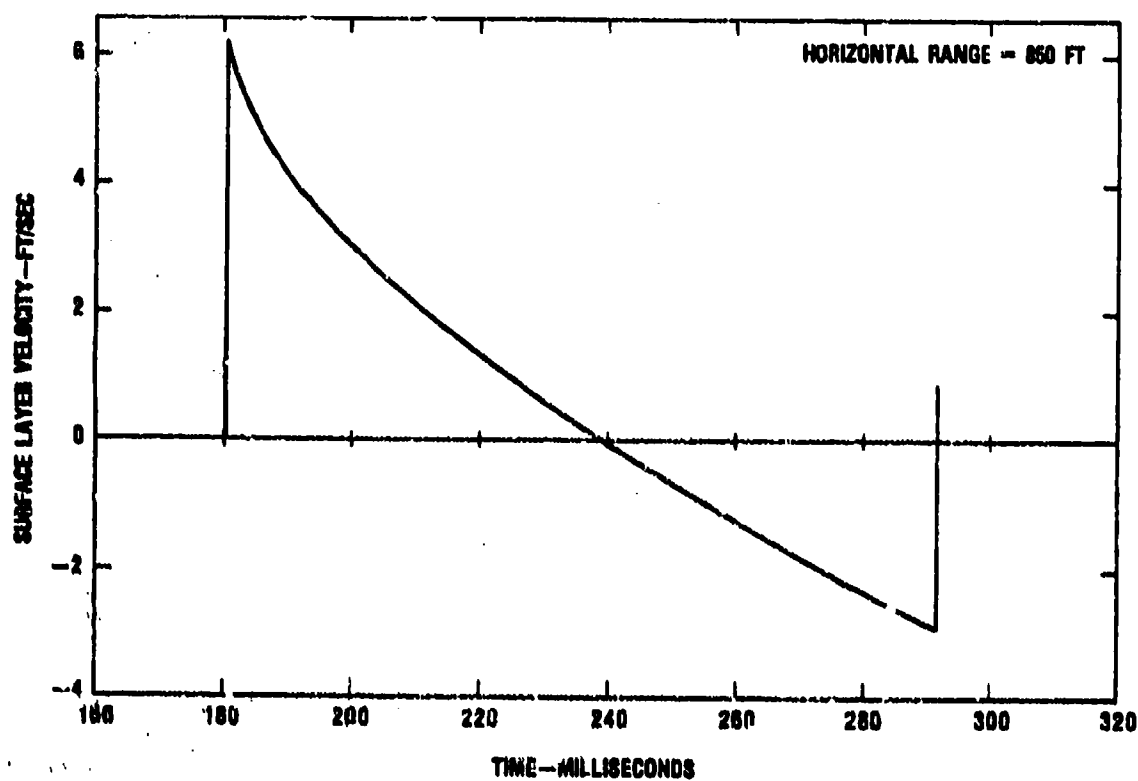


Fig. 18 - Surface Layer Velocity History (Vertical Component)

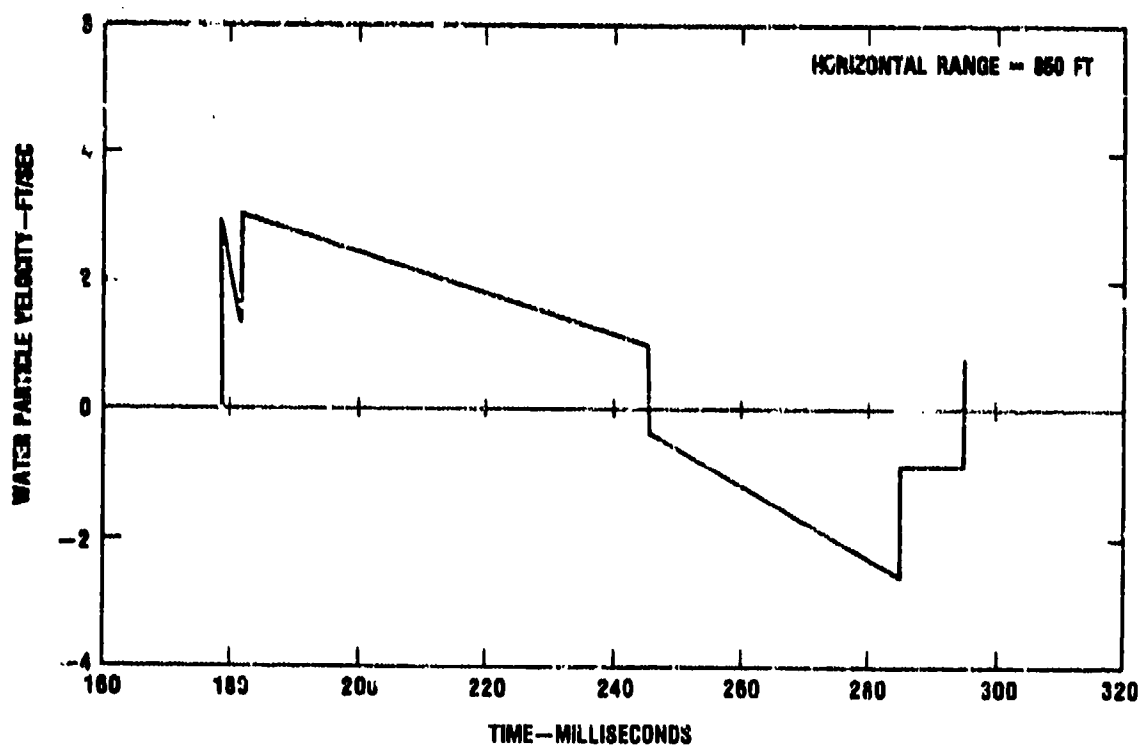


Fig. 19 - Water Particle Velocity History at 25-ft Gage Depth (Vertical Component)

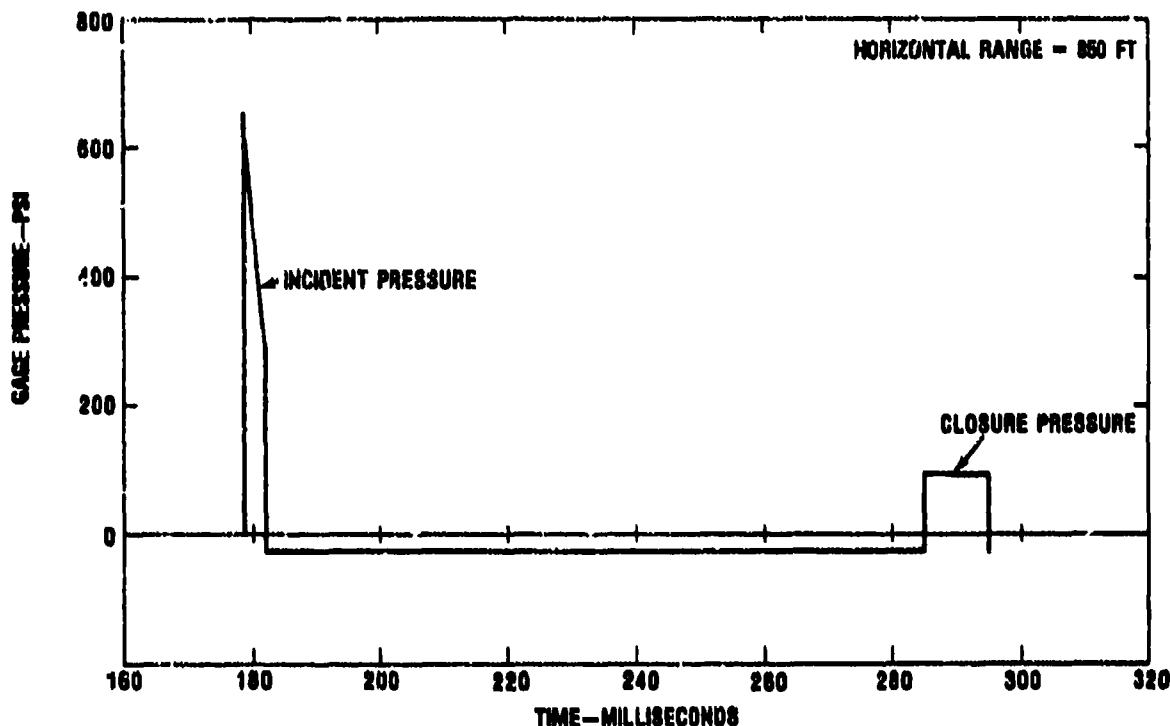


Fig. 20 - Pressure History at 25-ft Gage Depth

SUMMARY

The recent growth of interest in the phenomenon of bulk cavitation led to the development which was presented in this paper. Initially, the bulk cavitation problem was defined and the events leading up to its occurrence were explained. Then, the method of Arons [2] for determining the bulk cavitation envelope was derived from physical considerations, and the solutions for the upper and lower cavitation boundaries were given. Next, a model was developed for determining the depth and time of closure for any range within the extent of the cavitated region. This model proved to be consistent with the method of Arons [2] since the closure depth curve it generates passes through the point of intersection of the upper and lower cavitation boundaries at the maximum range of cavitation. From this closure model, it was then illustrated how to obtain the magnitude and direction of propagation of the closure pulse for various horizontal ranges within the extent of the cavitated region. Finally, the application of the method of Arons [2] and the closure model to a sample case was undertaken, and the results were presented in the form of a table and six plots.

REFERENCES

1. R. R. Walker and J. D. Gordon, "A Study of the Bulk Cavitation Caused by Underwater Explosions," David Taylor Model Basin Report 1896, Sept. 1966.
2. A. B. Arons, et al, "Long Range Shock Propagation in Underwater Explosion Phenomena II," Underwater Explosions Compendium, Vol. 1, Oct. 1949.
3. J. B. Gaspin and R. S. Price, "The Underpressure Field From Explosions in Water as Modified by Cavitation," Naval Ordnance Laboratory Report NOLTR 72-103, May 1972.
4. G. V. Waldo, Jr., "A Bulk Cavitation Theory With a Simple Exact Solution, Naval Ship Research and Development Center Report 3010, Apr. 1969.
5. R. H. Cole, "Underwater Explosions," Princeton University Press, 1948.
6. V. J. Cushing, "On the Theory of Bulk Cavitation," Engineering Physics Company Report, Dec. 1969.

DISCUSSION

Voice: Will this be more applicable to surface ships than to submarines? Second, can you apply this to nuclear as well as conventional weapons? Might it be more significant for a nuclear burst as opposed to a conventional burst?

Mr. Coglianese: The answer to your first question is yes; it is applicable to submarines as well as to surface ships. As I stated earlier, the evolution of our interest in bulk cavitation was due to the Surface Ship Shock Test program. However, it is just as applicable to any submarine problem that you might encounter. To answer the second question, there is no reason why we can't extend this analysis method to incorporate the nuclear type of pressure history, and we haven't done that yet. As soon as we are satisfied with what we did for the spherical bulk charges, then I think we will move on to look at the nuclear type of pressure signature.

A SOLUTION TO THE ONE DIMENSIONAL BULK CAVITATION PROBLEM

Benjamin M. Stow and John D. Gordon
David Taylor Naval Ship Research and Development Center
Underwater Explosions Research Division
Portsmouth, Virginia

The bulk cavitation analysis method presented in this paper eliminates the need to segment water for the purpose of solving simple equations of motion between water elements. The one dimensional problem analyzed in detail demonstrates the ease of application of the method. Plots of cavitation closure, water pressure, and water particle velocity are provided from the analysis. The results of the one dimensional analysis can be compared with results from other analysis methods to see what the differences are.

INTRODUCTION

Because of the immediate analytical needs of the surface ship shock test program, the axisymmetric bulk cavitation solution provided by Costanzo and Gordon [1] emphasized quick results over optimal mathematical description of the problem. The method used substitutes the labor of the computer solving a multiplicity of collisions between segmented water elements for the insight of the analyst determining and integrating the appropriate equations describing the accretion of the surface water layer. In keeping with the philosophy that the computer should be presented with the problem in the form best conditioned for solution, additional effort has been expended seeking an improved mathematical description based on the same physical assumptions.

OBJECTIVE

The primary objective of the analysis given in this paper is to eliminate the need for segmenting water for the purpose of solving simple equations of motion between water elements by providing an equation governing the displacement of the surface water layer which is already integrated with respect to the water elements. This equation is to be general enough to apply to the axisymmetric bulk cavitation problem. A secondary objective is to demonstrate an application of the new mathematical description by solving for the cavitation parameters resulting from a plane exponential shock wave moving along a line perpendicular to the water surface, and a tertiary objective of the analysis is to investigate the effect of dropping a complicating

term in the lower cavitation boundary displacement equation.

APPROACH

A momentum equation similar to that employed by Waldo [2] is used to describe the surface water layer velocity; however, this momentum equation is free of Waldo's assumption that water particle velocity kickoff occurs simultaneously along a vertical water column. This momentum equation is then integrated to yield the displacement of the surface water layer. The equation describing the displacement of a water particle in the cavitated state along with the equation describing the displacement of a water particle at the lower boundary of cavitation provide the remaining relationships necessary to support a solution for homogeneous water layer accretion above and below the closure depth. The water hammer pressure is calculated from the collision velocities of the two water layers at closure.

SURFACE WATER LAYER DISPLACEMENT

A surface reflected shock wave produces cavitation between two depths below the water surface by propelling free water particles vertically between these depths. Starting at the upper cavitation boundary depth, the action of atmospheric pressure and gravity causes a thickening of the surface layer of uncavitated water while at the same time the growing layer of uncavitated water is displaced with respect to the earth. To describe this motion mathematically the water particles lying along a

vertical column of undisturbed water are identified by a coordinate y equal to their depth below the water surface, and the motion of water particles is referred to inertial coordinates. Since the initial surface layer of uncavitated water starts accreting free water particles from underneath at the time of arrival of the relief wave at the upper cavitation boundary $y = a$, the time variable t in the equations is taken as zero at arrival of the relief wave at $y = a$. Water particles underneath $y = a$ are kicked off with a vertical component of velocity U with respect to the earth at a time $t = T$. When gravity is accounted for as an upward one g acceleration of the earth, a water particle kicked off at time $t = T$ can be represented as having been kicked off with a velocity $U + gT$ with respect to the stars. Treating the surface layer of uncavitated water as a rigid body having a velocity V with respect to the earth, the momentum per unit area of a water column of density ρ is $\rho y(V + gt)$ with respect to the stars. This momentum is equal to the sum of the kick off momentums of the water particles reduced by atmospheric pressure P_a as shown in Eq. (1).

$$\rho y(V + gt) = \rho aU(a) + \rho \int_a^y (U + gT) dy - P_a t \quad (1)$$

In the model of the problem described by Eq. (1), the initial layer of uncavitated water of thickness " a " is represented as being kicked off with a velocity equal to the water particle velocity at its under surface rather than the average velocity of the particles in the layer. This assumption is made to insure that final cavitation closure lies between the upper and lower boundaries even when these boundaries coincide. When Eq. (1) is divided by ρ and integrated with respect to time Eq. (2) describing the displacement D of the surface water layer is obtained.

$$yD = aD_1(a) + taU(a) + t \int_a^y (U + gT) dy - \frac{1}{2} \frac{P_a}{\rho} t^2 - \frac{1}{2} ygt^2 + F \quad (2)$$

where D_1 is the vertical component of the displacement of the water particle at depth y at the time of arrival of the relief wave at y , and $aD_1(a)$ is a constant of integration chosen such that at $t = 0$ and $y = a$, $D = D_1$. F is the sum of the remaining parts of the integration of Eq. (1).

$$F = \int_0^t [D_1 \dot{y} - t(U + gT) \dot{y} + \frac{1}{2} gt^2 \dot{y}] dt \quad (3)$$

with the dot meaning differentiation with respect to time. Differentiating Eq. (3) with respect to time and solving for D results in

$$D = F' + t(U + gT) - \frac{1}{2} gt^2 \quad (4)$$

where the prime means differentiation with respect to y . Recognizing that D is also the displacement of a free water particle at the time it joins the surface layer of uncavitated water, an additional equation for D is

$$D = D_1 + (t - T)U - \frac{1}{2} g(t - T)^2 \quad (5)$$

When D is eliminated from Eqs. (4) and (5) and F is solved for and integrated with respect to y , the result is

$$F = \int_a^y (D_1 - UT - \frac{1}{2} gT^2) dy \quad (6)$$

For a given depth y , Eqs. (2) and (5) solved simultaneously for t and D give the time it takes for the surface layer of uncavitated water to grow from a depth " a " to a depth y and the displacement of the surface layer at t .

CLOSURE FROM BELOW

Cavitation closure from below starts at the lower cavitation boundary $y = b$ at relief wave arrival $t = T(b)$ and proceeds upward until the surface layer of uncavitated water is met. The forces involved in closure from below are the elastic forces in the water below the lower cavitation boundary, the force of gravity acting on free water particles above the lower cavitation boundary and the force on the lower boundary due to the acceleration of the free particles as they are accreted. The elastic force in the water below $y = b$ causes a water particle at $y = b$ to be displaced upward, packing the water particles falling from above into homogeneous water. When a free water particle is accreted by the lower homogeneous water, its velocity is increased from $U - g(t - T)$ to V_b the velocity of the water particle at $y = b$, and the pressure P_p on the lower boundary due to the packing above is the time rate of change of momentum per unit area given by Eq. (7).

$$P_p = [U - g(t - T) - V_b] \rho \dot{y} \quad (7)$$

The displacement D_b of the water at the lower boundary of cavitation is the same as the displacement of a free water particle at the time it is accreted by the lower homogeneous water, therefore,

$$D_b = D_1 + (t-T)U - \frac{1}{2}g(t-T)^2 \quad (8)$$

When \dot{D}_b from Eq. (8) is substituted for V_b in Eq. (7), it is seen that the term in the parentheses is the difference between the time derivative of D_b treating y as constant and the time derivative of D_b treating y as a function of time.

A second equation for D_b can be determined from the pressure-time history at $y = b$ including the pressure on the lower boundary due to packing particles above given in Eq. (7). The two equations for D_b solved simultaneously give the depth-time relationship of the cavitation closure from below.

ONE DIMENSIONAL SOLUTION

The general equations previously given will be illustrated by solving for the bulk cavitation parameters caused by a plane exponential shock wave moving perpendicular to the water surface. This case was chosen because the integrals of the exponentials appearing in the equations can be evaluated in closed form and attention can be concentrated on the method of solution rather than the labor of solution. The shock wave under consideration travels upward with a velocity c and a pressure-time history given by the equation

$$P = P_0 e^{-t/\theta} \quad (9)$$

where P_0 is the peak pressure above hydrostatic, θ is the shock wave time constant and τ is the time after shock arrival at any depth y . At a given depth y , the time τ_0 between shock wave arrival and the arrival of the relief wave from the surface is

$$\tau_c = \frac{2y}{c} \quad (10)$$

The depth of the upper cavitation boundary may be found by solving for the shallowest depth at which the surface reflected wave reduces the absolute pressure in the water to zero. This occurs when the absolute pressure just prior to arrival of the reflection is equal to the peak pressure of the reflected wave. Accordingly,

$$P_0 e^{-2a/c\theta} + \rho g a + P_a = P_0 \quad (11)$$

is the equation governing the upper boundary.

The lower cavitation boundary is the shallowest depth below the upper boundary at which the pressure discontinuity at relief wave arrival can propagate downward without causing additional cavitation. This propagation becomes possible at the depth at which the absolute pressure in the water just prior to relief wave arrival stops decreasing with depth and starts increasing with depth. Therefore,

$$\frac{d}{dy} (P_0 e^{-2y/c\theta} + \rho g y + P_a) = 0 \quad (12)$$

$$\text{at } y = b, \text{ and } b = \frac{c\theta}{2} \ln \frac{2P_0}{\rho g c\theta}$$

At the lower cavitation boundary the relief wave pressure drop is equal to the absolute pressure in the water at $y = b$ just prior to relief wave arrival less the packing pressure P_p given by Eq. (7). This relief wave propagates downward linearly, and the water particle velocity and displacement at the lower boundary of cavitation is the linear superposition of the incident and relief velocities and displacements. The equations for V_b and D_b will be written with time starting at relief wave arrival at the upper cavitation boundary so as to be consistent with the general equations previously discussed.

$$V_b = \frac{P_0}{\rho c} e^{-\frac{t + [(a+b)/c]}{\theta}} + \frac{P_0 e^{-2b/c\theta} + \rho g b + P_a}{\rho c}$$

$$- \rho y \frac{U - g(t-T) - \frac{d}{dt} [D_1 + (t-T)U - \frac{1}{2}g(t-T)^2]}{\rho c} \quad (13)$$

$$t \geq \frac{b-a}{c}$$

$$D_b = D_1(b) + \int_{\frac{b-a}{c}}^t V_b dt \quad (14)$$

$$t \geq \frac{b-a}{c}$$

For the one dimensional case under consideration, the functions appearing in the equations are

$$D_1 = \frac{P_0 \theta}{\rho c} (1 - e^{-2y/c\theta})$$

$$U = \frac{2P_0 e^{-2y/c\theta} + \rho g y + P_a}{\rho c}$$

$$T = \frac{Y-a}{c}$$

$$D_1(a) = \frac{P_0 \theta}{\rho c} (1 - e^{-2a/c\theta})$$

$$U(a) = \frac{2P_0 e^{-2a/c\theta} + \rho g a + P_a}{\rho c}$$

$$D_1(b) = \frac{P_0 \theta}{\rho c} (1 - e^{-2b/c\theta})$$

The analysis will be illustrated by solving for the cavitation produced by a 700 psi - 4 msec shock wave. For this shock wave,

$$P_0 = 700 \times 144 \text{ pounds per square foot}$$

$$\theta = .004 \text{ second}$$

$$P_a = 14.7 \times 144 \text{ pounds per square foot}$$

$$\rho = 1.9399 \text{ slugs per foot}^3$$

$$g = 32.2 \text{ feet per second}^2$$

$$c = 5000 \text{ feet per second}$$

and from Eqs. (11) and (12)

$$a = .21359 \text{ feet}$$

$$b = 50.83706 \text{ feet.}$$

Results of the analysis are plotted with time starting with shock wave arrival at the water surface. This means that a/c has been added to the time variable t appearing in the equations before plotting.

Fig. 1 is the cavitation closure as a function of time, and Fig. 2 is the surface water layer displacement and lower boundary displacement as a function of time. The upper curves of these figures come from the simultaneous solution of Eqs. (2) and (5) and the lower curves come from the simultaneous solution of Eqs. (8) and (14). The time and depth at which the curves of Fig. 1 come together are the origin

of the water hammer due to cavitation closure. This water hammer is a square pulse of pressure equal to ρc times half the relative velocity at closure of the surface water layer and the lower boundary and has a duration equal to the travel time to the surface and back. Plots of surface water layer velocity and lower boundary velocity are given in Figs. 3 and 4 respectively. Fig. 3 is from Eq. (1) and Fig. 4 is from Eq. (13) with the addition of the velocity due to the shock wave from arrival to surface cutoff. The remaining figures shown in this paper are piecewise constructions from linear shock wave theory and the cavitation theory already outlined. Fig. 5 is the pressure history at closure depth and shows the shock wave exponential reduced by surface reflection to absolute zero pressure until closure when the impact of the two columns of homogeneous water produces the closure pressure which is also cutoff by surface reflection. The corresponding water particle velocity at closure depth is shown in Fig. 6. The straight line portion of the plot between relief wave arrival and cavitation closure is the particle in free fall. The pressure and water particle velocity at mid-depth are shown in Figs. 7 and 8 respectively. A salient feature of the water particle velocity in Fig. 8 is the sudden drop in velocity when the particle is accreted by the surface water layer. Before accretion, the particle is in free fall. After accretion, the particle is moving with the surface water layer.

ANALYSIS NEGLECTING THE PACKING PRESSURE P_p

A second cavitation analysis for the same shock wave was made neglecting the packing pressure given by Eq. (7). This eliminates the last term in Eq. (13) for the lower boundary velocity. All other equations remain the same. A comparison of results from the two analyses with and without P_p is given in Table 1.

TABLE 1
Effect of P_p on Results

	Closure Depth (ft)	Closure Time (msec)	Pressure Pulse (psia)
With P_p	18.0607	199.57	306.84
Without P_p	18.0011	198.92	306.53

The comparison shown in Table 1 illustrates that including the force on the lower cavitation boundary due to the accretion of water particles from above is probably not worth the iteration effort required to solve Eqs. (8) and (14), simultaneously.

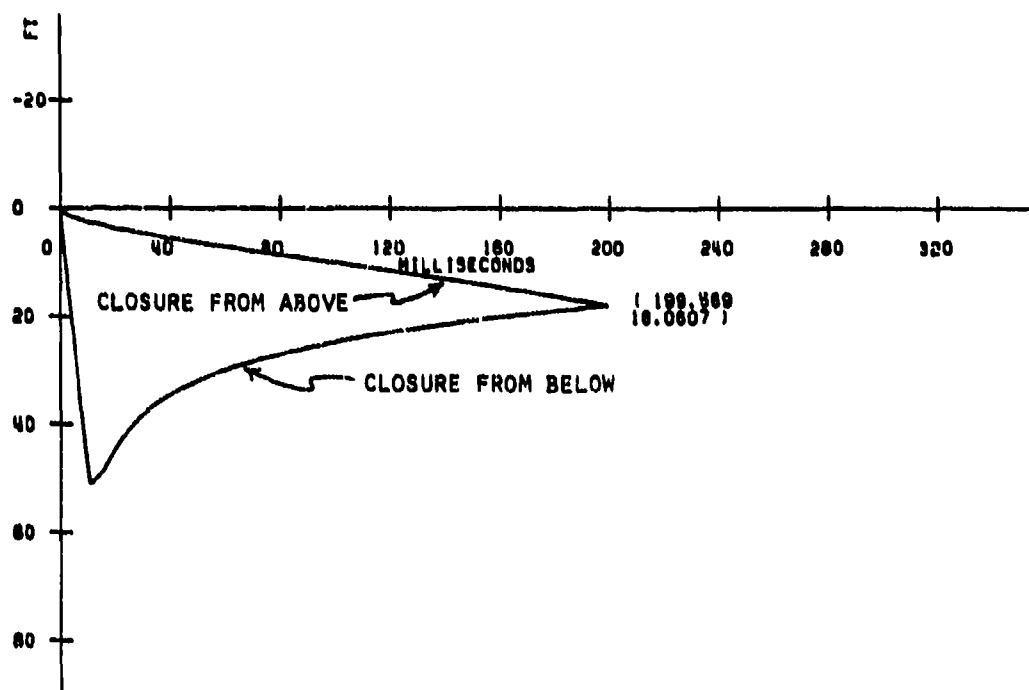


Fig. 1 - Cavitation Closure

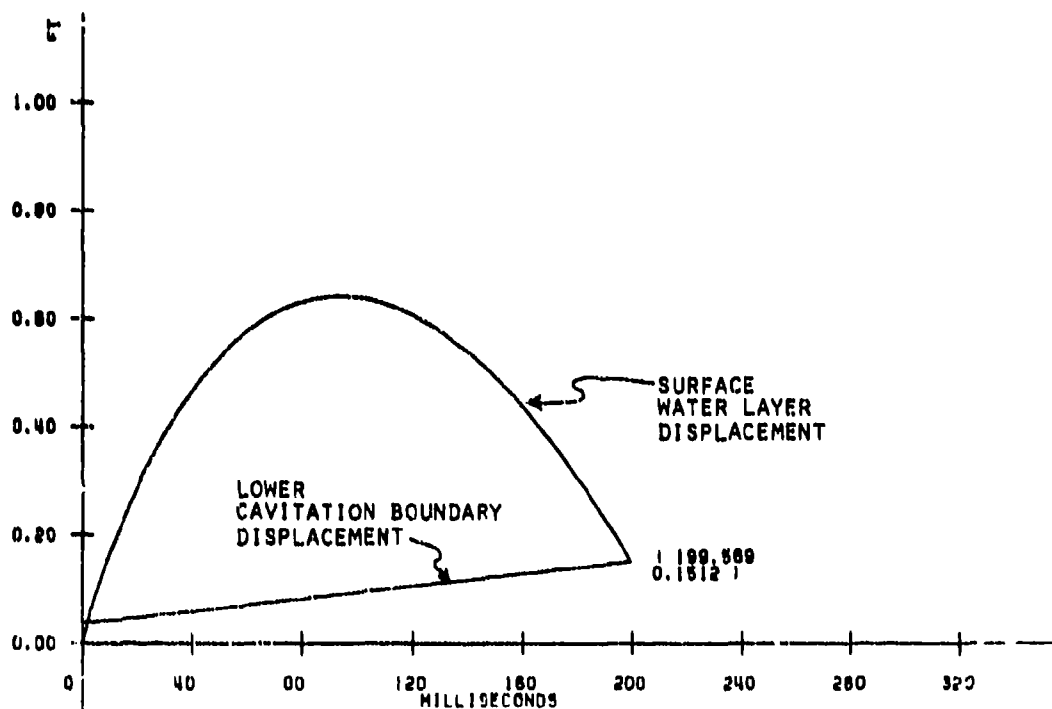


Fig. 2 - Surface Water Layer Displacement and Lower Cavitation Boundary Displacement

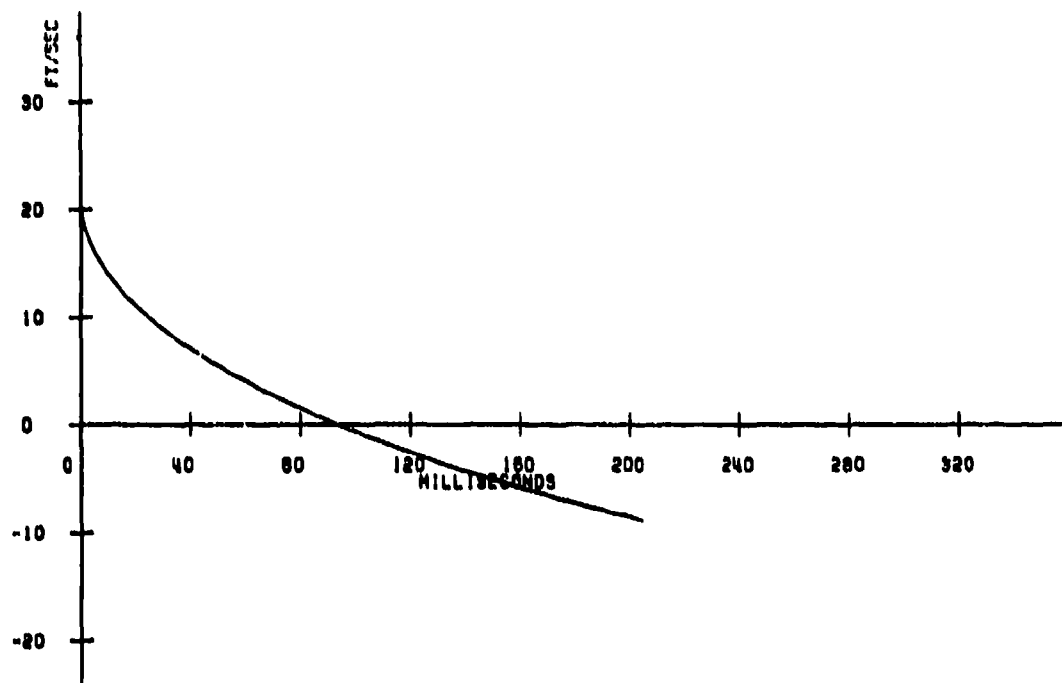


Fig. 3 - Surface Water Layer Velocity

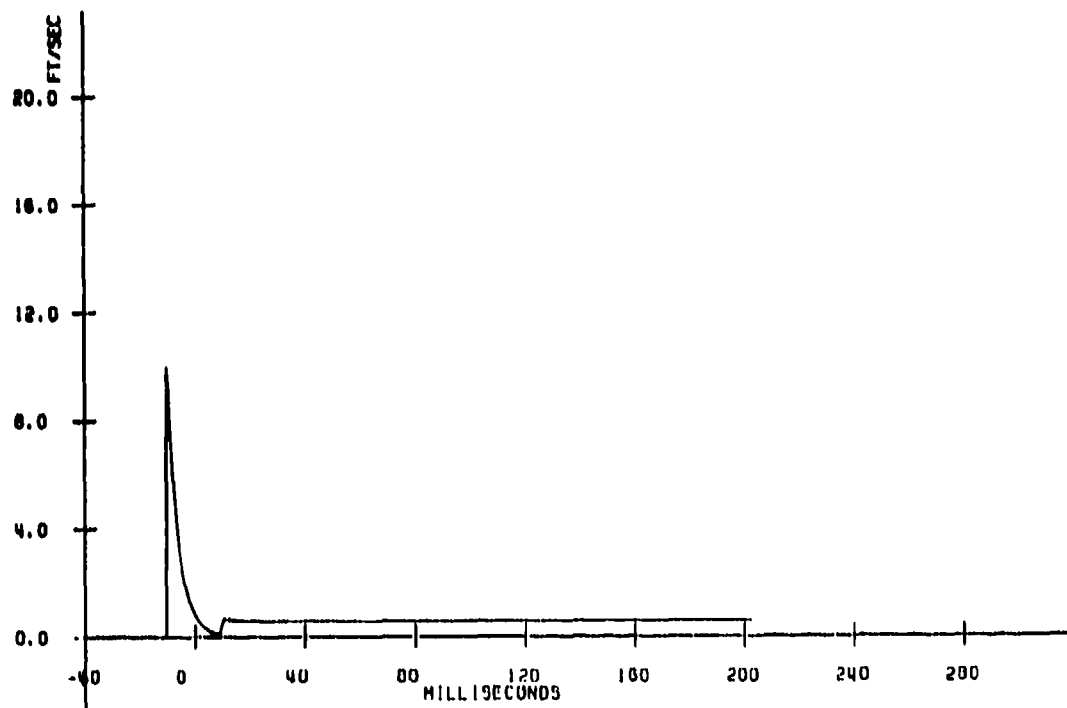


Fig. 4 - Lower Cavitation Boundary Velocity

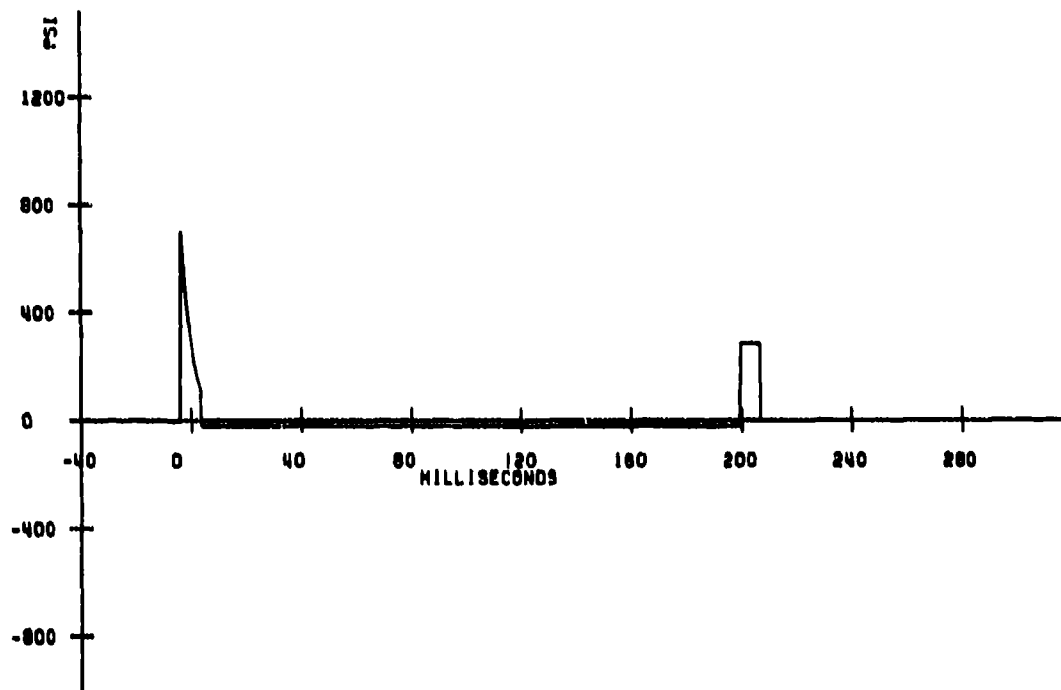


Fig. 5 - Pressure at Closure Depth

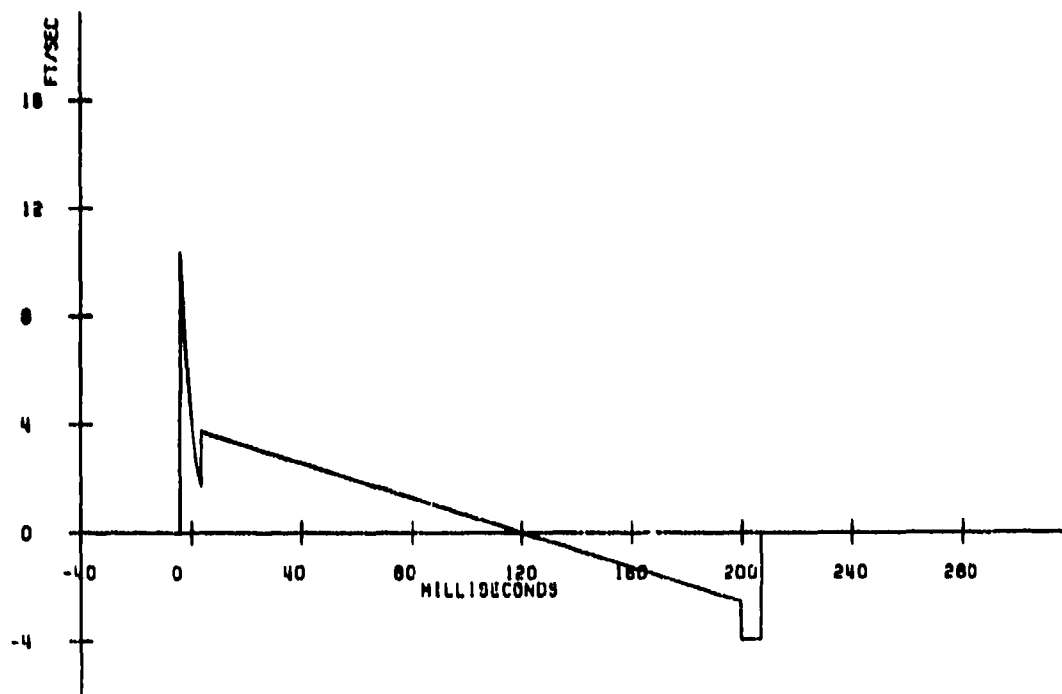


Fig. 6 - Water Velocity at Closure Depth

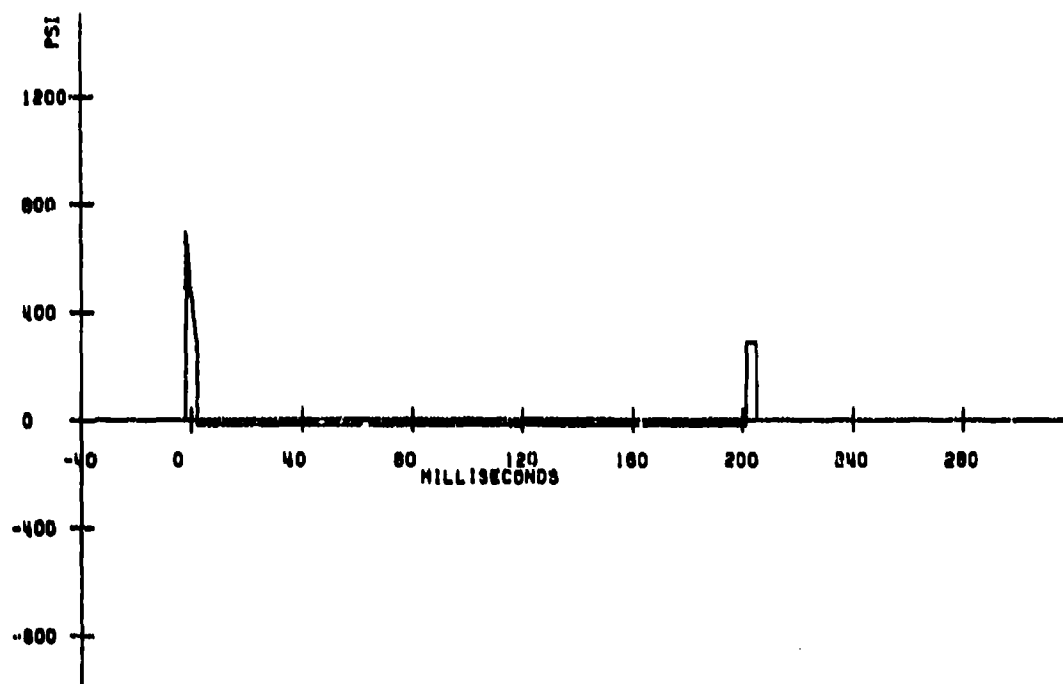


Fig. 7 - Pressure at Mid-Closure Depth

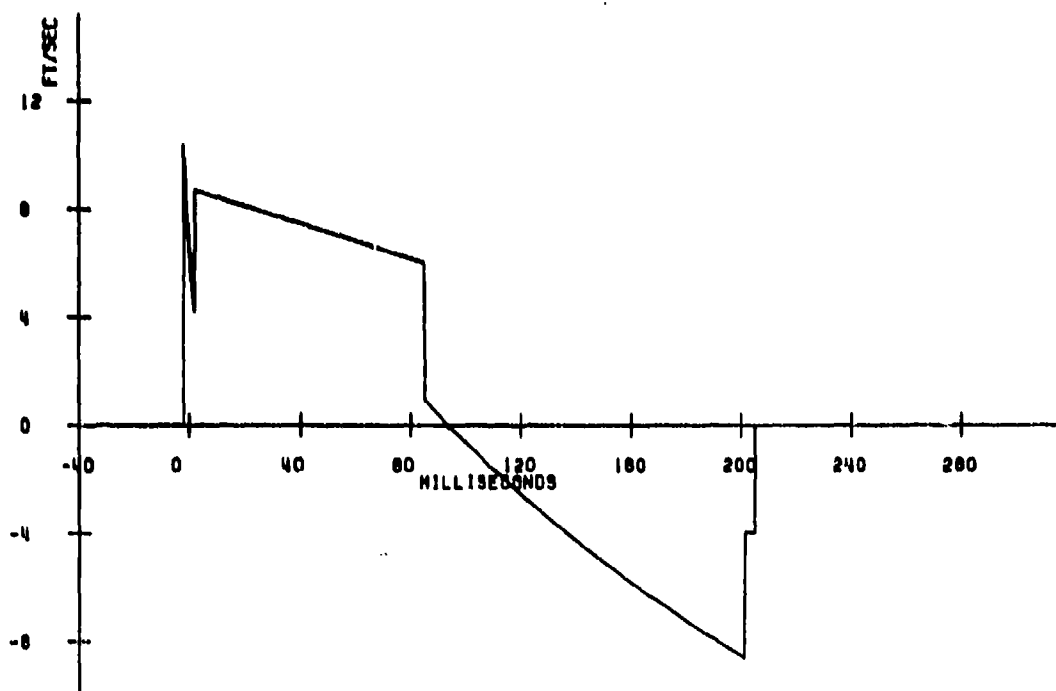


Fig. 8 - Water Velocity at Mid-Closure Depth

CONCLUSIONS

The bulk cavitation analysis method presented in this paper eliminates the need to segment water for the purpose of solving simple equations of motion between water elements. The one dimensional problem analyzed in detail demonstrates the ease of application of the method particularly when a negligible term in the lower cavitation boundary displacement equation is dropped. The method should be used to rework the axisymmetric bulk cavitation problem in order to save computation time. The results of one dimensional analysis should be compared with results from other analysis methods to see what the differences are.

REFERENCES

1. F. A. Costanzo and J. D. Gordon, "A Solution to the Axisymmetric Bulk Cavitation Problem," 53rd Shock and Vibration Bulletin, 1982.
2. G. V. Waldo, Jr., "A Bulk Cavitation Theory with a Simple Exact Solution," Naval Ship Research and Development Center Report 3010, April 1969.

DISCUSSION

Mr. Drakatos (University of Patras): Can we use the finite element method? What about boundary conditions using the finite element method?

Mr. Stowe: Mr. Costanzo's solution of the axisymmetric bulk cavitation problem, which was presented yesterday, was also run for the one-dimensional case. The results can be compared out to many decimal places with this method, and the answers are the same.

DYNAMIC ANALYSIS

DYNAMIC SIMULATION OF STRUCTURAL SYSTEMS WITH ISOLATED NONLINEAR COMPONENTS*

Levon Minnetyan
Clarkson College of Technology
Potsdam, New York

John A. Lyons
Niagara Mohawk Power Corporation
Syracuse, New York

Tony G. Gerardi
AFWAL/FIX
Wright-Patterson AFB, Ohio

Transient analysis of complex structural systems that contain both linear and nonlinear elements often presents a formidable computational problem. Nonlinear constitutive relationships in one or more of the structural elements necessitate a time-history integration of the equations of motion for the entire structure. Time-history analysis is usually carried out in terms of a limited number of generalized modal coordinates for the elastic substructure. However, a limited modal content is not sufficient to simulate the detailed structural response. To overcome this drawback a new hybrid method is formulated for the detailed dynamic analysis of complex structures. The new solution procedure incorporates a time-history analysis of the nonlinear response with a frequency domain analysis of the linear modes. The frequency domain analysis uses a larger number of modal coordinates to realistically simulate the details of structural response. The basic modal decoupling assumption of the hybrid method is studied by numerical application of the method to a simple elastic vehicle with nonlinear suspension properties, taxiing over an irregular profile.

INTRODUCTION

A new hybrid method is developed for the complete simulation of the transient response of certain structural systems with specially designed nonlinear energy absorption and attitude control devices. Many complex systems contain both linear and nonlinear structural components. The types of structures that are particularly addressed in this paper are those with mostly linear characteristics. However, significant nonlinearities exist in some limited regions of the

structure. Typically, nonlinear elements are connected to the remaining linear elastic substructure at a small number of nodes. Furthermore, the response of the nonlinear elements is primarily affected by the lowest or most fundamental frequencies and modes of vibration of the linear substructures.

The most immediate and relevant example of such a dynamic system is an aircraft taxiing over an irregular surface. Dynamic simulation of aircraft taxiing behavior requires a time-history integration of the equations of motion because of the typically nonlinear nature of the suspension strut properties. Nevertheless, the vehicle superstructure can be assumed to respond linearly for most aircraft. In theory, it is possible to simulate the total structural behavior by a direct dynamic analysis of a finite element model. However, the transient response

* Research sponsored by the Air Force Office of Scientific Research, Air Force Systems Command, USAF, under Grant Number AFOSR-82-0216. The United States Government is authorized to reproduce and distribute reprints for Governmental purposes notwithstanding any copyright notation thereon.

analysis of the full finite element model is prohibitively expensive. Also, past experience has shown that such analyses of complex structures can be numerically unreliable. The alternative to a direct finite element analysis is modal decomposition with substructuring that is being widely used at present for the simulation of aircraft taxiing response. Nonlinear terms are excluded from the dynamic equations by substructuring. For the linear substructures the vibration eigenvalue problem need be formulated only once at the beginning of the time-history solution. The modal superposition method is used for a change of basis from n nodal to p modal coordinates, $p \leq n$, prior to the time-history solution. The contributions of the nonlinear terms are treated as coordinate forces that are evaluated during the numerical integration of the equations of motion. If the objective of the time-history simulation is to predict the nonlinear suspension strut forces, the modal superposition series can be truncated after a few modes since the higher frequency vibrations do not affect the suspension response. Nevertheless, the dynamic response of some of the critical structural components may be significantly affected by high frequency modes. The necessity of including higher frequency vibration modes is especially relevant when force-related quantities such as internal loads are being estimated. Structural coordinate displacements can be expressed as the product of the mode shape matrix and the modal amplitude vector. On the other hand, the structure elastic forces can be written as the triple matrix product of the structure mass matrix, mode shape matrix, and a vector of modal displacements that are multiplied by the square of the corresponding modal frequencies. Since each modal contribution is multiplied by the square of its natural frequency, the higher frequency vibration modes are more important in simulating forces than displacements. If the transient behavior of such high frequency response quantities is to be predicted the original physical model must be sufficiently refined to yield meaningful vibration information on the high frequency modes which must be included in the modal superposition series. However, even if the high frequency vibration data is available to the required accuracy, the time-history analysis is not a useful technique to simulate the dynamic response of structural components that are affected by the high frequency modes. It is not practical to include the higher

frequency vibration modes with numerical reliability within the constraints of time-domain discretization. It would be necessary to decrease the time increment by several orders of magnitude to simulate the higher frequency modes consistently. Such refinement of the time step with the addition of a greater number of modal coordinates makes the time-history analysis approach prohibitively expensive for design calculations. A reliable and efficient method is needed to simulate total structural response for comparison with critical stress limits or to establish relevant design criteria.

To accomplish this task, a hybrid analytical method is formulated, aimed at defining an optimal solution path that will reliably predict dynamic response. The method incorporates a time-history analysis for the nonlinear response with a frequency domain analysis of the linear modes. First the time-history analysis including the nonlinear components and a small number of linear modes is conducted. Partial decoupling of the nonlinearities from the rest of the structure constitutes the second step. The remaining linear dynamic subsystem is analyzed through the frequency domain under external forces and interactions from the nonlinear components.

The numerical objective of this paper is to validate the fundamental assumption made in the new hybrid formulation. The numerical results presented are chosen to corroborate partial decoupling as a realistic procedure. Notwithstanding with the fact that the new method is envisioned as a means for efficient dynamic simulation for complex structures, the first numerical application is made to a rather simple two-dimensional beam vehicle that is taxiing over an irregular profile. The choice of a simple beam to represent an elastic vehicle is to have complete assurance and control on the finite element model during this first stage validation of the hybrid method. The results show a reasonable justification of the modal decoupling assumption and indicate possible directions of research for the improvement and development of the method.

Although the hybrid simulation method is examined primarily with reference to the taxiing vehicle problem, it should be noted that other examples of physical systems can also be found in the same dynamic category. In general any combination of linear elastic substructures coupled together by nonlinear energy absorption and

dissipation devices can be analyzed with the developed method. Specific examples include earthquake resistant buildings incorporating nonlinear "Safety Fuse" elements and space structures that are composed of linear elastic substructures assembled together by means of nonlinear couplers that absorb vibration energy and are used for attitude control adjustments.

FORMULATION OF THE NONLINEAR PROBLEM

In general, the structure nodal coordinate dynamic equilibrium equations can be written as (1)

$$[m] \{\ddot{u}\} + [c] \{\dot{u}\} + [k] \{u\} = \{P\} \quad (1)$$

where

- $[m]$ = structure nodal coordinate mass matrix
- $\{u\}$ = list of nodal coordinate displacements
- $[c]$ = structure damping matrix
- $[k]$ = structure piecewise linear tangent stiffness matrix (includes both constant and variable stiffness coefficients)
- $\{P\}$ = list of external loads

Eq. (1) is not convenient for representation in terms of an orthogonal modal basis. When the structure stiffness matrix is reassembled at each solution step, it becomes also necessary to redefine and reanalyze the vibration eigenvalue problem.

The transformation to modal coordinates becomes practical only if the nonlinearities are accounted for in terms of additional effective loads. To achieve this, the total stiffness matrix $[k]$ in Eq. (1) is separated into its linear and nonlinear components

$$[k] = [k^0] + [k^{NL}] \quad (2)$$

where

- $[k^0]$ = constant linear elastic stiffness matrix
- $[k^{NL}]$ = nonlinear stiffnesses which depend on the state of deformation

Substituting Eq. (2) into Eq. (1)

$$[m] \{\ddot{u}\} + [c] \{\dot{u}\} + [k^0] \{u\} + [k^{NL}] \{u\} = \{P\} \quad (3)$$

The nonlinear effects can be expressed as additional coordinate loads:

$$\{P_{NL}\} = [k^{NL}] \{u\} \quad (4)$$

the equations of dynamic equilibrium are written as

$$[m] \{\ddot{u}\} + [c] \{\dot{u}\} + [k^0] \{u\} = \{P\} - \{P_{NL}\} \quad (5)$$

The effective $\{P_{NL}\}$ loads are determined at each time step from nonlinear component properties.

To change the solution basis from n nodal to p modal coordinates, $p < n$, an orthogonal transformation is written

$$\{u\} = [\phi] \{n\} \quad (6)$$

nx1 nxp px1

where n are the generalized modal coordinates and $[\phi]$ is the mode shape matrix whose columns are the orthogonal eigenvectors $\{\phi\}$ of the vibration problem defined by

$$[k^0] \{\phi\} = \omega^2 [m] \{\phi\} \quad (7)$$

where ω is the natural frequency corresponding to $\{\phi\}$. The vibration problem need be formulated only once at the beginning of time-history analysis due to the exclusion of the variable components from the stiffness matrix $[k^0]$. The equations of motion can be written in modal coordinates

$$[M] \{\ddot{n}\} + [C] \{\dot{n}\} + [K] \{n\} = [\phi]^T \{P - P_{NL}\} \quad (8)$$

pxpxpx1 pxpxpx1 pxpxpx1 pxn nx1

where

- $[M]$ = generalized mass matrix;
 $[M] = [\phi]^T [m] [\phi]$
- $[C]$ = modal damping matrix;
 $C_{jj} = 2\zeta_j \omega_j M_{jj}, C_{ij} = 0$
- $[K]$ = modal stiffness matrix;
 $K_{jj} = \omega_j^2 M_{jj}, K_{ij} = 0$
- ζ_j = j th modal damping ratio

The time-history integration of the equations of motion can now be accomplished more efficiently in terms of the modal coordinates. It should be noted that although time-history integration is performed using the modal coordinates, some nodal displacements must be calculated at each time step to evaluate the effective load vector $\{P_{NL}\}$ in Eq. (8). Generally this does not pose a problem since the effective loads usually act only at a small number of nodal coordinates.

It is relevant to take note of the modeling requirements for the free vibration problem of a linear substructure within the context of the orthogonal formulation given by Eq. (8). In Eq. (8), each linear substructure is considered separately from the surrounding nonlinear components. The interactive forces between a substructure and its surroundings are considered as external loads at the substructure boundaries.

The linear elastic substructure is represented by a finite element model that consists of a number of nodes connected by idealized discrete elements. The required refinement of the finite element model depends upon structural geometry, boundary conditions and applied loading. The vibration eigenvalue problem for the linear substructure is defined by Eq. (7). In order that the modal equations, Eq. (8), be entirely orthogonal including the rigid body modes, the stiffness $[k^0]$ and mass $[m]$ matrices in Eq. (7) are defined for the unconstrained structure. In Eq. (7) the mass matrix is positive definite, the stiffness matrix is semi-definite. Another requirement for the orthogonality of the elastic vibration modes to the rigid body modes is the definition of the mode shape vectors $\{\phi\}$ in Eq. (7) relative to the dynamic center of mass of the flexible substructure. The dynamic center of mass can be defined as the instantaneous center of structural mass during dynamic response. The behavior of the dynamic center of mass is described by the rigid body modes of motion. Thus, the dynamic center of mass will remain stationary during free vibrations of an unconstrained structure [2].

In general, any structure coordinate displacement can be expressed as the sum of rigid body displacement contributions plus the effect of elastic structural deformations. The elastic deformations can be expressed in terms of the amplitudes of flexible vibration modes. If we write the modal superposition equations for all structure coordinates in matrix form then

$$\{u\} = [\phi_R] \{u_R\} + [\phi_F] \{q\} \quad (9)$$

where

$\{u_R\}$ = vector of rigid body displacements

$[\phi_R]$ = vector or rigid body modal influence coefficients. Each column of $[\phi_R]$ lists the displacements at

structure coordinates due to a unit displacement of the corresponding rigid body coordinate.

$[\phi_F]$ = mode shape matrix of the flexible modes. Each column of $[\phi_F]$ represents a mode shape vector.

$\{q\}$ = flexible mode amplitudes

The superposition equations, Eq. (9) may be combined into a single matrix of rigid body plus flexible modal influence coefficients

$$\begin{matrix} \{u\} & = & [\phi_R & \phi_F] & \begin{Bmatrix} u_R \\ q \end{Bmatrix} \\ n \times 1 & & n \times p & p \times 1 \end{matrix} \quad (10)$$

defining new symbols for the combined matrices

$$\{u\} = [\phi] \{n\} \quad (11)$$

which is the same as Eq. (6). It should be noted that the rigid body modes must have the specific scales to render the generalized mass equal to the physical mass or inertia of the corresponding rigid body mode. Accordingly, in Eq. (9) if u_i is in the same direction as the j th rigid body mode u_{Rj} , then ϕ_{Rij} is the moment arm of u_i from the j th rigid body rotation axis [2].

COMPUTATION OF STRUCTURAL RESPONSE

The first step is the computation of time-history response of nonlinear components. A time-history integration of the modal equations of motion, Eq. (8), is performed including a small number of modes that are sufficient to represent the flexible deformations of the elastic structure for the purpose of estimating the behavior of the nonlinear components. Although the mass, damping and stiffness matrices are diagonal in Eq. (8), the time-history integration of the equations must progress simultaneously since the equations are coupled with F_{NL} nonlinear terms on the right hand side.

After the time-history determination of the nonlinear forces the total structural response is evaluated through the frequency domain. The basic requirements for a frequency domain analysis are that the nonlinear interaction forces are known and the linear systems are represented by orthogonal generalized coordinates. At this stage a much greater number of modes can be included to represent the linear

substructure in detail for the determination of its internal response due to the numerical stability and efficiency of frequency domain analysis.

The time-history dynamic forces, including the nonlinear interaction forces, acting on the linear substructure are first converted to the frequency domain by Discrete Fourier Transformation (DFT). The DFT coefficients are defined as [1]

$$C_{n+1}(\bar{\omega}_n) = \Delta t \sum_{t=0}^{N-1} F(t) e^{-2\pi i n t / N}, \quad n=0, \dots, N-1 \quad (12)$$

where

- $i = \sqrt{-1}$
- $\Delta t = T/N$
- T = total time period considered (includes an attached period of $F(t)$ = 0 to take into account the periodic nature of DFT)
- N = number of discrete time intervals in T
- $\bar{\omega}_n$ = forcing frequency
- $C(\bar{\omega}_n)$ = coefficients defining the discretized harmonic amplitude function

The Complex-Frequency-Response-Function (CFRF), $H_j(\bar{\omega}_n)$, for each j th generalized structural mode under the forcing frequency $\bar{\omega}_n$ is defined as [1]

$$H_j(\bar{\omega}_n) = \frac{1}{-\bar{\omega}_n^2 M_{jj} + i \bar{\omega}_n C_{jj} + K_{jj}} \quad (13)$$

where

- $i = \sqrt{-1}$
- M_{jj}, C_{jj}, K_{jj} = j th generalized modal mass, damping, and stiffness, respectively

For the rigid body modes $C_{jj} = K_{jj} = 0$, and

$$H_j(\bar{\omega}_n) = \frac{1}{-\bar{\omega}_n^2 M_{jj}} \quad (14)$$

It can be shown that the total response of a system to any forcing input can be written by means of Inverse Fourier Transformations (IFT). The displacements of the j th modal coordinate are

given by [1]

$$\eta_j(t) = \frac{\Delta \bar{\omega}}{2\pi} \sum_{n=0}^{N-1} H_j(\bar{\omega}_n) C_j(\bar{\omega}_n) e^{i \bar{\omega}_n t} \quad (15)$$

or since $\bar{\omega}_n = n \Delta \bar{\omega}$ and $\Delta \bar{\omega} = \bar{\omega}_n / N$; (16)

$$\eta_j(t) = \frac{\Delta \bar{\omega} N}{2\pi n} \sum_{n=0}^{N-1} H_j(n+1) C_j(n+1) e^{2\pi i n t / N} \quad (17)$$

Both the DFT harmonic amplitude coefficients of the generalized forces, Eq. (12), and the IFT to solve for generalized displacements, Eq. (17), can be rapidly generated by modern Fast Fourier Transform (FFT) algorithms.

Modal accelerations can be evaluated from the second time derivative of Eq. (17)

$$\ddot{\eta}_j(t) = \frac{\Delta \bar{\omega}}{2\pi} \sum_{n=0}^{N-1} H_j(n+1) C_j(n+1) \left(\frac{-4\pi^2 n^2}{N^2} \right) e^{2\pi i n t / N} \quad (18)$$

The structure nodal coordinate displacements can be obtained from the modal superposition equations

$$\{u(t)\}_{n \times 1} = \{\phi\}_{n \times p} \{\eta(t)\}_{p \times 1} \quad (19)$$

Other response parameters such as stresses or loads developed in various structural components can be evaluated directly from the displacements. For example, the elastic forces $\{f\}$ which resist the deformation of the structure are given directly by the displacements and the structure stiffness coefficients.

$$\{f(t)\} = [k^0] \{u(t)\} = [k^0] \{\phi\} \{\eta(t)\} \quad (20)$$

An alternative expression for the elastic forces can be written in terms of the structure mass matrix and natural frequencies. Expanding Eq. (20) in terms of the modal contributions

$$\{f(t)\} = [k^0] \{\phi_1\} \eta_1(t) + [k^0] \{\phi_2\} \eta_2(t) + \dots + [k^0] \{\phi_p\} \eta_p(t) \quad (21)$$

Substituting Eq. (7) in each term of Eq. (21)

$$\{f(t)\} = \omega_1^2 [m] \{\phi_1\} \eta_1(t) + \omega_2^2 [m] \{\phi_2\} \eta_2(t) + \dots + \omega_p^2 [m] \{\phi_p\} \eta_p(t) \quad (22)$$

Combining back into matrix form

$$\{f(t)\} = [m][\phi] \left(\omega_j^2 \eta_j(t) \right) \quad (23)$$

where $\{\omega_j^2 \eta_j(t)\}$ represents a vector of modal amplitudes, each multiplied by the square of its modal frequency.

In Eq. (20), if $[k^0]$ is the substructure stiffness matrix and $\{u(t)\}$ is the list of substructure coordinate displacements then $f(t)$ are the total elastic forces at the substructure nodal coordinates. To obtain the internal stresses at particular locations in the substructure, the elemental stiffness matrices and the corresponding element vertex displacements are used.

$$\{f'(t)\} = [k'] \{u'(t)\} \quad (24)$$

where prime indicates the quantities that are defined with respect to elemental vertex coordinates.

APPLICATION TO TAXIING VEHICLE

The basic premise of the formulated hybrid method; that the response of the nonlinear components is influenced primarily by the most fundamental vibration modes and frequencies must be verified by numerical application of the method to a model problem. A simple taxiing vehicle model is used to compare the new method with time-history analysis and to validate the practicality of partial modal decoupling. The physical model consists of a two-dimensional simple beam vehicle taxiing over an irregular profile. The choice of a taxiing vehicle example at this first stage of numerical verification is due to the availability of the FDL-TAXI program that is used for time-history analysis. The FDL-TAXI program is a relatively simple program, yet it has been validated by comparison to extensive testing. Details of the TAXI program are well documented in reference [3].

The choice of a simple beam to represent an elastic vehicle is to have complete assurance and control on the finite element model. The vehicle model used is depicted in Fig. 1. The vehicle is represented by twelve beam elements. Individual beam elements are taken to be 100 in. long and weigh 4608 lbs each with a bending rigidity of 29×10^8 lbs-in². These elemental properties are selected to render the overall weight of the vehicle compatible with the suspension properties that are designed for a vehicle of about 55,000 lbs. The suspension system consists of nonlinear, oleo-pneumatic energy absorption devices. Typical nonlinear landing gear load-deflection relation-

ships are used to represent the suspension gear properties. Each suspension strut force is represented as the sum of pneumatic spring force, hydraulic damping force and strut friction force. The procedures in the existing FDL-TAXI program are used to model the suspension system similar to that of a typical fighter aircraft [4].

Prior to the transient analysis it is necessary to define the vibration problem and to determine the unconstrained vibration modes and the natural frequencies of the linear vehicle substructure. The vibration problem for the unconstrained vehicle is solved by an eigensolution algorithm based on the generalized Jacobi method with eigenvalue shifts [1]. The solution of the eigenproblem supplies the vibration mode shape, natural frequency and generalized mass data which is needed both in time-history and frequency domain analyses. Once the free vibration properties are determined, nonlinear time-history simulations are made using various dimensions for the modal basis as defined by Eq. (8). Two percent modal damping is assumed for each flexible mode. For the simple vehicle model with 12 elements and 26 geometric coordinates a maximum of 14 modes are considered including 2 rigid body modes and 12 flexible modes. In theory it would be possible to include the entire set of 26 modes. However, it has been found that the vibration problem solution for the higher modes is susceptible to numerical inaccuracies. It has been observed that only the first half of the vibration modal data is numerically reliable [5]. Accordingly, time-history simulations are made using 4, 8 and 14 orthogonal modes. The vehicle is assumed to travel at a constant velocity of 44 ft/sec. The total runway length traveled is 230 ft. with a standard 78 ft. AM-2 mat beginning at 106 ft. The AM-2 mat is 1.5 in. high and includes 4 ft. linear ramps at both ends. The same time discretization interval of 0.00025 seconds is used in all time-history analyses. This is the maximum discretization interval which can be used to secure numerical convergence with time-history integration when the maximum number of 14 modes are included. With the 14-mode time-history analysis the vehicle structure geometric coordinate response is also computed for later comparison with the hybrid results. Internal loads are chosen as controlling test cases because of the inherent difficulty of predicting them on the basis of a small number of modes. Specifically, the internal bending moment at coordinate 4 and the shear

forces at coordinates 5 and 9, as referenced by Fig. 1, are presented in comparative results in Fig. 2 through Fig. 10. In these figures the time increment is 0.002 seconds which is the same as the discretization interval in frequency domain analysis and the horizontal axis spans 5.2 seconds. The broken lines represent the time-history simulations and the solid lines represent the hybrid simulations using the time-history nonlinear suspension forces combined with frequency domain analysis. All time-history curves (broken lines) are computed on the basis of 14 orthogonal generalized modes used in the TAXI program. All hybrid curves also use 14 modes in the frequency domain analysis. However, in the hybrid method the time-history nonlinear forces that are converted to the frequency domain are computed on the basis of various number of modes. The different hybrid solutions are distinguished from one another on the basis of the modal content represented in their nonlinear force time-history inputs.

In Figs. 2, 3, and 4 comparisons between the hybrid method and time-history integration for the dynamic response of the internal bending moment at coordinate 4 is presented. In Fig. 2 both the hybrid method and the time-history integration are based on 14 modes. The initial phase of the response, which is seen as the relatively flat portion of the plot, corresponds to the perfectly flat portion of the runway. Theoretically, the dynamic response in this region should not be different from zero. However, both the hybrid and time-history integration schemes as implemented in this first study are vulnerable to small numerical perturbations, seen here as a deviation from a zero response. The previously described AM-2 mat is encountered by the taxiing vehicle at time increment 1205. The dynamic response of interest appears after the mat is encountered. The hybrid method simulation (solid line) is seen to follow the character of the response as calculated by complete time-history integration quite closely. There are differences, however, in the peak values as predicted by the two methods. It is not known at this time which solution gives a better estimate of the peak values. However, it is expected that the time-history solution will overshoot the peaks because of numerical constraints and the hybrid solution may flatten them out. It is expected that improvement in the numerical algorithms used to obtain both the time-history and frequency domain analysis will eliminate much of the

discrepancy seen in these comparisons.

Fig. 3 shows the dynamic response of the same internal bending moment at coordinate 4 as in Fig. 2. However, in the hybrid method the number of modes included in the determination of the nonlinear strut forces has been reduced to 8 from the reference value of 14. The time-history integration plot remains the same as in Fig. 2, containing 14 modes. Comparison of the two curves in Fig. 3 again shows that the dynamic response as predicted by the two methods is characteristically in good agreement. Comparing Figs. 2 and 3, it is seen that the reduction of the number of modes in the hybrid analysis has had very little effect on the response simulation. A preliminary conclusion may thus be drawn that apparently the nonlinear suspension response can be represented with negligible error on the basis of 8 modes as in Fig. 3, compared to a basis of 14 modes as in Fig. 2. Thus, the comparison of the solid line plots of the hybrid method from Figs. 2 and 3 demonstrate the validity of partial modal decoupling assumption for this example.

Fig. 4 again shows the bending moment response at coordinate 4. The time-history integration with 14 modes and the hybrid solution with only 4 modes including two rigid body and two flexible modes are plotted for comparison. It is immediately obvious that the hybrid simulation in Fig. 4 differs greatly in character and magnitude from the time-history solution. It is concluded that 2 flexible modes are simply too few to adequately represent the vehicle elastic behavior in the computation of the dynamic response of the nonlinear suspension struts.

Figs. 5, 6, and 7 are analogous to Figs. 2, 3, and 4, respectively in comparing the hybrid simulations with time-history analysis. The dynamic response of the internal shear force at vehicle coordinate 5, as referenced by Fig. 1, is plotted in Figs. 5, 6, and 7. Fig. 5 shows the hybrid solution on the basis of 14 modes. Figs. 6 and 7 show the hybrid solution on the basis of 8 and 4 modes, respectively, included in the determination of the nonlinear suspension forces. The numerical perturbations discussed in Figs. 2, 3, and 4 are similarly present in Figs. 5, 6, and 7. Nevertheless, comparing Figs. 5 and 6 it is again observed that the 8 mode simulation give as good an approximation as does the 14 mode simulation. Also, the 4 mode simulation is again inadequate as can be seen from Fig. 7.

The dynamic response of the internal shear force at coordinate 9 is shown in Figs. 8, 9, and 10. Coordinate 9 is of special interest because it is the attachment point for the main suspension gear strut. Fig. 8 shows the hybrid solution with 14 modes. Figs. 9 and 10 show the hybrid solution with 8 and 4 modes, respectively. From these three figures it is seen that the numerical perturbations in the initial smooth profile differ significantly from zero. However, comparison of this response as predicted by the hybrid method in each of the Figs. 8, 9 and 10 shows that these non zero perturbations are most likely contained in only the lowest modes, possibly the rigid body modes. Even though the response differs from the expected zero response in the initial phase, the character of the hybrid response curve still follows the general character of time-history simulation plot. As before, there is virtually no difference between the hybrid simulations containing 14 and 8 modes, as depicted in Figs. 8 and 9, respectively. Again, however, the 4 mode hybrid response of Fig. 10 is inadequate for predicting the dynamic behavior.

CONCLUSION

The basic premise of the hybrid method, that the nonlinear response in a structure with discrete nonlinear components is influenced primarily by the low frequency vibration modes of the linear substructure, has been verified in a preliminary way. In the case of the vehicle model which has been the subject of numerical work in this paper, the nonlinear component response was successfully modeled by including only six flexible modes or one quarter of the total number of flexible modes of the linear substructure. It is thus concluded that the postulated partial modal decoupling of the nonlinear components from the linear structure actually occurs, making the hybrid solution method a viable approach for the analysis of structures with distinct nonlinearities. In practical cases where the total number of modes which must be included to adequately represent the dynamic response of the linear structures is quite large, it is expected that the hybrid method will greatly reduce the computational effort required in dynamic simulations.

The promise of the hybrid method has been demonstrated, however, the results reported in this paper must be regarded as preliminary. Additional research is needed before the hybrid method can be developed into a reliable

and efficient analysis tool. Specifically, more information must be obtained on numerical requirements such as the maximum time-step size constraint to achieve reasonable accuracy and the modal content needed for a realistic solution for large and complex systems. Studies must be done to better understand the nature of partial decoupling of the nonlinear component response from the higher frequency vibration modes of the linear substructure. In this regard the extent of decoupling which could be expected to occur in actual complex structures must be determined in a realistic way. In the study presented in this paper the modal structure was a simple 26 degree-of-freedom system and the nonlinear component response was adequately represented by one quarter of the flexible modes. However, in larger and more complex systems, the required number of modes for simulation of the nonlinear forces is not expected to increase in proportion to the degree of complexity of the problem. The nonlinear response is expected to be contained within the lowest 12 modes even for very large systems. This assumption must be verified through extensive testing of the new hybrid method.

Finally, as a result of the particular numerical insight gained in this paper, it seems appropriate to contemplate the reorganization of the hybrid method to act more interactively with time-history integration. Namely, a piecewise linear hybrid iterative method is envisioned in future work in which nonlinear time-history integration and linear structural analysis proceed in parallel with mutual checking and corrections.

REFERENCES

1. Clough, R.W., and Penzien, J. Dynamics of Structures, McGraw-Hill Book Company, 1975.
2. Minnetyan, L., Transient Analysis of Structures with Distinct Nonlinearities, 1981 USAF-SCEE Summer Faculty Research Report, September 1981.
3. Gerardi, A.G., Digital Simulation of Flexible Aircraft Response to Symmetrical and Asymmetrical Runway Roughness, AFFDL-TR-77-37, Air Force Flight Dynamics Laboratory, Wright-Patterson AFB, OH 45433, August 1977.

4. Gerardi, T.G., and Riechers, J.T., Test and Evaluation of the High Pressure Strut Concept on the F-4 Main Landing Gear, Report No. AFWAL/FIBE-81-1, May 1981.
5. Przemieniecki, J.S., Theory of Matrix Structural Analysis, McGraw-Hill Book Company, 1968.

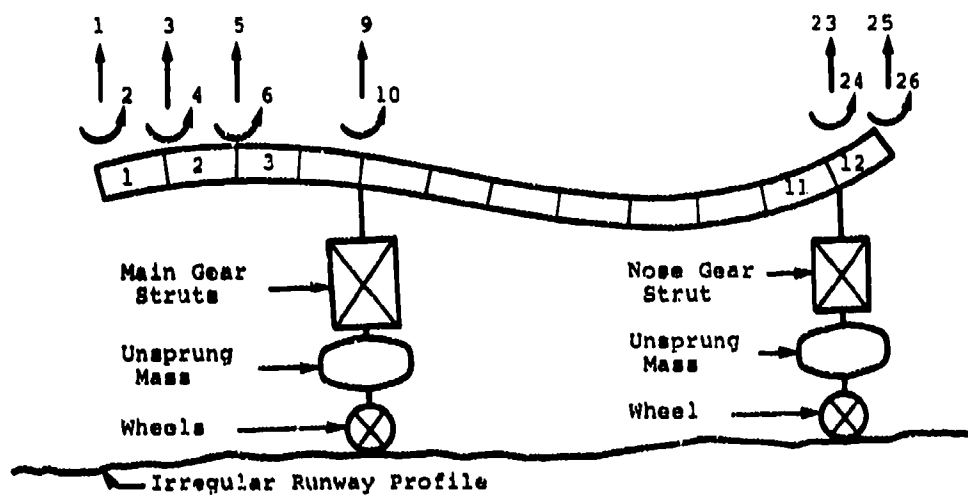


Fig. 1. Simple Beam Vehicle Model

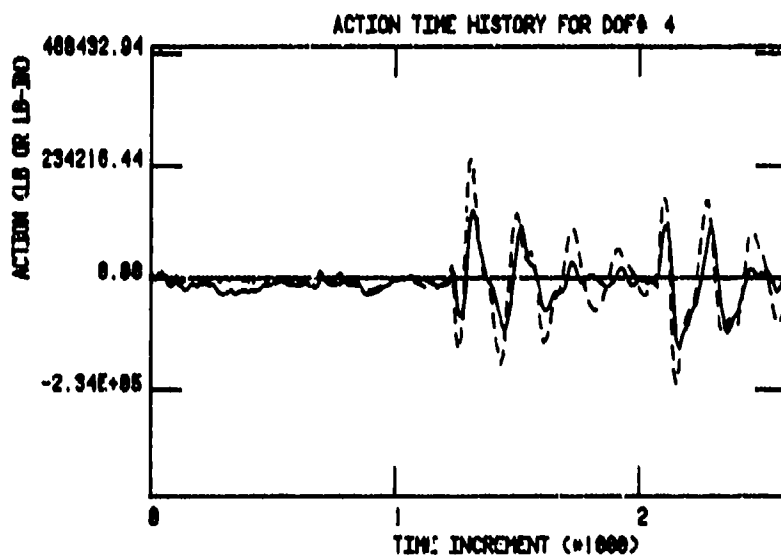


Fig. 2. Bending Moment at Coordinate 4
Solid: Hybrid Simulation with 14 Modes
Dashed: Time History Simulation with 14 Modes

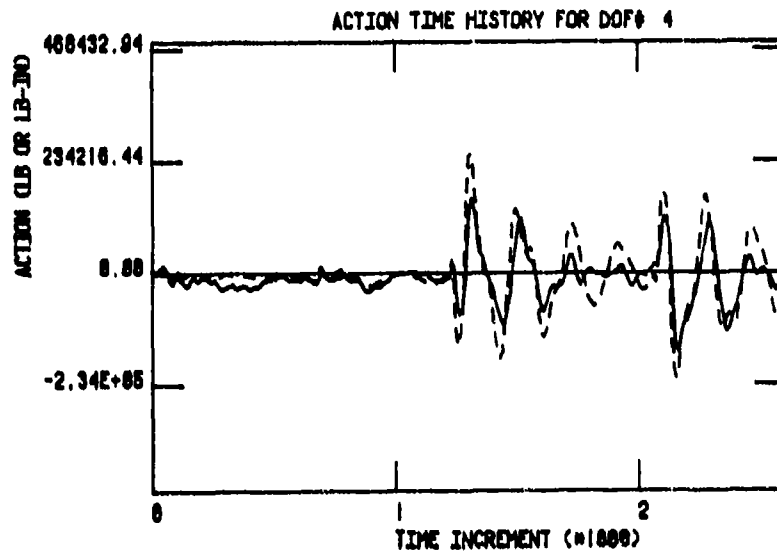


Fig 3. Bending Moment at Coordinate 4
Solid: Hybrid Simulation with 8 Modes
Dashed: Time History Simulation with
14 Modes

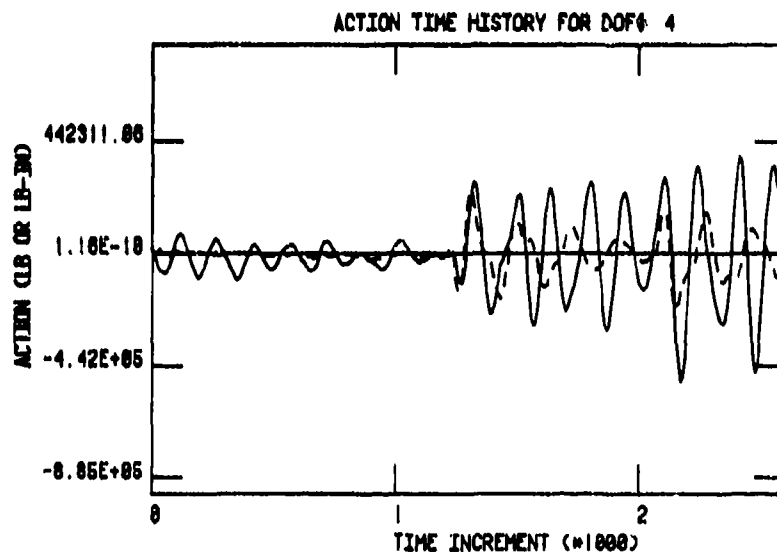


Fig. 4. Bending Moment at Coordinate 4
Solid: Hybrid Simulation with 4 Modes
Dashed: Time History Simulation with
14 Modes

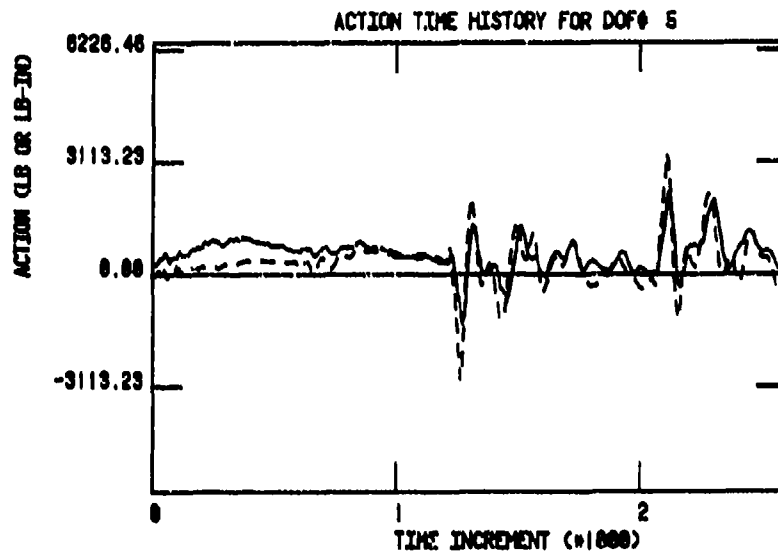


Fig. 5. Shear Force at Coordinate 5
Solid: Hybrid Simulation with 14 Modes
Dashed: Time History Simulation with 14 Modes

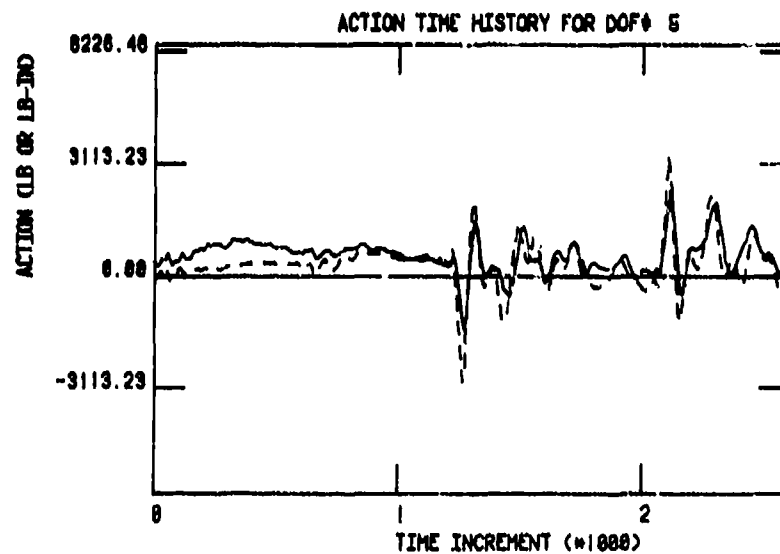


Fig. 6. Shear Force at Coordinate 5
Solid: Hybrid Simulation with 8 Modes
Dashed: Time History Simulation with 14 Modes

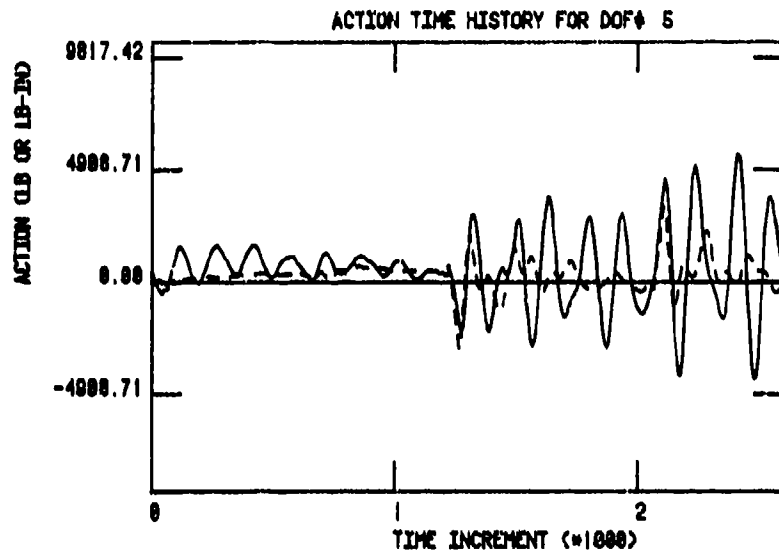


Fig. 7. Shear Force at Coordinate 5
Solid: Hybrid Simulation with 4 Modes
Dashed: Time History Simulation with 14 Modes

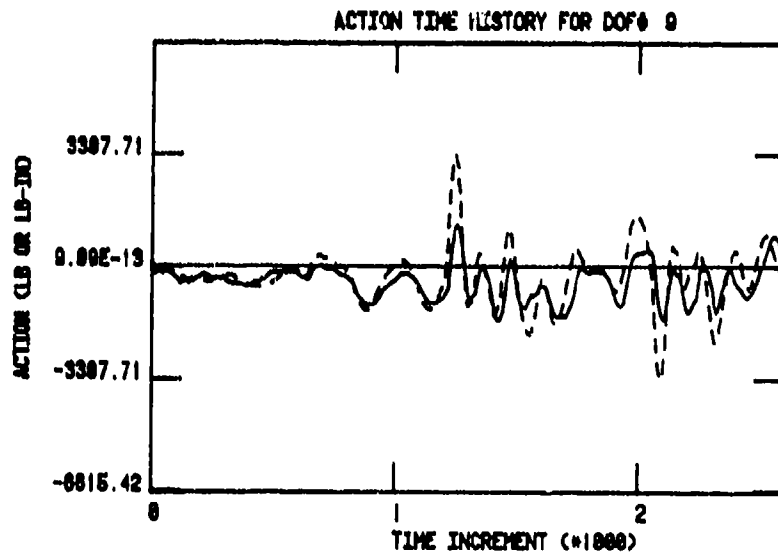


Fig. 8. Shear Force at Coordinate 9
Solid: Hybrid Simulation with 14 Modes
Dashed: Time History Simulation with 14 Modes

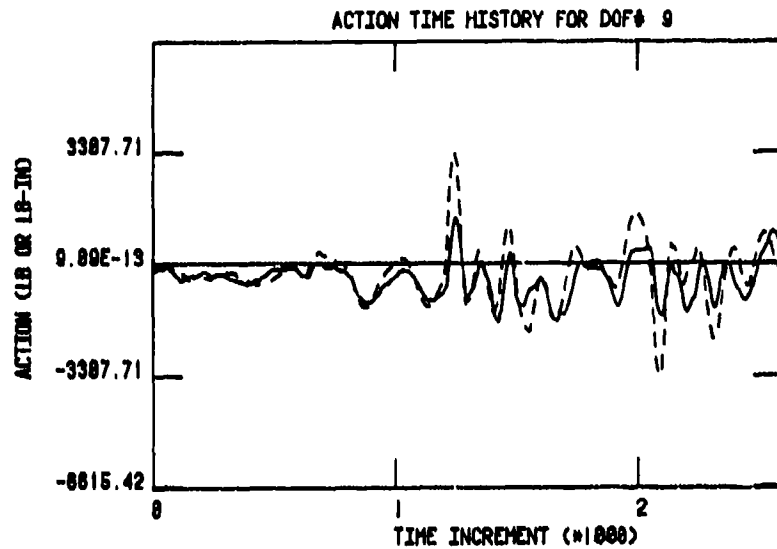


Fig. 9. Shear Force at Coordinate 9
Solid: Hybrid Simulation with 8 Modes
Dashed: Time History Simulation with 14 Modes

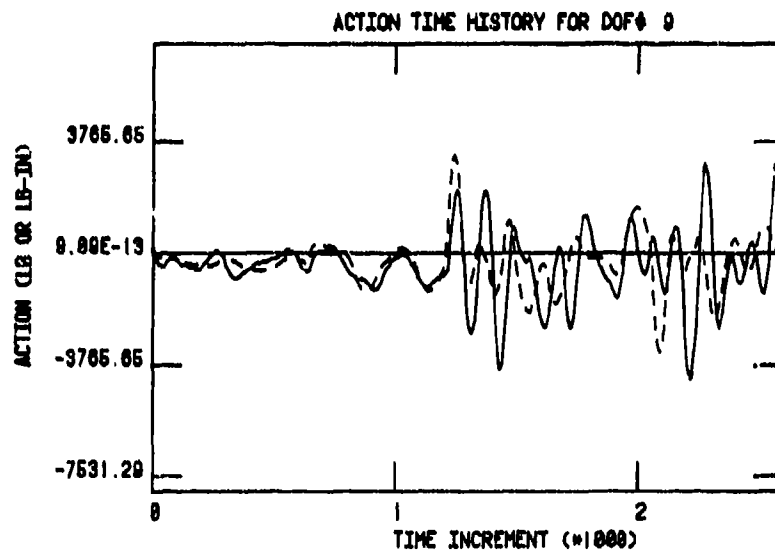


Fig. 10. Shear Force at Coordinate 9
Solid: Hybrid Simulation with 4 Modes
Dashed: Time History Simulation with 14 Modes

DISCUSSION

Mr. Roos (McDonnell Douglas Aircraft Corporation): Do you plan to acquire any data from any HAVE BOUNCE or BDR tests to correlate this analysis?

Mr. Minnetyan: The next step in this mini-grant is to apply this method to an actual aircraft. I am glad you asked that question because I have two choices; I can either apply it to the F4 or to the F15 aircraft, whichever I can find the data for. I know there are test data for those aircraft, and I can compare those test data to see how the simulation will work. Without being able to compare this with actual test data, I can't really say much. And even if I compare it with the actual data, as you know, the actual test data for tested aircraft can have certain shortcomings. Perhaps a controlled loading environment type of test would be more appropriate to verify and validate this method of analysis.

EXPERIMENTAL AND ANALYTICAL INVESTIGATION
OF ACTIVE LOADS CONTROL FOR AIRCRAFT LANDING GEAR

David L. Morris
Air Force Wright Aeronautical Laboratories
Wright-Patterson Air Force Base, Ohio

and

John R. McGehee
NASA Langley Research Center
Hampton, Virginia

Experimental and analytical investigations of a series-hydraulic, active loads control main landing gear from a light, twin-engine civil aircraft have been conducted. The experimental tests were conducted both at the NASA Langley Research Center Aircraft Landing Dynamics Facility and at the Air Force Wright Aeronautical Laboratory Landing Gear Development Facility. These tests included landing impact and traversal of simulated runway roughness. The results of these investigations show that the active gear is feasible and very effective in reducing the force transmitted to the airframe. Preliminary validation of a multi-degree-of-freedom Active Gear Flexible Airframe Takeoff and Landing analysis computer program, which may be used as a design tool for active gear systems, has been accomplished by comparing experimental and computed data for the passive and active gears.

INTRODUCTION

Aircraft dynamic loads and vibrations resulting from landing impact and from traversing runway and taxiway unevenness are recognized as significant factors in causing fatigue damage, excessive airframe loads, crew and passenger discomfort, and reduction in the pilot's ability to control the aircraft on the ground. One potential solution for alleviating these ground operational problems is the application of active-control technology to the landing gears to reduce ground loads applied to the airframe.

An active control system has been designed and fabricated to remove or add fluid to the landing gear shock strut piston to regulate the shock strut force. A main landing gear from a Piper Navajo, a light, twin-engine civil aircraft, was modified to accommodate the control system. This approach is called "series-hydraulic" control because the control servovalve is in series with the landing gear strut and the hydraulic fluid is pumped in and out of the strut to affect control.

Landing simulation tests employing the series-hydraulic active control gear

have been conducted at the NASA Langley Research Center Aircraft Landing Dynamics Facility to determine the feasibility and potential of the active gear for reducing ground loads transmitted to the airframe. These tests simulated touchdown impact and rollout over a surface having discrete and long wavelength unevenness for passive and active versions of the gear.

As a result of U.S. Air Force interest in potential solutions to the runway denial problem, shaker tests of the passive and active versions of the gear were conducted at the Air Force Wright Aeronautical Laboratories (AFWL). These tests were made to investigate possible performance limitations of the active gear during the rollout phase of a landing by utilizing a hydraulic shaker to provide sinusoidal and step inputs at various amplitudes and frequencies. The inputs are representative of the traversal of runway unevenness. A multi-degree-of-freedom Active Gear Flexible Airframe Takeoff and Landing analysis computer program (acronym AGFATL) has been developed and data from the tests are presently being employed to validate the computer program.

This paper presents results of the

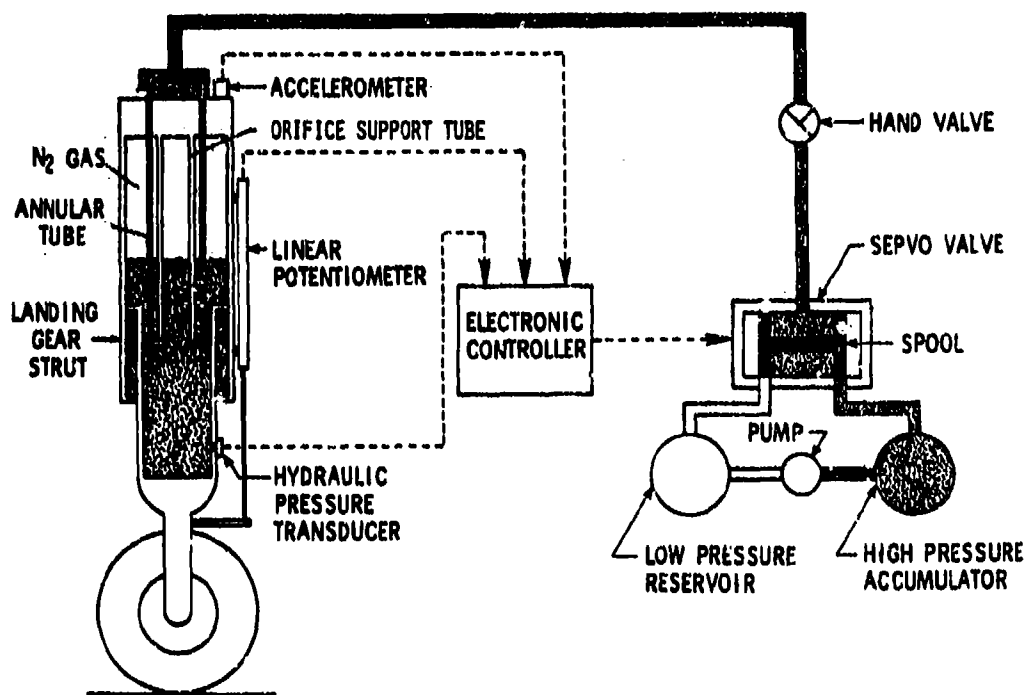


Figure 1. Schematic of active control landing gear.

experimental and analytical investigations to demonstrate the feasibility and potential of this type of active loads control gear. The landing simulation tests were conducted with a mass on the gear of 104 slugs (one-half the mass of Navajo airplane), pitch attitudes from 0° to 13° , touchdown sink rates from 3 to 5.5 ft/sec, and ground speeds from 8 to 80 knots. The shaker tests were conducted with a mass on the gear of 93 slugs, sinusoidal inputs of 0.5 to 2.0 inches double amplitude at frequencies from 1 to 20 Hz. The amplitudes of the step inputs investigated were varied at 0.5 inch intervals from 0.5 to 4.5 inches.

DESCRIPTION OF ACTIVE CONTROL GEAR

A schematic of the active control landing gear is shown in Figure 1. The landing gear strut was modified by replacing the single-wall orifice support tube with a doubled-walled tube. This annular tube exposes the fluid in the strut piston, through the cylinder head adapter, to the servovalve. The control hardware required for the active gear test program was a 200 gallon-per-minute servovalve, a low-pressure reservoir, a

hydraulic pump, a high-pressure accumulator, an electronic controller, and feedback transducers. The hand valve shown permitted isolation of the gear from the control hardware, thus allowing the conduction of passive gear tests.

The electronic controller amplifies and shapes feedback transducer signals, determines the operating mode (takeoff or landing), and implements control laws. The control laws programmed into the controller are based on the following logic. Assuming the airplane mass remains constant during a landing, the controller employs the touchdown sink rate to compute the touchdown energy. During gear compression the shock strut hydraulic force increases, and the controller computes and compares the remaining work capability of the shock strut (determined from the accelerometer and linear potentiometer signals) with the touchdown energy. When the shock strut work capability equals or exceeds the touchdown energy, the controller stores the instantaneous value of the acceleration (wing-gear interface force) for use as the control limit force. This force is maintained by the removal/addition of hydraulic fluid from/to the

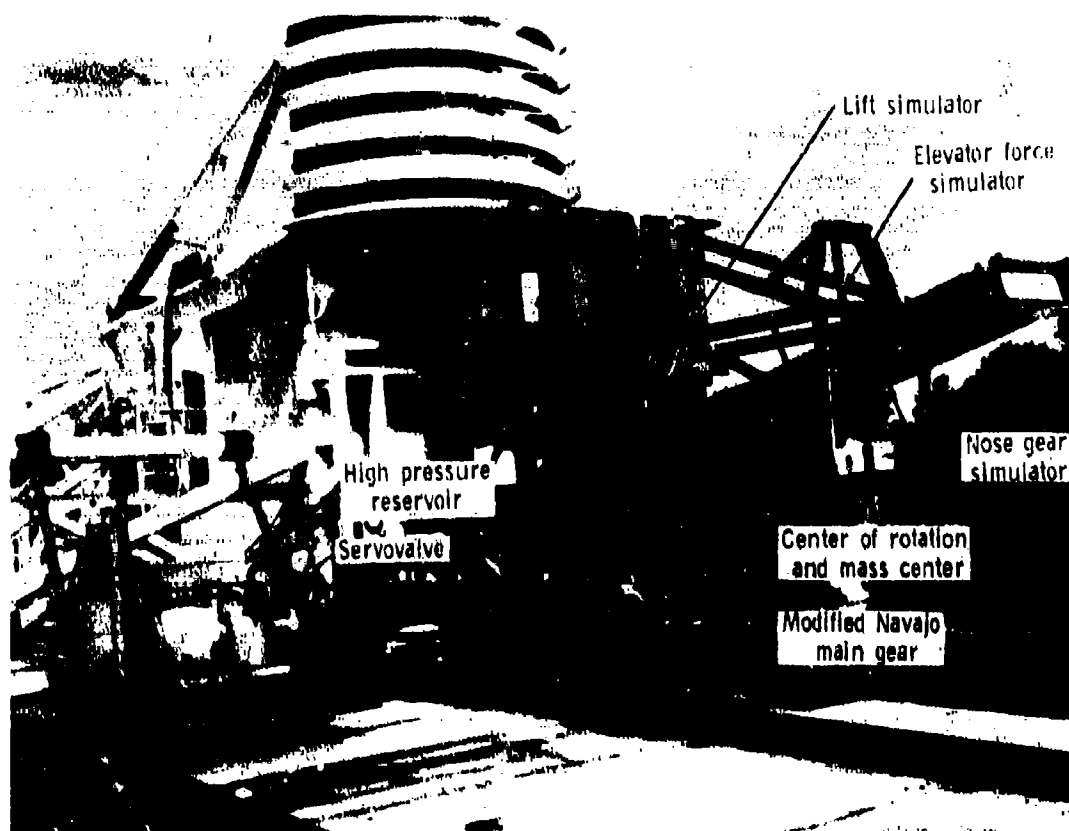


Figure 2. Active control landing gear test apparatus.

shock strut piston. At a predetermined momentum level, for a specific airplane-gear design, the controller linearly transitions the control-limit force to zero for rollout. During rollout, the controller maintains the wing-gear interface force within a specified tolerance about zero force. After control initiation, the controller continuously operates with a long time-constant control to return the gear shock-strut to the designed static position.

LANDING SIMULATION TESTS

Test Apparatus

Figure 2 shows the active control landing gear test apparatus installed on the test carriage at the NASA/LaRC Aircraft Landing Dynamics Facility. The essential elements of the apparatus are a drop frame, a pitching beam, the modified Navajo main gear, a lift force simulator, an elevator force simulator, and a nose-gear force simulator. The landing gear is attached to the pitching

beam at a distance aft of the center of rotation and mass center equal to the distance the main gear is located aft of the center-of-gravity on the Navajo airplane. The elements of the active control hydraulic power unit which would be required on board an airplane with an active gear system are the high-pressure reservoir and the servovalve.

Figure 3 shows the elevation profile of the runway unevenness investigated. Two step bumps were installed on the surface at spacing distances, determined by the carriage forward speed, to produce encounter frequencies of 2 to 4 Hz. In a recently repaired section of the runway surface, long-wave-length changes in surface elevation of approximately the same magnitude (1.25 inches) as that of the step bumps were measured. This unevenness is referred to as natural bumps in this paper.

Touchdown Impact

The touchdown impact phase is

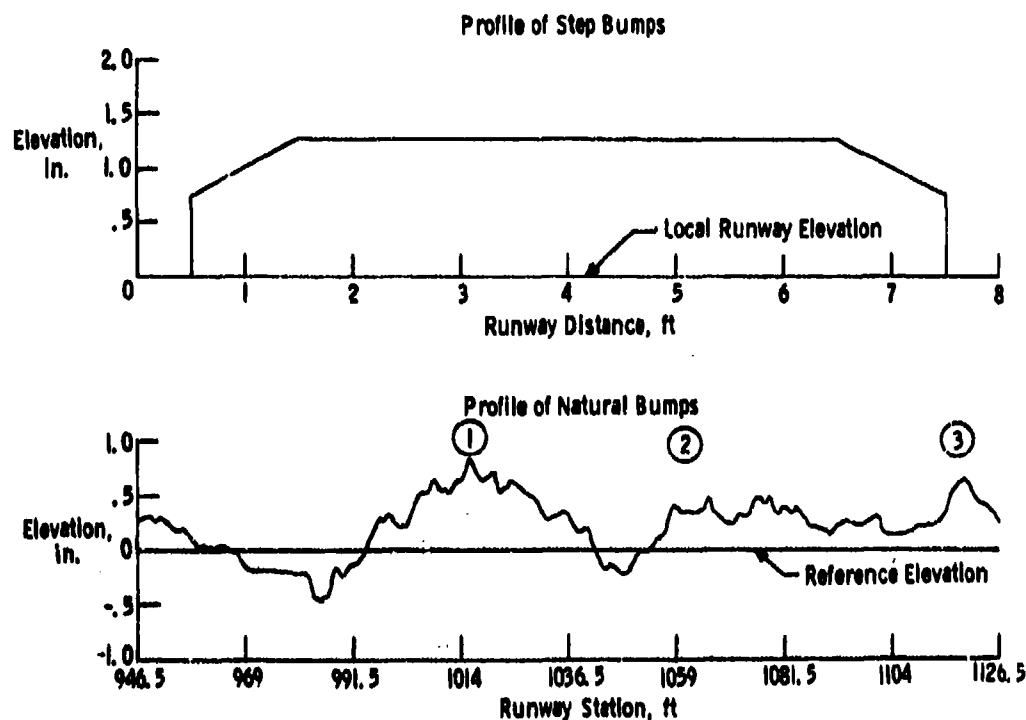


Figure 3. Runway unevenness investigated.

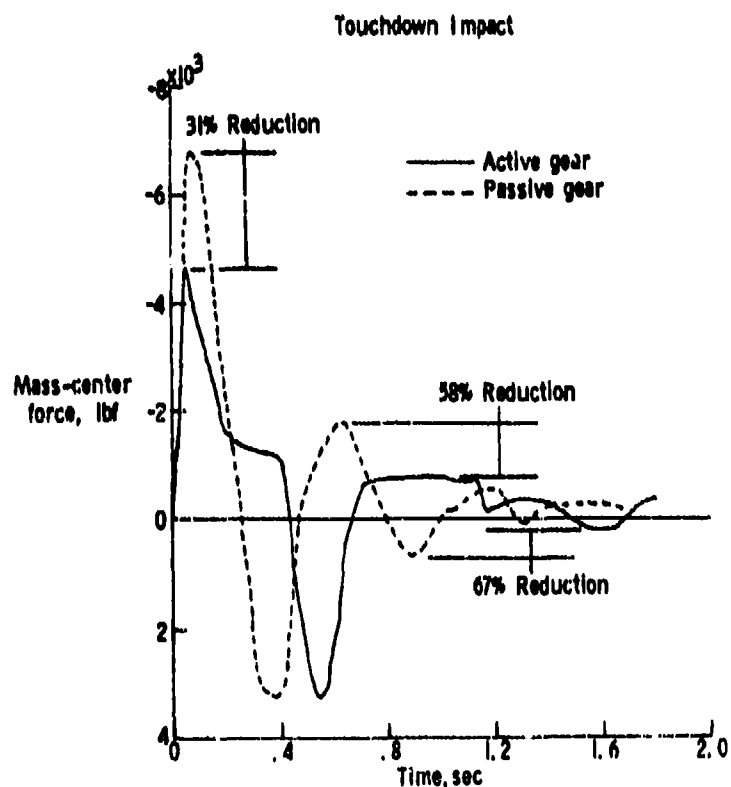


Figure 4. Experimental data obtained during touchdown impact.

Traversing Step Bumps at 40 knots

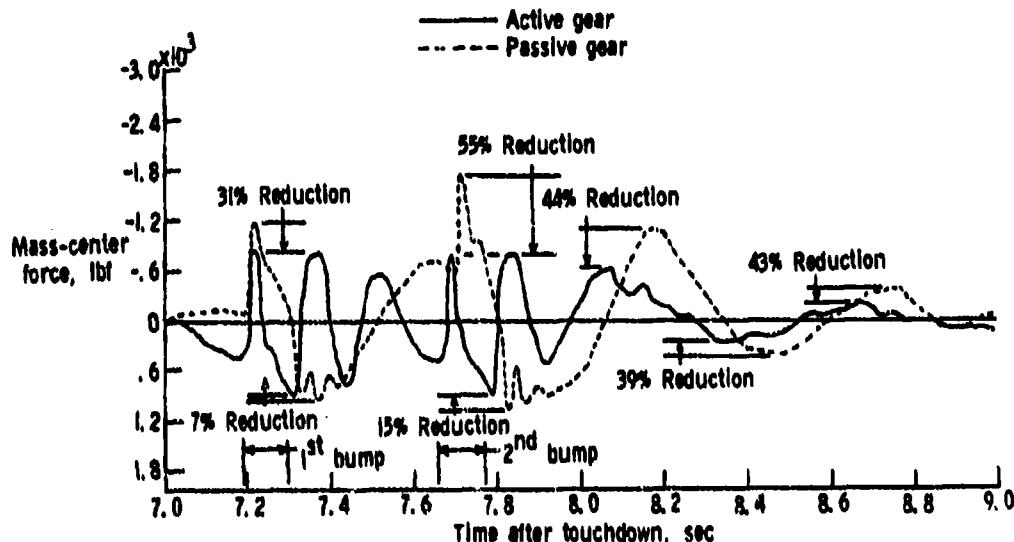


Figure 5. Experimental data obtained during traverse of step bumps.

defined as that portion of the landing which includes initial impact, rebound, and secondary impact to essentially static equilibrium for rollout. Data obtained from the passive and active gears during the touchdown impact phase of a simulated landing are shown in Figure 4. Mass-center forces are presented as a function of time after touchdown which occurs at time zero. The initial impact for the passive gear requires approximately 0.2 seconds; but the active gear, because of the approximately 31% lower force, requires approximately 0.4 seconds to dissipate the touchdown energy. Subsequent to the initial impact, the mass rebounds and both passive and active gears fully extend and lose contact with the surface as indicated by the accelerative mass-center force of approximately 3300 pounds-force. Logic programmed into the electronic controller deactivates control when the shock strut is fully extended, hence the active gear was not under control during rebound from initial impact. During secondary impact, the deceleration force of the active gear is limited by the controller to approximately 800 pounds-force, which results in a 58% reduction relative to that generated with the passive gear. During rebound from the secondary impact, the accelerative force of the active gear was reduced 67% relative to that of the passive gear.

Traverse of Step Bumps

Figure 5 shows mass-center force data as a function of time after touchdown for the passive and active gears traversing the step bumps, which were spaced to provide an encounter frequency of 2 Hz at the 40 knot ground speed. The time related location, duration, and spacing of the two step bumps are indicated along the time scale. For encounter with the first step bump, the active gear reduced the decelerating, mass-center force (negative force) by 31% relative to that of the passive gear. The reduction in accelerating force was 7% during rebound. Following rebound and prior to encounter with the second bump, the active gear exhibited damped force oscillations due to control response. The magnitude of these oscillations did not exceed that which occurred initially. At encounter with the second step bump, the active gear was effective in reducing the decelerating force by 55% relative to that generated by the passive gear. This increased effectiveness of the active gear may be attributed, since the active gear force level is about the same as that which occurred during encounter with the first bump, to the fact that the 2 Hz spacing of the bumps resulted in a reinforcement of the passive gear mass-center force. During rebound the active gear resulted in a reduction of accelerating mass-center force of 15%. Subsequent to rebound from the second step bump, the active gear was effective in reducing the mass-center decelerating and accelerating

Traversing Natural Bumps at 80 knots

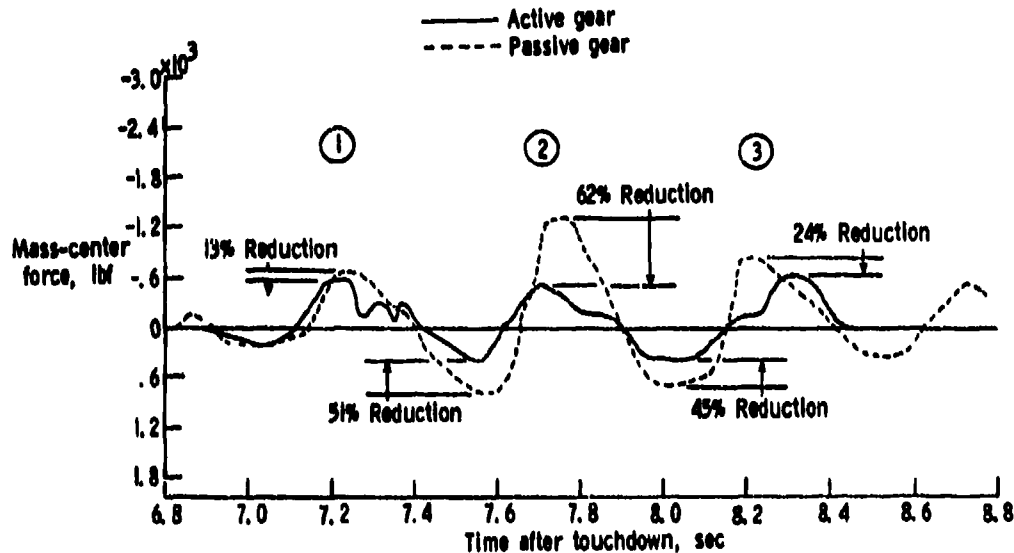


Figure 6. Experimental data obtained during traverse of natural bumps.

forces by approximately 40% as the gears returned to static equilibrium.

Traverse of Natural Bumps

Typical mass-center force data obtained from active and passive gear tests during traverse of the natural bumps at a ground speed of 80 knots are presented in Figure 6. Mass-center force is shown plotted as a function of time after touchdown. The numbers assigned to the mass-center decelerating force peaks correspond to those shown on the track surface (Figure 3) and are used to correlate mass-center forces with the changes in surface profile. To illustrate the effects of bump amplitudes and the rate of change of these amplitudes on gear forces, hence mass-center forces, the data obtained during the traversal of bumps 1 and 2 are discussed. The track surface profile of Figure 3 shows that bump 1 has an amplitude almost twice that of bump 2, but has a shallower slope than bump 2. The mass-center force for the passive gear during traversal of bump 2 is approximately twice that developed during traversal of bump 1. Thus, the rate of change of surface elevations has a greater influence on the force developed by the gear than the amplitude of the elevation changes. This agrees with oleopneumatic shock strut theory that defines the hydraulic force (which accounts for about 90% of the dynamic force de-

veloped by the shock strut) as a function of the shock strut velocity. Therefore, the series-hydraulic control system, assuming adequate control system response and similar strut binding friction effects, should be more effective during traversal of bumps with steeper slopes. This is shown in Figure 6 where the active gear reduced the decelerating force by 62% during traversal of the second bump and by only 13% during traversal of the first bump. The active gear also reduced the accelerating forces during traversal of the first and second bumps by 51 and 45%, respectively. During traversal of the third bump the active gear reduced the decelerating force by 24%.

Shaker Tests

The test apparatus setup for the conduct of the shaker tests is shown in Figure 7. The modified Navajo gear is shown attached to the drop tower bucket and resting on the shaker table. The gear is supporting the 93 slug drop tower bucket in static equilibrium with the gear stroked approximately 5 inches. The flexible hose which connects the cylinder head adapter of the modified gear to the hydraulic power unit is also shown. Testing was conducted on both the passive and active gears by programming the shaker to provide various haversine and step inputs.



Figure 7. Test apparatus for shaker tests.

Forcing Function: 5 Cycles at 1.3 Hz with Double Amplitude of 2 Inches
Strut Resonance Frequency = 1.25 Hz

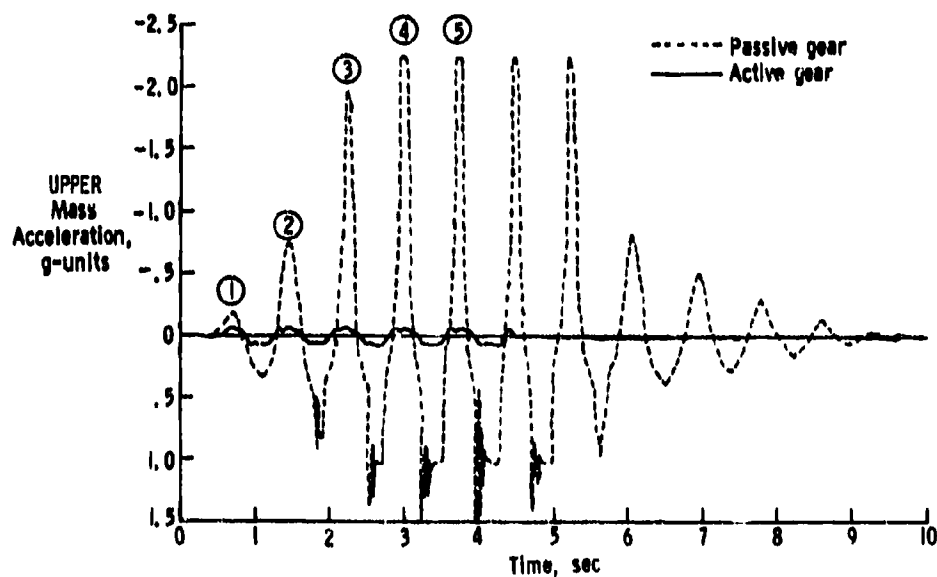


Figure 8. Acceleration response near resonance frequency.

Forcing Function: 5 Cycles at 1.3 Hz with Double Amplitude of 2 Inches
Strut Resonance Frequency = 1.25 Hz

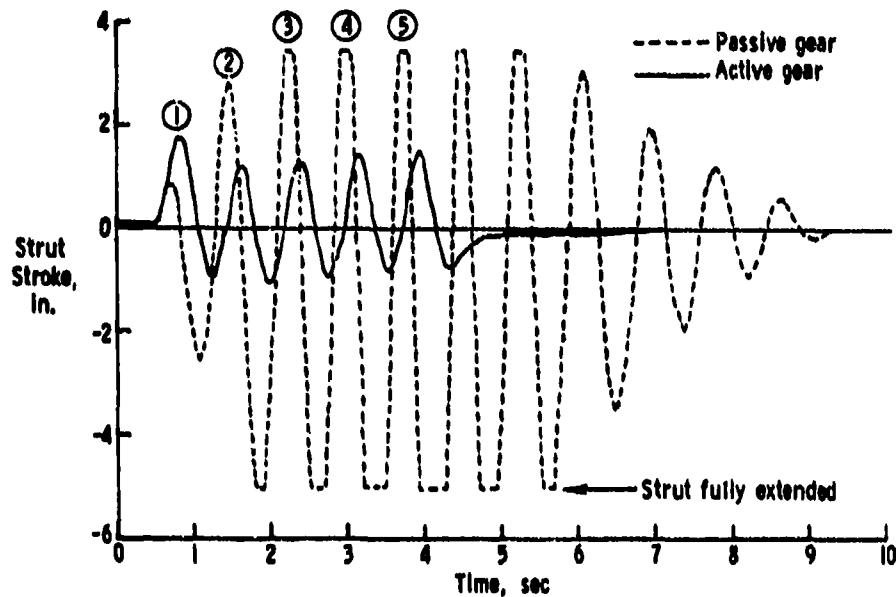


Figure 9. Stroke response near resonance frequency.

Acceleration Response Near Resonance Frequency

The responses of the passive and active gears to a forcing frequency near strut resonance frequency are shown in Figure 8. The strut resonance frequency is approximately 1.25 Hz and the forcing function applied consisted of five cycles at a frequency of 1.3 Hz with a double amplitude of two inches. The data are presented as upper mass acceleration as a function of time. Negative acceleration represents load applied upward on the mass by the gear. The circled numbers indicate the compressive peaks of the five cycles of excitation. The effect of resonance on the passive gear accelerations is very pronounced. The accelerations increase to maximum values of approximately -2.25 and 1 g-units after three excitation cycles. Subsequent to the five excitation cycles, the passive gear continues to generate the maximum accelerations for approximately two cycles before appreciable damping occurs. In contrast, the active gear is very effective in limiting the accelerations of the mass. The accelerations are controlled to values of approximately ± 0.1 g-unit during the five excitation cycles. Subsequent to the five excitation cycles, the active gear returns to static equilibrium in approximately one cycle.

Gear Stroke Response Near Resonance Frequency

The stroke responses of the passive and active gears to a forcing frequency near passive strut resonance frequency are shown in Figure 9. The data are presented as variations of strut stroke about the static equilibrium stroke (approximately five inches) shown as zero stroke on the figure. The circled numbers on the figure indicate the compressive peaks of the five excitation cycles. The passive gear stroke data more graphically illustrate the effect of resonance. After approximately two excitation cycles, the strut is stroking between the stroke limits of maximum compression and maximum extension, with the tire leaving the shaker table. The strut continues to operate in this mode for approximately two cycles after cessation of the input excitation and before significant damping becomes apparent. The active gear stroke indicates no resonant response since the stroke approximates the amplitude of the input excitation with the exception of the response to the first compressive peak of the input excitation. During the first compressive peak, the stroke is greater than that which occurs during subsequent compressive peaks and is twice as great as the stroke which occurred with the passive gear. This

Forcing Function: Step Input with Amplitude of 2.5 inches

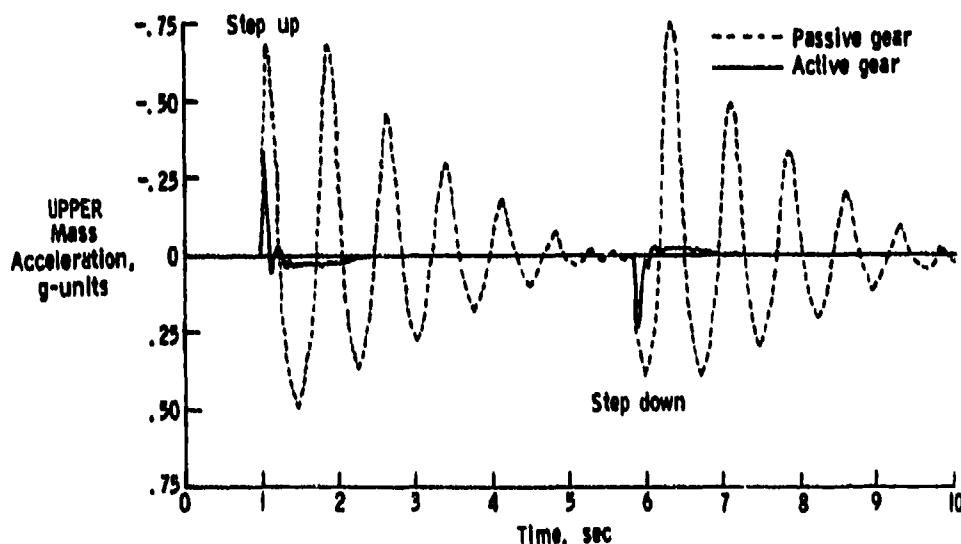


Figure 10. Acceleration response to a step input.

illustrates the basic principle of the active gear, which is the dissipation of the energy input to the mass, over greater stroke at a lower force level.

Acceleration Response to a Step Input

The acceleration responses of the mass to a step input with an amplitude of 2.5 inches are shown for the passive and active gears in Figure 10. Mass accelerations are plotted as a function of time. A step bump is simulated by an initial compressive (step up) input and a step down input after the passive gear had returned to static equilibrium. Comparison of the active and passive gear data illustrate two significant advantages of the active gear. First, the mass accelerations experienced with the active gear during the step up and step down inputs were approximately one half of those generated by the passive gear. Secondly, the active gear was very effective in attenuating the response following the step up and step down inputs. This capability virtually eliminates the possibility of mutual reinforcement of responses from consecutive inputs and thus avoids the detrimental effects associated with such reinforcement of responses.

Preliminary Validation of AGFATL

An examination of the experimental

shock strut data revealed the presence of large binding friction forces in the gear and the test apparatus. For example, during the initial and secondary impact phases when the gear was compressing at its maximum stroking rate, the stroke data showed that the gear stopped stroking for a short period and then resumed compressive stroking. This phenomenon was observed during tests of both the passive and active gears with multiple cycles occurring during gear compression, particularly during secondary impact where maximum gear stroke was encountered. During initial computer (AGFATL) simulations of the test data, it became obvious that these binding friction effects would have to be included to obtain acceptable agreement between the computed and experimental data.

A comparison of experimental and computed data is presented in Figure 11 for the active and passive gears during the touchdown impact phase of a landing. Mass-center forces are plotted as a function of time from touchdown which occurs at time zero. The maximum values of the experimental and computed mass-center forces for both the active and passive gears are in good agreement. However, the computed values of these forces occur at a later time than the experimental values. This difference is attributed to the difficulty of including

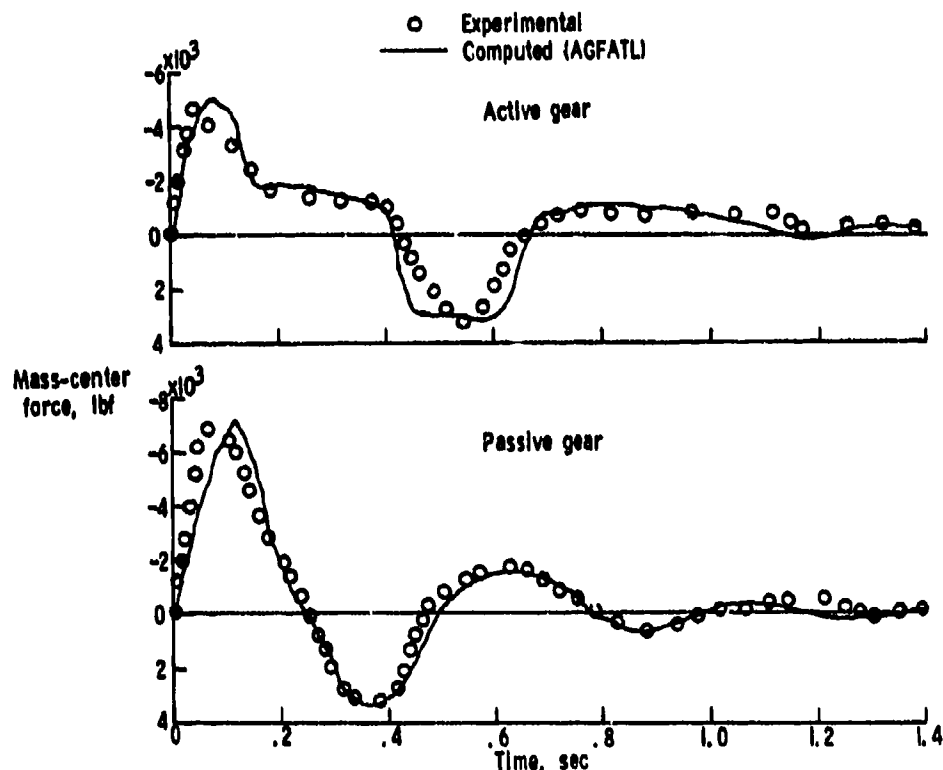


Figure 11. Comparison of experimental and computed data for touchdown impact.

in the computer simulations the binding friction forces in the timing sequence that occurred in the experiment. Subsequent to the initial impact, the agreement between computed and experimental data for the rebound and secondary impact phases is good for both the passive and active gears.

Concluding Remarks

Experimental and analytical investigations of passive and active loads control versions of a main landing gear from a light, twin-engine civil aircraft have been conducted to determine the feasibility and potential of the active gear in reducing ground loads applied through the gear to the airframe. The potential of the active gear was evaluated by employing landing simulation tests and shaker tests of both passive and active versions of the gear. The performance of the gear was determined during touchdown impact and traverse of two types of surface unevenness: abrupt discontinuities representative of uneven settlement of runway sections, and longer wave length variations in runway elevation.

Results of the landing simulation

tests show that the active gear was very effective in reducing mass-center forces relative to forces generated by the passive gear during touchdown impact, traversal of step bumps, and traversal of natural bumps. Results of the shaker tests also showed that the active gear provided large reductions in upper mass accelerations throughout the range of test parameters. No responses indicative of active system resonant frequency were obtained during the testing, and the active gear was very effective in the elimination of resonance effects which occurred at 1.3 Hz with the passive gear. Another benefit of the active gear results from the rapid attenuation of strut response which eliminates the possibility of mutual reinforcement of responses over consecutive runway roughness profiles. Preliminary validation of a computer program call AGFATL which is useful in analysis and design of active gear systems was accomplished.

DISCUSSION

Mr. Calapodas (U.S. Army Applied Technology Lab): Have you projected the weight penalty for such an optimized version of that system?

Mr. Morris: We went through a full iteration with Fairchild. They are doing some work for us on an A-10 rough soft field landing gear. They went through and calculated all of the penalties associated with the active landing gear versus other alternatives for improving our capability. We have numbers as far as everything that is involved, all the way down through life cycle cost and reliability and maintainability. We can see right now there are some penalties. We see that the active gear system basically offers us about the best improvement that we have today for increasing our capability. But at the same time, there are penalties that have to be weighed against that. We hope this new active system that I talked about, on the F4, might alleviate some of these penalties.

Mr. Calapodas: What about meeting the crashworthiness specifications? I think it is about 20 G's, or something similar, for helicopters.

Mr. Morris: In landing impact, you are still limited by the sink speed the gear can take, and your strut stroke. Basically, we can't get a large increase in actual sink speed of the aircraft, so we reduce the loads at the design sink speeds.

Voice: Is the device fail-safe? How does it work when it is not working quite right?

Mr. Morris: It fails passively. It just reverts back to a passive mode. The valve will close, and then it will be back into a passive strut.

Lt. Col. Allen (Air Force Office of Scientific Research): Are there any plans to take this modified F4 over some actual crater repairs, such as they did with the passive gear F4?

Mr. Morris: We only have a single modified gear, so we don't have a full set of gear to actually mount on the aircraft. We would like to have both the main gear and the nose gear. We have an upcoming program in the Air Force to look at a STOL aircraft technology demonstrator, and it will incorporate a rough soft field gear system. If the contractor that gets selected goes through the iteration, and if he determines that the active gear is the best solution, at that time we will probably go toward full scale development and actually flight test this gear.

ON THE MODAL IDENTIFICATION OF MULTIPLE DEGREE OF
FREEDOM SYSTEMS FROM EXPERIMENTAL DATA

by

David I. G. Jones
Materials Laboratory, AFWAL/MLLN,
Wright-Patterson AFB, Ohio 45433

and

Agnieszka Muszyńska
Bently Nevada Corporation
P.O. Box 157, Minden, NV 89423

In this paper the authors discuss the relative merits of frequency domain model identification procedures using receptance (response/excitation) and structural dynamic stiffness (excitation/response) representations of measured structural response data. It is shown that, while the receptance representation leads to adequate and easily obtained parameters for systems having low damping and stiffness characteristics which vary slowly with frequency, the dynamic stiffness representation has distinct advantages when the system is nonconservative and/or has characteristics which vary rapidly with frequency.

1. INTRODUCTION

Present day modal identification techniques and/or software most frequently utilize measured values of the ratios of response at one set of points of a system to the dynamic excitation at another set of points. Depending on the pickup technique, the response quantity could be amplitude of acceleration, velocity, displacement or strain, and the excitation quantity could be a force or a moment. The measurements can be obtained using digitally controlled Sine-Sweep tests, as is quite common in Europe, or the Fast Fourier Transform (FFT) applied to impulsively excited systems, as is common in the U.S.A. Each approach has its practical advantages and disadvantages but ideally (i.e., for linear systems and for sufficiently fine frequency increments) they should yield identical plots in the frequency domain.

The identification process applied to the measured response and excitation data is essentially that of determining estimates of the various modal parameters (such as resonant frequencies, modal damping, modal stiffness, modal mass, modal shape functions and number of modes) needed to best fit the measured data by a finite series of standard linear response solutions, in the frequency domain [1-15], or by complex exponential response solutions, in the time domain [16-18]. The software needed

to perform these calculations, developed over the past several years, is sophisticated and effective, and is readily available for routine applications by users having access to the appropriate test and analysis equipment and related software. Each combination of software and equipment, properly and equally used, gives essentially the same values for the parameters needed to fit the data, though some differences will always arise because of scatter, errors, slight nonlinearities, interference of additional degrees of freedom, non-reproducibility of tests and so forth. Even for those individuals who need apply modal identification techniques only occasionally, hand calculations on a mode-by-mode basis can readily be accomplished using at most a programmable calculator, provided that the modes are well separated. For closely spaced modes, iterative methods are required for hand calculation as well as for the more sophisticated commercial software. Accuracy and convenience are thereby reduced. No totally insurmountable obstacles arise, however, unless the number of very closely spaced modes is very great.

Present day modal identification techniques are less able to give good representations of the true system properties for strongly nonconservative systems such as those containing high damping polymeric materials, or for rotating machinery systems with continuous flow and transfer of energy within the system. In these

cases, an alternative approach, which has no such special advantages for low damped systems, becomes much more attractive. This approach is the dynamic stiffness technique, for which one examines, and fits parameters to, the measured dynamic stiffness, or ratio of excitation to response. For well separated modes, the modal mass or stiffness can be directly read off the graph of dynamic stiffness versus frequency squared even for high damping levels, or for rapid variation of properties with frequency. Table 1 illustrates some of the main variations of the mobility and impedance concepts, as discussed by Ewins [14, 15]. Allemang [18] gives a very useful bibliography of recent contributions on modal analysis.

In view of the extensive work done by many investigators in the area of modal identification during the past several years, attested to in part by the aforementioned references, it is the purpose of the authors in this paper to concentrate attention on a single aspect only, namely that of better establishing, as far as possible, the advantages and disadvantages of the dynamic stiffness approach as compared with the receptance approach [19, 20]. We shall illustrate the relative effectiveness of these two modal identification techniques as applied to (a) a one degree of freedom system and (b) a multiple degree of freedom system, using both: a made-up problem (initially prescribed parameters with observation of effectiveness in recovering these parameters) and some actual experimental results for systems with one, two and several degrees of freedom.

2. RECEPTANCE AND DYNAMIC STIFFNESS CONCEPTS

2.1. Frequency Domain Receptance Concept

If a structure S , as illustrated in Fig. 1(a), is excited by a force $S_e \exp(i\omega t)$ at point e , the response $W_j \exp(i\omega t)$ at any point j (including $e = j$) will depend on the structure geometry, materials and boundary conditions. From any given test, the transfer receptance α_{ej} , defined as W_j/S_e , is a complex quantity having both amplitude and phase relative to that of S_e . Typically, the variation of α_{ej} with frequency will be as illustrated in Figure 1(b). The peaks correspond to resonant modes of the system and between the resonant peaks lie either sharp antiresonances or shallow troughs. Point receptances (α_{ee} or α_{jj}) will always have antiresonances between resonances but transfer receptances ($e \neq j$) may or may not. The phase angles change by about 180° at each resonance. The variation of α_{ej} with frequency can also be plotted as an Argand or Nyquist diagram, as in Figure 1c, in which

TABLE 1

MOBILITY AND IMPEDANCE DEFINITIONS

RESPONSE / EXCITATION	EXCITATION / RESPONSE
Displacement/Force = Receptance	Force/Displacement = Dynamic (Apparent) Stiffness
Velocity / Force = Mobility	Force / Velocity = Mechanical Impedance
Acceleration / Force = Inertance	Force/Acceleration = Dynamic (Apparent) Mass
Strain / Force = No name given	Force / Strain = No name given

the real part of α_{ej} , is plotted against the imaginary part. The circular shapes near each resonance allow one to estimate the modal parameters unless the modes are too closely spaced. The modal representation of mobility, particularized to receptance (displacement/force) is:

$$\alpha_{ej}(\omega) = \sum_{n=1}^N \frac{\bar{\theta}_n(x_e) \theta_n(x_j)}{m_n [\omega_n^2 (1 + i\eta_n) - \omega^2]} \quad (1)$$

where $\theta_n(x_e)$ is the n -th modal response

function at point x_e , ω_n is the n -th resonant frequency, η_n the n -th mode loss factor, and m_n the n -th modal mass. The goal of modal identification is to obtain the best estimate of $\bar{\theta}_n(x_e)$, $\theta_n(x_j)$, m_n , ω_n for a finite number N of selected modes. For well separated modes, equation (1) gives the value of $|\alpha_{ej}|$ at $\omega = \omega_n$ as:

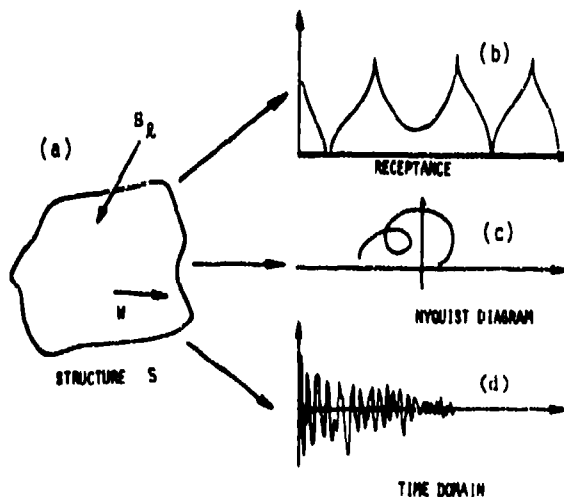


Figure 1. Structural response behavior of an ideal structure.

$$|\alpha_{2j}(\omega)|_{\omega=\omega_n} = \frac{\theta_n(x_i) \theta_n(x_j)}{m_n \omega_n^2 \eta_n} \quad (2)$$

Hence, if η_n is determined from the half-power

TABLE 2

Results for One Degree of Freedom System
Identification (Analytical)

CASE	Quantity	Approach	ω_n - Hz	η	ω_1 - Hz
(a) Hysteretic	Given	2910	0.007382	0.180	100
	Acceptance	2911	0.70787	0.148	100
	Dyn. Stiffness	2910	0.00738	0.180	100
(b) Hysteretic	Given	2910	0.007382	1.40	100
	Acceptance	2147	0.00787	1.52	100
	Dyn. Stiffness	2910	0.00738	1.80	100
(c) Visco-elastic	Given	1184(1+999i)	0.007382	0.180	100
	Acceptance	2911 at 100 Hz	0.00787	0.148	100
	Dyn. Stiffness	2911 at 100 Hz	0.00738	0.180	100
(d) Viscous	Given	2910	0.007382	2.39×10^{-4}	100
	Acceptance	2911	0.00787	0.148 at 100 Hz	100
	Dyn. Stiffness	2910	0.00738	2.39×10^{-4}	100

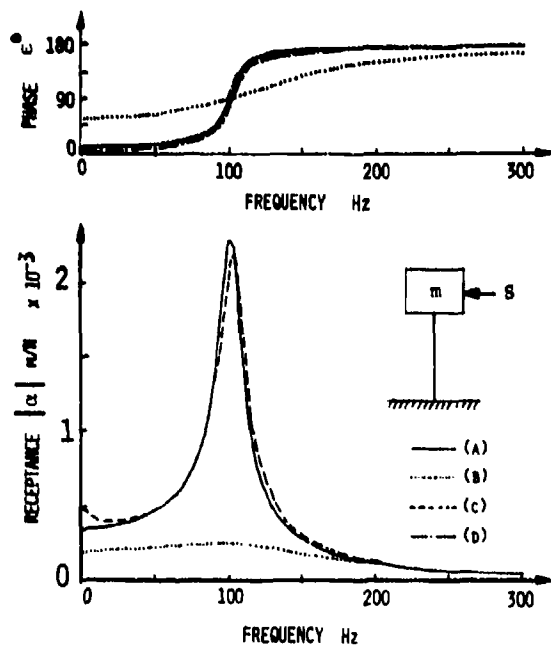


Figure 2. Single degree of freedom system: Graphs of phase (c) and receptance ($|\alpha|$) versus frequency, for case (a) to (d) (see Table 2).

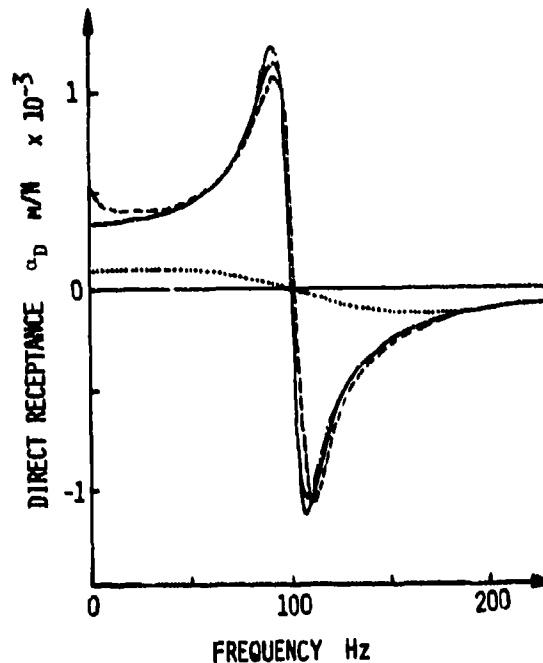


Figure 3. Single degree of freedom system: Graph of direct receptance versus frequency, for cases (a) to (d) (see Table 2).

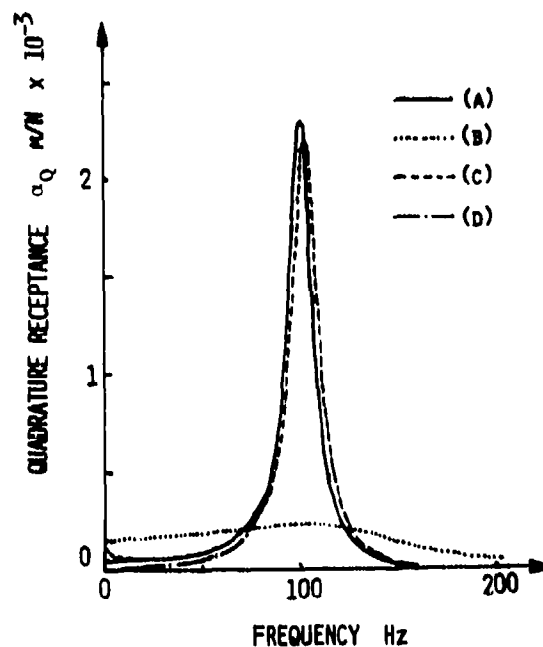


Figure 4. Single degree of freedom system: Graph of quadrature receptance α_Q versus frequency for cases (a) to (d) (see Table 2).

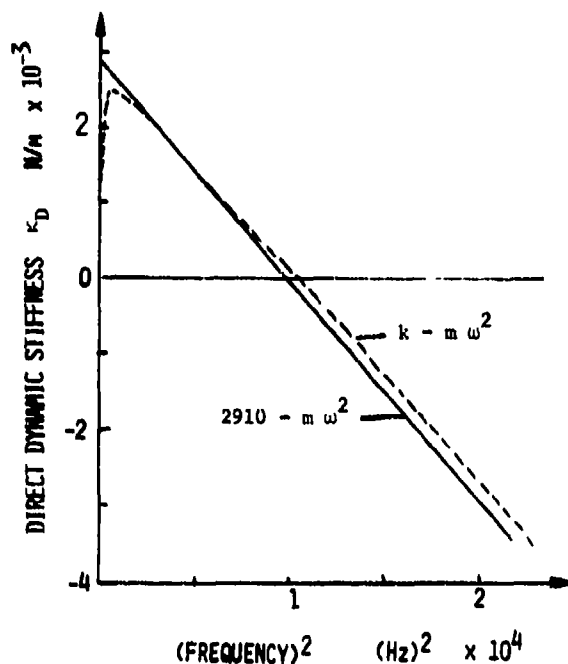


Figure 5. Single degree of freedom system: Graph of direct dynamic stiffness κ_D versus frequency squared for cases (a) to (d). (See Table 2).

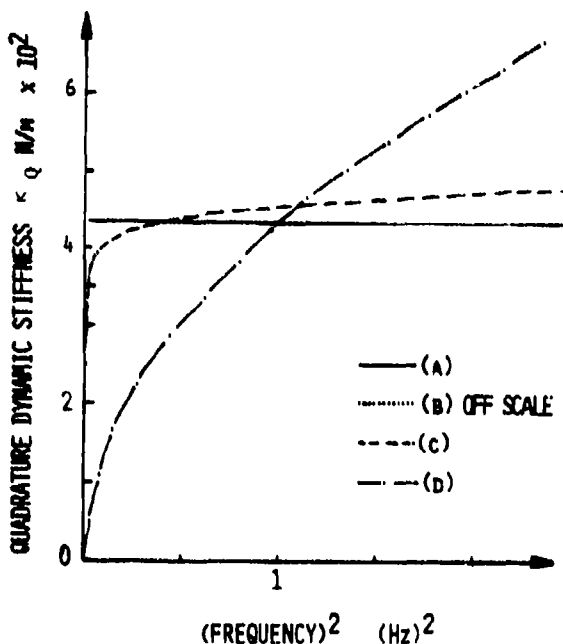


Figure 6. Single degree of freedom system: Graph of quadrature dynamic stiffness κ_Q versus frequency squared for cases (a) to (e). (See Table 2.)

bandwidth approach, and ω from the frequency at which $|\alpha_{ij}|$ is a maximum, one can estimate $m/\theta(x_i)\theta^2(x_j)$ and if i and j correspond to the antinodal point for the given mode, $\theta_n(x_i) = \theta_n(x_j) = 1$ ($i = j =$ antinodal point), then at that point m_n is determined, and from the transfer receptances relating response at this point to that at all others, $\theta_n(x_i)$ is determined, $\theta_n(x_j)$ remaining 1.0.

2.2. Time Domain Receptances

Figure 1(d) illustrates the time-domain receptance, which is the inverse Fourier transform of Figure 1(b), and corresponds to the unit impulse response of the system, for $S_i(t) = S_i\delta(t)$. The inverse Fourier transform of equation (1), for $\eta \ll 1$, gives to a sufficient degree of approximation:

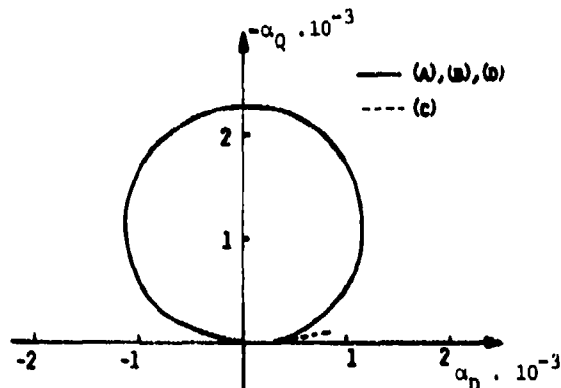


Figure 7. Single degree of freedom system: Graphs of α_Q versus α_D (Nyquist diagram) for cases (a) to (e). (See Table 2).

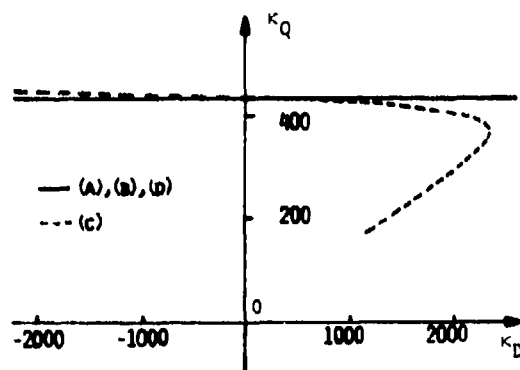


Figure 8. Single degree of freedom system: Graphs of κ_Q versus κ_D for cases (a) to (e). (see Table 2).

$$\alpha_{lj}(t) = \sum_{n=1}^N \left\{ \frac{\theta_n(x_l) \theta_n(x_j)}{m_n \omega_n} \right\} e^{-\eta_n \omega_n t/2} \sin(\omega_n t) \quad (3)$$

Again, by choosing $m_n, \omega_n, \eta_n, \theta_n(x_l)$ and $\theta_n(x_j)$, one can obtain a best fit of available data. We shall not pursue this particular approach further, since it has received considerable attention in the literature [16-18].

2.3. Dynamic Stiffness Concept

The dynamic stiffness of the system at the points l, j is obtained by inverting the equation (1):

$$\kappa_{lj} = (\alpha_{lj})^{-1} = \left[\sum_{n=1}^N \frac{\theta_n(x_l) \theta_n(x_j)}{m_n [\omega_n^2 (1 + i\eta_n) - \omega^2]} \right]^{-1} \quad (4)$$

Away from resonance, this expression is complicated, but near the n -th resonance ($n = 1, 2, 3, \dots, N$), only the n -th term of the series in equation (4) is important, so that:

$$\begin{aligned} \kappa_{lj}(\omega) &\approx m_n [\omega_n^2 (1 + i\eta_n) - \omega^2] / [\theta_n(x_l) \theta_n(x_j)] = \\ &= \kappa_{ljD} + i\kappa_{ljQ} \end{aligned} \quad (5)$$

where κ_{ljD} is the direct dynamic stiffness and κ_{ljQ} is the quadrature dynamic stiffness, and:

$$\kappa_{ljD} = m_n (\omega_n^2 - \omega^2) / [\theta_n(x_l) \theta_n(x_j)] \quad (6)$$

$$\kappa_{ljQ} = \eta_n m_n \omega^2 / [\theta_n(x_l) \theta_n(x_j)] \quad (7)$$

We see that $\kappa_{ljD} = 0$ when $\omega = \omega_n$ and that:

$$\partial \kappa_{ljD} / \partial \omega^2 = -m_n / [\theta_n(x_l) \theta_n(x_j)] \quad (8)$$

so that ω and m can be determined from the measurement of the behavior of the direct dynamic stiffness $\kappa_{ljD}(\omega)$ near the zero crossing point $\omega = \omega_n$.

Note that, in this analysis, we are looking at the matrix $[\kappa_{lj}]$ whose elements are $1/\alpha_{lj}$ i.e. $[\kappa_{lj}] = [1/\alpha_{lj}]$ and not the more general concept $[\kappa_{lj}] = [\alpha_{lj}]^{-1}$.

3. ANALYTICAL EVALUATIONS OF IDENTIFICATION TECHNIQUES

3.1 Single Degree of Freedom System

To illustrate the various approaches to modal identification, consider first an ideal single degree of freedom system, as illustrated in Figure 2.

Four cases are considered, corresponding to (a) a low damping hysteretic system, (b) a high damping hysteretic system, (c) a typical silicone isolator material having stiffness varying with frequency and (d) a classical viscously damped system. The case parameters k, m, η , and ω_1 (natural frequency) are summarized in Table 2, in the first row. The receptance $\alpha = W/S$ is given by:

$$\alpha = \alpha_D + i\alpha_Q = |\alpha| e^{-i\epsilon} = (k - m\omega^2 + i\kappa\eta)^{-1} \quad (9)$$

where $|\alpha|$ is the amplitude of the receptance, ϵ is the phase, α_D is the direct (in-phase) receptance and α_Q is the quadrature (90 degrees out of phase) receptance and:

$$\begin{aligned} |\alpha| &= 1 / \sqrt{(k - m\omega^2)^2 + (\kappa\eta)^2} \\ \epsilon &= \tan^{-1}[\kappa\eta / (k - m\omega^2)] \\ \alpha_D &= (k - m\omega^2) / [(k - m\omega^2)^2 + (\kappa\eta)^2] \\ \alpha_Q &= -\kappa\eta / [(k - m\omega^2)^2 + (\kappa\eta)^2] \end{aligned} \quad (10)$$

Figure 2 shows the variation of $|\alpha|$ and ϵ with frequency for a typical case, while Figures 3 and 4 show the variation of α_D and α_Q respectively with frequency. The impedance (dynamic stiffness) κ is given by:

$$\kappa = 1/\alpha = \kappa_D + i\kappa_Q = k - m\omega^2 + i\kappa\eta \quad (11)$$

where κ_D is the direct dynamic stiffness and

κ_Q is the quadrature dynamic stiffness and:

$$\begin{aligned} \kappa_D &= k - m\omega^2 \\ \kappa_Q &= \kappa\eta \end{aligned} \quad (12)$$

Figures 5 and 6 illustrate the variation of κ_D and κ_Q respectively, with frequency squared, and Figures 7 and 8 show the variation of α_Q with α_D and κ_Q with κ_D , respectively. The graph of α_Q versus α_D is the well known Nyquist diagram, and can be used to measure the damping. The graph of κ_Q versus κ_D seems to have no special use.

3.1.1. Identification from Receptance

Now that the analytically derived receptances have been plotted for each case, the next step is to reverse the process and observe how faithfully the initial values of m, k , and η are recovered. For cases (a), (c) and (d), it is easiest to measure η using the customary half power bandwidth method:

$$\eta = \frac{\Delta\omega}{\omega_1} \quad (13)$$

where $\Delta\omega$ is the separation of the two frequencies for which the amplitude $|a|$ is $1/\sqrt{2}$ times the peak amplitude. For case (d), it is not possible to determine η in this way, but one can use the quadrature receptance α_Q instead, through the relationship:

$$\Delta\omega_Q/\omega_1 = \sqrt{1 + 0.6436\eta} - \sqrt{1 - 0.6436\eta} \quad (14)$$

where $\Delta\omega_Q$ is the separation of the two

frequencies where α_Q is $1/\sqrt{2}$ times the peak value of α_Q . (See Appendix 1 for details.) Table 2 shows the values of η obtained in this way for each case. To estimate k and/or m , one may examine the value of $|a|$ at $\omega = \omega_1$, and note from equation (1) that:

$$|a|_{\omega=\omega_1} = 1/k\eta. \quad (15)$$

For cases (a) through (d), we can read off the value of $|a|$ at $\omega = \omega_1$ and hence, with η already determined, find k . m is then found from the relationship $k = m\omega_1^2$. The results are again summarized in Table 2, second row. Note that, for case (b), the high loss factor hysteretic case, considerable error occurs in the estimate of η and this is reflected as a comparable error in k and m . Note also that for case (c), we have determined k only at $\omega = \omega_1$, and have no clear indication of its value at other frequencies. Also, for case (d), η has been determined only at $\omega = \omega_1$ and again no clear indication is given that η is actually proportional to ω for this case.

TABLE 3
Results of Four Degree of Freedom
System Identification (Analytical)

QUANTITY	n	GIVEN VALUES	METHOD			
			RECEPTANCE		DYN. STIFFNESS	
			α_{2j}	α_{3j}	α_{2j}	α_{3j}
m_n	1	0.0574	0.0567	-	0.0403	-
	2	0.0487	0.0457	-	0.0460	-
	3	0.0443	0.0441	-	0.0437	-
	4	0.0339	0.0393	-	-	-
η_n	1	0.01	0.01	-	0.0098	-
	2	0.01	0.01	-	0.0092	-
	3	0.01	0.01	-	0.0099	-
	4	0.01	0.01	-	-	-
ω_n Hz	1	122	122	-	122.5	-
	2	423	423	-	423.1	-
	3	453	453	-	452.8	-
	4	933	933	-	-	-
$\phi_n(x_2)$	1	+0.06	+0.088	+0.0608	+0.0613	+0.061
	2	-0.18	-0.132	-0.156	-0.151	-0.169
	3	-0.30	-0.293	-0.299	-0.287	-0.305
	4	+0.40	+0.378	+0.385	-	-

3.1.2. Identification from Dynamic Stiffness

From the graph of k_D versus frequency squared, in Figure 5, it is seen that k is given by the intercept on the k_D axis and m is given by the slope near $\omega = \omega_1$. The value of η is given by the value of k_Q/k at all frequencies, as in Figure 6. If k varies with frequency, one can estimate its value at any frequency from the relationship $k = k_D + m\omega^2$, provided that the estimate of m is accurate. The values of k and m determined in this way are summarized for cases (a), (b) and (d) in Table 2, row 3, since k and m are constant. Similarly, the values of η for cases (a) and (b), determined from $\eta = k_Q/k$, are summarized. For case (c), η is still equal to k_Q/k , but it is clearly seen to vary with frequency. Actually, a plot of k_Q versus frequency, instead of frequency squared, would be more useful for this particular case since it would graphically illustrate the fact that η is proportional to frequency. Nevertheless, it is easily shown that $\eta = 2.39 \times 10^{-4} \omega$, a fact which is very difficult to derive from the receptance plots. Table 2 shows that, for cases (a), (c) and (d), the dynamic stiffness and receptance approaches give comparable accuracy in recovering the initial data, apart from the frequency dependence of k in case (c) and of η in case (d). In case (b), meaningful data is obtainable only through the dynamic stiffness approach.

3.2. Multiple Degree of Freedom System

Consider a four degree of freedom system, having two well separated modes and two closely spaced modes, typical of many practical systems, such as a turbine blade, and having the modal parameters summarized in Table 3, the first column, in accordance with equation (1). Again, the purpose of this example is to illustrate how well, or how badly, one can recover the original parameters from the calculated values of α_{2j} or α_{3j} .

3.2.1. Identification from Receptances

Figure 9 gives the plot of $|\alpha_{2j}|$ versus frequency obtained by substituting the above parameters in equation (1), and figures 10 and 11 show the variation α_{2jD} and α_{2jQ} with frequency squared.

In this example, the modes are not so closely spaced that damping cannot be measured by the half power bandwidth method. For each peak in Figure 9, η bandwidth η_n ($\pm 5\%$), even for the closely spaced modes, as the expanded insert in Figure 9 shows; the values of η_n so determined

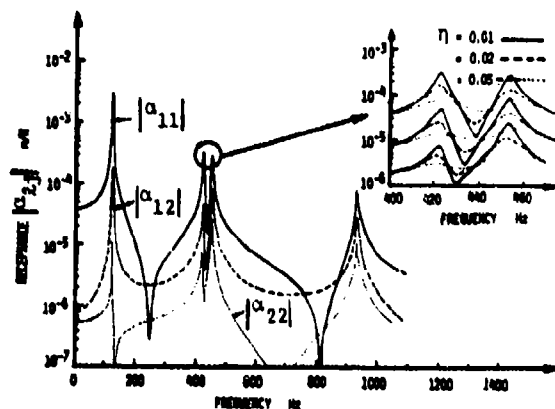


Figure 9. Multiple degree of freedom system with hysteretic damping: Graphs of receptance $|\alpha_{jj}|$ versus frequency (See Table 3).

are summarized in Table 3, column 2. Now at each resonance peak, equation (1) gives:

$$|\alpha_{jj}|_{\max} = \beta_n(x_j) \beta_n(x_j) / m_n \omega_n^2 \eta_n \quad (16)$$

so that, for the point receptance where $j = j$, and $\beta_n(x_j) = \beta_n(x_j) = 1$:

$$m_n = \omega_n^2 \eta_n |\alpha_{jj}|_{\max} \quad (17)$$

The four values of m_n ($n = 1, 2, 3, 4$), obtained using equation (16) and the peak values of $|\alpha_{jj}|$ from Figure 9, are given in Table 3, column 2. The greatest discrepancy between these values and the given initial values is 1.5% for m_4 .

The modal functions $\beta_n(x_j)$, with $\beta_n(x_j) = 1$, are obtainable from equation (10), for $j = j$:

$$\beta_n(x_j) = \pm |\alpha_{jj}|_{\max} m_n \omega_n^2 \eta_n \quad (18)$$

with the signs chosen to correspond to the phase of α_{jj} : "plus" for angles near zero and "minus" for angles near 180° . Since m_n and η_n have been determined, $\beta_n(x_j)$ is determined. Table 3, column 2, summarizes the results. It is seen that the largest error is 5.7% for mode 4. While the error could doubtless be reduced by more careful plotting, in practice one does not have comparisons with an ideal case to make, so this gives us some indication of the errors which may be expected in practical cases.

Another, independent, estimate of $\beta_n(x_j)$ may be obtained from $|\alpha_{jj}|$, and it is useful to compare the results obtained in this way with those given above. From equation (15):

$$\beta_n(x_j) = \pm \sqrt{m_n \omega_n^2 \eta_n |\alpha_{jj}|_{\max}} \quad (19)$$

with the signs again corresponding to the phases of α_{jj} . The values of $\beta_n(x_j)$ determined in this way are summarized in Table 3, column 3, and are seen to agree quite well with the initial values. On the whole, it is clear that all the parameters have been recovered with quite modest errors and without very great effort. This reflects the general success with which present day software can identify these parameters by curve-fitting procedures.

Returning to Figure 9, for modes 2 and 3, we see that it becomes difficult to obtain an accurate estimate of η_1 and η_3 separately, by the bandwidth method, when $\eta > 0.05$. This is because the modal separation ratio defined here as $(\omega_3 - \omega_2)/\omega$, with $\omega = (\omega_3 + \omega_2)/2$, is equal to 0.07 and when η approaches this value, separate estimation of the modal

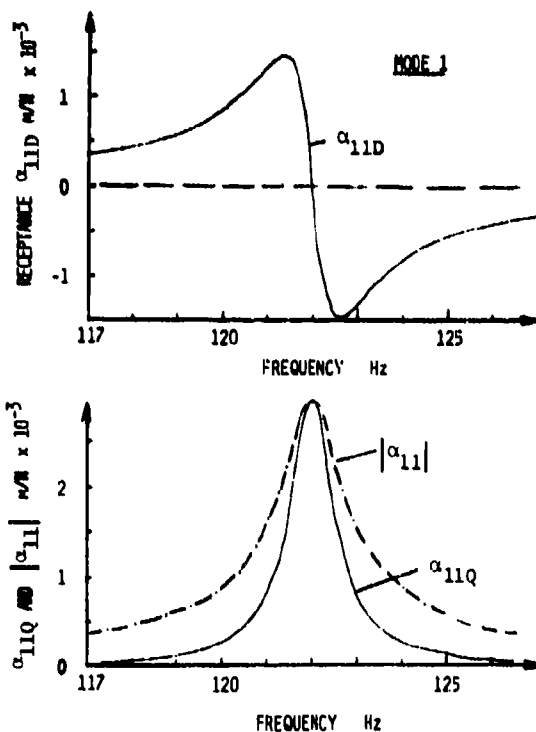


Figure 10. Multiple degree of freedom system with hysteretic damping: Graphs of direct receptance (α_{11D}), quadrature receptance (α_{11Q}) and receptance amplitude $|\alpha_{11}|$ versus frequency (mode 1). (See Table 3).

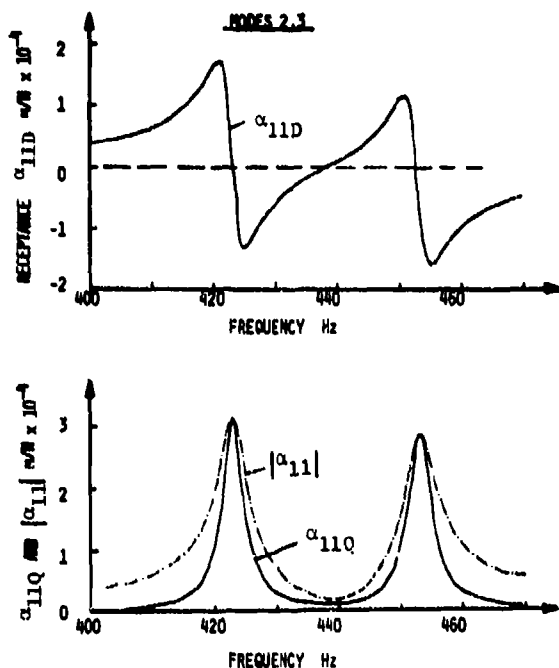


Figure 11. Multiple degree of freedom system with hysteretic damping. Graphs of direct receptances (α_{11D}), quadrature receptance (α_{11Q}) and receptance amplitude $|\alpha_{11}|$ versus frequency (modes 2 and 3), (See Table 3).

parameters becomes impossible and simultaneous solutions for the two modes must be obtained by an iterative method. This has not been attempted here. Figures 10 and 11 illustrate the variation of α_{11D} , α_{11Q} and $|\alpha_{11}|$ with

frequency for modes 1, 2, and 3. In this particular example, no information can be obtained from these plots that has not already been obtained from Figure 9.

3.2.2. Identification from Dynamic Stiffness

Figure 12 shows the variation of κ_{2jD} and κ_{2jQ} ($j = 1, 2$) with ω^2 , for mode 1,

for $\eta_1 = 0.01$ and 0.05, Figure 13 shows the variation of these quantities with ω^2 for modes 2 and 3, for $\eta = 0.01$, and Figure 14 shows the corresponding plots for $\eta = 0.02$. These plots were derived using equation (3) with the parameters defined in Table 3, column 1.

The intercepts of the graphs of κ_{2jD} versus frequency squared with the frequency squared axis give the values of ω_n ($n = 1, 2, 3, 4$). The slopes of the graphs of κ_{11D} versus frequency

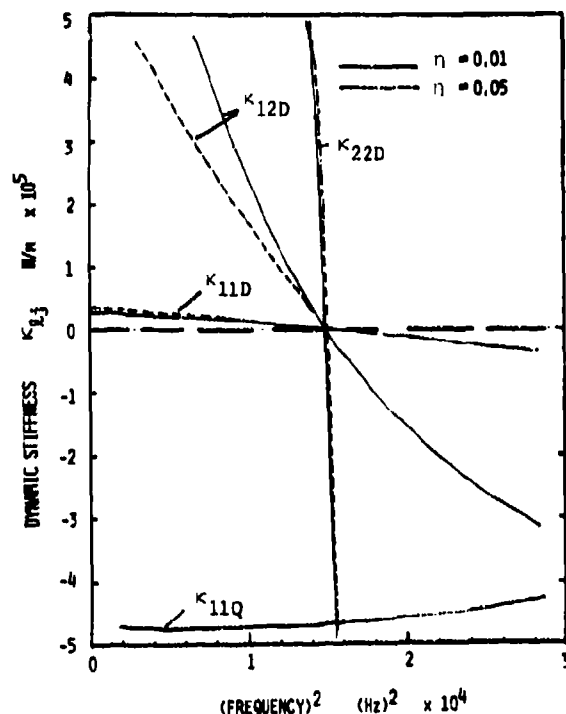


Figure 12. Multiple degree of freedom system for two cases of hysteretic damping: Graphs of direct dynamic stiffness (κ_{2jD}) and quadrature dynamic stiffness (κ_{2jQ}) versus frequency squared (Mode 1; $\eta = 0.01$ and 0.05) (See Table 3).

squared near each crossing point ω_n give the values of m_n directly. Then k_{11D} is determined from the relationship $k_{11D} = m_n \omega_n^2$. The values of m_n and ω_n so determined are summarized in Table 3, column 4. The maximum error in determining m_n is 3.8 percent for m_2 . The modal loss factors are determined from:

$$\eta_n = \kappa_{11Q} / k_{11D} = \kappa_{11Q} / m_n \omega_n^2 \quad (20)$$

for each mode, and are again summarized in Table 3, column 4. The maximum error in determining the loss factors is 8.6 percent for η_2 . This is partly due to the close proximity of modes 2 and 3.

So far, to determine m_n and η_n , we have concentrated on κ_{11D} and κ_{11Q} , since $\theta(x_1) = 1$ at this point. To determine the modal values $\theta(x_2)$, we can use the previously determined values of ω_n and m_n , along with the slopes of κ_{12D} versus frequency squared at ω_n , according to equation (7):

$$\beta_n(x_2) = -m_n / (\partial \kappa_{12D} / \partial \omega^2) \quad (21)$$

The values of $\beta_n(x_2)$ so obtained are summarized in Table 3, column 4. The maximum error is 4.4 percent for $\beta_2(x_2)$. Similarly, from the plots of κ_{22D} versus frequency squared, we can obtain an estimate of $\beta_n(x_2)$ since:

$$|\beta_n(x_2)|^2 = -m_n / (\partial \kappa_{22D} / \partial \omega^2) \quad (22)$$

The values of $\beta_n(x_2)$ so determined, apart from

signs, are summarized in Table 3, column 5. The maximum error is 12.5% for $\beta_2(x_2)$, and is rather high because of the anomalous behavior of κ_{22D} near $\omega = \omega_2$. Figure 14 illustrates this problem even more dramatically, since the curve of κ_{22D} versus frequency squared does not even intercept the frequency squared axis at all, making it impossible to estimate $\beta_2(x_2)$ from κ_{22D} . In summary, the receptance and dynamic stiffness approaches both gave good recovery of the initial data, but neither method gave a simple means of overcoming effects of closely spaced modes. Iterative methods remain necessary for either approach.

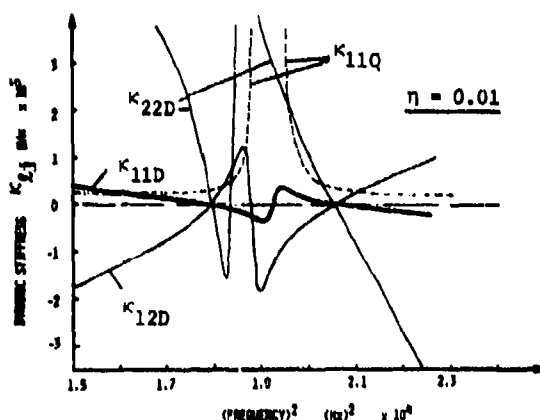


Figure 13. Multiple degree of freedom system with hysteretic damping. Graphs of direct dynamic stiffness (κ_{2jD}) versus frequency squared (Modes 2, 3; $\eta = 0.01$) (See Table 3).

4. IDENTIFICATION OF MODAL PARAMETERS FROM EXPERIMENTAL DATA

In order to compare the effectiveness of the various modal identification techniques, a number of tests were conducted on various structural systems, including a single degree of freedom system with variable stiffness and loss factor, a two degree of freedom system, and a turbine blade having several degrees of freedom.

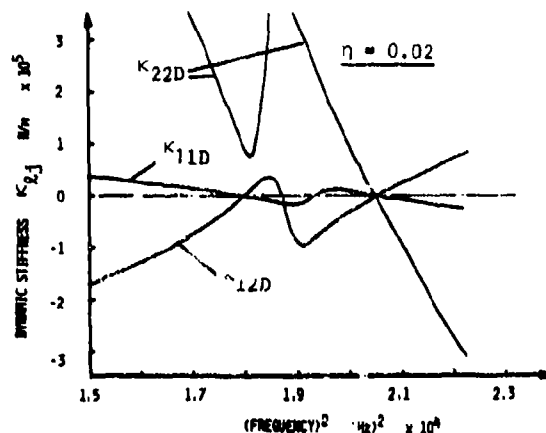


Figure 14. Multiple degree of freedom system: Graphs of direct dynamic stiffness (κ_{2jD}) versus frequency squared (Modes 2, 3; $\eta = 0.02$) (See Table 3).

4.1 Single Degree of Freedom System

The system considered is illustrated in Figure 15. It consists of a mass m (5.355 kg) attached to a large block of polymeric damping material [21] having the dimensions indicated. The specimen was impacted by a force gage - hammer system, and the response of the mass m was measured by an accelerometer. The time domain measurements were converted to frequency domain by state of the art Fast Fourier Transform (FFT) software. Table 4 gives some of the measured data and Figure 15 gives a plot of the measured receptance as a function of frequency.

TABLE 4

MEASURED DATA FOR SINGLE DEGREE OF FREEDOM SYSTEM

Freq. Hz	MEASURED RECEPTANCE		CALCULATED DYNAMIC STIFFNESS	
	$ A \text{ in/lbf}$	Phase α°	$\kappa_D^* \text{ Cons. } \eta \text{ in/m}$	$\kappa_D^* \text{ Single } \eta \text{ in/m}$
66	3.8 E -5	33	+ 4.21 E6	+ 2.74 E6
75	3.5 E -5	45	+ 3.59 E6	+ 2.74 E6
100	3.3 E -5	52	+ 3.28 E6	+ 4.20 E6
125	3.4 E -5	61	+ 2.51 E6	+ 4.51 E6
150	3.6 E -5	73	+ 1.43 E6	+ 4.67 E6
175	3.6 E -5	91	- 8.52 E4	+ 4.88 E6
200	3.3 E -5	112	- 2.00 E6	+ 4.93 E6
225	2.7 E -5	138	- 4.03 E6	+ 5.13 E6
250	2.1 E -5	143	- 6.67 E6	+ 5.04 E6
275	1.6 E -5	151	- 9.61 E6	+ 5.32 E6
300	1.3 E -5	157	- 1.24 E7	+ 5.27 E6
350	8.5 E -6	164	- 1.98 E7	+ 5.69 E6
400	6.1 E -6	171	- 2.84 E7	+ 4.50 E6
500	3.2 E -6	177	- 5.48 E7	-
600	2.1 E -6	169	- 8.20 E7	+ 1.63 E7
700	1.7 E -6	169	- 1.01 E8	+ 1.97 E7
800	1.3 E -6	174	- 1.34 E8	+ 1.41 E7

It is seen that the damping is so high that it would be very difficult to obtain estimates of stiffness and loss factor from a study of the receptance. Figure 16 illustrates the plots of the measured values of the direct dynamic stiffness κ_D and the quadrature dynamic stiffness κ_Q versus frequency squared. Also shown is a plot of the derived specimen stiffness k , given by:

$$k = \kappa_D + m\omega^2 \quad (23)$$

It is seen that k is a function of frequency. The loss factor η can be calculated at each frequency since:

$$\eta = \kappa_Q/k \quad (24)$$

The values of the Young's Modulus E of the specimen material are derived from k and the specimen dimensions:

$$k = E A/h \quad (25)$$

The specimen was long enough relative to its thickness dimensions for shape effects to be unimportant. E and η are plotted against frequency in Figure 17, and compared with data from other sources [22, 23]. Note that errors become excessive above about 300 Hz, as a result of excessively large inertia loads $m\omega^2$. This comparative data is plotted in Figure 18 as a function of reduced frequency and temperature. The reduced temperature nomogram, [23], in Figure 18, gives us an easy way to use graphical means of reading off E and η for any polymeric material for any chosen values of frequency and temperature. For example, to read E and η at 100 Hz and 100°F, we follow the 100 Hz frequency line from the left hand scale until it crosses the 100°F line from the

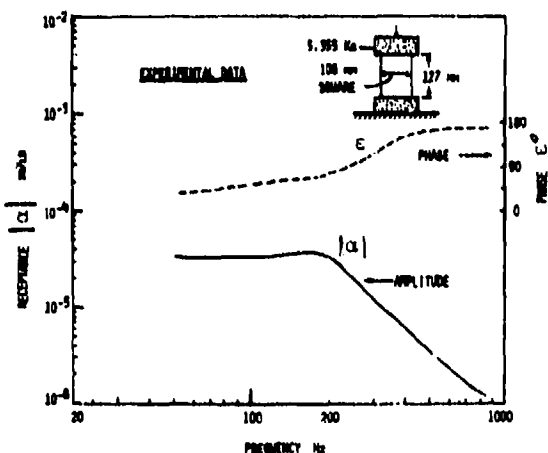


Figure 15. Single degree of freedom test: Graphs of receptance amplitude $|\alpha|$ and phase ϵ versus frequency (See Table 4).

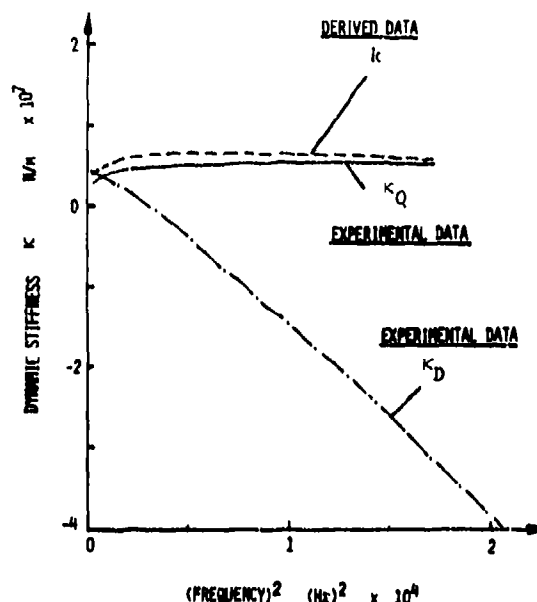


Figure 16. Single degree of freedom test: Graphs of direct dynamic stiffness (κ_D), quadrature dynamic stiffness (κ_Q) and specimen stiffness k versus frequency squared (See Table 4).

top scale. The point of intersection of the horizontal frequency line and the sloping temperature line gives the appropriate value of α_T , the reduced frequency, and one then simply reads vertically from this point to get E and η .

4.2. Two Degree of Freedom System

4.2.1. Identification from Receptances

The test system is illustrated in Figure 19, and was essentially the same as the one degree of freedom system except that the second mass m was now free. One mass was impacted axially, as before, and the acceleration of each mass was measured by an accelerometer, in the same manner as before. Figure 19 shows plots of the point and transfer receptances $|\alpha_{11}|$ and $|\alpha_{21}|$ as a function of frequency. Typical measured values are summarized in Table 5. Little if anything can be determined from the acceleration or receptance plots, because of the very high damping.

4.2.2. Identification From Dynamic Stiffnesses

From the measured values of $|\alpha_{11}|$ and phase ϵ_{11} at each frequency, the dynamic stiffnesses are calculated from the relationships:

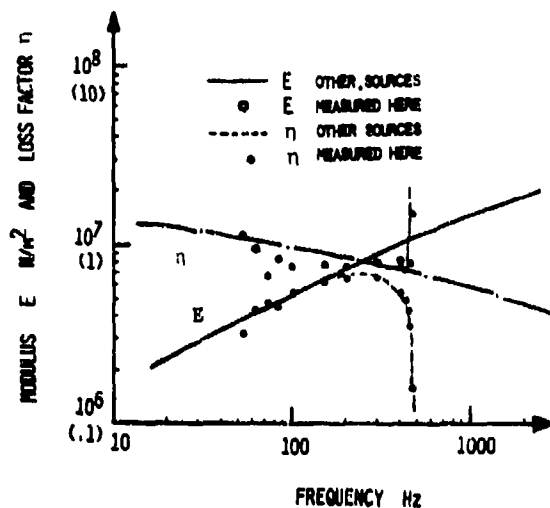


Figure 17. Graphs of Young's Modulus E and loss factor η versus frequency derived from test data for single degree of freedom system with high damping (See Table 4).

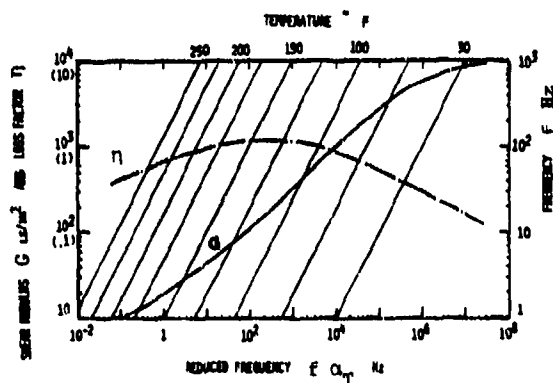


Figure 18. Complex modulus properties of 3M-ISO-110 damping material as a function of frequency and temperature (Nomogram) [23].

$$\kappa_{ejD} = \cos \epsilon_{ej} / |\alpha_{ej}| \quad (26)$$

$$\kappa_{ejQ} = \sin \epsilon_{ej} / |\alpha_{ej}| \quad (27)$$

These are summarized in Table 5. Figure 20 shows the plots of κ_{11} and κ_{12} , direct and quadrature, versus frequency squared. The

data is of no immediate value, since the relationships between the measured data and the mass, stiffness and damping parameters are not yet established. If the system in Figure 19 is analyzed to predict the response to a harmonic excitation $S e^{i\omega t}$ at a point 1, then the receptances are given by:

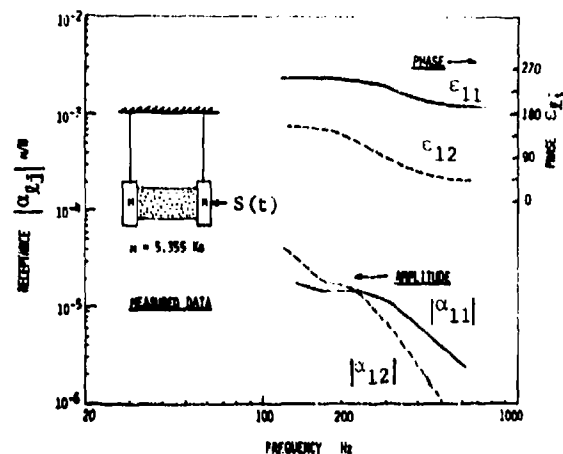


Figure 19. Two degree of freedom damped system test: Graphs of receptance amplitude $|\alpha_{ej}|$ and phase angles (ϵ_{ej}) versus frequency (See Table 5).

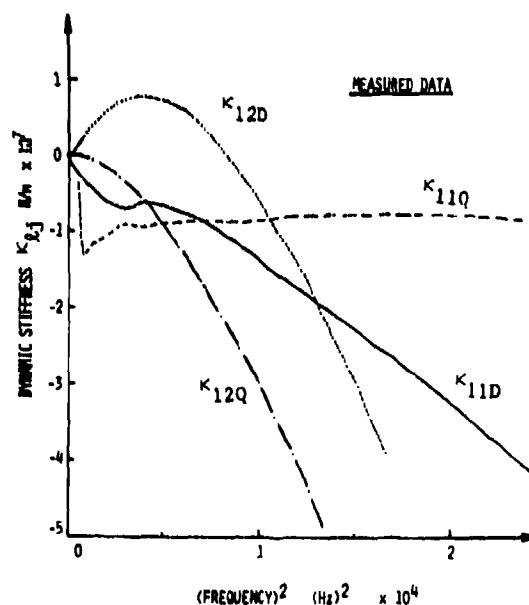


Figure 20. Two degree of freedom test: Graphs of dynamic stiffnesses (κ_{ejD} and κ_{ejQ}) versus frequency squared. (See Table 5).

$$\alpha_{11} = \frac{k(1 + i\eta) - m\omega^2}{m^2\omega^4 - 2m\omega^2 k(1 + i\eta)} \quad (28)$$

$$\alpha_{12} = \frac{k(1 + i\eta)}{m^2\omega^4 - 2m\omega^2 k(1 + i\eta)} \quad (29)$$

These relationships give no direct way of calculating k , m and η from α_{ej} or κ_{ej} , and the equations must first be put in modal form.

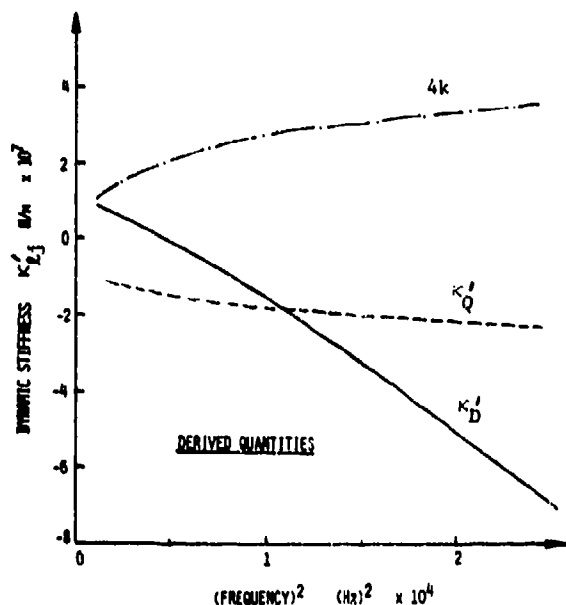


Figure 21. Two degree of freedom test: Graphs of corrected dynamic stiffnesses (κ'_{2jD} and κ'_{2jQ}) versus frequency squared. (See Table 5).

This matter is discussed in Appendix 2, and leads to the following more useful relationships:

$$\begin{aligned}\kappa'_{11} &= 1/(\alpha_{11} + 1/2m\omega^2) \\ &= 4k(1 + i\eta) - 2m\omega^2\end{aligned}\quad (30)$$

$$\begin{aligned}\kappa'_{12} &= 1/(\alpha_{12} + 1/2m\omega^2) \\ &= -4k(1 + i\eta) + 2m\omega^2\end{aligned}\quad (31)$$

These redefined dynamic stiffnesses are presented in Table 5 and plotted versus frequency squared in Figure 21. The slope of the graph of $\kappa'_{11D} = -\kappa'_{12D}$ for large values of frequency squared is equal to $-2m$; the quadrature component $\kappa'_{11Q} = -\kappa'_{12Q}$ is equal to $4k\eta$ and the stiffness K is derived from the relationships

$$4k = \kappa'_{11D} + 2m\omega^2 \quad (32)$$

$$\text{or } 4k = -\kappa'_{12D} + 2m\omega^2$$

The calculated values of $4k$ are plotted in Figure 21, and compare well with the values of k obtained from the same system in a one degree of freedom configuration. It is seen that, for this type of highly damped system, only the dynamic stiffness approach can give meaningful results in a reasonably simple manner.

TABLE 5

MEASURED DATA FOR TWO DEGREE OF FREEDOM SYSTEM

TYPE	Freq. Hz	MEASURED DATA			CALCULATED QUANTITIES						
		$ \alpha_{2j} $ Lbf/in	Phase ϕ_{2j}	α'_{2jD} m/N	α'_{2jQ} m/N	$1/2m\omega^2$ m/N	$\alpha'_{2jD} = \alpha_{2jD} + 1/2m\omega^2$ m/N	$\kappa'_{2jD} = \frac{\alpha'_{2jD}}{K_{2j}}$ N/m	$\kappa'_{2jQ} = \frac{\alpha'_{2jQ}}{K_{2j}}$ N/m	κ'_{2jD} N/m	κ'_{2jQ} N/m
α_{11}	152	1.71 E -5	233	-5.86 E-8	-7.78 E-8	1.02 E-7	+ 4.34 E -8	- 6.18 E6	- 8.2 E6	+ 5.47 E6	- 9.80 E6
	176	1.50 E -5	236	-4.78 E-8	-7.08 E-8	7.63 E-8	+ 2.85 E -8	- 6.55 E6	- 9.71 E6	+ 4.89 E6	- 1.22 E7
	200	1.53 E -5	237	-4.75 E-8	-7.31 E-8	5.91 E-8	+ 1.16 E -8	- 6.25 E6	- 9.63 E6	+ 2.12 E6	- 1.33 E7
	252	1.42 E -5	227	-6.52 E-8	-5.91 E-8	3.72 E-8	- 1.80 E -8	- 8.43 E6	- 9.04 E6	- 4.72 E6	- 1.55 E7
	300	1.18 E -5	218	-6.30 E-8	-4.14 E-8	2.63 E-8	- 2.67 E -8	- 1.17 E7	- 9.16 E6	- 1.10 E7	- 1.71 E7
	352	8.88 E -6	203	-4.65 E-8	-1.98 E-8	2.74 E-8	- 2.74 E -8	- 1.82 E7	- 7.73 E6	- 2.40 E7	- 1.73 E7
	400	6.64 E -6	197	-3.62 E-8	-1.11 E-8	1.48 E-8	- 2.14 E -8	- 2.53 E7	- 7.76 E6	- 3.68 E7	- 1.91 E7
	452	4.90 E -6	194	-2.71 E-8	-6.75 E-9	1.16 E-8	- 1.55 E -8	- 3.48 E7	- 8.67 E6	- 5.42 E7	- 2.36 E7
	500	3.96 E -6	192	-2.21 E-8	-4.69 E-9	1.26 E-8	- 1.26 E -8	- 4.34 E7	- 9.22 E6	- 6.97 E7	- 2.59 E7
α_{12}	152	2.56 E -5	155	+ 1.32 E-7	+6.16 E-8	1.02 E-7	+ 3.00 E -8	- 6.22 E6	+ 4.95 E6	- 6.39 E6	+ 1.31 E7
	176	1.88 E -5	148	-9.08 E-8	+5.67 E-8	7.63 E-8	+ 1.45 E -8	- 7.92 E6	+ 4.95 E6	- 4.23 E6	+ 1.66 E7
	200	1.77 E -5	137	-7.37 E-8	+6.87 E-8	5.91 E-8	+ 1.46 E -8	- 7.26 E6	+ 6.77 E6	- 2.96 E6	+ 1.39 E7
	252	1.12 E -5	109	-2.09 E-8	+6.03 E-8	3.72 E-8	+ 1.64 E -8	- 5.10 E6	+ 1.48 E7	+ 4.20 E6	+ 1.34 E7
	300	6.72 E -6	82	+5.71 E-10	+3.79 E-8	2.63 E-8	+ 2.69 E -8	+ 3.64 E6	+ 2.59 E7	+ 1.25 E7	+ 1.75 E7
	352	4.06 E -6	69	+6.29 E-9	+2.16 E-8	1.91 E-8	+ 2.74 E -8	+ 1.55 E7	+ 4.04 E7	+ 2.25 E7	+ 1.77 E7
	400	2.38 E -6	64	+5.94 E-9	+1.22 E-8	1.48 E-8	+ 2.07 E -8	+ 3.23 E7	+ 6.63 E7	+ 3.59 E7	+ 2.11 E7
	452	1.42 E -6	46	+5.62 E-9	+5.82 E-9	1.16 E-8	+ 1.72 E -8	+ 8.59 E7	+ 8.90 E7	+ 5.22 E7	+ 1.77 E7
	500	1.04 E -6	45	+4.19 E-9	+4.19 E-9	9.46 E-9	+ 1.37 E -8	+ 1.19 E8	+ 1.19 E8	+ 6.67 E7	+ 2.04 E7

4.3. Multiple Degree of Freedom System (Turbine Blade)

The blade, of typically modern construction, was supported in a broach block at the dovetail, as illustrated in Figure 22, and was excited by impact of a small hammer/force-gage combination. The response was measured by a small accelerometer at several points on the blade. Two of the points of most interest are the tip trailing edge (point 1) and the platform, at point 2. Measured accelerance (α acceleration/force) plots are shown in Figure 23 [24]. Some of the test data is summarized in Tables 6, 7 and 8, in terms of the numerical values of the receptance amplitude $|\alpha_{ij}|$ and the phases ϵ_{ij} for several frequencies, as obtained by means of Fast Fourier Transform data processing. The accelerances are seen to have four major resonances in the frequency range of interest. The receptances are plotted versus frequency in Figure 24, and Figure 25 shows the receptance amplitudes in the close vicinity of each resonance.

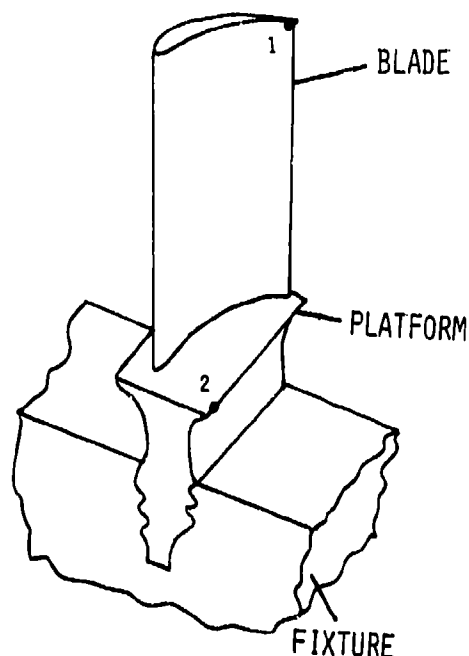


Figure 22. Sketch of turbine blade.

4.3.1. Identification from Receptances

On the expanded scale of Figure 25, it was possible to estimate η_n for each mode, using the values of $|\alpha_{11}|$, $|\alpha_{12}|$ and $|\alpha_{22}|$ in conjunction with the half-power bandwidth method. Table 9, column 1, gives the averaged data. It is seen that the damping levels are very low. The resonant frequencies, estimated from the frequencies nearest to the peak values of $|\alpha_{2j}|$ are also summarized.

From equation (17), one can estimate m_n , given that $\beta_n(x_1) = 1.0$, which was established from the modal survey, not reported here. With ω_n and η_n and $|\alpha_{11}|_{\max}$ known, m_n is readily calculated and the results are summarized in Table 9, column 1. From equation (18), the values of $\beta_n(x_2)$ can be estimated from $|\alpha_{12}|_{\max}$ now that m_n , ω_n and η_n are known. The results are summarized in Table 9, column 1. Finally, from equation (19), an estimate of $\beta_n(x_2)$ can be obtained using $|\alpha_{22}|_{\max}$. The results are summarized in Table 9, column 2.

4.3.2. Identification from Dynamic Stiffnesses

Table 6 gives a tabulation of the direct and quadrature dynamic stiffnesses. k_{110} and k_{110} , in accordance with equations (26) and (27). The phase angles ϵ_{ij} are so close to 0 or 180 degrees most of the time that errors in calculating k_{210} are excessive and no estimate of damping was possible. The bandwidth measurements, obtained earlier, had to be used. However, the modal masses and

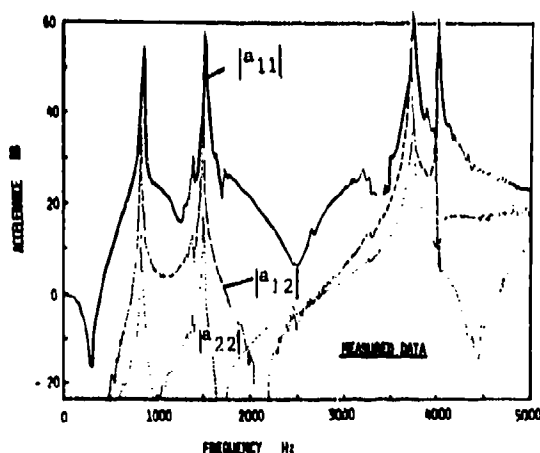


Figure 23. Measured accelerances $|\alpha_{2j}|$ versus frequency for blade.

stiffnesses could be obtained without using these values of η_n , by equation (7), so this is a considerable advantage. Figures 26, 27, and 28 illustrate the plots of k_{110} , k_{120} and k_{220} versus frequency squared for the first two modes. The resonant frequencies were determined from the intersection of the plot of k_{210} with the frequency squared axis, and are summarized in Table 9, column 3. From the plots of k_{110} versus frequency squared, m_n is determined, using equation (7), and recognizing again that $\beta_n(x_1) = 1$. The

results are summarized in Table 9, column 3. From the plots of κ_{12D} versus frequency squared, with m_0 determined, the values of $\theta(x_2)$ are obtained using equation (8), with $\theta^n(x_1) = 1$, and the results are summarized in Table 9, column 3. Finally, from the plots of κ_{22D} versus frequency squared, and equation 8, estimates of $|\theta(x_2)|$ are obtained, and the results are summarized in Table 9, column 4.

The overall average values of the various identified parameters are summarized in Table 9, column 5. It is seen that the maximum variation in the values obtained by the various methods are: 0 percent in m_1 , 8.6% in m_2 , 10.7% in $\theta_1(x_2)$ and 6.8% in $\theta_2(x_2)$.

A graph of $|\alpha_{21}|$ is plotted against frequency in Figure 29, on the basis of equation (1) and the identified parameters from Table 9, column 5. In view of the fact that no effort was made to seek a minimum error identification,

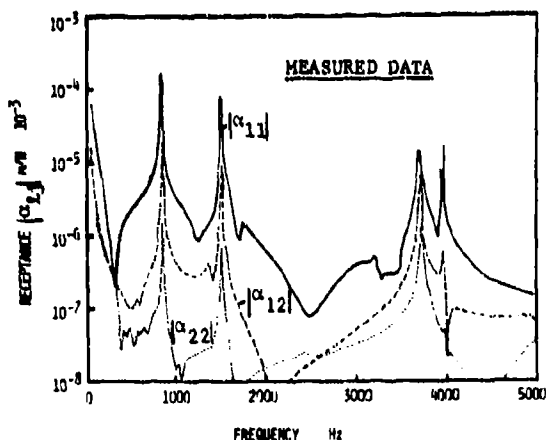


Figure 24. Measured receptances $|\alpha_{21}|$ versus frequency for blade (See Table 6 to 8).

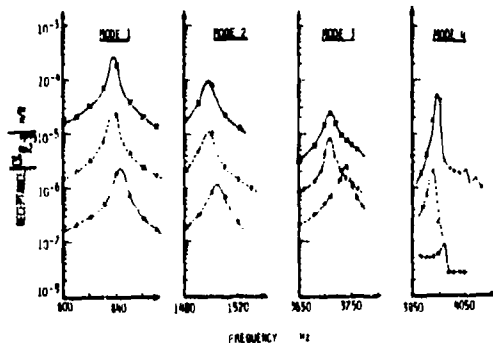


Figure 25. Measured receptances $|\alpha_{21}|$ versus frequency for blade, near each resonance (See Table 6 to 8).

using statistical techniques or otherwise, or to allow for effects of high or low frequency residuals from modes not allowed for, the agreement with the original data in Figure 21 is very satisfactory.

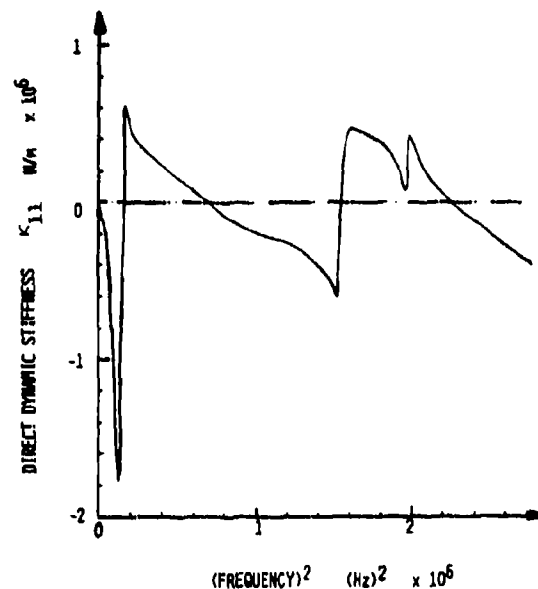


Figure 26. Graph of direct dynamic stiffness (κ_{11D}) versus frequency squared for blade (See Table 6).

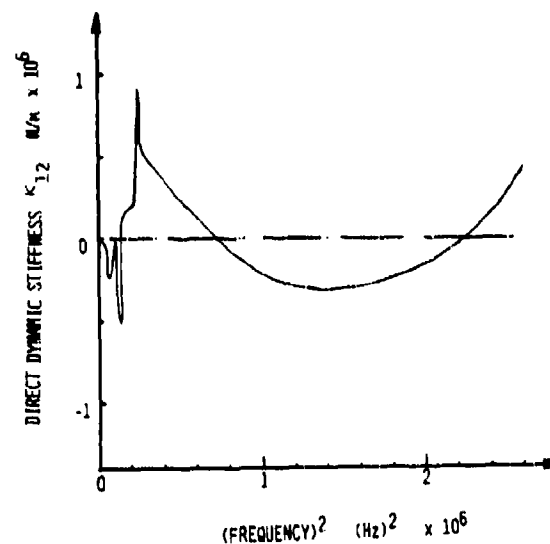


Figure 27. Graph of direct dynamic stiffness (κ_{12D}) versus frequency squared for blade (See Table 7).

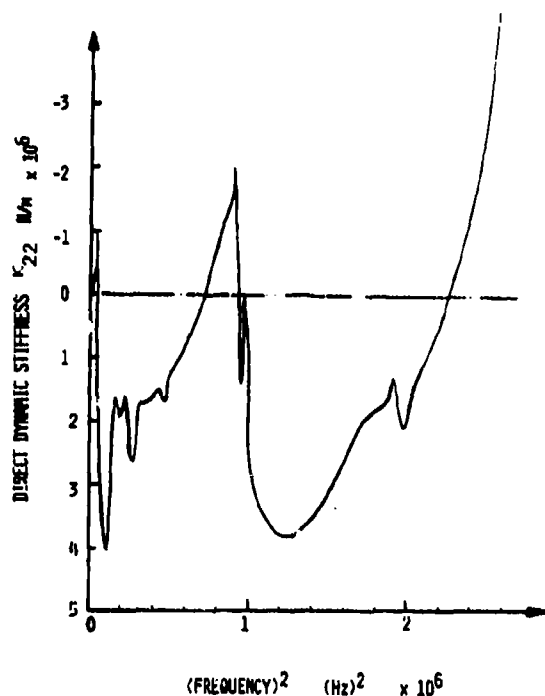


Figure 28. Graph of direct dynamic stiffness (K_{22}) versus frequency squared for blade (See Table 8).

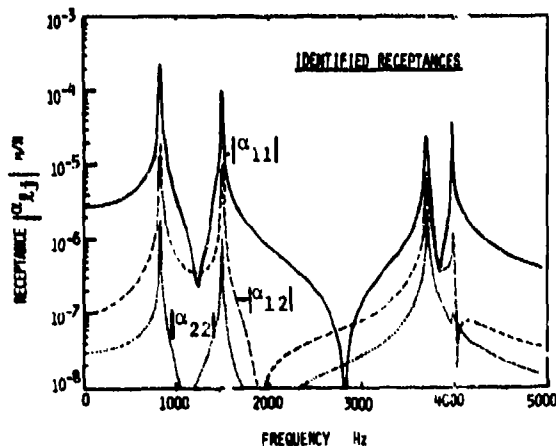


Figure 29. Identified receptances for blade. Compare with Figure 24.

5. CONCLUSIONS

It has been shown that for highly damped structures or those having parameters which vary strongly with frequency, the advantages of using a dynamic stiffness representation are considerable, allowing the possibility to identify mass, stiffness and damping parameters quite accurately not only at resonance but over

a wide frequency range. This is very important, because it leads to the ability to make accurate, repeatable, measurements of the damping properties of materials by means of a simple, familiar, procedure. Furthermore, the modal identification process applied to damped structures can form the basis for further calculations, such as the use of the modelled parameters to predict effects of structural modifications or to generate discrete models of the identified system.

Identification of the modal parameters of a lightly damped system, having properties which vary slowly with frequency, is best accomplished in most cases by means of current state-of-the-art identification techniques based on measured receptance data.

ACKNOWLEDGEMENTS

Thanks due to Roxanne Lemaster and Joan Lowe of AFWAL and the Word Processing Center of Bently Nevada Corporation for preparation of drafts, tables and manuscripts.

Test data of the polymer specimen was provided by A.D. Nashif of Anatrol Corporation in Cincinnati, and on the turbine blade by T. Lagnese of AFWAL.

This work was conducted in part under AFWAL project No. 2307P102. The constructive comments of the reviewers and the helpful corrections suggested by J.P. Henderson of AFWAL are greatly appreciated.

REFERENCES

1. D.J. Ewins, "On Predicting Point Mobility Plots From Measurements of Other Mobility Parameters", Imperial College Report No. 79004/2, Dynamics Section, Mechanical Engineering, London 1979.
2. D.J. Ewins and P.T. Gleeson, "Experimental Determination of Multidirectional Mobility Data for Beams", Shock and Vibration Bulletin, 45, Part 5, 1975.
3. D.J. Ewins, "Why's and Wherefores of Modal Testing", SEE Seminar on Modal Testing, SEE Journal, 18(3), 1979.
4. R.G. White and H.G.H. Goyder, "Some Experimental Dynamic Structure Analysis Techniques". SEE Journal, 18(1), 1979.
5. D.J. Ewins, "Measurement and Application of Mechanical Mobility Data", Solartron/Schlumberger Publication, Farnborough, U.K.

6. B.M. Hall, E.D. Calkin and M.S. Shalor, "Linear Estimation of Structural Parameters from Dynamic Test Data", Proc. 11th AIAA/ASME Structures, Structural Dynamics and Materials Conference, New York, pp 193-197, 1970.
7. J.D. Collins et al, "Statistical Identification of Structures", AIAA Journal, 12(2), pp 185-190, 1974.
8. P. Van Loon, "Modal Parameters of Mechanical Structures", PH.D. Thesis, University of Leuven, Belgium 1974.
9. H.G.H. Goyder, "Methods and Application of Structural Modeling from Measured Structural Frequency Response Data", J. Sound, Vib., 68(2), pp 209-230, 1980.
10. A.L. Klosterman, "On the Experimental Determination and Use of Modal Representations of Dynamic Characteristics", PH.D. Thesis, University of Cincinnati, 1971.
11. A.L. Klosterman and J.R. Lemon, "Dynamic Design Analysis Via the Building Block Approach", Shock and Vibration Bulletin 42, pp 97-104, 1972.
12. R. Dat and J.L. Meurzac, "Exploitation by Mathematical Smoothing of Admittance Measurements of a Linear System", Recherche Aerospatiale, 4, p 209, 1972.
13. W.G. Flannelly, A. Berman and R.M. Barnsby, "Theory of Structural Dynamic Testing Using Impedance Techniques", Kaman Aerospace Corporation Report No. R-823 (2 vols), 1970.
14. D.J. Ewins and M.G. Sainsbury, "Mobility Measurements for the Vibration Analysis of Connected Structures", Shock and Vibration Bulletin, 42, pp 105-122, 1972.
15. D.J. Ewins, "State of the Art Assessment of Mobility Measurements - A Summary of European Results", Shock and Vibration Bulletin, 51, Part 1, pp 15-35, 1981.
16. R.G. White, "Evaluation of the Dynamic Characteristics of Structures by Transient Testing", J. Sound Vib., 15, pp 147-161, 1971.
17. S.R. Ibrahim, "Limitations on Random Input Forces in Randomdec Computation for Modal Identification", Shock and Vibration Bulletin, 50, Part 3, pp 99-112, 1980.
18. R.J. Allemang, "Experimental Modal Analysis Bibliography," Proc. 1st International Modal Analysis Conference, Orlando, Florida (Sponsored by Union College, Schenectady, NY.), pp 714-726, 1982.
19. D.E. Bently and A. Muszyńska, "Oil Whirl Identification by Perturbation Test", Proc. ASME/ASLE Conference, Washington, D.C., 5-7 Oct 1982.
20. D. E. Bently and A. Muszyńska, "Stability Evaluation of Rotor/Bearing System by Perturbation Tests", Rotor Dynamic Instability Problems in High Performance Turbomachinery, Proc. of a Workshop, Texas A & M University, College Station, NASA Conf. Publ. 2250, 1982.
21. Adhesive ISD-110, Manufactured by 3M Company, St. Paul, MN.
22. M.L. Drake and G.E. Terborg, "Polymeric Material Testing Procedures to Determine damping properties and the Results of Selected Commercial Materials", AFWAL-TR-80-4093, Air Force Wright Aero. Labs., 1980.
23. D.I.G. Jones, "An Attractive Method for Displaying Material Damping Data", J. Aircraft, 18(8), pp 644-649, 1981.
24. T. Lagnese and D.I.G. Jones, "Measurement and Analysis of Platform Damping in Advanced Turbine Blade Response", Shock and Vibration Bulletin, 53, 1983.

NOMENCLATURE

A	Cross sectional area of specimen
E	Young's modulus
G	Shear modulus
h	Height of 1 DOF specimen
i	$\sqrt{-1}$
j, l	Points on structure
k	Stiffness of 1 DOF specimen
k_n	Modal stiffness of n-th mode
m	Mass of 1 DOF system
m_n	n-th modal mass
N	Number of modes
S_2, S_j	Exciting forces at points 2, j

t	Time
w_x, w_j	Response at points x, j
x_x, x_j	Coordinates of points x, j
α	Receptance of 1 DOF system
α_D	Direct receptance of 1 DOF system
α_Q	Quadrature receptance of 1 DOF system
α_{xj}	Transfer receptance (w_x/S_j)
α_{xx}	Point receptance (w_x/S_x)
α_{xjD}	Direct transfer receptance
α_{xjQ}	Quadrature transfer receptance
ϵ	Phase between excitation and response
ϵ_{xj}	Phase between excitation and response
η	Loss factor of 1 DOF specimen
η_n	Loss factor of n-th mode
k	Dynamic stiffness of 1 DOF system
k_D	Direct dynamic stiffness of 1 DOF system
k_Q	Quadrature dynamic stiffness of 1 DOF system
k_{xj}	Dynamic stiffness
k_{xjD}	Direct dynamic stiffness
k_{xjQ}	Quadrature dynamic stiffness
$\delta(t)$	Delta function
ρ	Density
$\phi_n(x_x)$	n-th modal function at point x
ω	Frequency
ω_n	n-th resonant frequency
ω_m	Mean resonant frequency of two closely spaced modes

APPENDIX 1

Relationship Between Half-power Bandwidth and Loss Factor

The relationship between the half-power bandwidth measure of damping ($\Delta\omega/\omega$) and the actual loss factor η , or viscous damping coefficient, depends on the fraction of the peak amplitude which is being measured and whether $|\alpha|$ or α_Q is being considered.

Normally a factor of $1/\sqrt{2}$ is used, which corresponds to a 3.01 db reduction, giving the name "3 db bandwidth". From equation (10), the maximum value of $|\alpha|$ at resonance ($k = m\omega^2$) is $1/k\eta$, and if we seek the values of ω for which $|\alpha|$ is $n|\alpha|_{\max} = n/k\eta$, (where n is a number) then equation (10) gives:

$$1/\sqrt{(k - m\omega^2)^2 + (k\eta)^2} = n/k\eta \quad (1.1)$$

Squaring, cross-multiplying and solving for ω , we get:

$$\omega_{1,2} = \sqrt{\frac{k}{m}} \left[1 \pm \eta \sqrt{\frac{1}{n^2} - 1} \right] \quad (1.2)$$

The two roots lie one above and one below the resonant frequency $\omega_1 = \sqrt{k/m}$. The bandwidth $\Delta\omega$ is equal to $\omega_2 - \omega_1$ so:

(1.3)

$$\frac{\Delta\omega}{\omega_1} = \sqrt{1 + \eta \sqrt{\frac{1}{n^2} - 1}} - \sqrt{1 - \eta \sqrt{\frac{1}{n^2} - 1}}$$

for $n = 1/\sqrt{2}$ and $\eta \ll 1$, this leads at once to equation (13). For other values of n , other relationships between η and $\Delta\omega/\omega_1$ can be found and used. This is especially useful for very low damping: for example, $n=1/3$ (10 db bandwidth) gives:

$$\eta = 0.3536 \Delta\omega/\omega_1 \quad (1.4)$$

On the other hand, if we examine α_Q from equation (10), and seek the same values of ω for which $\alpha_Q = n\alpha_{Q\max}$, then:

$$\frac{\Delta\omega}{\omega_1} = \sqrt{1 + \eta \sqrt{\frac{1}{n^2} - 1}} - \sqrt{1 - \eta \sqrt{\frac{1}{n^2} - 1}} \quad (1.5)$$

from which equation (14) emerges for $n = 1/\sqrt{2}$. For viscous damping, equation (10) gives the following expression for $|\alpha|$:

$$|\alpha| = 1/\sqrt{(k - m\omega^2)^2 + (c\omega)^2} \quad (1.6)$$

so that $|\alpha|_{\max}$ must now be found by seeking the minimum value of the denominator of equation (1.6). The classical expression found from this is:

$$\omega_1 = \sqrt{\frac{k}{m} (1 - 2\zeta^2)} \quad (1.7)$$

where $\zeta = c/2\sqrt{km}$ is the damping ratio. Again, seeking the values of ω for which $|\alpha| = |\alpha|_{\max}$, we can show that:

$$\frac{\Delta\omega}{\omega_1} = \sqrt{1 + 2\zeta \sqrt{\left(\frac{1}{n^2} - 1\right) \frac{1-\zeta^2}{(1-2\zeta^2)^2}}} - \sqrt{1 - 2\zeta \sqrt{\left(\frac{1}{n^2} - 1\right) \frac{1-\zeta^2}{(1-2\zeta^2)^2}}} \quad (1.8)$$

which gives $2\zeta = \Delta\omega/\omega_1$ for $n = 1/\sqrt{2}$ and $\zeta \ll 1$.

APPENDIX 2

Derivation of Modified Equations for Two Degree of Freedom System

The receptances of the two degree of freedom, free-free, system shown in Figure 19, are given by equations (28) and (29). Using partial fractions, they can be put in the modal form:

$$\alpha_{11} = -\frac{1}{2m\omega^2} + \frac{1}{4k(1 + i\eta) - 2m\omega^2} \quad (2.1)$$

$$\alpha_{12} = -\frac{1}{2m\omega^2} - \frac{1}{4k(1 + i\eta) - 2m\omega^2} \quad (2.2)$$

If the term $1/2m\omega^2$ is carried to the left hand side, one can define a modified receptance which corrects for the rigid body motion terms:

$$\alpha'_{11} = \alpha_{11} + \frac{1}{2m\omega^2} = \frac{1}{4k(1 + i\eta) - 2m\omega^2} \quad (2.3)$$

$$\alpha'_{12} = \alpha_{12} + \frac{1}{2m\omega^2} = \frac{-1}{4k(1 + i\eta) - 2m\omega^2} \quad (2.4)$$

While, therefore, the dynamic stiffness κ_{11} and κ_{12} , defined by $\kappa_{11} = 1/\alpha_{11}$ and $\kappa_{12} = 1/\alpha_{12}$, have no special usefulness, the modified dynamic stiffness, defined by $\kappa'_{11} = 1/\alpha'_{11}$ and $\kappa'_{12} = 1/\alpha'_{12}$, certainly do, since:

$$\kappa'_{11} = 4k(1 + i\eta) - 2m\omega^2 \quad (2.5)$$

$$\kappa'_{12} = -4k(1 + i\eta) + 2m\omega^2 \quad (2.6)$$

These are the relationships used in Section 4.2.2.

TABLE 6

MEASURED VALUES OF $\alpha_{11}(\omega)$ FOR BLADE

Freq Hz	α_{11} m/N	Phase ϕ_{11}	α'_{11D} N/m	α'_{11Q} N/m
100	2.22E-6	-164.1	-4.33E5	-1.23E5
200	3.97E-7	-174.8	-2.51E6	-2.28E5
300	3.53E-8	-116.6	-1.27E7	-2.53E7
400	1.59E-7	- 6.7	6.25E6	-7.34E5
500	2.67E-7	- 7.3	3.71E6	-4.76E5
600	3.61E-7	- 7.6	2.75E6	-3.66E5
650	4.58E-7	- 8.9	2.16E6	-3.38E5
700	5.63E-7	-10.2	1.75E6	-3.15E5
750	7.94E-7	-12.1	1.23E6	-2.64E5
800	1.57E-6	-10.9	6.25E5	-1.20E5
810	2.08E-6	-11.0	4.72E5	-9.17E4
820	3.18E-6	-11.7	3.08E5	-6.38E4
830	6.85E-6	-17.9	1.39E5	-4.49E4
840	1.87E-5	-164.7	-5.16E4	-1.41E4
850	3.69E-6	-174.0	-2.70E5	-2.83E4
860	2.08E-6	-172.6	-4.77E5	-6.19E4
870	1.35E-6	-171.7	-7.33E5	-1.07E5
880	1.02E-6	-168.2	-9.60E5	-2.00E5
890	8.00E-7	-164.5	-1.20E6	-3.34E5
900	6.85E-7	-160.4	-1.38E6	-4.90E5
1000	3.65E-7	-135.0	-1.94E6	-1.94E6
1050	3.14E-7	-135.0	-2.25E6	-2.25E6
1100	2.41E-7	-128.7	-2.59E6	-3.24E6
1150	1.87E-7	-128.6	-3.34E6	-4.18E6
1200	1.30E-7	-126.8	-4.61E6	-6.16E6
1250	9.75E-8	- 90.0	0	-1.03E7
1300	1.13E-7	- 53.1	5.31E6	-7.08E6
1350	1.74E-7	- 33.9	4.77E6	-3.21E6
1400	2.07E-7	- 66.8	1.90E6	-4.44E6
1450	5.32E-7	-14.9	1.82E6	-4.83E5
1460	7.64E-7	-14.7	1.27E6	-3.33E5
1470	1.06E-6	-13.0	9.28E5	-2.14E5
1480	1.74E-6	-14.8	5.56E5	-1.47E5
1490	3.98E-6	-24.5	2.29E5	-1.04E5
1500	8.71E-6	-163.3	-1.10E5	-3.30E4
1510	2.36E-6	-164.1	-4.08E5	-1.16E5
1520	1.36E-6	-169.7	-7.23E5	-1.31E5
1540	8.25E-7	-163.3	-1.16E6	-3.48E5
1550	6.55E-7	-164.1	-1.47E6	-4.18E5
1600	3.39E-7	-153.4	-2.64E6	-1.32E6
1650	2.01E-7	+180.0	-4.98E6	0
1700	9.10E-8	+180.0	-1.10E7	0
1800	1.28E-7	171.9	-3.73E7	1.10E6
1900	9.40E-8	167.1	-1.04E7	2.38E6
2000	6.34E-8	167.1	-1.54E7	3.52E6
2200	3.02E-8	173.9	-3.29E7	3.52E6
2400	1.21E-8	-161.6	-7.84E7	-2.61E7
2600	1.17E-8	- 69.5	2.99E7	-8.01E7
2800	2.47E-8	- 55.6	2.23E7	-3.38E7
3000	4.30E-8	- 74.1	6.37E6	-2.24E7
3200	5.60E-8	- 90.0	0	-1.79E7

TABLE 6 (Cont.)

3420	3.53E-8	0	2.83E7	0
3600	1.65E-7	0	6.06E6	0
3700	1.43E-5	-31.3	5.98E5	-3.63E5
3710	2.34E-6	-70.0	1.46E5	-4.02E5
3720	1.55E-6	-124.8	-3.68E5	-5.30E5
3730	9.35E-7	-129.3	-6.77E5	-8.28E5
3740	7.61E-7	-138.4	-9.83E5	-8.72E5
3750	6.42E-7	-143.1	-1.25E6	-9.35E5
3800	3.13E-7	-146.3	-2.66E6	-1.77E6
3900	1.23E-7	-90.0	0	-8.13E6
3950	1.11E-7	-90.0	0	-9.01E6
3960	8.16E-7	-90.0	0	-1.23E6
3970	1.97E-7	-63.5	2.26E6	-4.54E6
3980	4.06E-7	-63.4	1.10E6	-2.20E6
3990	1.88E-6	-123.0	-2.90E5	-4.46E5
4000	4.39E-7	168.7	-2.23E6	4.46E5
4010	3.21E-7	166.0	-3.02E6	7.54E5
4020	2.24E-7	180.0	-4.46E6	0
4030	2.14E-7	180.0	-4.67E6	0
4040	1.93E-7	180.0	-5.18E6	0
4100	1.10E-7	153.6	-8.14E6	4.06E6
4200	6.97E-8	161.6	-1.36E7	4.53E6
4300	4.27E-8	161.7	-2.22E7	7.35E6

TABLE 7

MEASURED VALUES OF $\alpha_{12}(\omega)$ FOR BLADE

Freq Hz	$ \alpha_{12} $ m/N	Phase ϵ_{12}^0	$\kappa_{110} \frac{\cos \epsilon_{12}}{ \alpha_{12} }$ N/m	$\kappa_{120} \frac{\sin \epsilon_{12}}{ \alpha_{12} }$ N/m
100	2.53E-7	-136.0	-2.79E6	-2.79E6
200	6.33E-8	-116.6	-7.07E6	-1.41E7
300	3.53E-8	-98.0	-3.94E6	-2.81E7
400	1.58E-8	76.0	1.53E7	6.14E7
500	1.01E-8	21.8	9.19E7	3.68E7
600	1.32E-8	36.0	6.13E7	4.45E7
650	2.06E-8	37.9	3.83E7	2.98E7
700	3.40E-8	34.8	2.42E7	1.68E7
750	5.64E-8	28.8	1.55E7	8.54E6
800	1.41E-7	24.8	6.44E6	2.97E6
810	1.97E-7	21.8	4.71E6	1.89E6
820	3.07E-7	18.6	3.09E6	1.04E6
830	6.82E-7	8.7	1.45E6	2.22E5
840	2.27E-6	-133.0	-3.00E5	-3.22E5
850	4.20E-7	-147.4	-2.01E6	-1.28E6
860	2.41E-7	-150.7	-3.62E6	-2.03E6
870	1.70E-7	-151.9	-5.19E6	-2.77E6
880	1.32E-7	-152.4	-6.71E6	-3.51E6
890	1.10E-7	-153.4	-8.13E6	-4.07E6
900	9.49E-8	-153.8	-9.45E6	-4.65E6
1000	4.36E-8	-159.4	-2.15E7	-8.07E6
1050	3.74E-8	-163.8	-2.57E7	-7.46E6
1100	3.15E-8	-165.8	-3.08E7	-7.79E6
1150	3.00E-8	-167.5	-3.25E7	-7.21E6
1200	2.97E-8	-169.5	-3.31E7	-6.14E6
1250	3.15E-8	-172.1	-3.14E7	-4.36E6
1300	3.52E-8	-174.7	-2.83E7	-2.62E6
1350	4.22E-8	-174.7	-2.36E7	-2.19E6
1400	2.75E-8	168.6	-3.56E7	-7.19E6
1450	8.36E-8	-176.3	-1.19E7	-7.72E5

TABLE 7 (Cont.)

1460	1.06E-7	-177.8	-9.43E6	-3.62E5
1470	1.43E-7	-179.9	-6.99E6	-1.22E4
1480	2.23E-7	176.1	-4.47E6	3.05E5
1490	4.82E-7	162.0	-1.97E6	6.41E5
1500	1.07E-6	38.9	7.27E5	5.87E5
1510	2.56E-7	16.3	3.75E6	1.10E6
1520	1.47E-7	13.0	6.63E6	1.53E6
1540	7.65E-8	9.0	1.29E7	2.04E6
1550	6.10E-8	8.5	1.62E7	2.42E6
1600	2.82E-8	6.0	3.53E7	3.71E6
1650	1.66E-8	7.0	5.98E7	7.34E6
1700	1.10E-8	7.7	9.01E7	1.22E7
1800	4.89E-9	12.7	1.99E8	4.50E7
1900	3.29E-9	0	3.04E8	0
2000	1.19E-9	26.6	7.51E8	3.76E8
2200	6.56E-10	180.0	-1.52E9	0
2400	1.51E-9	175.0	-6.60E8	5.77E7
2600	2.70E-9	170.1	-3.65E8	6.37E7
2800	3.74E-9	167.6	-2.61E8	5.74E7
3000	5.73E-9	168.6	-1.71E8	3.45E7
3200	8.83E-9	165.6	-1.10E8	2.82E7
3420	1.52E-8	160.1	-6.19E7	2.24E7
3600	4.46E-8	155.1	-2.03E7	9.44E6
3700	4.31E-7	114.5	-9.62E5	2.11E6
3710	7.92E-7	59.5	6.41E5	1.09E6
3720	3.72E-7	-1.1	2.69E6	-5.16E4
3730	2.19E-7	-9.7	4.50E6	-7.69E5
3740	1.55E-7	-16.3	6.19E6	-1.81E6
3750	1.20E-7	-19.1	7.87E6	-2.73E6
3800	5.53E-8	-21.2	1.69E7	-6.54E6
3900	3.19E-8	-26.1	2.82E7	-1.38E7
3950	3.42E-8	-29.9	2.53E7	-1.46E7
3960	3.78E-8	-31.3	2.26E7	-1.37E7
3970	4.53E-8	-33.7	1.84E7	-1.22E7
3980	6.98E-8	-44.4	1.02E7	-1.00E7
3990	2.12E-7	-111.6	-1.74E6	-4.39E6
4000	2.33E-8	158.2	-3.98E7	+1.59E7
4010	4.43E-9	159.5	-2.11E8	7.91E7
4020	2.45E-9	-32.4	3.45E8	-2.19E8
4030	5.61E-9	-27.9	1.58E8	-8.34E7
4040	7.23E-9	-28.5	1.22E8	-6.60E7
4100	1.02E-8	-30.8	8.42E7	-5.02E7
4200	9.97E-9	-32.2	8.49E7	-5.34E7
4300	9.86E-9	-36.1	8.19E7	-5.98E7

TABLE 8

MEASURED VALUES OF $\alpha_{22}(\omega)$ FOR BLADE

Freq Hz	$ \alpha_{22} $ m/N	Phase ϵ_{22}^0	$\kappa_{220} \frac{\cos \epsilon_{22}}{ \alpha_{22} }$ N/m	$\kappa_{220} \frac{\sin \epsilon_{22}}{ \alpha_{22} }$ N/m
100	3.97E-8	-135.0	-1.78E7	-1.78E7
200	6.33E-9	-90.0	0	-1.58E8
300	6.61E-9	-156.0	-1.39E8	-5.96E7
400	6.19E-9	180.0	-1.62E8	0
500	3.96E-9	180.0	-2.53E8	0
600	5.51E-9	159.8	-1.70E8	6.27E7
650	6.10E-9	164.9	-1.58E8	4.27E7
700	6.87E-9	162.1	-1.39E8	4.47E7
750	8.45E-9	157.5	-1.09E8	4.53E7

TABLE 8 (Cont.)

800	1.70E-8	152.5	-5.22E7	2.72E7	1700	1.37E-10	-135.0	-5.16E9	-5.16E9
810	2.05E-8	151.4	-4.28E7	2.34E7	1800	1.22E-9	172.9	-8.13E8	1.01E0
820	2.80E-8	149.1	-3.06E7	1.83E7	1900	1.43E-9	169.1	-6.87E8	1.32E0
830	4.88E-8	145.8	-1.69E7	1.15E7	2000	1.78E-9	167.3	-5.48E8	1.24E0
840	1.73E-7	129.1	-3.27E6	4.02E6	2200	2.17E-9	167.6	-4.50E8	9.90E7
850	7.32E-8	-35.4	1.11E7	-7.91E6	2400	2.71E-9	166.2	-3.58E8	8.80E7
860	2.84E-8	-36.8	2.82E7	-2.11E7	2600	2.69E-9	164.6	-3.58E8	9.87E7
870	1.73E-8	-38.9	4.50E7	-3.63E7	2800	3.28E-9	162.1	-3.90E8	9.37E7
880	1.13E-8	-41.4	6.64E7	-5.85E7	3000	3.85E-9	160.2	-2.44E8	8.80E7
890	8.25E-9	-45.0	8.57E7	-8.57E7	3200	4.80E-9	156.2	-1.91E8	8.41E7
900	6.36E-9	-48.1	1.06E8	-1.17E8	3420	6.85E-9	155.4	-1.33E8	6.08E7
1000	1.98E-9	-111.8	-1.88E8	-4.69E8	3600	1.39E-8	152.4	-6.38E7	3.33E7
1050	1.80E-9	-143.1	-4.44E8	-3.34E8	3700	5.10E-8	140.4	-1.51E7	1.25E7
1100	2.46E-9	-164.6	-3.92E8	-1.08E8	3710	6.02E-8	131.4	-1.10E7	1.25E7
1150	2.40E-9	180.0	-4.17E8	0	3720	8.29E-8	127.5	-7.34E6	9.57E6
1200	2.89E-9	-169.2	-3.40E8	-6.48E7	3730	1.42E-7	112.0	-2.64E6	6.53E6
1250	3.68E-9	180.0	-2.72E8	0	3740	2.57E-7	59.7	1.96E6	3.36E6
1300	4.45E-8	177.0	-2.24E7	1.18E6	3750	1.21E-7	-8.3	8.18E6	1.19E6
1350	4.78E-8	174.8	-2.08E7	1.90E6	3800	2.76E-8	-20.6	3.97E7	1.49E7
1400	3.53E-9	137.3	-2.08E8	1.92E8	3900	8.27E-9	-23.4	1.11E8	4.80E7
1450	8.95E-9	170.6	-1.10E8	1.82E7	3950	5.89E-9	-24.3	1.55E8	6.99E7
1460	1.08E-8	170.1	-9.12E7	1.59E7	3960	5.60E-9	-24.2	1.63E8	7.32E7
1470	1.36E-8	169.5	-7.33E7	1.34E7	3970	5.47E-9	-24.0	1.67E8	7.44E7
1480	1.85E-8	167.2	-5.27E7	1.20E7	3980	5.13E-9	-23.2	1.79E8	7.68E7
1490	3.01E-8	163.1	-3.18E7	9.66E6	3990	5.15E-9	-23.2	1.28E8	7.65E7
1500	8.01E-8	145.1	-1.02E7	7.14E6	4000	5.79E-9	-26.0	1.55E8	7.57E7
1510	6.98E-8	4.4	1.43E7	1.10E6	4010	8.63E-9	-96.5	-1.30E7	1.14E8
1520	2.34E-8	-3.3	4.27E7	-2.46E6	4020	2.67E-9	-32.1	3.17E8	1.99E8
1540	9.19E-9	-7.0	1.08E8	-1.33E7	4030	2.87E-9	-26.6	3.12E8	1.56E8
1550	6.51E-9	-8.3	1.52E8	-2.22E7	4040	2.86E-9	-26.6	3.13E8	1.57E8
1600	2.01E-9	-15.1	4.80E8	-1.30E8	4100	2.24E-9	-19.8	4.20E8	1.51E8
1650	5.10E-10	-16.0	1.88E9	-5.40E8	4200	1.46E-9	-20.7	6.41E8	2.42E8
					4300	7.49E-10	0	1.34E9	0

TABLE 9

IDENTIFIED PARAMETERS FOR TURBINE BLADE

METHOD		RECEPTANCE		DYN. STIFFNESS		OVERALL SUMMARY (average)
Quantity	n	α_{11}	α_{1j}	κ_{11}	κ_{1j}	
m_n Kg	1	0.0161	-	0.0181	-	0.0171
	2	0.0221	-	0.0231	-	0.0226
	3	0.0196	-	*	-	0.0196
	4	0.0122	-	*	-	0.0172
η_n	1	0.0086	-	+	-	0.0086
	2	0.0051	-	+	-	0.0051
	3	0.0039	-	+	-	0.0039
	4	0.0039	-	+	-	0.0039
ω_n Hz	1	840	-	837	-	840
	2	1500	-	1503	-	1500
	3	3719	-	*	-	3719
	4	3999	-	*	-	3999
$\phi_n(x_2)$	1	+0.092	+0.094	+0.074	+0.091	0.088
	2	-0.100	0.108	-0.103	-0.106	-0.104
	3	-0.300	0.329	*	*	-0.330
	4	+0.0385	+0.039	*	*	+0.039

* Not determined
+ Not measurable

AN APPLICATION OF THE KINETIC ENERGY CALCULATION AS AN AID IN MODE IDENTIFICATION

J. J. Brown and G. R. Parker
Hughes Helicopters, Inc.
Culver City, California

Presented at

53rd SHOCK AND VIBRATION SYMPOSIUM
Danvers, Massachusetts

October 26-28, 1982

In recent years, the ability to economically and efficiently solve large order finite element dynamic problems has become a reality.

However, the task of modal identification has proportionately increased. By applying the kinetic energy calculation to the modal data, candidates for structural as well as local modes and possible modeling errors can be quickly isolated.

This technique was applied during the analysis of the Hughes Advanced Attack Helicopter (AAH). The results show the obvious advantages offered by this method.

INTRODUCTION

Recent additions to most finite element dynamic programs have made the solution of large models a reality. These additions are in the form of fast eigenvalue extraction techniques which employ a variation of subspace iteration. The analyst is thereby freed from the task of applying reduction methods which generally require expertise and unavoidably introduce errors and sacrifice fidelity.

The modal information obtained from the solution of these large problems provides the analyst with more detailed information about structures than ever before possible. However, this greater detail usually results in the solution of problems having high modal densities; i. e., many modes within a given frequency range. Plotting routines which are available allow thorough examination of the modes, but they are both time consuming and costly to use. Identifying modes from these high modal density problems has become a formidable task.

By applying the kinetic energy calculation to the modal data, this task has been greatly reduced. Structural and local modes, as well as potential model errors are quickly isolated, thus enabling more efficient use of the plotter and the analyst's time.

TECHNICAL APPROACH

The use of the kinetic energy calculation, based on modal data, in a practical application is not new but, up to now, has received little attention throughout the industry.

The modal kinetic energy expression is quite simple and is based on a variation of certain orthogonal principles as shown in Equations 1 and 2.

$$\begin{aligned} & [\phi]^T [M] [\phi] \\ & NM \times DOF \quad DOF \times DOF \quad DOF \times NM \\ & = [I] = \text{Generalized Mass} \quad (1) \\ & NM \times NM \end{aligned}$$

$$\begin{aligned}
& [\phi]^T \quad [K] \quad [\phi] \\
& \text{NM} \times \text{DOF} \quad \text{DOF} \times \text{DOF} \quad \text{DOF} \times \text{NM} \\
& = [\omega^2] = \text{Generalized Stiffness} \quad (2) \\
& \text{NM} \times \text{NM}
\end{aligned}$$

where

$[\phi]$ is a matrix of orthonormalized modes

$[M]$ is the mass matrix

$[K]$ is the stiffness matrix

$[I]$ is an identity matrix

$[\omega^2]$ is the squared natural frequencies

DOF = degrees-of-freedom

NM = number of modes

A variation of Equation 1 forms the modal kinetic energy (KE) expression as shown in Equation 3.

$$\begin{aligned}
& [\phi]^T \quad \begin{matrix} E \\ * \end{matrix} \quad [M] \quad [\phi] \\
& \text{DOF} \times \text{NM} \quad \text{DOF} \times \text{DOF} \quad \text{DOF} \times \text{NM} \\
& = [KE] \\
& \text{DOF} \times \text{NM} \quad (3)
\end{aligned}$$

where $\begin{matrix} E \\ * \end{matrix}$ is a special element by element multiply.

Equations 1 and 2 result in square matrices in generalized, or modal coordinates (NM x NM), Equation 3 results in a rectangular matrix of discrete model coordinates by modes (DOF x NM), where detailed information is retained in terms of physical degrees-of-freedom for each mode.

Each element of a column of Equation 3 is equal to

$$KE_{ij} = \phi_{ij} \sum_{k=1}^{\text{DOF}} M_{ik} \phi_{kj} \quad (4)$$

or the percent of the total kinetic energy of the jth mode as a decimal, and the total kinetic energy of each column is equal to 1.0, i.e.:

$$KE_{j(\text{TOTAL})} = \sum_{i=1}^{\text{DOF}} KE_{ij} = 1.0 \quad (5)$$

This important unity relationship is made possible due to the unique properties of the orthonormalized modal matrix.

APPLICATION

This approach was applied during the dynamic analysis of the Hughes Advanced Attack Helicopter (AAH) shown in Fig. 1. The dynamic model used for the analysis is shown in Fig. 2. The relatively large model contained 4357 structural elements, 1632 grid points and 9792 degrees-of-freedom. In this analysis, the analytical modes were to be compared with the results of the AV06 modal test.

The AV06 test configuration was an earlier flight test vehicle on which a modal test was performed. Correlation with these test data was done to verify the analytical model.

The analysis was performed using the MSC/NASTRAN Ref. [1] computer program. MSC/NASTRAN is a large scale general purpose digital computer program which solves a wide variety of engineering problems by the finite element method. The program is used worldwide in virtually every type of industry. In addition, NASTRAN has a unique capability that allows the user to "get inside" the fixed programs and alter them. This is called altering with "direct matrix abstraction programming" or DMAP. Using this DMAP capability, the kinetic energy program was added to Hughes Helicopters' version of NASTRAN.

A thorough explanation of the DMAP program is contained in Ref. [2]. This capability can also be added to any analysis job stream with a FORTRAN post-processing program.

During the analysis, modes and frequencies were calculated to 25 Hz. A frequency summary table of the results is shown in Table 1. This table is part of the normal output from a NASTRAN modal run. The first column is the mode number, the second column the extraction order, the third the eigenvalue (ω^2), the fourth is the frequency in radians, the fifth is the frequency in hertz (Hz), and the last two columns are generalized mass and stiffness, respectively. As shown, 87 modes were calculated below 25 Hz. Each mode contains approximately

10,000 values, so the job of identifying all of the modes is a formidable task without an aid such as modal kinetic energy.

Having calculated the modal data, Equation 3 was solved for the kinetic energy matrix. This matrix was then filtered such that only those values greater than 3 percent of the largest value in each column were retained. This greatly reduces the non-zero numbers that are printed out. The procedure can best be demonstrated through a simple example of the 3 degree-of-freedom problem shown in Fig. 3. The kinetic energy matrix for this example is shown in Equation 6. Each column or mode in Equation 6 is normalized to the largest value of unity as shown in Equation 7. In Equation 7, only those values equal to or greater than 1 percent of the largest value in each column are retained, resulting in the sparse matrix shown in Equation 8 which has been scaled back to the original values. The important feature is that we have reduced out the very small numbers and can now concentrate on the larger contributors.

A typical kinetic energy output for the first 39 modes from the analysis is shown in Fig. 4. In this case, a filter was set at 3 percent of the largest value. In reading the output, column numbers identify the mode number; the point identifies the grid point number within the model and its direction, where T1, T2, T3 refer to translations in X, Y, Z, and R1, R2, R3 refer to rotations about the X, Y, and Z axes; and finally the value corresponds to the kinetic energy contributor of that point as a decimal.

A quick look at the matrix is all that is necessary to pick out candidates for local as well as structural modes. A potential structural mode is identified by a column containing many numbers, since a great deal of the structure is moving and the energy is distributed throughout the structure. Conversely, a local mode is identified by very few numbers, since only a localized part of the structure is moving.

The first six columns in Fig. 4 are rigid body modes, and as one would expect, they have many values as the entire structure moves in a prescribed direction. Other examples can quickly be picked out, such as columns 13, 17, 21, 25, 33, 35, 37, 38, and possibly 28 and 31, just to name a few. In the same manner, local modes can be quickly isolated, such as columns 7 through 12, 22, and 23. Two modes stand out in particular; i. e., modes 22 and 23, where 99 and 96 percent of the energy is contained at one grid point. These modes turned out to be

modeling errors, where the grid point was not properly restrained in rotation.

As one might expect, the amount of output is a function of the filter selected. Several filters were used on the 87 modes. Figs. 5 through 7 show partial outputs using filters of 1, 5 and 10 percent for modes 33 through 35 respectively. It is highly recommended that any post-processing program allow the user to choose the filter value.

An additional aid was a maximum values matrix. This output contains the maximum value of each column (mode) taken from the kinetic energy matrix. This output which is shown in Fig. 8 provided quick-look data and each column represents a mode and each value, again, describes the grid point, its direction (as in the kinetic energy matrix) and the value is the maximum modal kinetic energy as a decimal.

A quick scan of these data can help to separate the modes. Low values indicate large structural motion and large values local motion. One can become quite proficient with the maximum values matrix such that most of the candidates can be isolated from this matrix. Finally, Table 2 shows a list of the fundamental structural modes that were correlated with the results of the AV06 modal test, along with their percent deviation, and Table 3 shows a complete list of the structural modes identified in the analysis.

In reviewing Table 3, it should be noted that particular attention had to be paid to the mode shape as well as frequency. Terms such as first and second lateral bending, although adequate for simple beam type models, are far too general. The analyst must look at local coupling, including phase between wings, stabilator, and tail in order to describe a mode. A good example of this was the second vertical bending mode at 18.97 Hz. There were several candidate modes, but after comparing the mode shapes with the test data, the 18.97 Hz mode was selected.

The next few figures show selected plots of some of the modes that were identified using this method. All plots were produced using McAuto's FASTDRAW Ref. [3] inter-active graphics post-processing program. FASTDRAW was chosen because it allowed quick rotation of the deflected shape in Cartesian space. Also, it should be noted that the detail in these plots are made possible by being able to solve the large eigenvalue problem. Fig. 9 shows a section view

looking aft of the first torsional mode at 4.08 Hz. Fig. 10 shows the first symmetric wing bending mode at 4.70 Hz (note the configuration) where only the inboard pylons were loaded. Fig. 11 shows the first wing anti-symmetric bending mode at 5.4 Hz. In this case, note the inboard pylons are in phase. Next, Fig. 12 shows the first vertical bending mode at 5.55 Hz. Figs. 13 and 14 show the first anti-symmetric and symmetric wing/pylon torsional modes respectively at 7.59 and 7.91 Hz. These modes are due to the forward and aft motion of the inboard pylons, and as you would expect, the tail has much lateral motion in the anti-symmetric mode and very little in the symmetric mode. The next figure (15), shows the first lateral bending mode at 8.85 Hz. And finally, Fig. 16 shows the second vertical bending mode at 18.97 Hz.

SUMMARY

The ability to solve large dynamic problems has enabled the analyst to gain more detailed information about a structure than ever before.

But with this greater detail comes problems associated with high modal density. This has resulted in a much larger task of modal identification.

By applying the kinetic energy calculation to the modal data, candidates for structural as well as local modes can be quickly isolated. This results in a tremendous savings in time and cost at the plotter. The cost of performing the kinetic energy calculation is negligible when compared to the cost of plotting each mode.

REFERENCES

1. NASTRAN Users and Programmers Manuals, MacNeal-Schwendler Corporation, February 1981.
2. Parker, G.R., and Brown, J.J., "Kinetic Energy DMAP for Mode Identification", presented at MSC/NASTRAN Users' Conference, March 18-19, 1980, Pasadena, California.
3. McAUTO FASTDRAW/3 Interactive Post-Processing Manual, McDonnell Douglas Automation Company, November 1979.

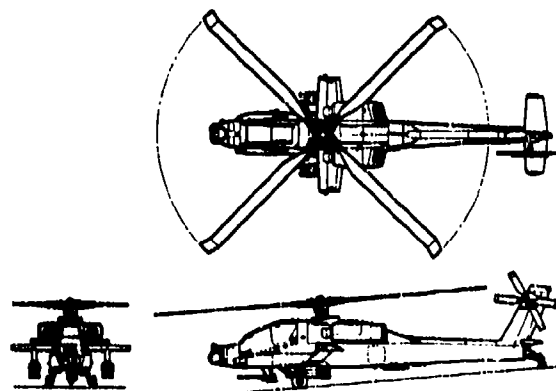


Fig. 1 - Hughes Advanced Attack Helicopter

1032 0000
4307 0000070
0702 0000000 OF FREEDOM

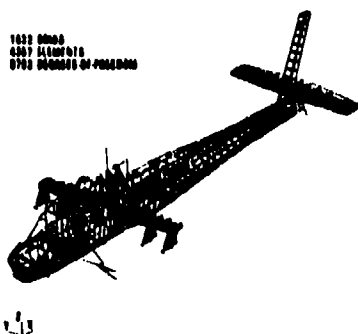


Fig. 2 - AAH dynamic Nastran model

EXAMPLE -

$$[K] = \begin{bmatrix} 1 & 0 & 0 \\ 0 & 100 & 0 \\ 0 & 0 & 100 \end{bmatrix} \quad (6)$$

NORMALIZE [K] TO LARGEST COLUMN VALUE

$$[K] = \begin{bmatrix} 1 & 0 & 0 \\ 0 & 1 & 0 \\ 0 & 0 & 1 \end{bmatrix} \quad (7)$$

$$[M] = \begin{bmatrix} 1 & 0 & 0 \\ 0 & 1 & 0 \\ 0 & 0 & 1 \end{bmatrix} \quad (8)$$

Fig. 3 - Sample 3 degree-of-freedom problem

POINT	KENO	VALUE	POINT	VALUE	POINT	VALUE	POINT	VALUE	POINT	VALUE	
COLUMN 1											
43	T2	2.15161E-03	44	T2	4.87552E-03	64	T3	2.61543E-03	2499	T2	3.43659E-02
5701	T2	2.01703E-03	5702	T2	8.26709E-03	5702	T3	4.58335E-03	5709	T2	3.92408E-03
8008	T2	2.30623E-03	8016	T2	2.15925E-03	8025	T2	4.22751E-03	8025	T3	2.63013E-03
9135	T2	2.92447E-03	10011	T2	9.82320E-03	10011	T3	5.80587E-03	10012	T2	8.31544E-03
10013	T2	7.83244E-03	10013	T3	4.37423E-03	10031	T2	3.52802E-03	10031	T3	2.56283E-03
10502	T2	2.74160E-03	10509	T2	2.09242E-03	10510	T2	1.93582E-03	10514	T2	3.23900E-03
11501	T2	2.22344E-03	11508	T2	2.06054E-03	11571	T2	1.33604E-02	11571	T3	7.03724E-03
12021	T3	2.92088E-03	12022	T2	3.80445E-03	12023	T3	1.94661E-03	13508	T2	2.31717E-03
14303	T2	2.63640E-03	13411	T2	3.35414E-03	13499	T2	3.49061E-02	13499	T3	3.75324E-02
10020	T2	1.93901E-02	10020	T3	1.30690E-02	10066	T2	4.49162E-03	10066	T3	2.68875E-03
20019	T2	2.46362E-03	21303	T2	2.64361E-03	21305	T2	2.46389E-03	23899	T2	2.98788E-02
17	T2	3.63892E-03	51	T2	7.94948E-03	51	T3	3.54698E-03	53	T2	2.04107E-03
54	T2	2.59792E-02	59	T2	4.63508E-03	59	T3	1.98899E-03	60	T2	1.21360E-02
42	T2	4.62115E-03	62	T3	2.16718E-03	900	T2	3.48288E-03	90060	T2	9.58561E-03
21231	T2	3.97323E-03	24739	T2	1.95449E-03	124003	T2	1.70599E-02	124003	T3	4.52113E-03
21250	T2	2.77405E-03	924602	T2	1.72727E-02	124002	T3	1.25044E-02	206002	T2	1.17366E-02
924602	T2	4.66804E-03	924602	T3	2.42033E-03	206003	T2	1.17366E-02	206003	T3	1.43876E-02
924603	T3	7.68369E-03									
COLUMN 2											
44	T3	3.48388E-03	2499	T2	2.37771E-02	2499	T3	2.52351E-02	5701	T3	1.70863E-03
5702	T3	3.79815E-03	5709	T2	3.83759E-03	5709	T3	1.42991E-03	5702	T2	2.19244E-03
8008	T2	2.78512E-03	8016	T2	2.24267E-03	8025	T2	4.42991E-03	8025	T3	2.98942E-03
9135	T2	2.80179E-03	10011	T2	6.87956E-03	10011	T3	7.40131E-03	10012	T2	1.39942E-02
10013	T2	2.69644E-03	10013	T3	5.84976E-03	10031	T2	3.41771E-03	10031	T3	4.67338E-03
10502	T3	3.23091E-03	10510	T2	2.45360E-03	10510	T3	1.90490E-03	10514	T2	4.10939E-03
11501	T3	1.74934E-03	11508	T3	8.43079E-03	11571	T2	3.41239E-03	11571	T3	9.07215E-03
12021	T3	5.83111E-03	12022	T2	5.58771E-03	12023	T3	5.60127E-03	12023	T3	4.32285E-03
13508	T2	2.34823E-03	13508	T3	3.36149E-03	13524	T2	2.37305E-03	13541	T2	2.41513E-03
13499	T3	4.93046E-02	17400	T2	1.88404E-03	17400	T3	1.99432E-03	10020	T2	1.91289E-02
18064	T4	4.34208E-03	20403	T3	8.25569E-03	21303	T3	2.91028E-03	23899	T2	4.00734E-02
17	T3	2.40948E-03	51	T3	4.77441E-03	54	T3	3.49628E-02	53	T3	2.67828E-03
40	T3	9.20443E-03	62	T3	8.91988E-03	500	T3	6.41305E-03	90060	T2	1.87193E-03
924003	T2	3.21492E-03	924003	T3	2.80028E-03	21250	T3	6.48993E-03	24739	T3	3.98098E-03
924002	T3	3.06282E-02	206002	T2	2.48962E-02	206006	T2	1.90781E-03	924002	T2	1.11008E-02
924003	T3	4.09584E-02	206007	T2	1.90760E-03	206007	T3	5.81819E-03	924003	T2	1.11008E-02
935050	T2	3.69336E-03	935050	T2	1.97141E-03						
COLUMN 3											
2499	T3	7.59180E-03	10012	T2	9.97080E-03	15499	T1	1.86121E-02	90051	T2	1.97038E-02
54	T3	8.56315E-03	59	T2	1.38361E-02	62	T2	8.79774E-03	90060	T2	7.21733E-03
924003	T2	1.46823E-02	924003	T3	3.95403E-02	924002	T2	1.53109E-02	924002	T3	8.63816E-03
206002	T2	7.43284E-02	206006	T3	1.01075E-02	924002	T3	3.98393E-02	206003	T2	1.52936E-02
924603	T3	1.39304E-02	935050	T2	2.59126E-02	935050	T2	1.37526E-02			
COLUMN 4											
43	T1	3.13641E-03	44	T1	6.76962E-03	2499	T1	2.66537E-02	5702	T1	6.61827E-03
8025	T1	4.34111E-03	9003	T1	3.04311E-03	9135	T1	3.01658E-03	10011	T1	9.65222E-03
10013	T1	9.99461E-03	10031	T1	3.63175E-03	10502	T1	2.80791E-03	10514	T1	3.88561E-03
12021	T1	4.97915E-03	12022	T1	4.84032E-03	12023	T1	3.97319E-03	12024	T1	3.45929E-03
13508	T1	3.31688E-03	14303	T1	2.69791E-03	13411	T1	4.34274E-03	13499	T1	8.41046E-02
10080	T1	3.89137E-02	10028	T1	3.78253E-03	10066	T1	1.03289E-02	20003	T1	3.61059E-03
21303	T1	4.97912E-03	21303	T1	4.59315E-03	23899	T1	8.98618E-02	38001	T1	4.50460E-03
51	T1	1.08674E-02	84	T1	7.46324E-02	59	T1	5.74031E-03	60	T1	2.04943E-02
90060	T1	9.25015E-03	90060	T1	1.49314E-02	21250	T1	9.49501E-03	24739	T1	2.34448E-03
124003	T1	4.56909E-03	24739	T1	5.26361E-03	924002	T1	3.47579E-02	206002	T1	2.47930E-02
924602	T1	1.33294E-02	206003	T1	2.61779E-02	206007	T1	3.59807E-03	924603	T1	1.40644E-02
935050	T1	5.82147E-03	26933	T1	4.49406E-03	92500	T1	4.12117E-03			
COLUMN 5											
2499	T2	6.47407E-03	2499	T3	3.78064E-02	5702	T3	6.43006E-03	5709	T3	3.51050E-03
10080	T3	4.59850E-03	11571	T3	3.67000E-03	10028	T3	3.49899E-03	10066	T3	4.81924E-03
206002	T3	3.69718E-02	32001	T3	6.26436E-03	42386	T3	4.49911E-03	42386	T3	3.29191E-03
38584	T3	1.01168E-02	90318	T3	9.74322E-03	34750	T3	8.62370E-03	34750	T3	3.57214E-03
94739	T3	1.69392E-02	94760	T3	1.93759E-02	954739	T3	8.92007E-03	54	T1	2.48677E-02
924003	T3	6.59299E-03	24738	T3	4.47770E-03	924002	T1	3.34292E-03	924002	T3	1.09551E-02
924002	T1	3.86683E-03	35017	T2	4.23336E-03	35017	T3	2.47720E-02	35018	T3	6.34843E-03
35020	T3	5.48648E-03	35023	T3	8.89963E-03	35024	T3	1.08581E-02	35027	T3	3.94181E-03
35033	T2	2.65384E-02	35050	T1	3.99198E-03	35050	T2	1.69992E-02	35050	T3	1.07945E-01
935050	T3	5.57349E-02	36099	T3	4.76994E-03	36111	T3	4.36235E-03	31601	T3	8.89508E-03
92500	T3	3.59043E-02	936150	T3	5.53173E-03						
COLUMN 6											
2499	T2	3.47863E-02	2499	T3	5.08267E-03	5702	T2	6.86563E-03	10011	T2	4.45601E-03
10020	T2	3.73674E-03	10028	T2	4.35752E-03	10044	T2	4.22168E-03	23899	T2	5.46532E-02
32001	T2	6.80904E-03	42328	T2	3.36174E-03	42328	T2	3.80203E-03	49001	T2	6.44169E-03
35018	T2	1.13508E-02	34738	T2	3.21629E-03	34745	T2	3.92629E-03	34750	T2	9.75616E-03
94739	T2	4.13959E-03	34759	T2	1.89159E-02	34760	T2	1.25400E-02	954739	T2	1.06440E-02
24739	T2	3.78123E-03	924003	T1	5.34944E-03	924003	T2	6.35297E-01	924003	T3	5.20046E-03
924002	T2	7.03049E-03	206002	T1	4.29644E-03	206002	T2	3.02564E-03	206002	T3	3.37403E-03
206003	T2	3.02569E-03	924003	T1	5.65192E-03	35017	T2	2.45722E-02	35017	T3	4.31617E-03
35019	T2	5.70412E-03	35020	T2	5.70412E-03	35023	T2	7.94402E-03	35024	T2	1.05920E-02
35033	T2	2.33686E-02	35033	T2	4.59936E-03	35050	T2	9.59861E-02	35050	T3	1.81490E-02
35050	T2	2.91605E-03	935050	T2	4.33920E-02	935050	T3	9.36701E-03	36098	T2	3.32945E-03
36110	T2	3.38944E-03	36111	T2	4.59628E-03	31601	T2	7.62422E-03	32500	T2	3.48649E-02
936150	T2	5.99962E-03									
COLUMN 7											
20290	R1	1.93361E-01	20290	R3	6.06633E-01						
COLUMN 8											
23056	R3	6.76771E-01	23058	R3	4.40327E-02	25060	R2	3.21999E-02	25060	R3	3.98799E-02
COLUMN 9											
25057	R3	7.53721E-01	25059	R3	8.74358E-02	25061	R2	6.17168E-02	25061	R3	8.46551E-02
COLUMN 10											
11508	R3	9.84797E-01									

Fig. 4 - AAH kinetic energy distribution for 3 percent filter (sheet 1 of 3)

	POINT	KENG	VALUE	POINT	VALUE	POINT	VALUE	POINT	VALUE	POINT	VALUE					
COLUMN	11															
	20512	R1	4.99613E-01	920312	R1	5.00086E-01										
COLUMN	12															
	20312	R1	5.00086E-01	920312	R1	4.99613E-01										
COLUMN	13															
	2499	T2	4.49602E-02	25099	T2	3.59977E-02	54	T2	1.99197E-02	924003	T2	1.15089E-02	924002	T2	1.26887E-02	
	206002	T1	1.86654E-02	206003	T1	1.92727E-02	55017	T2	1.23207E-02	55033	T2	7.00738E-02	55037	T2	8.71463E-03	
	55050	T2	2.72716E-01	55050	R1	9.28408E-03	55000	T2	1.23368E-02	955050	T2	1.49343E-01				
COLUMN	14															
	206002	T2	3.86021E-01	926002	T2	8.42872E-02	206003	T2	3.84610E-01	926003	T2	8.39936E-02				
COLUMN	15															
	25055	R2	1.11255E-01	25055	R3	1.08971E-02	25057	R3	2.46059E-01	25059	R3	2.61232E-01	25061	R2	2.84496E-01	
	25061	R3	2.55403E-01													
COLUMN	16															
	10066	T1	3.76302E-01	10066	T3	4.44566E-02	10066	R2	4.10972E-01	24739	T2	1.67348E-02	24738	T2	1.37769E-02	
COLUMN	17															
	2499	T3	8.70494E-03	11571	R2	3.56592E-03	10066	T1	6.15089E-02	10066	T3	2.92603E-03	10066	R2	7.22526E-02	
	25009	T3	4.01238E-03	21251	T1	1.19809E-02	21251	T2	3.57767E-02	21251	T3	2.86140E-02	24739	T1	1.08492E-02	
	24739	T2	9.71793E-02	24739	T3	9.99741E-03	24739	R3	6.40979E-03	924003	T1	8.05996E-02	924003	T3	2.17123E-02	
	924003	R1	4.95507E-03	924003	R2	1.82745E-02	924003	R3	6.58382E-02	21250	T1	1.01966E-02	21250	T2	3.04810E-02	
	21250	T3	2.21983E-02	24738	T1	8.28235E-03	24738	T2	8.31203E-02	24738	T3	7.34821E-03	24738	R3	4.35507E-03	
	924002	T1	4.61601E-02	924002	T3	1.42182E-02	924002	R1	4.05049E-03	924002	R2	1.36537E-02	924002	R3	3.50222E-02	
	206002	T1	3.55569E-03	206003	T1	3.68360E-03	55033	T1	3.05330E-03	55033	T3	3.30951E-03	55050	T1	1.98798E-02	
	55050	T3	1.02951E-02	955050	T1	1.04969E-02	955050	T3	5.61921E-03							
COLUMN	18															
	25054	R2	1.93436E-02	25054	R3	1.26640E-02	25056	R3	1.21799E-01	25058	R3	3.01456E-01	25060	R2	2.48245E-01	
	25060	R3	2.75077E-01													
COLUMN	19															
	11570	R2	5.97063E-02	11570	T1	1.48940E-02	11571	T1	3.13780E-01	11571	R2	4.56667E-01	11572	T1	2.33283E-02	
COLUMN	20															
	2499	T2	1.04210E-02	13499	T2	2.62804E-02	25099	T2	1.59708E-02	54	T2	1.12263E-02	206002	T2	3.42202E-01	
	926002	T2	6.15708E-02	206003	T2	3.45403E-01	926003	T2	6.21587E-02							
COLUMN	21															
	2499	T3	5.68796E-02	5702	T3	1.84094E-02	5709	T3	4.92800E-03	6025	T3	3.74534E-03	10011	T3	5.92359E-03	
	10012	T3	5.22809E-03	10514	T3	3.84653E-03	11571	T1	7.73849E-03	11571	R2	4.22291E-02	15411	T1	2.67034E-03	
	10020	T3	4.46282E-03	10066	T3	5.90624E-03	25099	T3	3.29896E-02	32001	T3	3.26430E-03	94730	T3	8.99918E-03	
	24739	T3	8.01378E-03	24760	T3	6.86177E-03	934759	T3	5.69463E-03	51	T1	4.40922E-03	54	T1	5.68297E-02	
	54	T3	4.81714E-03	59	T1	3.13918E-03	21251	T2	9.04951E-03	24739	T2	3.03180E-02	24739	T3	1.38969E-02	
	924003	T1	7.75710E-03	924003	T3	3.83410E-03	924003	R2	7.26371E-03	924003	R3	1.91203E-02	21250	T2	7.57169E-02	
	24738	T2	2.40090E-02	24738	T3	1.34176E-02	924002	T1	7.08312E-03	924002	T3	6.10788E-03	924002	R2	8.62404E-03	
	924002	R3	1.59216E-02	206002	T2	2.79349E-03	55017	T1	9.79156E-03	55017	T3	4.86563E-03	55019	T3	8.87279E-03	
	55020	T3	2.87873E-03	55023	T3	4.54949E-03	55024	T1	2.89679E-03	55024	T3	4.86449E-03	55033	T1	2.89758E-02	
	955050	T1	4.55359E-02	955050	T3	2.48149E-02	92900	T3	5.53812E-03				55080	T1	3.84359E-03	
COLUMN	22															
	8004	R3	9.95549E-01													
COLUMN	23															
	5702	R2	9.58719E-01													
COLUMN	24															
	15411	T1	6.26794E-02	15411	R2	8.81807E-01										
COLUMN	25															
	54	T2	4.15240E-03	21251	T1	1.03438E-02	21251	T2	3.66187E-02	21251	T3	7.54881E-02	24739	T1	8.64056E-03	
	24739	T2	4.45264E-02	24739	T3	3.8963E-02	24739	R2	4.22346E-03	24739	R3	4.16049E-03	924003	T1	4.41461E-02	
	924003	T2	8.27189E-03	924003	T3	4.77148E-02	924003	R1	1.33148E-02	924003	R2	5.41770E-02	924003	R3	4.27310E-02	
	21250	T1	1.40520E-02	21250	T2	4.35800E-02	21250	T3	7.69219E-02	24738	T1	1.13958E-02	24738	T2	6.93311E-02	
	24738	T3	3.68040E-02	24738	R2	4.07702E-03	24738	R3	4.53594E-03	924002	T1	6.26201E-02	924002	T2	2.88758E-03	
	924002	T3	3.60039E-02	924002	R1	1.44121E-02	924002	R2	5.51055E-02	924002	R3	5.75073E-02	206002	T1	5.85185E-03	
	206002	T3	2.56234E-03	206003	T1	7.53430E-03	206003	T2	2.67111E-03	926003	T1	2.64620E-03				
COLUMN	26															
	10514	T2	2.49201E-02	10514	T3	1.09805E-01	10514	R1	2.80610E-01	15426	R3	6.49367E-01				
COLUMN	27															
	10514	T2	4.64193E-02	10514	T3	2.17794E-01	10514	R1	3.87009E-01	15426	R3	3.35935E-01				
COLUMN	28															
	54759	T2	1.84020E-02	54760	T2	1.73081E-02	934759	T2	1.50806E-02	206002	T1	2.55841E-01	206002	T3	2.14222E-02	
	926002	T1	8.49008E-02	926002	T3	9.63431E-03	206003	T1	2.94023E-01	206003	T3	2.44058E-02	926003	T1	9.70028E-02	
	926003	T3	1.89494E-02													
COLUMN	29															
	5722	R3	4.70788E-01	11508	R2	3.69086E-01	11571	R2	5.94963E-02	11571	R3	1.85057E-02				
COLUMN	30															
	5722	R3	3.96483E-01	11508	R2	4.06989E-01	11571	R2	2.80060E-02	11571	R3	2.17385E-02	206002	T1	1.81742E-02	
	206003	T1	2.26687E-02													
COLUMN	31															
	2499	T3	8.80297E-03	5722	R3	6.98430E-02	15406	R3	3.19531E-02	206002	T1	2.63161E-01	206002	T3	3.95623E-02	
	926002	T1	8.27710E-02	926002	T3	1.83931E-02	206003	T1	2.27115E-01	206003	T3	3.49117E-02	926003	T1	7.10483E-02	
	926003	T3	1.62567E-02													
COLUMN	32															
	15406	R3	9.49624E-01													
COLUMN	33															

Fig. 4 - AAH kinetic energy distribution for 3 percent filter (sheet 2 of 3)

POINT	KENO	VALUE	POINT	VALUE	POINT	VALUE	POINT	VALUE	POINT	VALUE
2499 T2	8.32971E-02		2499 R1	8.50472E-03	3534 T2	4.76156E-03	5701 T2	4.58779E-03	5702 T2	1.88699E-02
8401 T2	1.78909E-02		8401 R1	5.87151E-03	8403 T2	1.87400E-02	8403 R1	5.15308E-03	11506 T2	4.49711E-03
11506 R2	4.10404E-03		11530 T2	3.71721E-03	11570 T2	8.70400E-03	11571 T2	1.87916E-01	11572 T2	1.08035E-02
12023 T2	5.35385E-03		12024 T2	5.39360E-03	14303 T2	1.12203E-02	14303 R1	3.46613E-03	15405 R3	7.39597E-03
15499 T2	8.51267E-03		10020 T2	6.97967E-03	25499 T2	2.46490E-02	50506 T2	4.58468E-03	50518 T2	4.50470E-03
54738 T2	3.28812E-03		54745 T2	3.61742E-03	54750 T2	8.66494E-03	54757 T2	1.09006E-02	54758 T2	1.09006E-02
54759 T2	5.72171E-02		54760 T2	5.72471E-02	954759 T2	4.29071E-02	924003 T2	4.49865E-03	924002 T2	5.44264E-03
206002 T1	1.50537E-02		206002 T2	3.35688E-03	926002 T1	4.39705E-03	206003 T1	1.79400E-02	926003 T1	5.23694E-03
55050 T2	1.23638E-02		55050 R1	6.82417E-03	55050 R3	5.18771E-03	955050 T2	8.01531E-03	56009 T1	3.81297E-03
56032 T1	3.68927E-03		56098 T1	4.27539E-03	56098 T2	5.89150E-03	56098 T3	3.47911E-03	56099 T1	5.72747E-03
56099 T2	9.29263E-03		56099 T3	4.75215E-03	56110 T1	4.11379E-03	56110 T2	5.89167E-03	56111 T1	5.79906E-03
56111 T2	9.29178E-03		56111 T3	4.18205E-03	52500 T2	1.30605E-02	956150 T2	5.59484E-03		
COLUMN 34			COLUMN 34		COLUMN 34		COLUMN 34		COLUMN 34	
15411 T1	6.34853E-01		15411 T3	4.44835E-02	15411 R2	7.81788E-02	15413 T1	2.43908E-02	15415 T1	5.65160E-02
COLUMN 35			COLUMN 35		COLUMN 35		COLUMN 35		COLUMN 35	
2499 T3	1.88670E-02		10510 T3	5.44388E-03	10510 R1	4.28595E-03	15411 T1	2.15228E-02	21251 T3	5.32915E-02
24739 T2	2.14260E-02		24739 T3	8.00464E-02	924003 T1	1.92578E-02	924003 T2	2.82751E-02	924003 T3	5.94390E-02
924003 R1	7.54921E-03		924003 R2	2.34328E-02	21250 T3	5.97197E-02	24738 T2	1.48787E-02	24738 T3	9.08379E-03
924002 T1	1.15341E-02		924002 T2	3.68359E-02	924002 T3	5.80346E-02	924002 R1	9.91853E-03	924002 R2	2.80720E-02
55017 T1	7.43085E-03		55033 T1	3.75256E-02	55037 T1	4.61963E-03	55050 T1	1.42830E-01	55050 T3	7.98866E-03
55050 T1	6.53275E-03		955050 T1	7.63743E-02	52500 T3	1.21550E-02				
COLUMN 36			COLUMN 36		COLUMN 36		COLUMN 36		COLUMN 36	
10510 T2	8.26210E-02		10510 T3	3.42027E-01	10510 R1	4.71918E-01				
COLUMN 37			COLUMN 37		COLUMN 37		COLUMN 37		COLUMN 37	
2499 T3	2.40958E-02		5702 T3	5.51235E-03	10510 T3	1.46574E-02	10510 R1	2.22657E-02	11571 T2	8.06633E-03
10020 T3	3.64012E-03		10064 T3	4.65264E-03	25001 T3	3.58473E-03	25099 T3	6.58586E-03	54 T3	5.81000E-03
21251 T3	3.68096E-02		24739 T2	2.48834E-02	24739 T3	1.79198E-02	924003 T2	3.42191E-02	924003 T3	2.19988E-02
924003 R1	7.25684E-03		924003 R2	2.49674E-02	924003 R3	5.49822E-03	21250 T3	3.64611E-02	24738 T2	1.93800E-02
24738 T3	9.60588E-03		924002 T2	3.44511E-02	924002 T3	2.45587E-02	924002 R1	4.45033E-03	924002 R2	2.05911E-02
924002 T1	3.57816E-03		206002 T1	4.71234E-03	206002 T2	1.32954E-02	924002 T3	7.12787E-03	206003 T3	1.32900E-02
924003 T3	7.10440E-03		55017 T1	4.91991E-03	55017 T3	3.70758E-03	55033 T1	3.60418E-02	55037 T1	3.79932E-03
55050 T1	1.16382E-01		55050 T3	1.17171E-02	55050 R1	5.94485E-03	955050 T1	6.24038E-02	955050 T3	4.69458E-03
17431 T2	1.74079E-02		17435 T2	5.52293E-03	52500 T3	1.32943E-02				
COLUMN 38			COLUMN 38		COLUMN 38		COLUMN 38		COLUMN 38	
2499 T2	1.03422E-02		8401 T2	1.16732E-02	8401 R1	6.38066E-03	8403 T2	1.22074E-02	8403 R1	8.81952E-03
10012 T2	1.18208E-03		10510 T2	8.05114E-03	10510 R3	1.59150E-03	11506 T2	6.45594E-03	11508 R1	4.58074E-03
11530 T2	5.48389E-03		11570 T2	1.21321E-02	11571 T2	1.99446E-01	11572 T2	1.59873E-02	14303 T2	4.18984E-02
14303 R1	9.11756E-02		14303 R3	9.44841E-03	15499 T2	1.03588E-02	25499 T2	2.66032E-02	54759 T2	1.10550E-02
54740 T2	1.19933E-02		954759 T2	8.86307E-03	54 T2	2.88551E-02	924003 T3	6.87024E-03	21250 T3	7.28249E-03
24738 T3	1.37363E-02		924002 T2	4.92491E-03	924002 T3	1.06453E-02	206002 T1	6.08838E-03	206003 T1	9.19992E-03
55050 T1	8.56409E-03		17431 T2	1.15519E-01	17435 T2	4.99319E-02				
COLUMN 39			COLUMN 39		COLUMN 39		COLUMN 39		COLUMN 39	
8401 R1	5.96247E-02		8401 R3	5.11478E-02	11570 T1	1.24352E-02	11571 T1	9.41740E-02	11571 R2	9.89107E-02
11571 R3	2.53723E-02		14303 T2	2.88964E-02	14303 T3	4.74361E-02	14303 R1	3.91521E-01	17431 T2	3.13836E-02

Fig. 4 - AAH kinetic energy distribution for 3 percent filter (sheet 3 of 3)

K001																	
POINT		VALUE	POINT		VALUE	POINT		VALUE	POINT		VALUE	POINT		VALUE	POINT		VALUE
206004 T1	4.48153E-03		926002 T1	8.27710E-02		926002 T3	1.83931E-02		206003 T1	2.27113E-01		206003 T3	3.49117E-02				
206007 T1	3.75294E-03		926003 T1	7.10483E-02		926003 T3	1.62367E-02		55050 T1	4.01898E-03							
COLUMN	32																
	15406 R3	9.49624E-01															
COLUMN	33																
2499 T2	8.32971E-02		2499 R1	8.50472E-03		3502 T2	1.30009E-03		3534 T2	4.76154E-03		5701 T2	4.58779E-03				
5702 T2	1.88699E-02		3703 T2	2.44644E-03		3709 T2	1.32184E-03		5722 R3	2.86881E-03		8401 T2	1.78909E-02				
8401 R1	5.87151E-03		8401 R3	1.58121E-03		8403 T2	1.87400E-02		8403 R1	5.15308E-03		8403 R3	1.38656E-03				
10012 T2	1.35890E-03		10012 T3	1.83867E-03		11502 T2	2.93499E-03		11506 T2	4.49711E-03		11508 R1	3.13571E-03				
11508 R2	4.18948E-03		11530 T2	3.71133E-03		11534 T2	1.39894E-03		11840 T2	2.23784E-03		11570 T2	8.26240E-02				
11571 T2	1.07914E-01		11572 T2	1.08000E-02		12021 T2	1.20683E-03		12022 T2	1.21248E-03		12023 T2	5.35385E-03				
12024 T2	5.39360E-03		14301 T2	2.44807E-03		14303 T2	1.12203E-02		14303 R1	3.46613E-03		14303 R3	2.24323E-03				
15406 R3	7.39597E-03		15426 R3	2.72366E-03		15499 T2	6.51267E-03		10020 T2	6.97967E-03		10028 T2	1.11557E-03				
10064 T2	3.11733E-03		25099 T2	2.46890E-02		50306 T2	4.58468E-03		50318 T2	4.32470E-03		53135 T2	1.56340E-03				
54735 T2	1.42792E-03		54738 T2	3.28812E-03		54745 T2	3.61742E-03		54750 T2	8.66494E-03		54757 T2	1.09006E-02				
54758 T2	1.09006E-02		54759 T2	5.72171E-02		54759 R1	2.08170E-03		54760 T2	5.72471E-02		934759 T2	4.29071E-02				
924003 T2	1.48994E-03		924003 T3	4.49865E-03		21250 T2	1.15023E-03		924002 T2	5.44264E-03		206002 T1	1.50937E-02				
206002 T2	3.35688E-03		926002 T1	4.39705E-03		206003 T1	1.79400E-02		206003 T2	2.85508E-03		926003 T3	5.23694E-03				
55017 T2	8.01531E-03		55019 T2	2.25264E-03		55020 T2	2.25264E-03		55023 T2	2.04173E-03		55024 T2	2.72263E-03				
55033 T1	1.18880E-03		55033 R1	1.24235E-03		55033 T3	1.25392E-03		55050 T2	1.23638E-02		55050 R1	6.82417E-03				
55050 R3	5.18771E-03		55060 T2	2.44525E-03		55060 T3	1.14829E-03		955050 T2	6.01531E-03		56020 T1	3.81297E-03				
56020 T2	1.40394E-03		56020 T3	2.70468E-03		56032 T1	3.69927E-03		56032 T2	1.40413E-03		56032 T3	3.00834E-03				
56071 T1	1.43931E-03		56071 T3	1.13774E-03		56074 T2	1.69233E-03		56082 T2	1.69245E-03		56087 T1	1.44182E-03				
56087 T3	1.10886E-03		56099 T1	4.27539E-03		56098 T2	5.89150E-03		56098 T3	3.47911E-03		56099 T1	5.72247E-03				
56099 T2	9.29263E-03		56099 T3	4.75215E-03		56110 T1	4.11379E-03		56110 T2	5.89167E-03		56110 T3	3.06173E-03				
56111 T1	9.29178E-03		56111 T2	2.91929E-03		56111 T3	4.18205E-03		56121 T2	1.38258E-03		56127 T2	1.58293E-03				
56140 T2	1.82440E-03		56141 T2	2.24400E-03		56142 T2	1.52448E-03		56143 T2	2.24404E-03		56144 T2	1.87515E-03				
56147 T2	8.13628E-03		17431 T2	3.22667E-03		17435 T2	1.22310E-03		51601 T2	3.09295E-03		52500 T2	1.30605E-02				
56150 T2	1.93631E-03		956150 T2	5.59484E-03		956150 R1	1.58087E-03										
COLUMN	34																
15411 T1	6.34853E-01		15411 T3	4.44835E-02		15411 R2	7.81788E-02		15413 T1	2.43908E-02		15415 T1	5.65160E-02				
15415 R3	6.89315E-03		15417 R3	7.69375E-03		15419 R3	8.39912E-03		55050 T1	8.18760E-03							
COLUMN	35																
2499 T3	1.88670E-02		3702 T3	4.24735E-03		3709 T3	1.53480E-03		10011 T3	1.65140E-03		10510 T3	5.44388E-03				
10010 R1	4.28595E-03		15411 T2	2.13228E-02		15411 T3	1.71239E-03		15411 R2	2.62407E-03		15415 T1	1.82384E-03				
25001 T3	1.37831E-03		38001 T3	2.52207E-03		42326 T3	1.56905E-03		45001 T3	2.26101E-03		50306 T3	3.28905E-03				
50318 T3	3.08700E-03		54 T3	2.09980E-03		21251 T3	5.32915E-02		21251 T3	5.32915E-02		24739 T1	2.62574E-03				
24739 T2	2.14260E-02		24739 T3	8.00464E-02		24739 R2	1.98272E-03		25059 T2	1.42874E-03		924003 T1	1.92578E-02				
924003 T2	2.82751E-02		924003 T3	5.94390E-02		924003 T3	7.86921E-03		924003 R2	2.82751E-02		924003 R3	4.24180E-03				
21250 T3	5.97197E-02		12020 T2	2.04510E-03		21250 T3	5.97197E-02		24738 T1	1.48787E-02		24738 T2	1.48787E-02				
24738 T2	1.48787E-02		24738 T3	2.07493E-03		924002 T2	1.15341E-02		924002 T2	3.68359E-02		924002 T3	5.80346E-02				
924002 T3	5.80346E-02		206002 T2	2.80720E-02		924002 T3	1.84473E-03		206002 T3	1.74098E-03		206003 T3	1.96094E-02				
55017 T1	7.43085E-03		55017 T3	3.65393E-03		55018 T1	1.93317E-03		55023 T1	2.93973E-03		55024 T1	3.89475E-03				
55027 T1	2.85642E-03		55033 T1	3.75256E-02		55037 T1	4.61963E-03		55038 T1	1.48044E-03							
55050 T1	7.78804E-03		55052 T1	1.40822E-03		55055 T1	2.78029E-03		55700 T1	2.37494E-03		55800 T1	6.53275E-03				
955050 T1	7.63743E-02		955050 T3	2.89928E-03		956051 T3	2.11419E-03		52500 T3	1.21550E-02							

	POINT	KE05	VALUE	POINT	VALUE	POINT	VALUE	POINT	VALUE	POINT	VALUE
COLUMN	31										
	5722 R3	6.90430E-02	15406 R3	5.19531E-02	206002 T1	2.63161E-01	206002 T3	5.95623E-02	926002 T1	8.27710E-02	
	926002 T3	1.83931E-02	206003 T1	2.27115E-01	206003 T3	3.49117E-02	926003 T1	7.10463E-02	926003 T3	1.62567E-02	
COLUMN	32										
	15406 R3	9.49624E-01									
COLUMN	33										
	2499 T2	8.32971E-02	2499 R1	8.50472E-03	5702 T2	1.88699E-02	8401 T2	1.78909E-02	8401 R1	5.87151E-03	
	8403 T2	1.87480E-02	11570 T2	8.20400E-03	11571 T2	1.07914E-01	11572 T2	1.08088E-02	14303 T2	1.12203E-02	
	15406 R3	7.39597E-03	15499 T2	8.51267E-03	10020 T2	6.97967E-03	25899 T2	2.46890E-02	54750 T2	8.66494E-03	
	54757 T2	1.89084E-02	54758 T2	1.09007E-02	54759 T2	5.72171E-02	54760 T2	5.72471E-02	934759 T2	4.29071E-02	
	924002 T2	5.44264E-03	204002 T1	1.50537E-02	204003 T1	1.79400E-02	55050 T2	1.23638E-02	55050 R1	6.82417E-03	
	935050 T2	8.81531E-03	56096 T2	5.89130E-03	56099 T1	5.72247E-03	56099 T2	9.29263E-03	56110 T2	5.89167E-03	
	56111 T1	5.70996E-03	56111 T2	9.29178E-03	52500 T2	1.30605E-02					
COLUMN	34										
	15411 T1	6.34853E-01	15411 T3	4.64835E-02	15411 R2	7.81768E-02	15415 T1	5.65160E-02			
COLUMN	35										
	2499 T3	1.80670E-02	15411 T1	2.15228E-02	21251 T3	5.32913E-02	24739 T2	2.14260E-02	24739 T3	8.00464E-03	
	924003 T1	1.52578E-02	924003 T2	2.82751E-02	924003 T3	5.94390E-02	924003 R1	7.56421E-03	924003 R2	2.54328E-02	
	21250 T3	5.97197E-02	24738 T2	1.46787E-02	24738 T3	9.08379E-03	924002 T1	1.15341E-02	924002 T2	3.68359E-02	
	924002 T3	5.80366E-02	924002 R1	9.91833E-03	924002 R2	2.80720E-02	55017 T1	7.43085E-03	55033 T3	3.75256E-02	
	55050 T1	1.42830E-01	55050 T3	7.98866E-03	935050 T1	7.63743E-02	52500 T3	1.21550E-02			
COLUMN	36										
	10510 T2	8.26210E-02	10510 T3	5.62027E-01	10510 R1	4.71918E-01					
COLUMN	37										
	2499 T3	2.40958E-02	10510 T3	1.46574E-02	10510 R1	2.22657E-02	11571 T2	8.06663E-03	25899 T3	6.58586E-03	
	21251 T3	3.68096E-02	24739 T2	2.68834E-02	24739 T3	1.79198E-02	924003 T2	3.42151E-02	924003 T3	7.19988E-02	
	924003 R1	7.23684E-03	924003 R2	2.69679E-02	21250 T3	3.64611E-02	24738 T2	1.93890E-02	24738 T3	9.60588E-03	
	924002 T2	3.44519E-02	924002 T3	2.65587E-02	924002 R1	9.45635E-03	924002 R2	2.05931E-02	206002 T3	1.32954E-02	
	924002 T3	7.32707E-03	204003 T3	1.32960E-02	926003 T3	7.10460E-03	55033 T1	3.00410E-02	55050 T1	1.16302E-01	
	55050 T3	1.17171E-02	935050 T1	6.24030E-02	17631 T2	1.28079E-02	52500 T3	1.32943E-02			
COLUMN	38										
	2499 T2	1.03422E-02	8401 T2	1.16732E-02	8403 T2	1.22076E-02	8403 R1	8.81958E-03	10510 T3	8.03516E-03	
	10510 R1	8.39935E-03	11370 T2	1.21321E-02	11371 T2	1.99666E-01	11372 T2	1.89073E-02	14303 T2	4.14966E-02	
	14303 R1	9.11756E-02	14303 R3	9.44841E-03	15499 T2	1.03588E-02	25899 T2	2.64832E-02	54759 T2	1.10550E-02	
	54760 T2	1.19933E-02	934759 T2	8.86307E-03	94 T2	2.88341E-02	24738 T3	1.37363E-02	924002 R2	1.06453E-02	
	206003 T1	9.19992E-03	93050 T1	8.56499E-03	17631 T2	1.15519E-01	17633 T2	4.93319E-02			
COLUMN	39										
	8401 R1	5.96247E-02	8401 R3	3.11478E-02	11571 T1	9.41740E-02	11571 R2	9.85107E-02	11571 R3	2.53723E-02	
	14303 T2	2.88964E-02	14303 T3	4.74361E-02	14303 R1	3.91921E-01	17631 T2	3.13036E-02			
COLUMN	40										

Fig. 6 - AAH kinetic energy distribution for 5 percent filter

	POINT	KE10	VALUE	POINT	VALUE	POINT	VALUE	POINT	VALUE	POINT	VALUE				
	24739	T3	3.50963E-02	924003	T1	4.41401E-02	924003	T2	8.27189E-03	924003	T3	4.71489E-02	924003	R1	1.31168E-02
	924003	R2	5.41778E-02	924003	R3	4.27310E-02	21250	T1	1.40522E-02	21250	T2	4.95000E-02	21250	T3	7.49219E-02
	24738	T1	1.13938E-02	24738	T2	6.93311E-02	24738	T3	3.68040E-02	924002	T1	6.26201E-02	924002	T3	3.60039E-02
	924002	R1	1.44121E-02	924002	R2	5.51035E-02	924002	R3	5.73073E-02						
COLUMN	26														
	10514	T3	1.09885E-01	10514	R1	2.00618E-01	15426	R3	6.49367E-01						
COLUMN	27														
	10514	T2	4.64193E-02	10514	T3	2.17796E-01	10514	R1	3.87009E-01	15426	R3	5.35935E-01			
COLUMN	28														
	206002	T1	2.55841E-01	926002	T1	8.49088E-02	206003	T1	2.94023E-01	926003	T1	9.70028E-02			
COLUMN	29														
	5722	R3	4.70788E-01	11508	R2	3.69086E-01	11571	R2	5.54563E-02						
COLUMN	30														
	5722	R3	3.96483E-01	11508	R2	4.04989E-01									
COLUMN	31														
	5722	R3	6.90430E-02	15406	R3	3.19531E-02	206002	T1	2.63161E-01	206002	T3	5.95623E-02	926002	T1	8.27710E-02
	206003	T1	2.27115E-01	206003	T3	3.49117E-02	926003	T1	7.10463E-02						
COLUMN	32														
	15406	R3	9.49624E-01												
COLUMN	33														
	2499	T2	8.32971E-02	5702	T2	1.88699E-02	8401	T2	1.78909E-02	8403	T2	1.87480E-02	11571	T2	1.07914E-01
	11372	T2	1.08088E-02	14303	T2	1.12203E-02	25899	T2	2.46890E-02	54757	T2	1.09006E-02	54758	T2	1.09007E-02
	54759	T2	5.72171E-02	54760	T2	5.72471E-02	934759	T2	4.29071E-02	206002	T1	1.50537E-02	206003	T1	1.79400E-02
	55050	T2	1.23638E-02	52500	T2	1.30605E-02									
COLUMN	34														
	15411	T1	6.34853E-01	15411	R2	7.81768E-02									
COLUMN	35														
	2499	T3	1.80670E-02	15411	T1	2.19228E-02	21251	T3	5.32913E-02	24739	T2	2.14260E-02	924003	T1	1.52578E-02
	924003	T2	2.82731E-02	924003	T3	5.94390E-02	924003	R2	2.54328E-02	21250	T3	5.97197E-02	24738	T2	1.40787E-02
	924002	T2	3.40535E-02	924002	T3	5.80366E-02	924002	R2	2.80720E-02	55033	T1	5.75256E-02	55050	T1	1.42830E-01
	935050	T1	7.63743E-02												
COLUMN	36														
	10510	T2	8.26210E-02	10510	T3	5.62027E-01	10510	R1	4.71918E-01						
COLUMN	37														
	2499	T3	2.40958E-02	10510	T3	1.46574E-02	10510	R1	2.22657E-02	21251	T3	3.68096E-02	24739	T2	2.68834E-02
	24739	T3	1.79198E-02	924003	T2	5.94390E-02	924003	T3	2.19988E-02	924003	R2	2.69679E-02	21250	T3	3.64611E-02
	24738	T2	1.93890E-02	924002	T2	3.44519E-02	924002	T3	2.65587E-02	924002	R2	2.05931E-02	206002	T3	1.32954E-02
	206003	T3	1.32960E-02	55033	T1	3.00410E-02	55050	T1	1.16302E-01	935050	T3	1.17171E-02	935050	T1	6.24030E-02

Fig. 7 - AAH kinetic energy distribution for 10 percent filter

	POINT	MAX	VALUE	PC		POINT	MAX	VALUE
COLUMN	1					24739 T2	9.71793E-02	
	54 T2	6.40100E-02		COLUMN	18			
COLUMN	2				25058 R3	3.01456E-01		
	15499 T2	5.63392E-02		COLUMN	19			
COLUMN	3				11571 R2	4.56667E-01		
	54 T2	2.40146E-01		COLUMN	20			
COLUMN	4				206003 T2	3.45403E-01		
	25899 T1	8.98618E-02		COLUMN	21			
COLUMN	5				55050 T1	8.58553E-02		
	55050 T3	1.07995E-01		COLUMN	22			
COLUMN	6				8004 R3	9.95549E-01		
	55050 T2	9.59861E-02		COLUMN	23			
COLUMN	7				5702 R2	9.58719E-01		
	20290 R3	8.06633E-01		COLUMN	24			
COLUMN	8				15411 R2	8.81207E-01		
	25056 R3	8.76771E-01		COLUMN	25			
COLUMN	9				21250 T3	7.69219E-02		
	25037 R3	7.53721E-01		COLUMN	26			
COLUMN	10				15426 R3	4.49367E-01		
	11508 R3	9.84797E-01		COLUMN	27			
COLUMN	11				10314 R1	3.87009E-01		
	920312 R1	5.00086E-01		COLUMN	28			
COLUMN	12				206003 T1	2.94023E-01		
	20312 R1	5.00084E-01		COLUMN	29			
COLUMN	13				5722 R3	4.70788E-01		
	55050 T2	2.72716E-01		COLUMN	30			
COLUMN	14				11508 R2	4.06989E-01		
	206002 T2	3.86021E-01		COLUMN	31			
COLUMN	15				206002 T1	2.63161E-01		
	25059 R3	2.61232E-01		COLUMN	32			
COLUMN	16				15406 R3	9.49624E-01		
	10066 R2	4.10972E-01		COLUMN	33			
COLUMN	17				11571 T2	1.07914E-01		
				COLUMN	34			

Fig. 8 - AAH kinetic energy maximum values

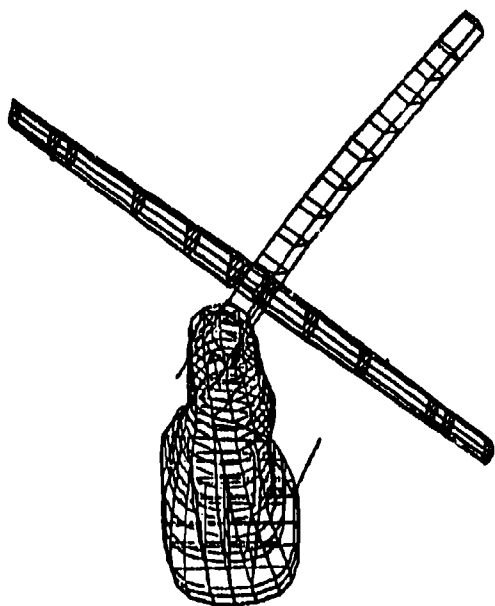


Fig. 9 - First torsion mode
(4.08 Hz)

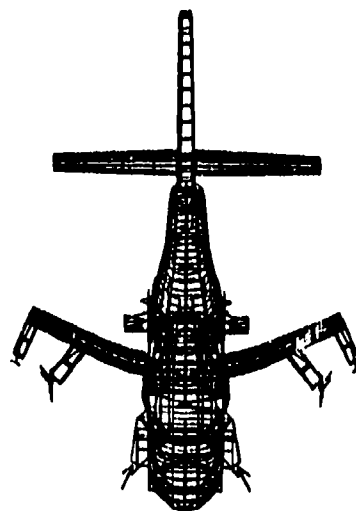


Fig. 10 - First symmetric wing
bending mode (4.70 Hz)



Fig. 11 - First wing antisymmetric mode (5.40 Hz)

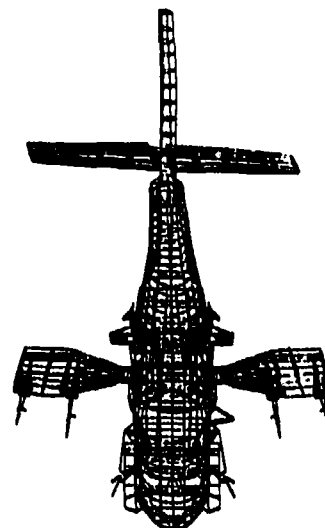


Fig. 14 - First symmetric wing/pylon torsion mode (7.91 Hz)



Fig. 12 - First vertical bending mode (5.55 Hz)

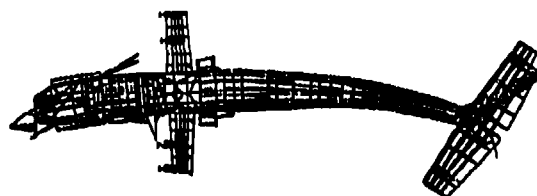


Fig. 15 - First lateral bending mode (8.85 Hz)

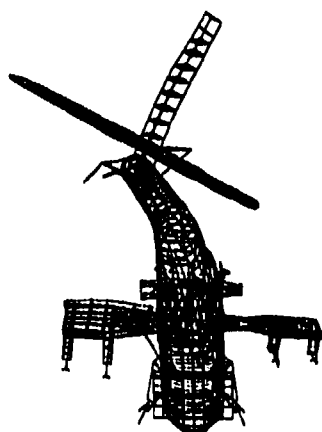


Fig. 13 - First antisymmetric wing/pylon torsion mode (7.59 Hz)



Fig. 16 - Second vertical bending mode (18.97 Hz)

TABLE 1
AAH Kinetic Energy Matrix

MODE NO.	EXTRACTION ORDER	EIGENVALUE	REAL EIGENVALUES		GENERALIZED MASS	GENERALIZED STIFFNESS
			RADIANS	CYCLES		
1	154	1.503159E-06	1.226034E-03	1.931294E-04	1.000000E+00	1.503159E-06
2	153	2.877026E-06	1.696413E-03	2.699929E-04	1.000000E+00	2.877026E-06
3	152	-6.397033E-06	2.097101E-03	3.337640E-04	1.000000E+00	-6.397033E-06
4	151	-1.329238E-05	4.043946E-03	6.436140E-04	1.000000E+00	-1.335350E-05
5	150	-1.022249E-04	1.020911E-02	1.624430E-03	1.000000E+00	-1.042269E-04
6	149	-1.124439E-04	1.668402E-02	1.687482E-03	1.000000E+00	-1.124452E-04
7	134	2.814975E+02	1.986498E+01	2.524999E+00	1.000000E+00	2.814975E+02
8	144	3.394329E+02	1.842370E+01	2.932224E+00	1.000000E+00	3.394329E+02
9	146	3.671488E+02	1.916111E+01	3.049508E+00	1.000000E+00	3.671488E+02
10	145	3.744222E+02	1.934999E+01	3.079647E+00	1.000000E+00	3.744222E+02
11	147	4.134077E+02	2.038136E+01	3.243826E+00	1.000000E+00	4.134077E+02
12	148	4.154104E+02	2.038148E+01	3.243836E+00	1.000000E+00	4.154104E+02
13	135	4.951513E+02	2.697394E+01	4.084135E+00	1.000000E+00	4.951513E+02
14	137	6.739556E+02	2.956274E+01	4.785454E+00	1.000000E+00	6.739556E+02
15	138	8.995762E+02	2.999294E+01	4.773524E+00	1.000000E+00	8.995762E+02
16	141	1.036046E+03	3.219370E+01	5.124103E+00	1.000000E+00	1.036046E+03
17	142	1.054047E+03	3.247848E+01	5.149098E+00	1.000000E+00	1.054047E+03
18	143	1.070243E+03	3.271437E+01	5.206486E+00	1.000000E+00	1.070243E+03
19	140	1.092594E+03	3.309440E+01	5.269772E+00	1.000000E+00	1.092594E+03
20	139	1.132577E+03	3.394909E+01	5.403105E+00	1.000000E+00	1.132577E+03
21	136	1.182578E+03	3.487657E+01	5.551121E+00	1.000000E+00	1.182578E+03
22	133	1.445548E+03	3.882032E+01	6.439450E+00	1.000000E+00	1.445548E+03
23	132	1.675495E+03	4.693281E+01	6.514668E+00	1.000000E+00	1.675495E+03
24	131	1.814368E+03	4.259466E+01	6.779151E+00	1.000000E+00	1.814368E+03
25	130	1.842669E+03	4.292632E+01	6.831937E+00	1.000000E+00	1.842669E+03
26	128	1.962234E+03	4.429734E+01	7.080101E+00	1.000000E+00	1.962234E+03
27	129	1.973041E+03	4.441892E+01	7.069491E+00	1.000000E+00	1.973041E+03
28	127	2.279596E+03	4.774302E+01	7.598337E+00	1.000000E+00	2.279596E+03
29	126	2.352183E+03	4.809931E+01	7.718490E+00	1.000000E+00	2.352183E+03
30	125	2.410700E+03	4.809135E+01	7.801400E+00	1.000000E+00	2.410700E+03
31	124	2.472794E+03	4.872719E+01	7.914329E+00	1.000000E+00	2.472794E+03
32	123	2.538250E+03	4.938103E+01	8.018393E+00	1.000000E+00	2.538250E+03
33	122	3.094273E+03	5.364416E+01	8.836444E+00	1.000000E+00	3.094273E+03
34	121	3.201632E+03	5.658297E+01	9.809439E+00	1.000000E+00	3.201632E+03
35	120	3.412053E+03	5.841278E+01	9.296482E+00	1.000000E+00	3.412053E+03
36	119	3.786035E+03	6.148605E+01	9.785009E+00	1.000000E+00	3.786035E+03
37	118	4.084782E+03	6.324989E+01	1.086444E+01	1.000000E+00	4.084782E+03
38	117	4.090181E+03	6.399480E+01	1.017860E+01	1.000000E+00	4.090181E+03
39	115	4.812588E+03	7.173729E+01	1.089203E+01	1.000000E+00	4.812588E+03
40	114	4.687183E+03	6.646278E+01	1.089619E+01	1.000000E+00	4.687183E+03
41	116	4.762547E+03	6.981121E+01	1.098347E+01	1.000000E+00	4.762547E+03
42	113	4.872593E+03	6.980372E+01	1.110961E+01	1.000000E+00	4.872593E+03
43	112	5.881446E+03	7.128486E+01	1.134524E+01	1.000000E+00	5.881446E+03
44	111	5.276135E+03	7.243701E+01	1.136054E+01	1.000000E+00	5.276135E+03
45	109	5.633276E+03	7.318827E+01	1.196588E+01	1.000000E+00	5.633276E+03
46	110	5.882885E+03	7.633746E+01	1.214789E+01	1.000000E+00	5.882885E+03
47	108	6.474789E+03	7.687489E+01	1.243889E+01	1.000000E+00	6.474789E+03
48	107	6.892219E+03	7.889264E+01	1.243206E+01	1.000000E+00	6.892219E+03
49	106	6.184311E+03	7.864839E+01	1.231401E+01	1.000000E+00	6.184311E+03
50	105	6.497409E+03	8.066051E+01	1.242892E+01	1.000000E+00	6.497409E+03
51	104	7.113297E+03	8.435198E+01	1.342503E+01	1.000000E+00	7.113297E+03
52	103	7.172596E+03	8.469118E+01	1.347902E+01	1.000000E+00	7.172596E+03
53	102	7.190366E+03	8.479602E+01	1.349371E+01	1.000000E+00	7.190366E+03
54	101	7.503084E+03	8.668035E+01	1.378606E+01	1.000000E+00	7.503084E+03
55	99	7.617732E+03	8.787973E+01	1.388190E+01	1.000000E+00	7.617732E+03
56	98	7.914151E+03	8.961815E+01	1.415204E+01	1.000000E+00	7.914151E+03
57	97	7.992456E+03	8.948054E+01	1.422454E+01	1.000000E+00	7.992456E+03
58	96	8.017249E+03	8.953989E+01	1.425659E+01	1.000000E+00	8.017249E+03
59	95	8.144947E+03	9.024936E+01	1.436363E+01	1.000000E+00	8.144947E+03
60	94	8.363991E+03	9.149486E+01	1.435549E+01	1.000000E+00	8.363991E+03
61	93	9.176838E+03	9.579174E+01	1.824573E+01	1.000000E+00	9.176838E+03
62	92	9.274713E+03	9.630531E+01	1.532747E+01	1.000000E+00	9.274713E+03
63	91	9.318743E+03	9.628266E+01	1.537806E+01	1.000000E+00	9.318743E+03
64	90	9.667599E+03	9.867599E+01	1.538185E+01	1.000000E+00	9.667599E+03
65	89	1.027569E+04	1.013639E+02	1.413339E+01	1.000000E+00	1.027569E+04
66	88	1.046912E+04	1.032914E+02	1.643934E+01	1.000000E+00	1.046912E+04
67	87	1.089468E+04	1.043783E+02	1.661233E+01	1.000000E+00	1.089468E+04
68	86	1.167572E+04	1.080542E+02	1.719737E+01	1.000000E+00	1.167572E+04
69	85	1.194183E+04	1.092787E+02	1.739224E+01	1.000000E+00	1.194183E+04
70	84	1.204504E+04	1.097499E+02	1.746724E+01	1.000000E+00	1.204504E+04
71	83	1.209909E+04	1.099938E+02	1.750638E+01	1.000000E+00	1.209909E+04
72	82	1.308407E+04	1.143891E+02	1.820359E+01	1.000000E+00	1.308407E+04
73	81	1.359436E+04	1.164231E+02	1.859232E+01	1.000000E+00	1.359436E+04
74	80	1.389628E+04	1.176825E+02	1.876159E+01	1.000000E+00	1.389628E+04
75	79	1.421188E+04	1.192136E+02	1.897343E+01	1.000000E+00	1.421188E+04
76	78	1.517835E+04	1.232013E+02	1.960809E+01	1.000000E+00	1.517835E+04
77	77	1.581879E+04	1.257728E+02	2.001736E+01	1.000000E+00	1.581879E+04
78	76	1.614858E+04	1.270771E+02	2.022494E+01	1.000000E+00	1.614858E+04
79	75	1.721972E+04	1.312239E+02	2.088494E+01	1.000000E+00	1.721972E+04
80	74	1.768014E+04	1.328914E+02	2.115033E+01	1.000000E+00	1.768014E+04
81	73	1.780116E+04	1.342102E+02	2.123461E+01	1.000000E+00	1.780116E+04
82	72	1.807441E+04	1.344911E+02	2.139496E+01	1.000000E+00	1.807441E+04
83	71	1.834283E+04	1.361721E+02	2.187246E+01	1.000000E+00	1.834283E+04
84	70	1.911240E+04	1.382476E+02	2.200279E+01	1.000000E+00	1.911240E+04
85	69	1.963132E+04	1.401118E+02	2.229949E+01	1.000000E+00	1.963132E+04
86	68	2.041288E+04	1.428736E+02	2.273905E+01	1.000000E+00	2.041288E+04
87	67	2.142814E+04	1.463635E+02	2.329766E+01	1.000000E+00	2.142814E+04
88	66	2.202301E+04	1.484815E+02	2.361883E+01	0.0	0.0
89	65	2.221770E+04	1.490560E+02	2.372300E+01	0.0	0.0
90	64	2.318244E+04	1.537831E+02	2.430343E+01	0.0	0.0
91	63	2.461962E+04	1.549964E+02	2.497984E+01	0.0	0.0
92	62	2.532725E+04	1.597725E+02	2.542858E+01	0.0	0.0
93	61	2.661328E+04	1.631358E+02	2.596386E+01	0.0	0.0
94	60	2.707541E+04	1.649461E+02	2.618832E+01	0.0	0.0
95	59	2.731590E+04	1.658767E+02	2.640010E+01	0.0	0.0
96	58	2.771614E+04	1.664817E+02	2.649638E+01	0.0	0.0
97	57	2.839774E+04	1.685163E+02	2.682020E+01	0.0	0.0
98	56	3.123282E+04	1.767266E+02	2.812691E+01	0.0	0.0
99	55	3.160885E+04	1.770844E+02	2.831468E+01	0.0	0.0
100	54	3.306885E+04	1.818484E+02	2.894207E+01	0.0	0.0

TABLE 2
Frequency Correlation Between Test Data and
Dynamic Nastran Analysis

Description	Frequency (Hz)		
	Test	Nastran	Percent Difference
Lat/Torsion	4.59	4.08	11.1
First Lateral Bending	9.37	8.85	5.54
First Vertical Bending	5.76	5.55	3.64
Second Vertical Bending	19.39	18.97	2.17
Second Lateral/Torsion	20.6	21.2	2.91

TABLE 3
Mode Identification Showing Comparison with Test Data

Nastran Mode No.	Nastran Frequency	Description	Test Mode, Frequency
13	4.08	Lat/Torsion	Lat/Tor 4.59
14	4.70	Sym Wing Bend	
17	5.17	Vert + Eng	
20	5.40	Anti/Sym Wing Bend	Vert 5.76
21	5.55	1st Vert	
25	6.83	Wing/Tor	
28	7.59	Anti/Sym Wing/Pylon Tor	
30	7.81	Sym Wing Tor	
31	7.91	Sym Wing/Pylon Tor	1st Lat Bend 9.37
33	8.85	1st Lat Bend	
35	9.30	Vert + Tail	
47	12.2	Stab Yaw	
49	12.5	Stab Yaw	
53	13.5	Wing Rigid Body	2nd Vert 19.38
57	14.2	Wing Tor Roll	
59	14.3	Wing Tor Roll	
60	14.5	Wing Sym	
63	15.7	Stab Roll	
64	15.8	Stab/Wing Roll	
66	16.4	Stab Yaw	
69	17.3	Tail/Stab Mode	
74	18.7	Vertical	
75	18.97	2nd Vert	
78	20.2	Lat/Tor Wing/Stab	2nd Lat/Tor 20.6
81	21.2	2nd Lat/Tor	
85	22.3	Vert + Stab	
86	22.7	Tail/Stab	

DISCUSSION

Mr. Wass (TKW): Has MSC added that to its capability?

Mr. Brown: No, not yet. They have stood behind their strain energy concept which we dynamicists don't care for, but so far, they haven't done that. They say they are looking into it.

DYNAMICS OF A SIMPLE SYSTEM SUBJECTED TO RANDOM IMPACT

T.T. Soong
Department of Civil Engineering
State University of New York at Buffalo
Amherst Campus, Buffalo, New York 14260

This paper is concerned with the impact characteristics of a simple mechanical system subjected to random collision or impact. The model analyzed is a simple one-degree-of-freedom mechanical system oscillating between two elastic reflectors when the supporting frame is subjected to a base motion modeled by a stationary random process. Quantities of interest are the statistical properties of the maximum force of impact when impact occurs and of the time to impact. Results are presented in a form so that they can be readily applied to the design of the restraining system for the oscillator as well as the reflectors.

INTRODUCTION

The study of dynamic behavior and impact characteristics of mechanical systems subjected to collision or impact is of importance in several engineering areas. In transportation and packaging, for example, systems being transported are subjected to frequent collisions with packaging material and with other contents. The dynamics of contents in structures under disturbances such as shocks or earthquakes also follows similar dynamic environment. Furthermore, many vibration isolation and damping devices, such as tuned mass dampers, operate with snubbers which produce collision forces.

In order to assess the integrity and survivability of systems in this kind of a dynamic environment, it is of practical importance to estimate the likelihood of impact occurrence and, when impact does occur, the maximum force of impact. The knowledge of these quantities can then lead to a safe system design for integrity and survivability.

In this paper, impact results are obtained for a simple mechanical system in one-dimensional motion between two elastic reflectors. As shown in Fig. 1, the frame which supports the system and the reflectors is assumed to be subjected to a stationary random excitation. Due to random nature of the base motion, probabilistic impact characteristics are of interest.

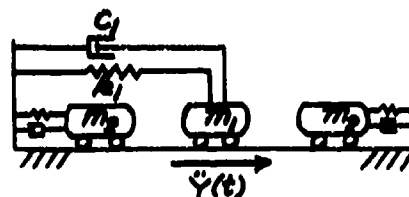


Fig. 1. A Simple Mechanical System

EQUATIONS OF MOTION

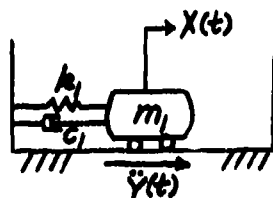
Consider the case in which the oscillator, m_1 , is executing stationary random motion due to base excitation. We are primarily interested in the maximum force of restitution when impact occurs between m_1 and one of the reflectors. The dynamic process for the purpose of this analysis can be divided into distinct phases as shown in Fig. 2 under a set of simplifying assumptions. As a first step, pertinent results are presented for each of these two dynamic phases.

Before Impact. Assuming that the rigidity of the reflectors is much greater than that of the oscillator so that their contribution to the impact velocity can be neglected, the system dynamics before impact can be modeled as that shown in Fig. 2(a) and the

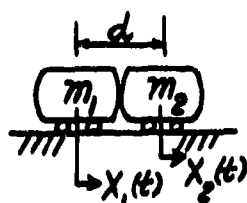
governing equation of motion is simply that of the oscillator given by

$$m_1 \ddot{X}(t) + c_1 \dot{X}(t) + k_1 X(t) = -m_1 \ddot{Y}(t) \quad (1)$$

where $\ddot{Y}(t)$ is a zero-mean Gaussian stationary random process with spectral density function $S(\omega)$.



(a) Before Impact



(b) During Impact

Fig. 2. Dynamic Process Approximations

Let

$$\begin{aligned} \omega_0^2 &= k_1/m_1 \\ 2\omega_0 \zeta &= c_1/m_1 \end{aligned} \quad (2)$$

Equation (1) becomes

$$\ddot{X}(t) + 2\omega_0 \zeta \dot{X}(t) + \omega_0^2 X(t) = -\ddot{Y}(t) \quad (3)$$

where ω_0 is the undamped natural frequency of m_1 and ζ the damping coefficient. The case where $\zeta < 1$ is of most practical interest.

The solution of Eq. (1) is well known [1, 2]. In particular, for a lightly-damped oscillator ($\zeta \ll 1$) and a smooth $S(\omega)$ with no sharp peaks, the response characteristics of the oscillator can be approximated by solving Eq. (1) with $\ddot{Y}(t)$ modeled by a white noise with zero mean and correlation function

$$E\{\ddot{Y}(t + \tau)\ddot{Y}(t)\} = 2D\delta(\tau) \quad (4)$$

with

$$D = \pi S(\omega_0)/2 \quad (5)$$

In this case, the stationary probability density functions of $X(t)$ and $\dot{X}(t)$ take the Gaussian form and the random variables X and \dot{X} are independent. Hence, the (stationary) joint density function of X and \dot{X} is

$$f_{X\dot{X}}(x, \dot{x}) = \frac{1}{2\pi\sigma_X\sigma_{\dot{X}}} \exp \left[-\frac{x^2}{2\sigma_X^2} - \frac{\dot{x}^2}{2\sigma_{\dot{X}}^2} \right] \quad (6)$$

where

$$\sigma_X^2 = \frac{D}{2\omega_0^3 \zeta}, \quad \sigma_{\dot{X}}^2 = \frac{D}{2\omega_0 \zeta} \quad (7)$$

During Impact. Figure 2(b) shows the dynamic process during impact by assuming that the force of restitution becomes dominant during impact so that all other forces acting on the oscillator and the reflector can be neglected. The equations of motion are thus

$$\begin{cases} m_1 \ddot{X}_1(t) = -g(t) \\ m_2 \ddot{X}_2(t) = g(t) \end{cases} \quad X_1 - X_2 \geq d \quad (8)$$

where the force of impact $g(t)$ takes the form

$$g(t) = [1 + \alpha(\dot{X}_1 - \dot{X}_2)] h(X_1 - X_2 + d) \quad (9)$$

In the above, d is the distance between the centers of mass of m_1 and m_2 at impact and the term $\alpha(\dot{X}_1 - \dot{X}_2)$ denotes energy consumption due to impact where α is a constant characterizing material properties of the impacting bodies; and function $h(X_1 - X_2 + d)$ represents the force due to static deformation. Using Hertz's theory [3], it can be expressed by

$$h(x) = \beta x^{3/2}, \quad x \geq 0 \quad (10)$$

where β is a function of the contact surfaces and their material properties.

Equations (8) can be integrated in the phase space and various impact characteristics can be obtained [4-6].

MAXIMUM FORCE OF RESTITUTION

Let $U = \alpha(\dot{X}_1 - \dot{X}_2)$ and let $V = U$ at impact. From Eqs. (8 & 10) it can be shown that the force of restitution

$$F = (1 + U) \beta (X_1 - X_2 + d)^{3/2} \quad (11)$$

takes the form [4]

$$F = m_1 \left(\frac{2}{1+r} \right)^{8/5} \left(\frac{5}{4} \right)^{3/5} \left(\frac{8}{m_1} \right)^{2/5} \alpha^{-6/5} \\ \times (1 + U) [V - U + \ln \left(\frac{1+U}{1+V} \right)]^{3/5} \quad (12)$$

where

$$r = m_1/m_2 \quad (13)$$

The maximum force of restitution F_m or maximum impact acceleration A_m is found by differentiating F in Eq. (12) with respect to U and setting it to zero. The result is

$$A_m = b U_m^{3/5} (1 + U_m) \quad (14)$$

where

$$b = \left[\frac{3}{2(1+r)} \right]^{3/5} \left(\frac{8}{m_1} \right)^{2/5} \alpha^{-6/5} \quad (15)$$

and U_m is the value of U at $F = F_m$ and it satisfies

$$U_m = \frac{5}{8} \left[V + \ln \left(\frac{1+U_m}{1+V} \right) \right] \quad (16)$$

Now, since V is governed by the equation of motion before impact and is a random variable, A_m is also a random variable and its distribution is of interest for design purposes.

Let $f_V(v)$ be the probability density function of V conditional upon the onset of impact. Using the joint probability distribution of X and \dot{X} as given in Eq. (6), it can be shown that V has a Rayleigh distribution with density function [5]

$$f_V(v) = \frac{v}{\sigma_V^2} \exp \left[-\frac{v^2}{2\sigma_V^2} \right], \quad v \geq 0 \quad (17)$$

where

$$\sigma_V^2 = \alpha^2 \sigma_{\dot{X}}^2 = \frac{\alpha^2 D}{2\omega_0 \zeta} \quad (18)$$

The probability distribution of A_m can now be found through standard transformation of random variables [7]. We have

$$f_{A_m}(a) = \frac{1}{b\sigma_V^2} \frac{U_m^{2/5}}{1+U_m} (v+1) \\ \times \exp \left[-\frac{v}{2\sigma_V^2} \right], \quad a \geq 0 \quad (19)$$

Equation (19) together with Eqs. (14) and (16) determines the probability density function of A_m . With $b = 2000g$, Fig. 3 gives $f_{A_m}(a)$ for various values of σ_V .

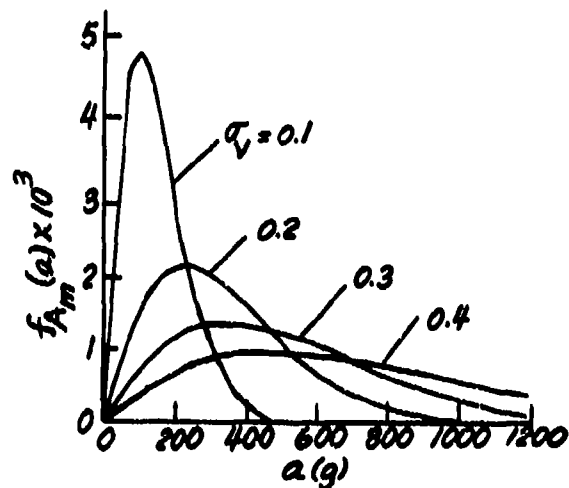


Fig. 3. Probability Density Function of A_m

Since the probability distribution of A_m is a function of the parameters associated with material properties of the oscillator and the reflectors (α, β), the restraining system of the oscillator (ω_0, ζ), and the base motion (D), the knowledge of $f_{A_m}(a)$ offers a means of determining the appropriate values of these parameters when conditions of survivability are specified. Consider, for example, the problem of choosing the design value of c_1 , the damping constant, when all other parameters are fixed and suppose the survivability condition is

$$P(A_m > 400g) < 0.2 \quad (20)$$

Fig. 4 shows that

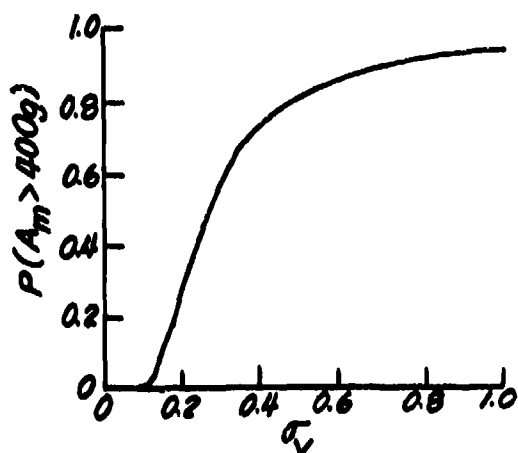


Fig. 4. Probability of $A_m > 400g$

$$\sigma_v = \alpha \sqrt{\frac{D}{2\omega_0 \zeta}} = \alpha \sqrt{\frac{Dm_1}{c_1}} < 0.317 \quad (21)$$

or

$$c_1 > 9.95 \alpha^2 D m_1 \quad (22)$$

TIME TO IMPACT

The likelihood of impact occurrence within a time interval is determined by the probability that the random displacement $X(t)$ defined in Eq. (1) will exceed a given level for the first time during the time interval. This first passage problem has been considered extensively and many approximate solutions have been offered. For the system considered in this paper, a procedure is given below which gives results in close agreement with simulation.

Consider the linear oscillator shown in Fig. 2(a) with γ being the initial oscillator-reflector gap. Let $X(t)$ start at zero with probability one and let

$$L(t, \gamma) = P(|X(t)| < \gamma; 0 \leq \tau \leq t) \quad (23)$$

be the probability that $|X(t)|$ remains below level γ in the interval $[0, t]$. Then $L(t, \gamma)$ is the probability of interest for a given t since it is the probability that the time to impact is greater than t .

In the case of $X(t)$ being stationary and for sufficiently large t , we can write [2]

$$L(t, \gamma) = L_0 \exp(-\lambda t) \quad (24)$$

where L_0 and λ depend on γ but not on t .

While no exact solution exists for L_0 and λ in the case of a linear oscillator described by Eq. (1), approximate solutions have been suggested. For our purposes, an approximate solution given in [8] based upon empirical observations appears to give most satisfactory results. Using this procedure, $L(t, \gamma)$ can be calculated from Eq. (24) with λ and L_0 approximated by

$$\frac{\lambda}{v} = 1 - 1.075 [k \exp(-k/2)]^w \quad (25)$$

$$L_0 = \exp[\exp(-1.195 - 0.3106 k^2)] \quad (26)$$

In the above, v is the mean rate of upcrossings at level γ and is given by

$$v = \frac{\sigma_X^2}{\sigma_X} \exp\left[-\frac{\gamma^2}{2\sigma_X^2}\right] \quad (27)$$

$$k = \gamma/\sigma_X \quad (28)$$

and

$$w = 0.2364 + 28.14 q^2 \quad (29)$$

where q is a measure of the bandwidth of $X(t)$ and is given by

$$q^2 = 1 - \frac{1}{1-\zeta^2} \left\{ 1 - \frac{1}{\pi} \tan^{-1} \left[\frac{2\zeta(1-\zeta^2)^{1/4}}{1-2\zeta^2} \right] \right\}^2$$

With the aid of Eqs. (25-30), Eq. (24) gives the first-passage probability of interest as a function of the physical parameters. The graphs of $L(t, \gamma)$ for $\zeta = 0.1$ and for several values of $k = \gamma/\sigma_X$ are shown in Fig. 5. Again, graphs such as shown in Fig. 5 are useful for design purposes under specified survivability conditions. For example, with all other physical parameters fixed, the necessary gap γ to be maintained can be readily determined when the minimum first-passage probability $l(t, \gamma)$ is specified at a given time t . Suppose that the survivability condition is

$$L\left(\frac{15\pi}{\omega_0}, \gamma\right) > 0.8 \quad (31)$$

Fig. 6 shows that γ must satisfy

$$\gamma > 2.79 \sigma_X \quad (32)$$

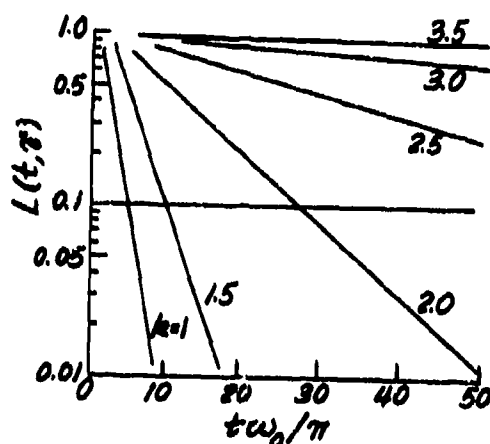


Fig. 5. First-Passage Probabilities

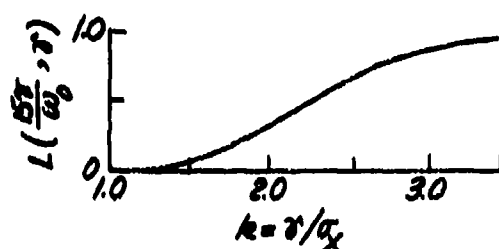


Fig. 6. First-Passage Probability at $t = 15 \pi / \omega_0$

CONCLUDING REMARKS

This paper presents a method of determining the impact characteristics of a simple mechanical system subjected to random excitations. The probability distributions of the maximum force of impact and of time to impact are given, which can be used as rational design tools for system integrity and survivability.

It is noted that $f_A(a)$ in Eq. (19), being a conditional f_m density function, is not a function of k_1 , the spring constant of the oscillator, and δ , the initial oscillator-reflector gap. These parameters, of course, appear in the time-to-impact calculations. The combined result of those given by Eq. (19) for the maximum impact force and Eq. (24) for time to impact thus provides a rational design procedure for the simple system considered here under various survivability conditions.

ACKNOWLEDGEMENT

This work was supported in part by the National Science Foundation under Grant CEE-8010891.

REFERENCES

1. T.K. Caughey and H.J. Stumpf, "Transient Response of a Dynamic System Under Random Excitation", *J. Appl. Mech.*, **28**, pp. 563-566, 1961.
2. T.T. Soong, *Random Differential Equations in Science and Engineering*, Academic Press, N.Y., Chapter 7 and Appendix A, 1973.
3. S.P. Timoshenko and J.N. Goodier, *Theory of Elasticity*, 3rd Ed., McGraw-Hill, N.Y., 1970.
4. T. Fujita and S. Hattori, "Periodic Vibration and Impact Characteristics of a Nonlinear System With Collision", *Bull. Japan Soc. Mech. Eng.*, **23**, pp. 409-418, 1980.
5. T. Fujita and S. Hattori, "Stationary Random Vibration of a Nonlinear System With Collision", *ibid.*, **23**, pp. 741-748, 1980.
6. T. Fujita and S. Hattori, "Nonstationary Random Vibration of a Nonlinear System With Collision", *ibid.*, **23**, pp. 1857-1864, 1980.
7. T.T. Soong, *Probabilistic Modeling and Analysis in Science and Engineering*, Wiley, N.Y., Chapter 5, 1981.
8. L.D. Lutes, Y.T. Chen, and S. Tzuang, "First-Passage Approximations for Simple Oscillators", *J. Eng. Mech. Div., ASCE*, **106**, pp. 1111-1124, 1980.

APPROXIMATE NUMERICAL PREDICTIONS OF IMPACT-INDUCED
STRUCTURAL RESPONSES

Richard W. Wu
Lockheed Missiles and Space Co., Inc.
Sunnyvale, California 94086

In the response prediction of a structural dynamic system impacting against a rigid object or with other flexural structural systems, the immediate consequence of the local impact interaction is often approximated by one of two means: the collision force method or the collision-imparted velocity method. In the present paper, the two methods are derived and evaluated. The limitations and advantages of the two methods are assessed via several numerical examples. Also considered in the derivation is the sliding behavior where the usual concept of friction is used. Based on the present evaluation, the collision-imparted velocity method is more versatile and less susceptible to numerical difficulty than the collision force method for the high velocity impact and for structures with high local indentation rigidity. The collision force method may be used very efficiently for the case of low velocity impact and/or low indentation rigidity.

1. Introduction

The response of structural system subjected to impact environment is often of important concern in the design of various types of structural component and equipment, and also in the crash-worthiness studies of automobile and nuclear power plant containment building. The phenomena encountered in the general impact condition can be very complex. For example, rebound and subsequent repeated-impact interaction may occur after the initial impact. Also, in the vicinity of impact region, severe impact and sharp contact edge may lead to cratering, gouging, penetration, and even perforation. In addition, the structure as a whole will respond in the manner of membrane and/or bending deformation. Because of the multiple and complex aspects involved in the general structural impact problem, principal interest in the present investigation centers upon the impact induced global (overall) structural response. The local deformation will not be treated explicitly; only the main consequence of the local deformation on the global structural response is accounted for. The present paper is to evaluate two methods that have been devised for predicting the immediate consequence of the local impact interaction: the collision force method [Refs. 1, 2, 3] and the collision imparted velocity method [4-7].

In the collision force method, the primary information predicted consists of the impact induced interaction force based on a prespecified local indentation rigidity relation (or gap/contact spring stiffness for reversible elastic local deformation). No explicit inertia (mass) effect is incorporated in this force prediction. This method is generally efficient and easy to apply. However, the main difficulty is the specification of a suitable local indentation rigidity. Too small a rigidity would lead to excessive indentation or penetration. Too large a rigidity would introduce numerical difficulties in the solution procedure of the global response.

In the collision-imparted velocity method, energy and momentum considerations are employed to predict the impact-induced velocity at the impact-affected region. The inertia effect is included in the prediction. The stress wave which propagates into the interior region of the structure is generated by this velocity disturbance at the impact region. The impact force is not determined directly but it can be deduced from the global dynamic equilibrium equation of the structure.

Having determined the force or velocity applied at the impact-affected region, this information is supplied to the dynamic equation of equilibrium of the structure which

can then be solved to obtain the global transient response. Because of the limited applicability of the conventional (closed-form) solution scheme and also the complex structural geometry and impact situation generally encountered, one is usually forced to employ a numerical approximate solution scheme, such as the finite-element method and the finite-difference method. Typically, in the numerical solution procedure, the spatial domain of the structure is first discretized into a finite number of regions or meshes; each having a finite number of nodes as control points. The resulting finite size system of second-order ordinary differential equations of motion are solved timewise by using an appropriate integration operator. In utilizing this procedure, the solution is obtained step-by-step in finite time increment, and the whole impact process is modeled as a sequence of incremental impacts which occur in the small timewise increments. Also, at each time step, an inspection needs to be performed in order to detect the possible occurrence and location of impact, rebound, and subsequent repeated-impact interaction.

In the following, the above-mentioned two approximate collision analysis methods are described in detail. The governing equation of motion of the structure using the finite-element modeling technique and the timewise solution procedure are also presented briefly. Numerical examples are carried out for two cases involving (a) longitudinal collinear impact of two rods, and (b) transverse impact of a rigid mass on a beam. The main features of each of the two collision procedures are clearly manifested in the example problems.

2. Approximate Collision-Interaction Analysis

2.1 Collision Force Method

In this method, the crucial quantity which needs to be determined first is the collision-induced interaction force. This force is transmitted to the structure at the impact location to affect a subsequent displacement, velocity, and acceleration responses of the structure. Although many papers utilizing this method have been written on structural impact response, there is scarcity of information available on impact force-time histories for general and complex structural systems. One of the simplest approaches for this force prediction is to assume a local indentation (or penetration) rigidity relation (force vs. local indentation).

Specifically, at any time during the impact process, the structure is allowed to indent locally or to penetrate infinitesimally at the impact region. This indentation is used in

combination with the local indentation rigidity to determine the impact interaction force magnitude and distribution:

$$F_N = K_N \delta^\alpha \quad (1)$$

where F_N is the impact force in the direction normal to the contact surface (denoted by subscript N), δ represents the local indentation at the center of impact. α is a constant depending upon the geometry and material properties; for example, $\alpha = 1$ for reversible elastic local indentation, and $\alpha = 3/2$ for Hertzian type of contact deformation [8]. K_N is the local indentation stiffness. Figure 1 gives the associated qualitative behavior of this approach.

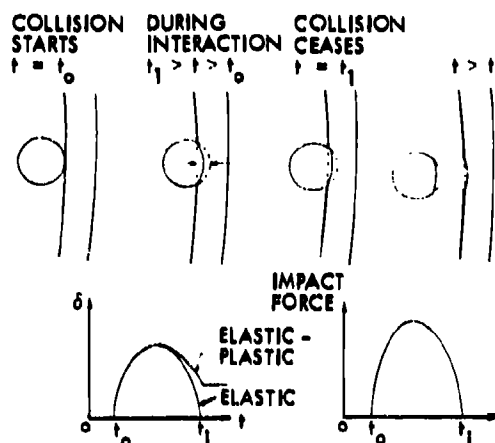


Fig. 1 Schematics of Collision Force Method

It is evident that success in this prediction hinges critically on the specification of a proper local indentation stiffness. Specifying too small a rigidity would result in excessive indentation (or penetration). Too large a value would introduce numerical stability difficulty in the solution procedure of the structural response, since the critical time increment required to ensure numerical computational stability decreases as the indentation rigidity increases. Generally, the local indentation rigidity will depend upon the geometry and material properties of the colliding bodies as well as the mesh size of the discretized structure system, and the integration time step size. Certain guidelines on the specification of this local indentation stiffness are provided in Ref. 2, in which it is proposed that from low velocity to intermediate high velocity impacts a stiffness of the order of the intermesh (membrane/bending) rigidity would be the most proper value to choose. For very high

velocity impact, an artificially high impact rigidity may be employed to ensure that the impenetrability condition is not violated. For cases lacking guideline and/or having complicated geometrical and material behavior, one may have to resort to experiments (numerical and/or model test) to establish this local crush rigidity relation.

The sliding behavior along the tangential direction of the contact surface (denoted by subscript T) can be accounted for using the usual concept of friction. The friction force is assumed to be opposed to the relative sliding movement. Defining a coefficient of friction, μ , the friction force has a value of μF_N as long as there is sufficient relative sliding displacement. When the sliding displacement is small, the friction force is controlled by a local stiffness, K_T ; thus,

$$F_T = \mu F_N \quad \text{if } K_T (d - d_0) > \mu F_N \quad (2)$$

and

$$F_T = K_T (d - d_0) \quad \text{if } K_T (d - d_0) \leq \mu F_N \quad (3)$$

where d_0 is the relative position of the contact points when the last sliding took place, and d is current relative displacement.

Knowing the impact-induced forces, F_N and F_T , these forces are inserted to the equation of equilibrium at the impact location, giving rise to a modified structural displacement, velocity, and acceleration.

2.2 Collision-Induced Velocity Method

In this method, energy and momentum conservation relations are employed in an approximate manner to compute the collision-induced changes in velocities of the impact-affected structural region. The basic assumption invoked in this approach is that the collision process is instantaneous and involves only the impact-affected zone of the structure. The impact-affected zone is defined as the fraction of the structure region that responds to impact instantaneously with momentum changes. The size of this impact-affected zone normally can be estimated from the speed of a longitudinal wave or from semi-empirical data in conjunction with the time integration step size [9]. Assuming that the instantaneous collision process results in a normal-direction impulse, P_N and a tangential-direction impulse, P_T applied to one structure (denoted by subscript 1), and in

equal but anti-parallel impulses to the other structure (subscript 2), the impulse-momentum law may be written as (see Figure 2 for the schematics):

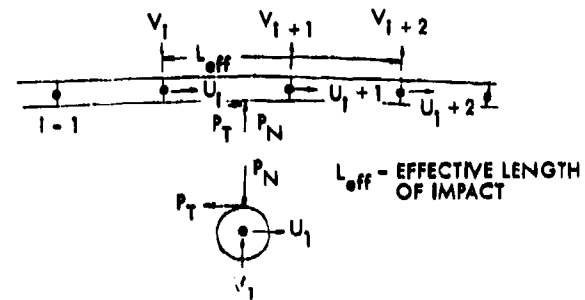


Fig. 2 Schematics of Collision-Induced Velocity Method

Normal-Direction Impulse-Momentum Law

$$M_1 (U'_1 - U_1) = -P_N \quad (4)$$

$$M_2 (U'_2 - U_2) = P_N$$

Tangential-Direction Impulse-Momentum Law

$$M_1 (V'_1 - V_1) = -P_T \quad (5)$$

$$M_2 (V'_2 - V_2) = P_T$$

where for the convenience of discussion the mass of structure is treated as having point masses lumped at each nodal station. U and V are the normal-direction and tangential-direction velocities before impact. U' and V' are the velocities after impact. The relative velocity of approach A and the relative velocity of sliding, S at the contact location are defined by

$$\begin{aligned} A &= A - P_N (M_1 + M_2) / M_1 M_2 \\ S &= S - P_T (M_1 + M_2) / M_1 M_2 \end{aligned} \quad (6)$$

where in Equation 6 by definition $A > 0$; otherwise, the two structures will not collide with each other. Also, if $S > 0$ the structures slide initially on each other. Note that sliding is assumed to occur at the value of 'limiting friction' which requires that $P_T = \mu P_N$. When $P_T < \mu P_N$, only rolling (i.e., no sliding) exists. There are six equations (Equations 4-6) which can be solved for the post-impact quantities U'_1 , U'_2 , V'_1 , V'_2 , as well as P_N and P_T ; these are six unknowns.

Thus, this approximate procedure provides the post-impact velocity information for the impact-affected nodes of the structure. They are then introduced to the equation of motion, leading to a modified position and acceleration. In addition, the contact forces are also deduced [6].

2.3 Equation of Motion and Solution Procedure

The governing equation of motion of the finite element (or finite-difference) discretized structural system may be written in the following form:

$$[M] \{\ddot{q}\} + [K] \{q\} = \{F\} \quad (7)$$

where q , \ddot{q} represent the global generalized displacement and acceleration, respectively. M and K are the structural mass and stiffness matrices, respectively. F represents the generalized applied force including impact force acting on the structure. The timewise solution of Equation 7 may be accomplished by employing an appropriate timewise integration operator, where the computational procedure is carried out in small time increment. For example, if the 3-point central-difference operator is chosen, the \ddot{q} and \dot{q} at any instant of time t_j may be expressed as

$$\ddot{q}_j = (q_{j+1} - 2q_j + q_{j-1})/(\Delta t)^2 \quad (8)$$

and

$$\dot{q}_j = (q_{j+1} - q_{j-1})/(2\Delta t) \quad (9)$$

where Δt is the time increment. Employing Equations 8 and 9 and assuming that all quantities are known at time t_j , Equation 7 can be solved for q_{j+1} . However, a collision may occur between time instants t_j and t_{j+1} ; this would require a correction to the predicted quantity at t_{j+1} .

Based on the predicted (tentative) region of space occupied by each structure, an inspection is performed to determine whether a collision has occurred during the small increment in time from the last instant at which the body locations were known to the present instant in time at which the body location data are sought. If a collision has not occurred, one follows the motion of each structure for another Δt , etc. However, if a collision has occurred, one proceeds to calculate the location of contact, the depth of penetration, and the duration of contact (within a small increment, Δt , in time). Having obtained these quantities, the appropriate collision-interaction procedure using either the collision force method or the collision-imparted velocity method can then be

carried out. For a detailed discussion of the solution procedures as well as various considerations and simplifying assumptions, one may consult References 2, 4, 6, and 7.

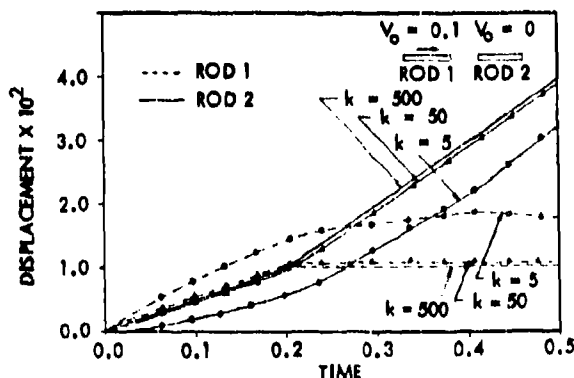
3. Numerical Examples and Discussion

As an illustration of the application of the two procedures for treating the impact-interface condition as discussed in the previous section, numerical examples have been carried out for two classical cases involving (a) longitudinal collinear impact of two rods and (b) transverse impact of a rigid mass on a beam. Comparisons are made between the solutions obtained by the two predicting procedures. For the longitudinal rod impact case, closed-form analytical solution is also available for comparison.

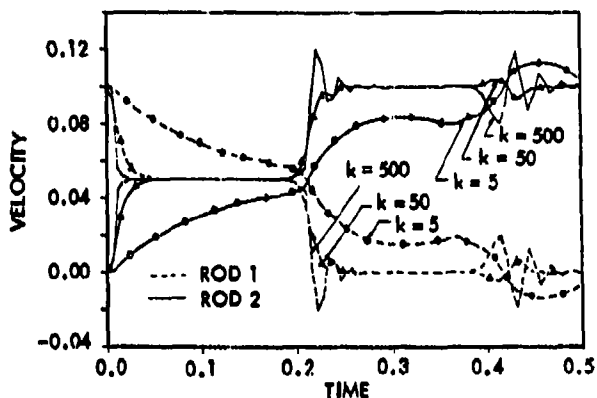
3.1 Longitudinal Collinear Impact of Two Rods

This problem consists of two identical elastic rods colliding with each other along their axial direction. The rods are selected to be (in using consistent units): length $L = 10$, cross-sectional area $A = 1$, density $\rho = 0.01$, and Young's modulus $E = 100$. Initially, one rod travels at a velocity of 0.1, and the other rod is at rest. This is the same problem as studied in Ref. 6, where the collision-induced velocity method is employed. For this problem, the fundamental impact process and the theoretical solution are well-known [Ref. 8]. In the finite-element modeling, 50 uniform meshes are used to model each of the two rods. First, the collision-induced force method is used for the analysis.

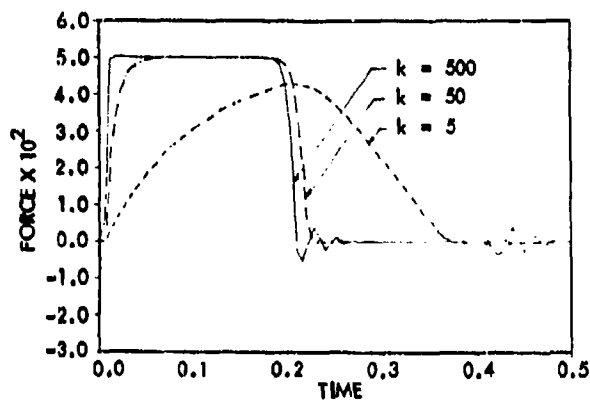
Shown in Fig. 3 is the effect of local indentation rigidity, K_N , on the predicted transient responses. Results were presented for three values of K_N : 5, 50, and 500. It can be seen that as value of K_N gets larger, the solution approaches the exact solution.



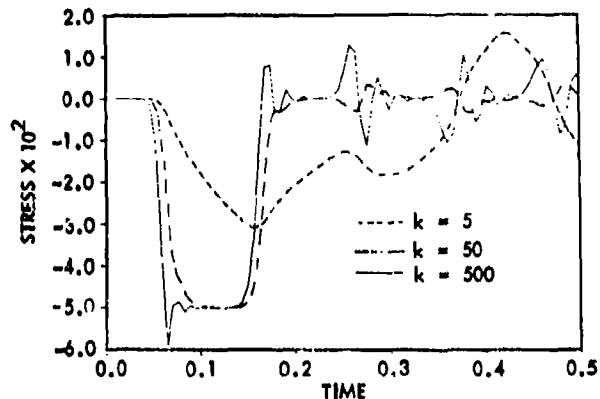
(a) Displacement Responses of Contact Points



(b) Velocity Time Histories of Contact Points



(c) Contact Force Time History



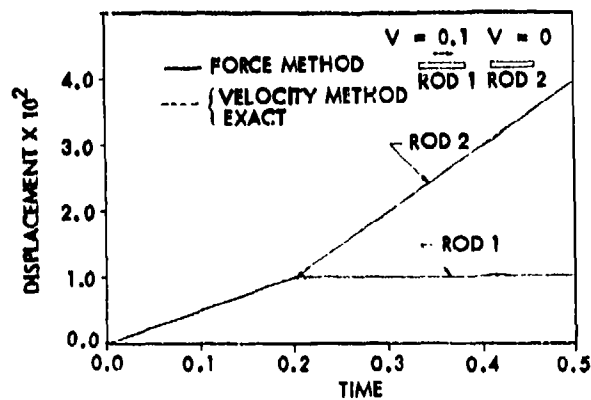
(d) Midspan Stress Responses

Fig. 3 Effects of Local Contact Stiffness on the Response Prediction of Two Impacting Identical Rods

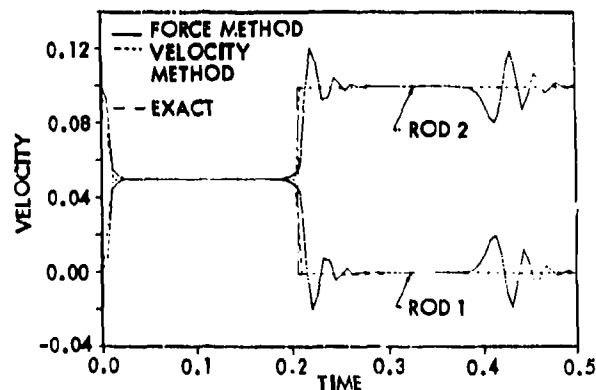
However, it exhibits spike overshoots at each of the wave fronts, ensued by damped oscillations and spurious release waves. Note that $K_N = 500$ corresponds to the inter-mesh stiffness of the rod element encompassing the

impacting node. Solutions have also been carried out by using even higher values of K_N . The responses obtained are close to that of $K_N = 500$, but with larger overshoots, more oscillations, and decreasingly smaller time increments required for computationally stable solution.

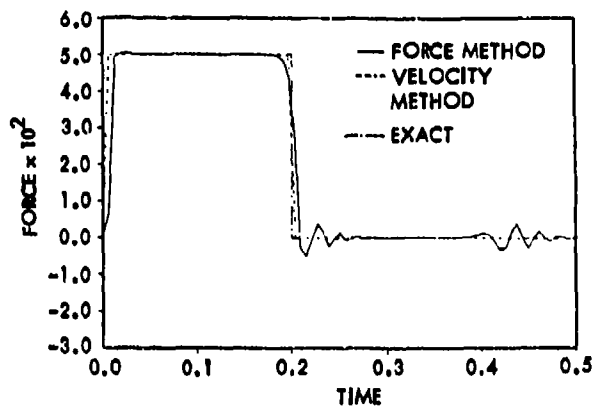
Compared in Fig. 4 are the predictions obtained by the collision force method, the collision velocity method, and the exact solution. The force method prediction using $K_N = 500$, and $\Delta t = 0.001$ is selected for comparison, since it represents the best solution of all cases that are evaluated. In the velocity method, a $\Delta t = 0.002$ is chosen, which is equal to the time it takes the longitudinal wave to travel between two adjacent nodes of the rod. Notice that the velocity method prediction agrees very well with the exact solution, whereas the force method prediction oscillates about the exact solution.



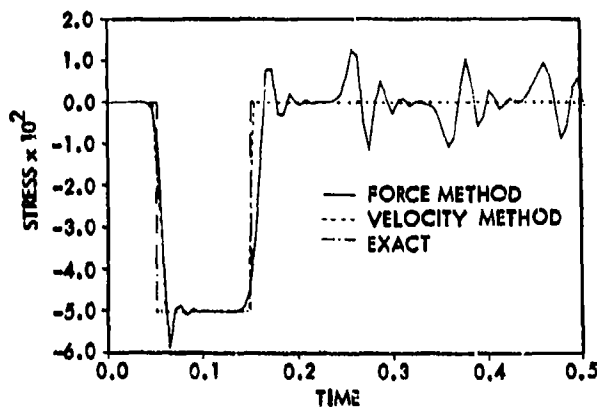
(a) Displacement Responses of Contact Point



(b) Velocity Time Histories of Contact Points



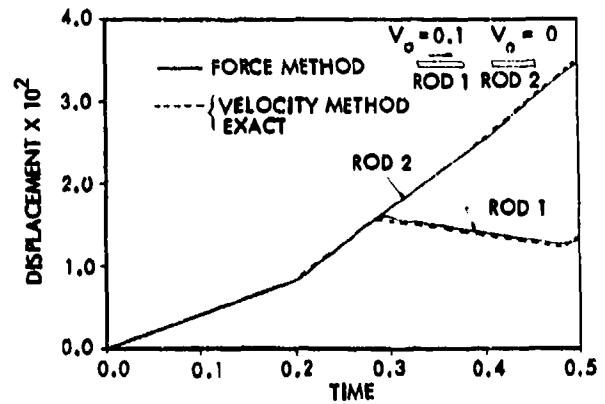
(c) Axial Force Response at Contact Points



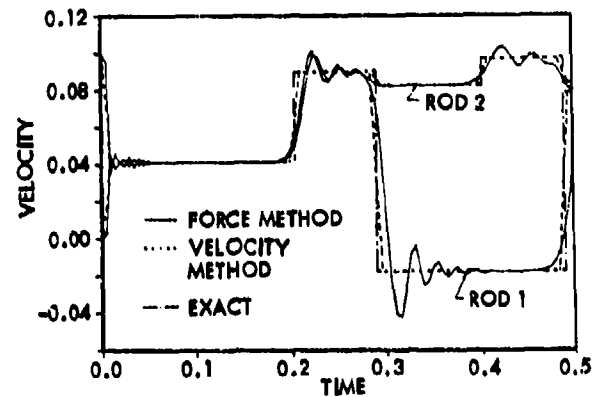
(d) Midspan Stress Response

Fig. 4 Comparison of the Response Predictions of Two Impacting Identical Rods by Using the Force Method Versus the Velocity Method

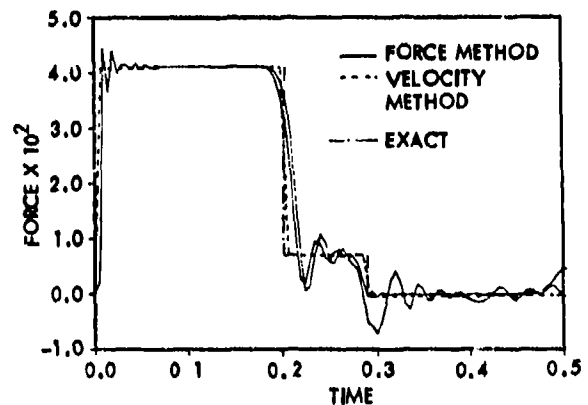
Also studied is the problem of two impacting dissimilar rods as discussed in Ref. 6. This is the same problem as described previously, except that the elastic moduli are taken to be $E_1 = 49$, and $E_2 = 100$ for rods 1 and 2 respectively. Shown in Fig. 5 are the approximate predictions and the exact solution. Again, the main characteristics of the collision force method and the collision velocity method are demonstrated.



(a) Displacement Responses of Contact Points



(b) Velocity Time Histories of Contact Points

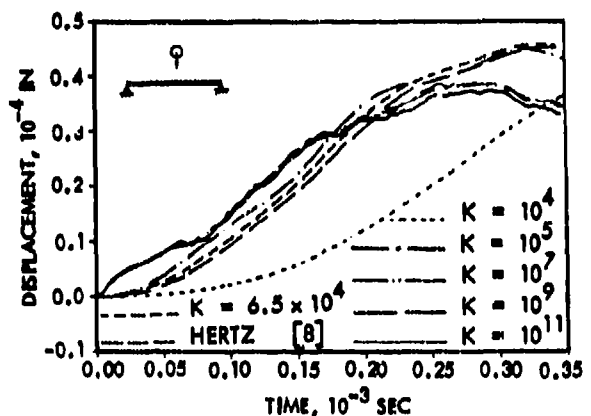


(c) Axial Force Response of Contact Point

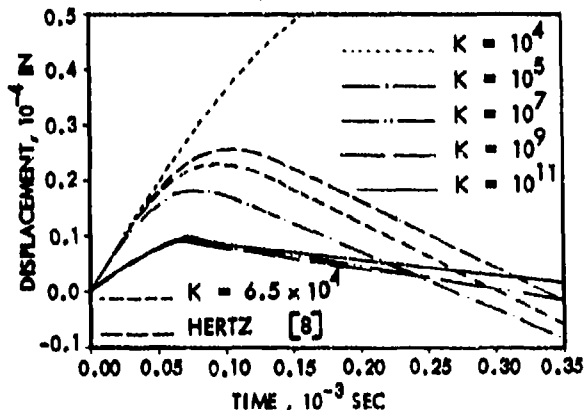
Fig. 5 Comparison of the Response Predictions of Two Impacting Dissimilar Rods by Using the Force Method Versus the Velocity Method

3.2 Transverse Impact of a Rigid Mass on a Beam

This example consists of the central transverse impact of a steel sphere having radius 0.39 in., on a simply supported beam with dimensions: 0.39 in. width, 0.39 in. thickness, and 6.04 in. span. The sphere has an initial velocity of 0.39 in./sec. In the present analysis, the sphere is treated as being rigid, and the beam is modeled by 10 uniform beam elements. Using the collision force methods, effects of local contact stiffness, K_N , on the displacement response are illustrated in Fig. 6, where values of K_N ranging from 1×10^4 lb./in. to 1×10^{11} lb./in. were evaluated. It is seen that excessive relative approach (or penetration) is predicted for low value of K_N . As K_N gets larger, the relative approach decreases, and high frequency mode appears in the beam responses. No appreciable difference in response is observed for $K_N \geq 10^7$ lb./in. Also presented in Fig. 6 is the prediction obtained by using the Hertz law of contact - a quasi-static approximation [8].



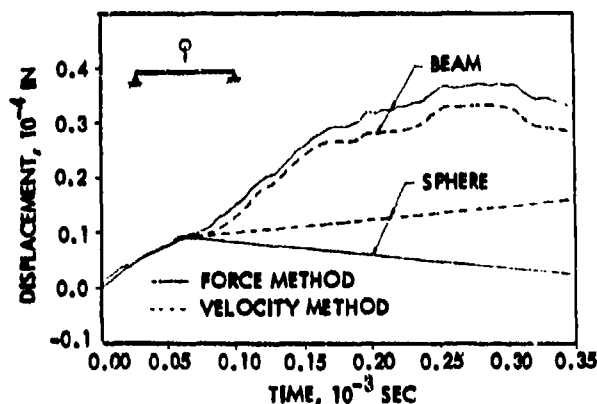
(a) Beam Midspan Displacement Time Histories



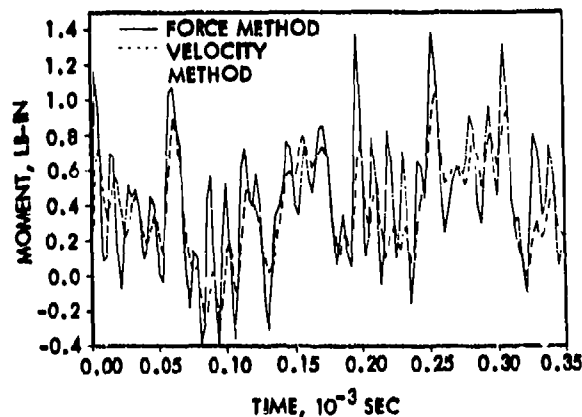
(b) Sphere Displacement Time Histories

Fig. 6 Effects of Local Contact Stiffness on the Response Prediction for the Transverse Impact of Sphere Mass on a Beam

Comparison of predictions using the collision force method versus that using the collision velocity method is made in Fig. 7. For the collision force method, prediction with $K_N = 1 \times 10^{11}$ lb./in. is selected for comparison. It is seen that, as far as the first impact is concerned, the beam responses predicted by both methods are very close. However, opposite directions are predicted for the sphere movement. Before any definitive conclusion can be drawn as to which of the two prediction schemes is superior for this type of problem, further study and evaluation against other pertinent theoretical/experimental result are required, these remain to be accomplished.



(a) Displacement Time Histories



(b) Beam Midspan Moment Time Histories

Fig. 7 Comparison of Predictions for the Transverse Impact of Sphere Mass on a Beam by Using the Force Method Versus the Velocity Method

4. Summary Remark

Based on the present evaluation of the two techniques commonly used to treat the impact-interaction (interface) of impacting structures, namely, the collision force method and the collision-induced velocity method, the following remarks are in order:

1. For structure with high local indentation rigidity, the structural response obtained by the collision force method has been observed to be very close to that predicted by the velocity method. However, the velocity method is more efficient in terms of computation time than the force method. This is because much larger solution time increment can be used by the velocity method to obtain a computationally stable solution.
2. For high velocity impact where inertia effect can no longer be ignored, the collision velocity method based on the momentum consideration is more suitable because it accounts for the mass of the local impact region explicitly. If the collision force method is used for high velocity impact, a high local indentation rigidity value, and hence small Δt , has to be used in order to ensure that local indentation (or penetration) would not be excessive.
3. For the case low velocity impact and/or low local indentation rigidity, the force method can be efficiently used.

It perhaps should be noted that although prediction of structural impact response obtained by both methods appear to be adequate and plausible, there is no theoretical basis to assure the convergence of either calculations. Also, another important factor affecting the accuracy of the prediction is the description of the dynamic material behavior (constitutive relation), since under rapid loading and impact, the material behavior differs significantly from that under slow or static load application [8, 10]. This factor has not been addressed explicitly in this paper. Finally, realizing the inherent nonlinear nature and difficulty of structural impact problem, considerable research efforts, both theoretical and experimental, are still needed in order to lead to better understanding of the impact mechanisms and higher degree of confidence in the prediction than that we currently have.

References

1. Timoshenko, S.P., Vibration Problems in Engineering, D. Van Nostrand Company, Inc., New York, 1937.
2. Pirotin, S.D. and Witmer, E.A., "Finite-Difference Analysis of Shells Impacting Rigid Barriers". Paper presented at the 4th International Conference on Structural Mechanics in Reactor Technology, San Francisco, California, August 1977.
3. Nimmer, R.P. and Boehman, L., "Transient, Nonlinear Response Analysis of Soft-Bodied Impact on Flat Plates Including Interactive Load Determination" AIAA/ASME/ASCE/AHS 22nd Structures, Structural Dynamics and Material Conference, Atlanta, Georgia, April 6-8, 1981.
4. Wu, R.W. and Witmer, E.A., "Approximate Analysis of Containment/Deflection Ring Responses to Engine Rotor Fragment Impact", Journal of Aircraft, Vol. 10, No. 1, 1973.
5. Hageman, L.J. and Walsh, J.M., "HELP, A Multimaterial Eulerian Program for Compressible Fluid and Elastic-Plastic Flows in Two Space Dimensions and Time", Vol. 1 - Formulation and Vol. II - Fortran Listing of HELP, NRL CR No. 39, Systems, Science and Software, La Jolla, California, May 1971.
6. Hughes, T., Taylor, R.L., and Sackman, J.L., "Finite Element Formulation and Solution of Contact-Impact Problems in Continuum Mechanics", PB-233 888, California University, Berkeley, California, May 1974.
7. Hallquist, J.O., "A Procedure for the Solution of Finite-Deformation Contact-Impact Problems by the Finite-Element Method", UCRL-52066, Lawrence Livermore Laboratory, Livermore, California, April 1976.
8. Goldsmith, W., Impact: The Theory and Physical Behavior of Colliding Solids, Edward Arnold Ltd., London, 1960.
9. Wu, R.W., Stagliano, T.R., Witmer, E.A., and Spilker, R.L., "User's Guide to Computer Program JETSA and CIVM-JETSB to Calculate the Large Elastic-Plastic Dynamically-Induced Deformations of Multilayer Partial and/or Complete Structural Rings", MIT, ASRL TR-134-10, November 1978 (Available as NASA CR-159484).
10. Zukas, J.A., Nicholas, T., Swift, H.F., Gresseruk, L.B., and Curran, D.R., Impact Dynamics, John Wiley and Sons, Inc., 1982.

ON THE FACE-SHEAR VIBRATIONS OF CONTOURED CRYSTAL PLATES

SASADHAR DE

National Research Institute
P.O. Bankisol, Bankura,
W. Bengal (India)

The face-shear vibration characteristics of monoclinic crystal plates of varying thickness are generalised and the special features of the frequency spectrum are shown. Solution for a crystal plate with piece-wise continuous boundary is obtained. The results are compared with those obtained for a plate of uniform thickness.

INTRODUCTION

The vibrations of monoclinic crystal plates have been studied by Mindlin [b,d,f,h,k], Mindlin & Lee [e], Mindlin & Spencer [g], Kaul & Mindlin [c,p] and by De [m]. The vibrations of quartz plates have been further analysed by Mindlin [w] by expansion in series of Bessel function; Cowdrey et al. [x] solved the problem by the use of finite element method. The face-shear and thickness-twist vibrations of a monoclinic crystal plate have been analysed by Deresiewicz & Mindlin [a]. The modes of motion of such plates (free-free flexure, low-frequency (face) shear,

high-frequency (thickness) shear) have been considered by Sykes [t]. The vibrations of contoured crystal plates have been considered among others by Mindlin & Porray [j], Jerrard [l], Blewstein [q], Loutsenheiser [r] and De [n]. Thickness-shear vibration modes of a beveled AT-cut quartz plate have been analysed from an equivalent three-dimensional equation of motion [y].

Mindlin & Porray [j], Jerrard [l] study the vibration characteristics which deal with the coupled thickness-shear and flexural vibrations in which there is a nonzero component of displacement in the direction along

Address for Communication :

S. De, 15, Ratanpalli, P.O. Santiniketan
Dist. Birbhum, W. Bengal (India)

which the thickness varies. Blonstein [2] investigates the thickness - twist and face-shear modes of motion in which the displacements are all perpendicular to the direction along which the thickness varies. Mindlin [3], Mindlin and Gasis [4] have pointed out that these are modes of technological interest since they can be strongly excited piezoelectrically in a quartz plate.

The equations of the approximate theory for the thickness-twist vibrations are given in [5, 6]. A more general approximate theory, however, has been developed [7] which takes into account the coupling of flexural, extensional and face-shear deformations with each other and with the lowest thickness orders of thickness-shear and thickness-twist deformations. The equations and the notations of the more general theory have been used here. The equations are specialized to the case of an infinite strip which has a linear taper in the direction perpendicular to its infinite dimension. The strip is considered simply as a plate. In the present paper, the modification of the frequency spectrum of face-shear vibrations of tapered crystal plates have been generalized and the same problem for a plate with piece-wise continuous boundary has been solved. The results are compared with those obtained for a plate of constant thickness. The possible influence of

manufacturing tolerance on the spectrum has been considered.

GOVERNING EQUATIONS

The equations of motion of 3-dimensional elasticity $\tau_{ij,j} = \rho \ddot{u}_i$ and the constitutive equations $\tau_{ij} = c_{ijkl} S_{kl}$ ($S_{ij} = s_{ijkl} \tau_{kl}$), $i, j, k, l = 1, 2$, or 3) can be written in the case of a 2-dimensional plate of area A and thickness 2h to give the following:

$$\begin{aligned} \tau_{ij,j}^{(0)} &= 2h \rho \ddot{u}_i^{(0)} \\ \tau_{ij}^{(0)} &= 2h c_{ijkl}^{(0)} S_{kl}^{(0)}, \end{aligned} \quad (1)$$

τ_{ij} represent the stresses and S_{ij} the strains; the c_{ijkl} are termed the elastic stiffnesses, s_{ijkl} the elastic compliances and ρ is the density of the material of the plate.

It can further be shown from thermodynamic arguments that

$$c_{ijkl} = c_{klij}, \quad s_{ijkl} = s_{klij},$$

and these reciprocal relations reduce the number of independent stiffnesses to 21 in the most general case.

Only those terms which are relevant to the problem are retained. The stress-strain relations of a rotated-Y-cut quartz plates referred to a rectangular Cartesian coordinate system, x_1, x_2, x_3 with x_1 a diagonal axis and $x_2 = 0$ the middle plane of the plate exhibits monoclinic symmetry (Mason, ref. 8). An abbreviated notation is employed whereby a pair of indices which

range over the integers 1,2,3 is replaced by a single index ranging over the integers 1,2,3,4,5,6 according to the scheme given below :

Replace ij=	11	22	33	23 or 32	31 or 13	12 or 21
by p =	1	2	3	4	5	6

Using this notation the governing equations (Mindlin, ref. 6) for the free vibrations of a plate of thickness $2h$ are :

Stress equations of motion

$$\begin{aligned}\tau_{1,1}^{(0)} + \tau_{5,3}^{(0)} &= 2h \rho \ddot{u}_1^{(0)}, \\ \tau_{6,1}^{(0)} + \tau_{4,3}^{(0)} &= 2h \rho \ddot{u}_2^{(0)}, \\ \tau_{5,1}^{(0)} + \tau_{3,3}^{(0)} &= 2h \rho \ddot{u}_3^{(0)},\end{aligned}\quad (1a)$$

where the dot denotes partial differentiation with respect to time and $a(a=1,3)$ denotes the partial derivative, $\partial/\partial x_a$;

Constitutive equations

$$\tau_p^{(0)} = 2h \bar{c}_{pq} S_q^{(0)}, \quad p, q = 1, 2, \dots, 6, \quad (2)$$

where

$$\begin{aligned}\bar{c}_{pq} &= k(p) k(q) \bar{c}_{pq}, \text{ no sum on } p \text{ or } q, \\ \bar{c}_{pq} &= c_{pq} - c_{p2} c_{2q} / c_{22}, \\ c_{15} &= c_{25} = c_{35} = c_{45} = c_{16} = c_{26} = c_{36} = c_{46} = 0, \\ \mu &= \cos^2(\theta\pi/2), \quad \nu = \cos^2(\varphi\pi/2), \\ k_4^2 &= n^2 \left\{ c_{1,2} + c_{4,4} - [(c_{2,2} - c_{4,4})^2 + 4 c_{2,4}^2]^{1/2} \right\} / 24 \bar{c}_{4,4}, \quad k_6^2 = n^2 / 12.\end{aligned}$$

Strain-displacement relations

$$\begin{aligned}S_1^{(0)} &= u_{1,1}^{(0)}, \\ S_3^{(0)} &= u_{3,3}^{(0)}, \\ S_4^{(0)} &= u_{2,3}^{(0)} + u_{3,2}^{(0)},\end{aligned}\quad (1)$$

$$\begin{aligned}S_5^{(0)} &= u_{3,1}^{(0)} + u_{1,3}^{(0)}, \\ S_6^{(0)} &= u_{2,1}^{(0)} + u_{1,2}^{(0)};\end{aligned}\quad (3)$$

Boundary conditions

For the free edges of a rectangular plate of length $2l$ and width $2w$,

$$\begin{aligned}\tau_1^{(0)} = \tau_5^{(0)} = \tau_6^{(0)} &= 0 \quad \text{on } x_1 = \pm w, \\ \tau_3^{(0)} = \tau_5^{(0)} = \tau_4^{(0)} &= 0 \quad \text{on } x_3 = \pm l.\end{aligned}\quad (4)$$

FORMULATION OF THE PROBLEM

We consider the case in which $h = h(x_3)$ and we assume

$$u_1^{(0)} = U(x_3) e^{i\omega t}, \quad u_2^{(0)} = u_3^{(0)} = 0. \quad (5)$$

The only nonzero component of displacement is the face-shear, $u_1^{(0)}$. The corresponding nonzero strain component is

$$S_5^{(0)} = U' e^{i\omega t}, \quad (6)$$

where $' \equiv d/dx_3$. The associated nonzero stress-resultant is

$$\tau_5^{(0)} = 2h c_{55} U' e^{i\omega t}. \quad (7)$$

For the AG-cut of quartz the elastic constant c_{56} is zero and for the AT-cut of quartz c_{56} is small relative to c_{55} and c_{66} and as a first approximation it can be taken identically equal to zero. This assumption should not prohibit the matching of theoretical with experimental results (Mindlin & Gasis, ref. 1). Moreover, with the assumption $c_{56} = 0$, the equations governing the thickness-twist and face-shear are completely uncoupled, and hence the motions can occur at different frequencies.

Using (7) and (1), we get

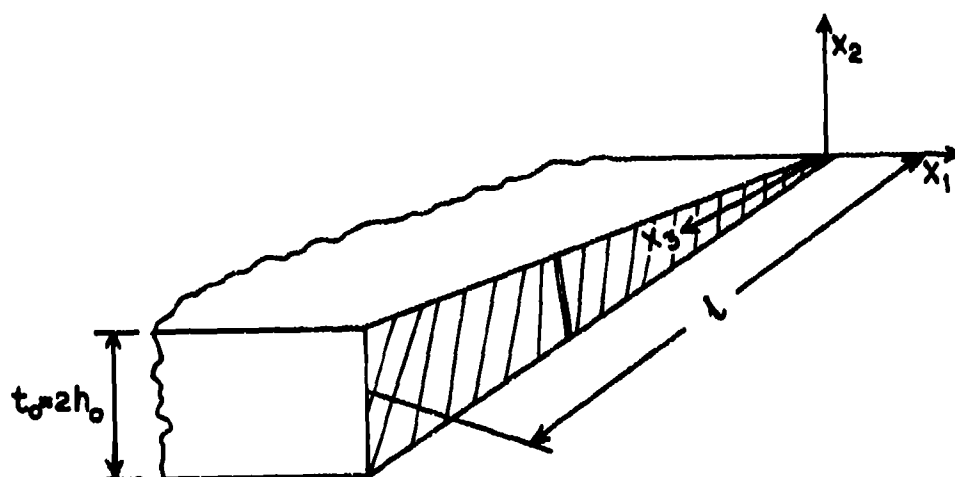


Fig.1- Tapered infinite strip

$$U'' + \frac{h'}{h} U' + \beta^2 U = 0, \quad (8)$$

where

$$\beta^2 \equiv \rho \omega^2 / c_{55}, \quad h' \equiv \frac{dh}{dx_3}.$$

An infinite strip with a linear taper in the x_3 - direction is considered (Fig.1). The taper is given by

$$h(x_3) = h_0 \left(a + \frac{bx_3}{l} \right)^m \quad (9)$$

$$\text{and } h = h_0 e^{x_3/l},$$

where a , b and m are constants.

The edges $x_2 = 0$ and $x_2 = l$ are free and consequently, the boundary conditions(4) become

$$U' = 0 \quad \text{on } x_3 = 0, l. \quad (10)$$

The problem is to find the solution of equation(8) satisfying(9), subject to the boundary conditions(10) given above.

The tapered plate is now assumed to be composed of two different parts having different thickness. The second

part(denoted by the suffix 2) has uniform thickness $h_2(x_3) = h_0$, while the first part(denoted by the suffix 1) is characterized by

$$h_1(x_3) = h_0/l_1 x_3 \quad (9a)$$

The conditions to be fulfilled are

$$U'_1 = 0 \quad \text{at } x_3 = 0$$

$$(c_{55})_1 U'_1 = (c_{55})_2 U'_2 \quad \text{at } x_3 = l_1 (0 < x_3 \leq l_1)$$

$$U_1(x_3) = U_2(x_3) \quad (11)$$

$$\text{at } x_3 = l_1 (0 < x_3 \leq l_1)$$

$$U'_2(x_3) = 0 \quad \text{at } x_3 = l (l_1 < x_3 \leq l),$$

where $/ \equiv d/dx_3$, 1,2 stand for the first and second part respectively.

Considering equations (8) and (9a), we can solve the problem provided the boundary conditions (11) are chosen.

SOLUTION OF THE PROBLEM

4.1.(Case-1). Inserting the first condition of (9) for the linear taper into (8) and substituting $\frac{bx_3}{l} = y$, we get

$$\frac{d^2 U}{dy^2} + \frac{m}{y} \frac{dU}{dy} + \left(\frac{\beta l}{b}\right)^2 U = 0. \quad (12)$$

The general solution of equation(12) is written as

$$U = \left(a + \frac{bx_2}{l}\right)^{\frac{1-m}{2}} \left[A J_{\frac{1-m}{2}} \left\{ \lambda \times \right. \right. \\ \left. \left. \times \left(a + \frac{bx_2}{l}\right) \right\} + B Y_{\frac{1-m}{2}} \left\{ \lambda \left(a + \frac{bx_2}{l}\right) \right\} \right], \quad (13)$$

J and Y are Bessel functions of the first and second kind respectively, A, B are any two constants, and

$$\lambda = \frac{\beta l}{b}. \quad (14)$$

Choosing $m = 1$ and applying boundary conditions(10), we can write the frequency equation as

$$J_1(\bar{\lambda}) Y_1(\alpha \bar{\lambda}) - J_1(\alpha \bar{\lambda}) Y_1(\bar{\lambda}) = 0, \quad (15)$$

where

$$\bar{\lambda} \equiv \beta l(a/b), \quad \alpha = 1 + \frac{b}{a}. \quad (16)$$

The first six roots of equation (15) for various values of α are given in Table-I [7].

Introducing as a reference frequency the frequency, ω_s , of the lowest x_1, x_2 thickness shear mode of a uniform plate of thickness $2h_0$, i.e

$$\omega_s = \frac{\pi}{2h_0} (c_{66}/\rho)^{1/2}, \quad (17)$$

We find for the dimensionless frequencies, Ω_n , of the n th mode of face-shear,

$$\Omega_n \equiv \omega_n/\omega_s = \frac{1}{\pi} (c_{55}/c_{66})^{1/2} \times \\ \times (t_0/l) (l/a) \bar{\lambda}_n \quad (18) \\ \equiv G (t_0/l) \bar{\lambda}_n \quad (a=b),$$

where $t_0 = 2h_0$, the maximum thickness of the plate and $\bar{\lambda}_n$ are the successive roots of equation (15). The dimensionless frequency is thickness independent; i.e., the face-shear mode has the same thickness as the face-shear mode used to normalise(equ.17). In Fig.2, the dimensionless frequencies Ω_n are plotted as functions of the length-to-thickness ratio (l/t_0).

If, however, $h(x_2) = h_0$, a constant, we get

$$U = A_0 \sin \beta x_2 + B_0 \cos \beta x_2, \quad (19)$$

where A_0, B_0 are constants.

Applying the boundary conditions(10), we get

$$\beta_m = m\pi/l, \quad m = \text{integer}. \quad (20)$$

Again, introducing ω_s as a reference frequency we find for the dimensionless frequencies, Ω_{m1} of the m th mode of face-shear,

Table - I

α	a/b	$\bar{\lambda}_1$	$\bar{\lambda}_2$	$\bar{\lambda}_3$	$\bar{\lambda}_4$	$\bar{\lambda}_5$	$\bar{\lambda}_6$
1.2	5.0	15.7014	31.4126	47.1217	62.8302	78.5385	94.2467
1.5	2.0	6.2702	12.5398	18.8451	25.1294	31.4133	37.6969
2.0	1.0	3.1230	6.2734	9.4182	12.5614	15.7040	18.8462

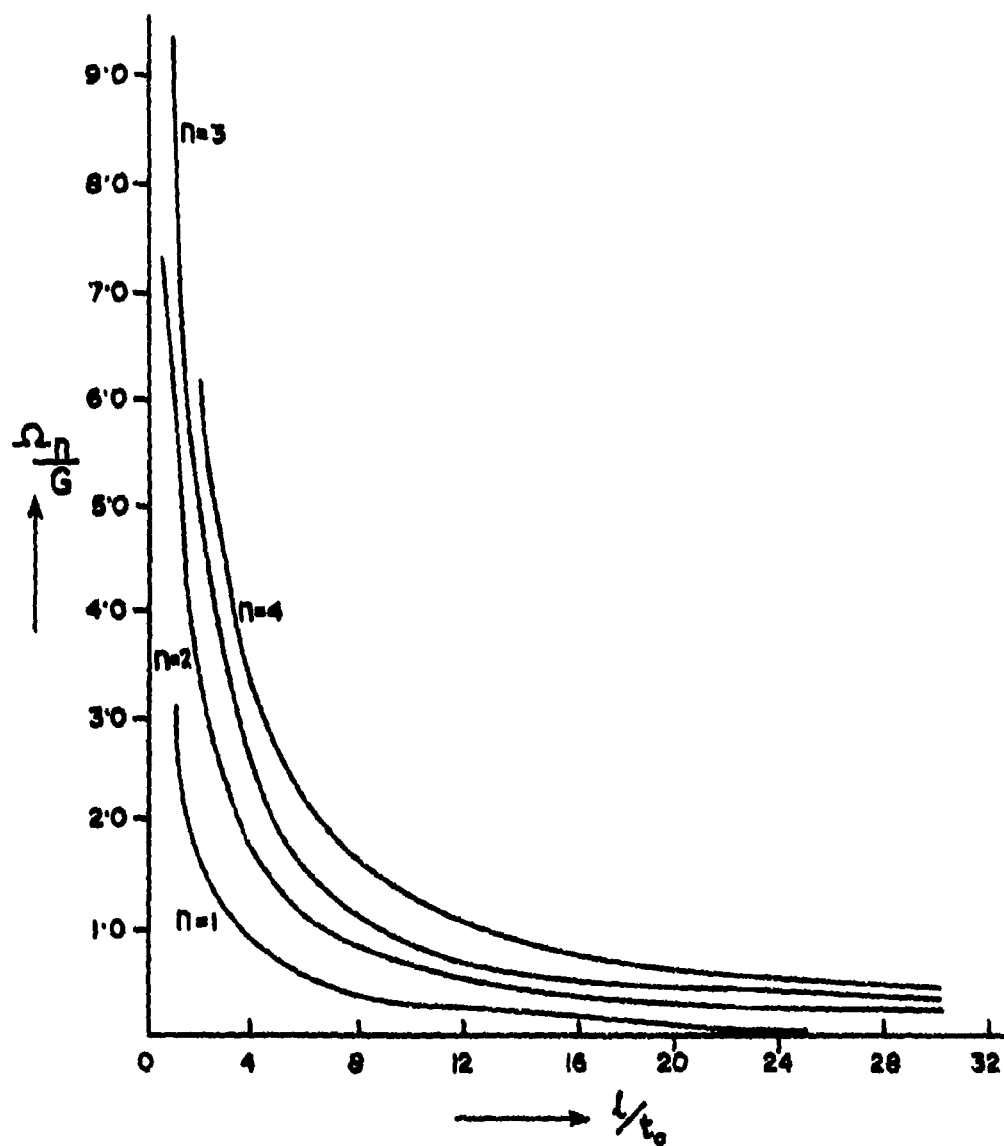


Fig. 2 Dimensionless frequencies of face-shear modes in a tapered plate as a function of length-to-thickness ratio

$$\Omega_{mc} \equiv \frac{\omega_{mc}}{\omega_s} = m \left(\frac{c_{55}}{c_{66}} \right)^{1/2} \times \left(\frac{t_0}{\ell} \right) \left(\frac{b}{a} \right). \quad (21)$$

We can now investigate the effects of tapering by comparing the influence of the length-to-thickness ratio on the frequencies calculated from equations (18) and (21).

We have

$$\frac{\Omega_n}{\Omega_{mc}} = \frac{\lambda_n}{\pi m}. \quad (22)$$

We see that there is very little difference between the frequency of the q th mode ($q = n = m$) of face-shear in a tapered plate and its frequency in a uniform plate. But if $a > b$, the frequencies in the tapered plate are improved. Although the solutions for the face-shear vibrations of uniform and tapered plates reveal that the frequencies of these vibrations are independent of the thickness of the plate, the frequencies change with the type of tapering and the displacement pattern is altered [9, 17].

4.2. (Case-2). If the thickness varies exponentially, we have

$$U = e^{-x_3/2\ell} \left[C \cos \frac{\delta x_3}{\ell} + D \sin \frac{\delta x_3}{\ell} \right], \quad (23)$$

where

$$\delta = \frac{\sqrt{4\ell^2\beta^2 - 1}}{2}. \quad (24)$$

Applying the boundary conditions (10), we obtain

$$\sin \delta = 0, \text{ i.e. } \beta_r^2 = \frac{1 + 4r^2\eta^2}{4\ell^2}, \quad (25)$$

$r = \text{integer.}$

Introducing ω_s as a reference frequency, we have for the dimensionless frequencies, Ω_r , of the r th mode of face-shear

$$\Omega_r \equiv \omega_r/\omega_s = \frac{\sqrt{1 + 4r^2\eta^2}}{2\pi} \times \left(\frac{c_{55}}{c_{66}} \right)^{1/2} \left(\frac{t_0}{\ell} \right). \quad (26)$$

If the dimensionless frequencies, Ω_r , are plotted as functions of the length-to-thickness ratio, $1/t_0$, the nature of the curves will be the same as given in Fig. 2.

To investigate the effects of tapering, we compare the influence of the length-to-thickness ratio on the frequencies as discussed previously. Thus, we have

$$\frac{\Omega_r}{\Omega_{mc}} = \sqrt{\frac{1 + 4r^2\eta^2}{4m^2\pi^2}}. \quad (27)$$

We see here that there is very little difference between the frequency of the k th mode ($k = r = m$) of the face-shear in a tapered plate and its frequency in a uniform plate. Although the displacement pattern is altered, the frequencies remain almost the same. The solution for the face-shear vibrations of a uniform plate and that of a tapered plate reveals that the frequencies of these vibrations are independent of the thickness of the plate. The only dependence on the thickness is the "Shape effect" which governs the motion [9, 17].

SOLUTION FOR A TAPERED PLATE WITH PIECEWISE CONTINUOUS BOUNDARY

In this case, the displacements are written as

$$U_1(x_3) = A J_0(\beta_1 x_3) + B Y_0(\beta_1 x_3) \quad (0 < x_3 \leq \ell_1) \quad (28)$$

and

$$U_2(x_3) = A_2 \sin \beta_2 x_3 + B_2 \cos \beta_2 x_3 \quad (\ell_1 < x_3 \leq \ell)$$

$\beta_{1,2}^2 = \rho_{1,2} \omega^2 / (c_{55})_{1,2}$. Applying boundary conditions (11), we get

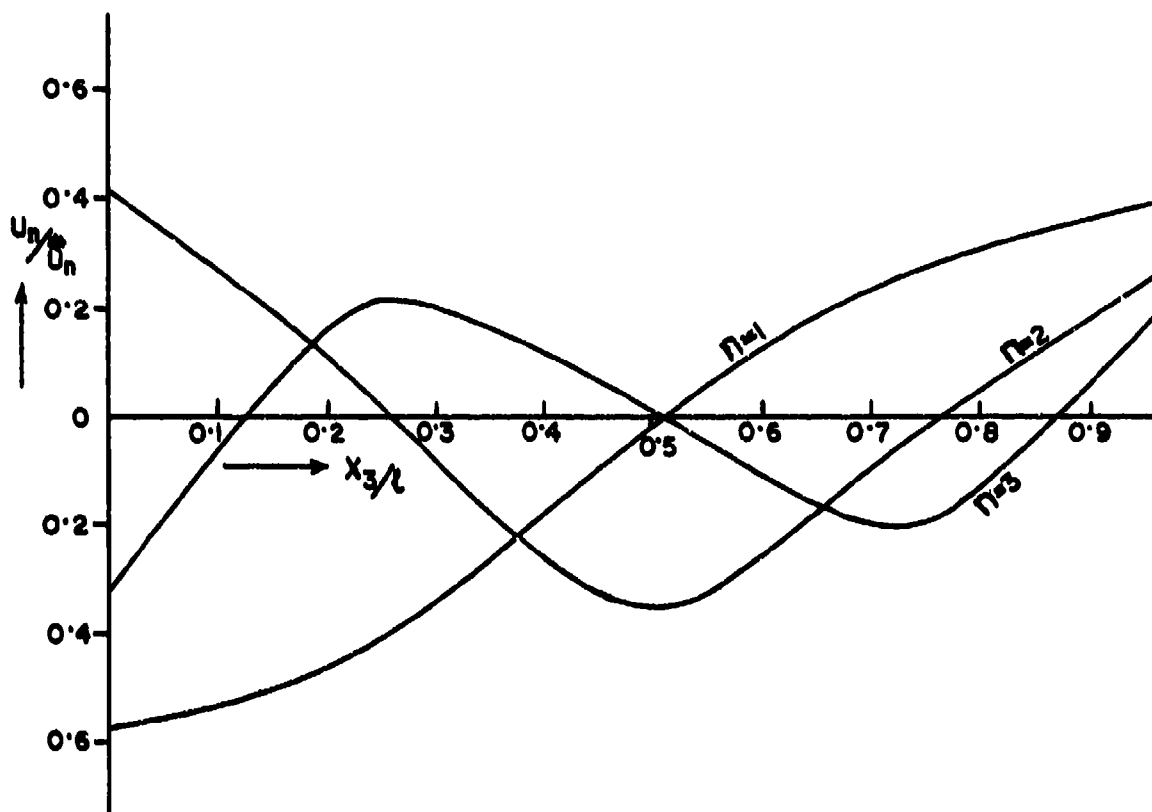


Fig. 3— Face-shear mode shapes for a tapered plate
(when the thickness varies linearly, a-b)

$$\frac{J_1(\beta_1 l_1)}{J_0(\beta_1 l_1)} + \frac{\beta_2 (c_{55})_2 \tan \beta_2 (l - l_1)}{\beta_1 (c_{55})_1} = 0. \quad (29)$$

If the two parts are composed of the same material, we have $\beta_1 = \beta_2 = \beta$ and for small values of β , we can write

$$\frac{\beta l_1}{2} + \tan \beta (l - l_1) = 0. \quad (30)$$

The equation shows that the frequency spectrum of a plate with piece-wise continuous boundary is independent of the thickness of the plate which agrees with the previous results.

If $l_1 = 0$, the equation reduces to that for a uniform plate. In this case, the

the possible values of frequency are given by

$$\beta_m = m\pi/l, \quad m = 1, 2, \dots \quad (31)$$

If, however, $l - l_1 = 0$, we have

$$J_1(\beta l) = 0, \quad (32)$$

the roots of which are $J_{1,7}$

$$\beta_{11} l = 3.8317, \quad \beta_{12} l = 7.0156, \quad \beta_{13} l = 10.1735, \quad \beta_{14} l = 13.3237, \text{ etc.}$$

The equation (32) represents the equation for a tapered plate which has been discussed by Bleustein (1966) [9].

Thus, we have

$$\frac{\omega_m}{\omega_{cr}} = \frac{3.8317}{\pi}, \quad \frac{7.0156}{2\pi}, \quad \frac{10.1735}{3\pi}, \text{ etc. i.e.,}$$

the frequencies are slightly increased.

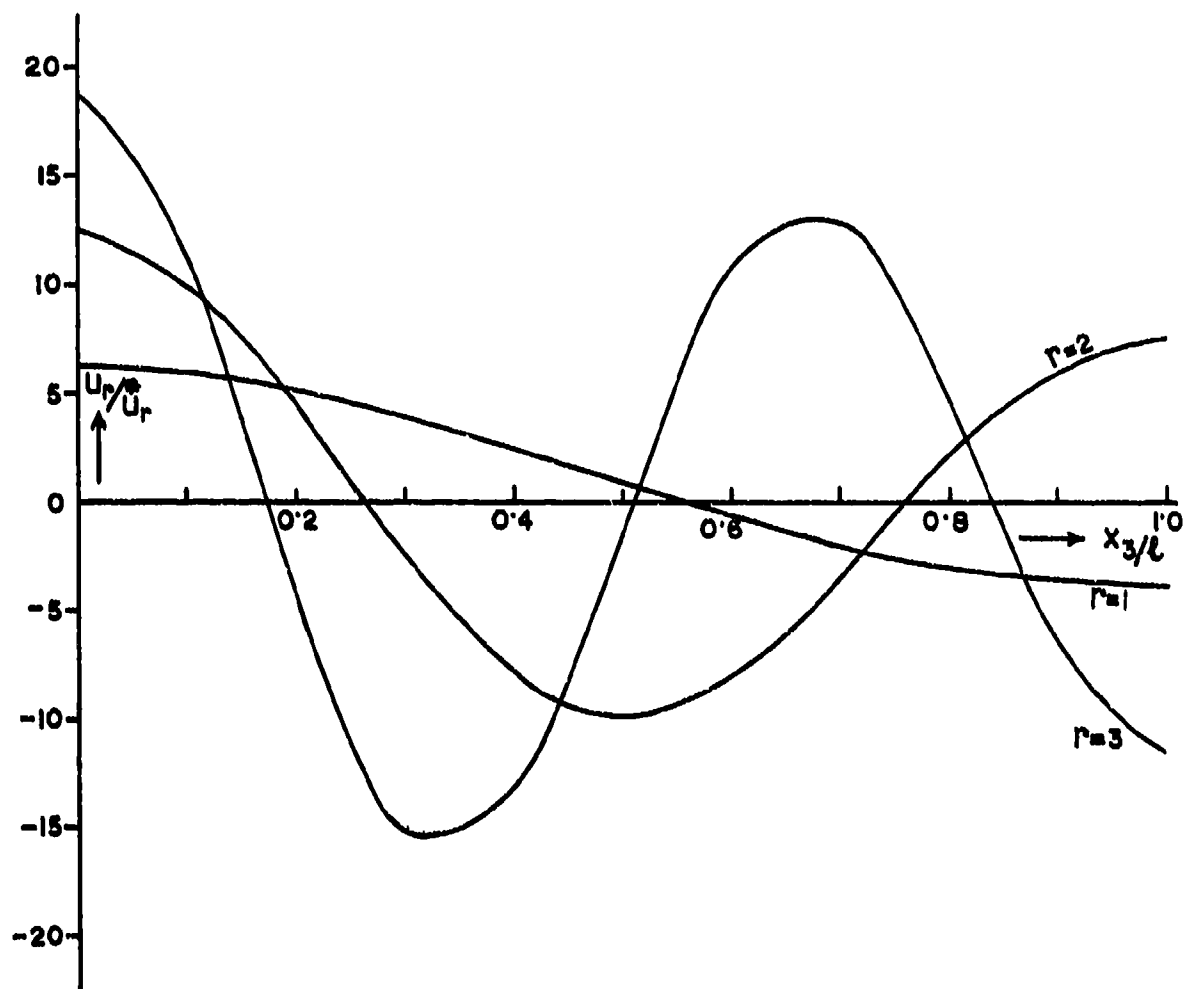


Fig. 4 — Face-shear mode shapes for a plate of exponentially varying thickness

MODE SHAPES

The n th mode of face-shear motion in the first case is described by

$$U_n = \bar{U}_n \left[J_0 \left\{ \bar{\lambda}_n \left(a + \frac{bx_3}{l} \right) \right\} - \frac{J_1(\bar{\lambda}_n)}{\bar{\lambda}_n} \gamma_0 \left\{ \frac{\bar{\lambda}_n}{a} \left(a + \frac{bx_3}{l} \right) \right\} \right] \quad (33)$$

where \bar{U}_n is an arbitrary constant. The r th mode of face-shear motion in the second case is described by

$$U_r = \bar{U}_r \left[e^{-x_3/2l} \left\{ 2\delta_r \cos \frac{\delta_r x_3}{l} + \sin \delta_r x_3/l \right\} \right] \quad (34)$$

where $\delta_r = \sqrt{4l^2\beta_r^2 - 1} = r\pi$ and \bar{U}_r is an arbitrary constant.

In Fig. 3 several mode shapes, U_r/\bar{U}_r and in Fig. 4, U_r/\bar{U}_r are plotted as a function of x_3/l . The motion in the fundamental mode and the low overtones of face-shear are more evenly distributed throughout the length of the plate although the maximum amplitude always occurs at the thin edge. In the higher overtones of face-shear, the motion tends to be more and more localised near the thin edge of the

plate. In Fig.4, we should note the interesting mode shapes.

CONCLUDING REMARKS

On analysing the results, we find that although the frequencies of the face-shear modes of uniform and tapered plates and plate with piecewise continuous boundary are independent of the thickness of the plate, the frequency spectrum and mode shapes are changed due to tapering. The type of tapering can slightly increase or decrease the frequency than that in a uniform plate. The study of the special features of the frequency spectrum of such plate might point the way to the design of new transducer devices and the results may be useful to determine the effects of small manufacturing errors on the frequency spectrum of a plate of uniform thickness.

REFERENCES

- a. H. Deresiewicz and R.D.Mindlin, "Waves on the Surface of a Crystal", J.Appl. Phys., Vol.28, No.6, pp.669-671, 1957
- b. R.D.Mindlin, J.Appl. Phys., Vol.27, 1462, 1956
- c. R.D.Mindlin, "High Frequency Vibrations of Crystal Plates," Q.Appl. Math., Vol. 19, 51, 1961
- d. R.D.Mindlin, "High Frequency Vibrations of Plated, Crystal Plates," in Progress in Applied Mechanics, The Prager Anniversary Volume, Macmillan, New York, 1963
- e. R.D.Mindlin & P.C.Y.Lee, "Thickness-shear and Flexural Vibrations of Partially Plated, Crystal Plates," Int. J.Solids Structures, Vol.2, pp.125-139, 1966
- f. R.D.Mindlin, "Thickness-Twist Vibrations of an Infinite, Monoclinic, Crystal Plate," Int. J.Solids Structures, Vol. 1, pp. 141-145, 1965
- g. R.D.Mindlin and W.J.Spencer, "Anharmonic, Thickness-Twist Overtones of Thickness-Shear and Flexural Vibrations of Rectangular, AT-Cut Quartz Plates," J.Acoust.Soc.Am., Vol.42, No.6, pp. 1268-1277, 1967
- h. R.D.Mindlin, "Bechmann's Number for Harmonic Overtones of Thickness/Twist Vibrations of Rotated-Y-Cut Quartz Plates," J. Acoust. Soc.Am., Vol.41, No.4, pp. 969-973, 1967
- i. R.D.Mindlin & D.C.Gasis, "Strong Resonances of Rectangular AT-cut Quartz Plates," Proc.4th U.S.Natn. Congr. of Applied Mechanics, pp. 305-310
- j. R.D.Mindlin & M.Forray, "Thickness-Shear and Flexural Vibrations of Contoured Crystal Plates," J.Appl. Phys., Vol.25, 12, 1954
- k. R.D.Mindlin, "Equations of High Frequency Vibrations of Thermo-piezoelectric Crystal Plates," Int. J.Solids and Structures, Vol.8, pp. 895-906, 1972
- l. R.P.Jerrard, "Vibrations of Quartz Crystal Plates," Q.Appl. Math., Vol. 18, 173, 1960
- m. S.De, "Problem on the Vibrations of an Infinite, Monoclinic, Crystal Plate," J.Tech. Phys., Vol. 16, no.3, pp. 363-376, 1975
- n. S.De, "Vibrations of Monoclinic Crystal Plates," Acta Geophy.Pol. (to be published).
- o. R.K.Kaul & R.D.Mindlin, "Frequency Spectrum of a Monoclinic Crystal Plate," J. Acoust. Soc. Am., Vol.34, No.12, pp. 1902-1910, 1962
- p. R.K.Kaul & R.D.Mindlin, "Vibrations of Infinite, Monoclinic Crystal Plate at High Frequencies and Long Wavelengths", J. Acoust.Soc. Am., Vol.34, No.12, pp.1895-1901, 1962
- q. J.L.Elaststein, "Thickness-Twist and Face-Shear Vibrations of a Contoured Crystal Plate," Int. J.Solids Structures, Vol.2, pp.351-360, 1966
- r. G.B.Loutsenheiser, "Thickness/Twist Vibrations of a Truncated Linearly Tapered, Crystal Strip," J.Acoust. Soc.Am., Vol.41, No.4(2), pp.962-968, 1972
- c. W.J.Spencer, "Transverse Thickness Modes in BT-Cut Quartz Plates," J. Acoust. Soc.Am., Vol.41, No.4(2), pp.994-1001, 1967

- t. R.A.Sykes, "Modes of Motion in Quartz Crystals, the Effects of Coupling and Methods of Design," in Quartz Crystals for Electrical Circuits (ed. R.A.Heising), D.Van Nostrand, New York, 1946
- u. W.P.Mason, Piezoelectric Crystals and their Applications to Ultrasonics, D.Van Nostrand, New York, 1950
- v. E.Jahnke, F.Ende & F.Lösch, Tables of Higher Functions, 6th ed., McGraw-Hill, New York, Toronto, London, 1960
- w. R.D.Mindlin, "High Frequency Vibrations of Quartz Plates by Expansion in Series of Bessel Function", Int. J.Solids & Struct., Vol. 16, No.9 pp. 785-91, 1980
- x. D.R.Cowdrey & J.R.Willis, "Application of Finite Element Method to the Vibrations of Quartz Plates," J. Acoust. Soc. Am., Vol.56, No.1, pp.94-98, 1974
- y. B.K.Sinha & D.S.Stevens, "Thickness-Shear Vibration of a Beveled AT-cut Quartz Plate," J. Acoust.Soc. Am., Vol.66, No.1, pp. 192-6, 1979

DYNAMIC BEHAVIOR OF COMPOSITE LAYERED BEAMS

BY THE FINITE ELEMENT METHOD

P. Trompette, R. Gaertner
I.N.S.A.
Laboratoire de Mécanique des Structures
E.R.A. 911 - Bâtiment : 113
20, avenue Albert Einstein
69621 Villeurbanne - FRANCE

A new finite element especially adapted to the study of unsymmetrical laminated straight or curved beams is presented - shear effects in all the laminates are included in the theory -. Both the different stress and displacement continuity conditions at each laminate interface as the free stress conditions on the top and bottom surfaces of the beam are satisfied. This model has been applied to the determination of resonance frequencies of a ski with different boundary conditions. Good agreement between experiences and calculations has been observed. Some of the calculated frequencies have been correlated to those measured during and actual ski run.

INTRODUCTION

Considerable attention has been devoted in the last twenty five years to composite materials and especially to straight and curved beams which are widely used in structural elements. A complete survey of this question is quite impossible as publications are numerous, however an elementary classification in order of increasing model sophistication can be attempted. First one can isolate the papers using non homogeneous theory of elasticity or microstructural theory which lead to equivalent homogeneous beams or plates. Amongst them one should mention the works of J.M. Whitney [1,2,3], S.B. Dong [4,5], C.T. Sun [6,7], Di Taranto [8, 9], P.C. Yang [10]. All these papers suffer from various simplifying assumptions imposed by the analytical approach to the problem. This explains why, as soon as the finite element method was developed, it was applied to the study of dynamic of the laminated beams. K.M. Ahmed [11,12] has investigated the static and the dynamic behaviour of straight and curved three laminate beams with a honeycomb core. A.V.K. Murty [13], T.P. Khatua and Y.K. Cheung [14], A.S. Mawanya and J.D. Davies [15] have developed various multilayer plate or beam finite elements. In [13] the effects of bending, shear flexibilities, rotatory and longitudinal inertia of all laminates have been included out the hypothesis limit the theory to symmetric laminated beams. In [14] and [15] the longitudinal displacements of each layer are retained in the analysis which may lead to numerous D.O.F. especially for the plates ; the same remark can be formulated when

the hybrid stress finite element formulation is used [16,17]. Such complex models are only justified for thick laminates. In this paper a new finite element (including the shear effects) is proposed which attempts to give precise stress results in each layer while retaining a small number of nodal variables. The thicknesses of the layers are constant. This element has been applied to predict the frequencies and mode shapes of an actual ski manufactured by ROSSIGNOL S.A. with various boundary conditions. This work can be extended to the dynamic behavior of laminated plates.

THEORY - GENERAL ASSUMPTIONS

Figure (1) represents the cross section of a laminated beam with its coordinate system. As

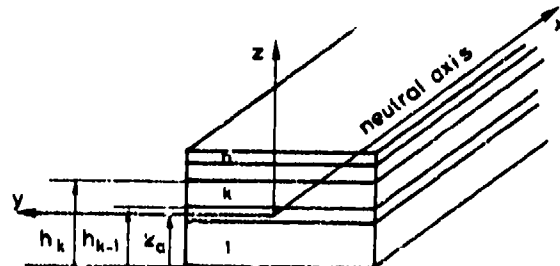


Fig. 1

the laminates can be located unsymmetrically, the reference plane xoy will contain the neutral axis which will be determined later. In this theory the effects of bending, shear, rotatory and longitudinal inertias of all laminates are included. The displacements of a point p_k of the layer k are noted $u^{(k)}$, $v^{(k)}$, $w^{(k)}$. The principal assumptions are the following :

a) - The beam is thin and the displacement $w^{(k)}$ of each layer is taken as independent of z , further it is the same for all the layers

$$w^{(k)} = w(x, y) \quad (1)$$

b) - The effect of the transverse normal stress σ_{zz} is assumed to be negligible and to simplify the presentation, the material of each layer is elastic. Thus the stress-strain relations for the layer k are :

$$\begin{pmatrix} \sigma_{xx}^{(k)} \\ \sigma_{yy}^{(k)} \\ \sigma_{xy}^{(k)} \\ \sigma_{xz}^{(k)} \\ \sigma_{yz}^{(k)} \end{pmatrix} = \begin{pmatrix} C_{11}^{(k)} & C_{12}^{(k)} & 0 & 0 & 0 \\ 0 & C_{22}^{(k)} & 0 & 0 & 0 \\ 0 & 0 & C_{33}^{(k)} & 0 & 0 \\ 0 & 0 & 0 & C_{44}^{(k)} & 0 \\ 0 & 0 & 0 & 0 & C_{55}^{(k)} \end{pmatrix} \begin{pmatrix} \epsilon_{xx}^{(k)} \\ \epsilon_{yy}^{(k)} \\ \epsilon_{xy}^{(k)} \\ \epsilon_{xz}^{(k)} \\ \epsilon_{yz}^{(k)} \end{pmatrix} \quad (2)$$

Sym.

c) - The strain-displacement relations are those of the classical theory of elasticity :

$$\begin{aligned} \epsilon_{xx}^{(k)} &= u_{,x}^{(k)} & \epsilon_{xz}^{(k)} &= w_{,x} + u_{,z}^{(k)} \\ \epsilon_{yy}^{(k)} &= v_{,y}^{(k)} & \epsilon_{yz}^{(k)} &= w_{,y} + v_{,z}^{(k)} \\ \epsilon_{xy}^{(k)} &= u_{,y}^{(k)} + v_{,x}^{(k)} \end{aligned} \quad (3)$$

d) - Following the work of [1] and [2], the shear stresses $\sigma_{xz}^{(k)}$, $\sigma_{yz}^{(k)}$ of the k th layer are assumed to vary parabolically. They take the form :

$$\begin{aligned} \sigma_{xz}^{(k)} &= \{ a_x^{(k)} + C_{44}^{(k)} (1+b_x(z+z_a)) - \frac{1}{h_n^2} (z+z_a)^2 \} \phi_x(x, y) \\ \sigma_{yz}^{(k)} &= \{ a_y^{(k)} + C_{55}^{(k)} (1+b_y(z+z_a)) - \frac{1}{h_n^2} (z+z_a)^2 \} \phi_y(x, y) \end{aligned} \quad (4)$$

in which

- $\phi_x(x, y)$, $\phi_y(x, y)$ are functions of the mean shear of a cross y section,

- $a_x^{(k)}$, $a_y^{(k)}$, b_x , b_y are constants which are determined from the conditions of continuity at each layer interface ;

$$\begin{pmatrix} \sigma_{xz}^{(k)} \\ \sigma_{yz}^{(k)} \end{pmatrix} \Big|_{z=h_k-z_a} = \begin{pmatrix} \sigma_{xz}^{(k+1)} \\ \sigma_{yz}^{(k+1)} \end{pmatrix} \Big|_{z=h_k-z_a} \quad k=1, 2, \dots, n-1 \quad (5)$$

and from the requirement that stresses vanish on the top and the bottom surfaces

$$\begin{pmatrix} \sigma_{xz}^{(1)} \\ \sigma_{yz}^{(1)} \end{pmatrix} \Big|_{z=-z_a} = 0 \quad \begin{pmatrix} \sigma_{xz}^{(n)} \\ \sigma_{yz}^{(n)} \end{pmatrix} \Big|_{z=h_n-z_a} = 0 \quad (6)$$

- z_a is the unknown z coordinate of the neutral axis with respect to the bottom of the beam. This coordinate is now calculated.

The two last relations (3) are integrated in z . Thus :

$$\begin{aligned} u^{(k)} &= u_0^{(k)} - z w_{,x} + f_x^{(k)}(z) \phi_x \\ v^{(k)} &= v_0^{(k)} - z w_{,y} + f_y^{(k)}(z) \phi_y \end{aligned} \quad (7)$$

with $u_0^{(k)}$, $v_0^{(k)}$, w only functions of x and y

$$\begin{aligned} f_x^{(k)} &= \left(\left(\frac{a_x^{(k)}}{C_{44}^{(k)}} + 1 \right) z + \frac{b_x}{2} (z+z_a)^2 \right. \\ &\quad \left. - \frac{1}{3h_n^2} (z+z_a)^3 \right) \end{aligned} \quad (8)$$

The same equation can be written with the subscript y . Then :

$$\epsilon_{xx}^{(k)} = u_{0,x}^{(k)} - z w_{,xx} + f_{x,x}^{(k)} \phi_{x,x} \quad (9)$$

$$\epsilon_{yy}^{(k)} = v_{0,y}^{(k)} - z w_{,yy} + f_{y,y}^{(k)} \phi_{y,y} \quad (10)$$

As the width of the beam is small, the curvature $w_{,yy}$ is neglected. With this hypothesis, the longitudinal stress in the layer k is the sum of three terms representing the extension, the bending and the shear :

$$\begin{aligned} \sigma_{xx}^{(k)} &= C_{11}^{(k)} u_{0,x}^{(k)} + C_{11}^{(k)} v_{0,y}^{(k)} - C_{11}^{(k)} z w_{,xx} \\ &\quad + C_{11}^{(k)} f_{x,x}^{(k)} \phi_{x,x} + C_{12}^{(k)} f_{y,y}^{(k)} \phi_{y,y} \end{aligned} \quad (11)$$

Retaining only the longitudinal stress due to the bending, its resultant N_{xxf} must be zero which leads to :

$$N_{xxf} = \sum_{k=1}^n \int_{h_{k-1}-z_a}^{h_k-z_a} -z C_{11}^{(k)} w_{,xx} dz = 0 \quad (12)$$

and gives the position of the neutral axis located in the layer λ :

$$z_a = \frac{\sum_{k=1}^n \left(\sum_{l=1}^n C_{11}^{(l)} (h_l^2 - h_{l-1}^2) \right) / \sum_{l=1}^n C_{11}^{(l)} (h_l - h_{l-1})}{\sum_{l=1}^n C_{11}^{(l)} (h_l - h_{l-1})} \quad (13)$$

DISPLACEMENTS

From [7] and [13] it is now possible to determine the displacements of each layer. If $u_\lambda(x, y)$ and $v_\lambda(x, y)$ are the displacements of the layer λ in which the neutral axis is located, the continuity at each layer interface gives the following formulae :

$$u_o^{(\lambda-1)} = u_o + \sum_{k=1}^{\lambda-1} (h_{\lambda-k} - z_a) \left(\frac{x}{C_{44}(\lambda-k+1)} \right) - \frac{x}{C_{44}(\lambda-1)} \phi_x \quad (16)$$

$$u_o^{(\lambda+1)} = u_o + \sum_{k=1}^{\lambda+1} (h_{\lambda+k-1} - z_a) \left(\frac{x}{C_{44}(\lambda+k-1)} \right) - \frac{x}{C_{44}(\lambda+1)} \phi_x \quad (15)$$

respectively for the layers i below and above the layer λ . [14] and [15] can be written

$$u_o^{(k)} = u_o + g_x^{(k)} \cdot \phi_x \quad (16)$$

Following the same procedure, it is easily shown that :

$$v_o^{(k)} = v_o + g_y^{(k)} \phi_y \quad (17)$$

Thus

$$u^{(k)} = u_o - z v_{,x} + p_x^{(k)}(z) \phi_x \quad (18)$$

$$v^{(k)} = v_o - z v_{,y} + p_y^{(k)}(z) \phi_y \quad (19)$$

with

$$p_x^{(k)} = f_x^{(k)} + g_x^{(k)} \quad (20)$$

$$p_y^{(k)} = f_y^{(k)} + g_y^{(k)} \quad (21)$$

POTENTIAL AND KINETIC ENERGIES

The general expressions of these energies are :

$$U = \frac{1}{2} \int_V \langle \epsilon \rangle \{ \sigma \} dv \quad (22)$$

$$T = \frac{1}{2} \int_V \rho \langle \dot{u} \rangle \{ \dot{u} \} dv \quad (23)$$

The integration can be performed in the z direction as $u^{(k)}$, $v^{(k)}$, w are explicit functions of z . Thus

$$U = \int_S \sum_{k=1}^n \int_{h_{k-1}-z_a}^{h_k-z_a} \frac{1}{2} \langle \epsilon^{(k)} \rangle \{ \sigma^{(k)} \} dz dx dy \quad (24)$$

$$T = \int_S \sum_{k=1}^n \int_{h_{k-1}-z_a}^{h_k-z_a} \frac{1}{2} \rho_k (\dot{u}_2^{(k)} + \dot{v}_2^{(k)} + \dot{w}_2^{(k)})^2 dz dx dy \quad (25)$$

To determine the stiffness and mass matrices it is now necessary to specify the shape functions in x and y .

The selected finite element has an isosceles trapezoidal form (figure 2). The nodal variables

are the three displacements, the slope in the x direction and the two shear parameters :

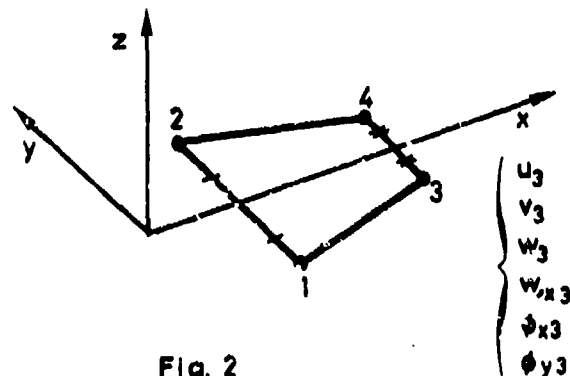


Fig. 2

The shape functions are the usual ones used in a quadrilateral element for u , v , ϕ_x and ϕ_y and are given by the polynomial basis \bar{x}

$$P_1 = \langle 1 \ x \ y \ xy \rangle$$

Unusually, an incomplete and non symmetric polynomial basis in x and y has been selected to represent the variation of w , which is :

$$P_2 = \langle 1 \ x \ x^2 \ x^3 \ y \ xy \ x^2y \ x^3y \rangle$$

This choice enables us to take into account beam torsion. It is convenient as it is well adapted to the desired applications which are described below, it has however the disadvantage of depending on the element orientation. The details of the matrix calculations are particularly tedious and will not be presented here. They have been performed explicitly to shorten the computer time. The final matrices (mass and stiffness) order is 24×24 .

APPLICATIONS

The proposed finite element has been applied to predict the dynamic behavior-frequencies and mode shapes - of a ski taken as a curved laminated beam. Figure (3) shows the physical dimensional parameters usually used to define a ski and figure (4) represents a typical cross section. Figure (5) gives the variations of the width, the camber and the thickness as functions of x . It is pointed out that the number of layers, their thickness or their material constituent may change from the tail to the shovel. It is added that the effects of the side wall and the steel edges, must be taken into account as they influence significantly the bending stiffness of the ski - i.e. the position of the neutral axis.

The material characteristic values, (complex Young modulus) of the different components used in the tested ski (SM 203 from ROSSIGNOL) are summarized in the following table. They are supposed

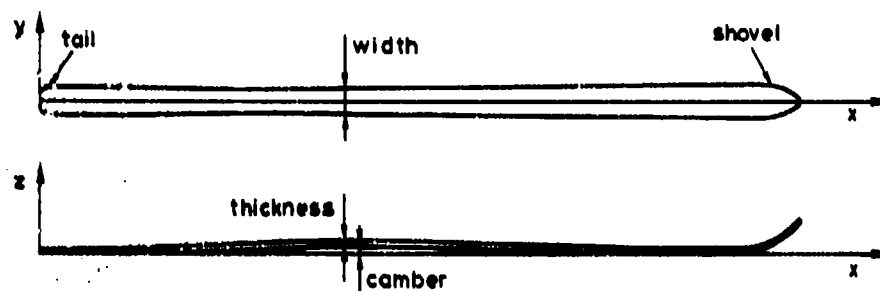


Fig. 3

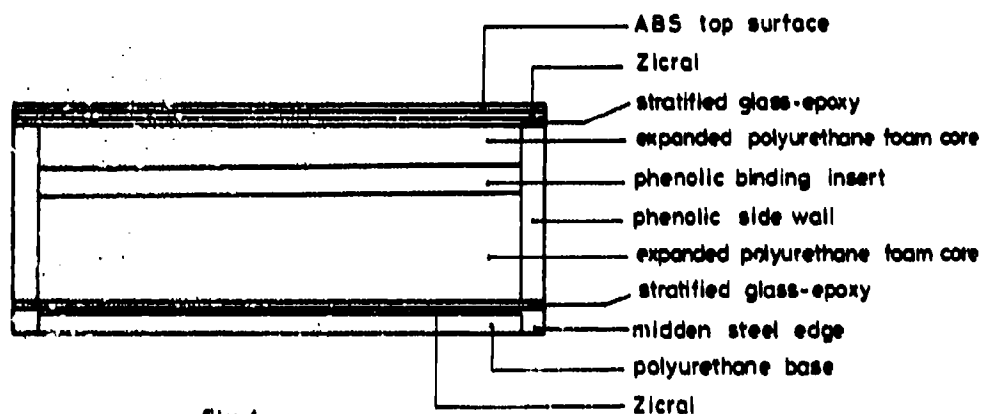


Fig. 4

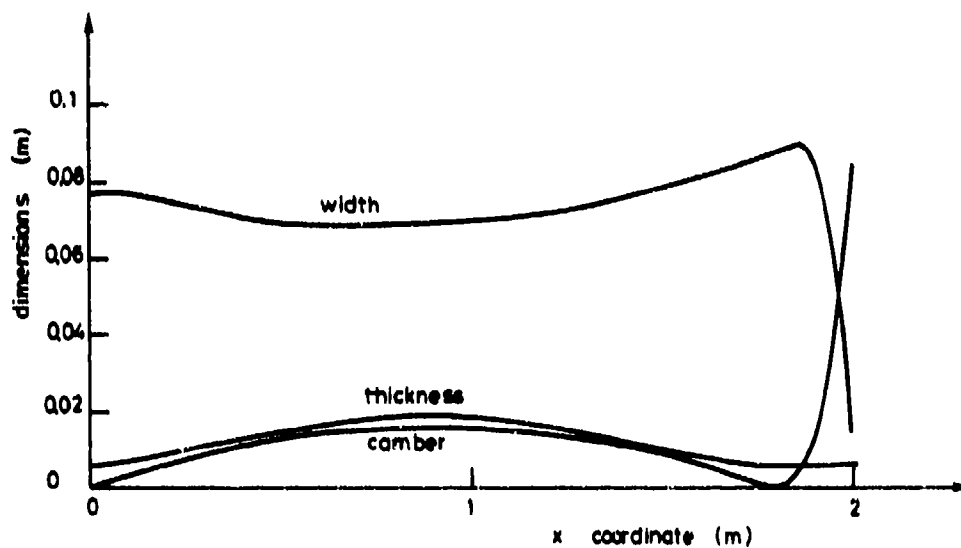


Fig. 5

to be constant in the frequency range studied and have been measured from simple vibratory

tests performed on simple specimens. Generally the Poisson ratio values have been estimated.

Table 1

Material	Young's modulus (N/m ²)	Poisson's ratio	Loss factor	Mass density (kg/m ³)
Zicral	7.0×10^{10}	0.34	0.	2788.
Polyethylene	1.70×10^9	0.40	0.024	1062.
Rubber	2.22×10^8	0.50	0.105	1300.
A.B.S.	2.08×10^9	0.40	0.014	991.
Glass-epoxy	4.34×10^{10}	0.22	0.	2165.
Polyurethane	7.32×10^8	0.45	0.026	600.
Phenolic resin	1.83×10^{10}	0.30	0.014	1404.
Steel	2.0×10^{11}	0.30	0.	7800.

FINITE ELEMENT MODEL. RESULTS

The ski has been discretized in twenty three elements. The stiffness and mass matrices have been modified to take into account the influence of the side wall and the steel edges

which have been considered as eccentric beams.

Experimental and theoretical resonance frequency results are shown in the table (2) on a free-free ski. Agreement is very good for the first flexural modes which are easy to identify experimentally. The other modes are generally coupled with flexure.

Table 2

Frequencies (Hz)		Mode shapes
Finite element	Experience	
19.2	18.9	1 st flexural mode (xs plane)
38.9	38.2	2 nd " " (xs ")
67.6	67.2	3 rd " " (xs ")
105.2	105.4	4 th " " (xs ")
111.2		1 st " " (ys ")
153.2		5 th " " (xs plane)

It has been established [18] that during a carved turn the weight of the skier and the centrifugal force initiate a very large pressure on the section of the ski below the shoe. In order to simulate such a situation two types of boundary conditions have been tested. First the skis are again calculated free-free but masses (20 kg per node) are added to the appropriate nodes, (Fig.6a), then the condition free-free is replaced by the condition : partially supported on an elastic foundation(Figure 6b). It appears that these two types of boundary conditions give similar results, (Table 3).

Table 3

Frequencies of the loaded ski (Hz)	
Free-Free	On elastic foundation
14.3	12.0
27.3	21.1
45.5	42.7
70.4	79.7
83.1	84.6
99.7	90.4
	106.0
	126.1

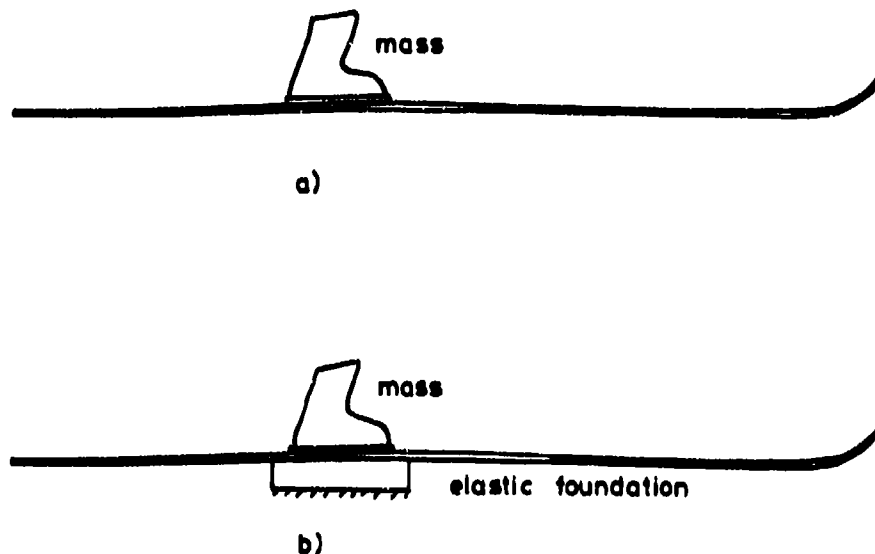


Fig. 6

Further some of the calculated frequencies can be related to those measured during a run on ski tracks (Figures 7a), 7b), 7c)). Obviously this relation cannot be beyond a doubt as the boundary conditions are always changing during an actual skiing test. However conclusive

evidence was obtained by modifying the ski structure which provoke shift in some of the frequencies. The different values of the damping factor for each of the calculated or measured frequencies have not been reported in the different tables as they are always around two or three per cent.

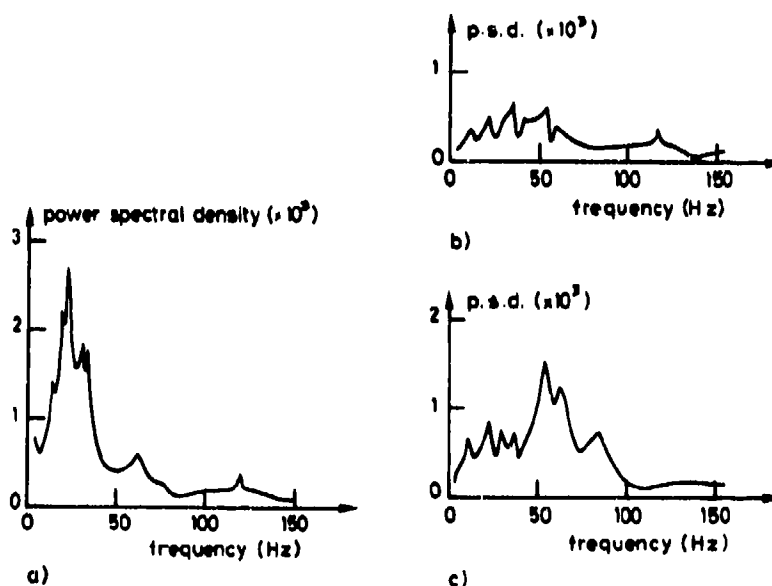


Fig. 7

CONCLUSION

A new finite element to calculate the behaviour of composite beams has been presented. It takes into account a parabolic variation of the shear stresses in the thickness layers, the continuity conditions at each interface both for the displacements and the convenient stress, and the free stress boundary conditions at the top and the bottom. Despite of all these refinements the number of D.O.F. at each node remains small. This element is commonly used in ski behaviour studies but can be used for other applications such as bumpers. In a recent development large strains have been included.

ACKNOWLEDGEMENTS

The authors are grateful to the ROSSIGNOL S.A. for their financial support and for authorizing the publication of this paper.

REFERENCES

- [1] J.M. Whitney, "The effect of transverse shear deformation on the bending of laminated plates", *J. Composite Materials*, vol.3, 1969, pp.534-547.
- [2] J.M. Whitney, N.J. Pagano, "Shear deformation in heterogeneous anisotropic plates", *J. Applied Mech.*, 1970, pp.1031-1036.
- [3] J.M. Whitney, A.W. Leissa, "Analysis of heterogeneous anisotropic plates", *J. of Appl. Mech.*, 1969, pp.261-266.
- [4] S.B. Dong, R.B. Nelson, "On natural vibrations and wave in laminated orthotropic plates", *J. of Appl. Mech.*, 1972, pp.739-745.
- [5] S.B. Dong, I.K.W. Tso, "On a laminated orthotropic, shells theory including transverse shear deformation", *J. of Appl. Mech.*, 1972, pp.1091-1095.
- [6] C.T. Sun, "Microstructure theory for a composite beam", *J. of Appl. Mech.*, 1971, pp.947-954.
- [7] C.T. Sun, J.D. Ashenbach, G. Herrmann, "Continuum theory for a laminated medium", *J. of Appl. Mech.*, 1968, pp.467-471.
- [8] R.A. Di Taranto, "Theory of vibratory bending for elastic and viscoelastic layered finite length beams", *J. of Appl. Mec.*, 1965, pp.881-886.
- [9] R.A. Di Taranto, W. Blasingame, "Composite damping of vibrating sandwich beams", *J. of Engng. for Industry*, 89, 1967, pp.633-638.
- [10] P.C. Yang, C. Norris, Y. Stavsky, "Elastic wave propagation in heterogeneous plates", *Int. J. Solids and Structures*, 1966, vol.2, pp.665-684.
- [11] K.M. Ahmed, "Free vibration of curved sandwich beams by the method of finite elements", *J.S.V.*, 1971, 18, pp.61-74.
- [12] K.M. Ahmed, "Static and dynamic analysis of sandwich structures by the method of finite elements", *J.S.V.*, 1971, 18, pp.75-91.
- [13] A.V.K. Murty, R.P. Shimp, "Vibration of laminated beams", *J.S.V.*, 1974, 36, pp.273-284.
- [14] T.P. Khatua, Y.K. Cheung, "Bending and vibration of multilayer sandwich beams and plates", *Int. J. Num. Meth. in Engng.*, 1973, 6, pp.11-24.
- [15] A.S. Mawanya, J.D. Davies, "Finite element bending analysis of multilayer plates", *Int. J. Num. Meth. in Engng.*, 1974, 8, pp.215-23.
- [16] S.T. Mau, P. Tong, T.H. Pian, "Finite element solutions for laminated thick plates", *J. of Composite Mat.*, 1972, 6, pp.304-309.
- [17] R.L. Spilker, "A hybrid stress finite element formulation for thick multilayer laminates", *Computer and Structures*, 1980, 11, pp.507-514.
- [18] The mechanics of ski show interaction during a carved turn. *Mechanics and Sports*, A.M.D., vol.4, 1973, pp.155-173.